An Investigation of Transition Metal and Oxygen Redox in Lithium-Rich Cathode Materials



Dominic Pascal Förstermann

Trinity College

University of Oxford

A thesis submitted for the degree of

Doctor of Philosophy

Michaelmas 2021

"To see what is in front of one's nose needs a constant struggle."

—*George Orwell*

Acknowledgements

First and foremost I want to thank my supervisor, Peter Bruce. Thank you for giving me the unique opportunities that working in your group and being at Oxford itself have offered me. I am incredibly fortunate to have worked alongside you and the world-class team you have created, learning every day in a driven environment, with access to a laboratory containing every piece of equipment one could wish for.

Second, I want to thank Oxford University Press and Trinity College. Without your unparalleled generosity, this would not have been possible. Thank you for awarding me the Trinity Whitehead Scholarship through a Clarendon Award, which allowed me to come to Oxford. I owe additional thanks to Trinity College, for further supporting me financially during my write-up period, as well as subsidising my language courses. Through both Clarendon and Trinity, I got to meet and befriend some of the most intelligent, inspiring people I have ever met, who will accompany me for the rest of my life. Thank you for fostering communities that bring people together and enable them to exchange views and ideas. Ultimately, this is one of the most important aspects of my time at Oxford.

I furthermore want to thank EPSRC and the Department of Materials for supporting me during my DPhil, and providing the world-class research facilities I was able to use, both at Oxford, as well as across the UK.

Robert House, you are one of the most talented scientists I have ever met, and I

am thankful for your support and much-valued input during my DPhil, as well as your consistently great mood during synchrotron and neutron diffraction trips. Matthew Roberts, thank you for your great input and sheer limitless knowledge of electrochemistry and cathode materials, as well as showing me that there is a scientific world outside of academia. James Somerville, thank you for your many suggestions for my research, your programming skills that helped the entire lab, and showing me the best-looking graphs I have ever seen. Shengda Pu, thank you for teaching me about TEM and collecting data for all of us at ungodly times of the day.

Thank you, Paul Adamson, for proofreading this thesis, giving me valuable feedback, and your constant scientific input.

Thank you, Gareth Hartley, John-Joseph Marie, Alexander Pateman, Conrad Holc, Liyu Jin, Xiangwen Gao, Samuel Wheeler, Isaac Capone, Ziyang (George) Ning, Edouard Boivin, Juan Lozano, Niccolo Guerrini, Rong Hao, Gregory Rees, Adam Sobkowiak, Christian Kuss, Francis Gachao Kinyanjui, and countless others, for many scientific and non-scientific discussion, and making the Bruce group what it is.

Thank you, Zsófia Szabó and Miki Bennett, for consistently supporting me and the whole group, ensuring we all submitted whichever form was required on time, and did not overspend our grants. Thank you, Nadia Abdul-Karim, for keeping us safe and the lab running.

Thank you, Leon Brandt, for our work on single-particles and teaching me about advanced SEM techniques. Thank you, Konstantin Borisenko, for your idea for electron PDF, as well your skills to actually extract it! Thank you Helen Playford, for your invaluable support with performing and analysing neutron PDF data and answering my countless questions about RMC, Olaf Borkiewicz and Kamila Wiaderek, for welcoming us at Argonne, showing me

how to analyse PDF, and collecting data on short notice. Thank you, Nonglak Meethong, Songyoot Kaewmala, and Linlin Patcharapohn Chantrasuwan, for welcoming me in Khon Khaen, letting me use your laboratory, showing me some of the best food I have ever had, and our shared work at SLRI. Thank you, Pieter Glatzel, for welcoming us at ESRF and teaching me about HERFD-XANES. Thank you Chiu Tang, Sarah Day, and Karin Kleiner, for having me at Diamond's I11 beamline countless times, and teaching me about XRD.

I am grateful for all my friends, those I made during my time at Oxford, those whom I have known for many years, and the ones I only met recently. Without you, none of this would be worth it. You know who you are.

Thank you, Daniel. As a brother, you continue to inspire me with your sheer endless drive and intelligence.
Lastly, I am indebted to my Mother. Thank you for supporting me during my DPhil, life in general, and your invaluable input. Without you, none of this would have been possible.

Abstract

Cathode materials remain one of the main limiting factors for increasing the specific energy of lithium ion batteries. The reversible storage of charge on lattice oxygen, called oxygen redox (O redox), has been identified as a promising route for addressing the problem in layered and disordered rocksalt materials. Currently, several interrelated challenges, including slow kinetics, voltage and capacity fade, as well as structural changes, remain, that are investigated in this thesis.

A dedicated *operando* cell, capable of applying significant stack pressure, was built to investigate layered Lithium-rich materials. It is used to study $Li_{1.2}Ni_{0.13}Co_{0.13}Mn_{0.54}O_2$ and $Li_{1.2}Ni_{0.2}Mn_{0.6}O_2$ using high energy-resolution fluorescence-detected X-ray absorption near edge structure (HERFD-XANES), as well as X-ray emission spectroscopy (XES). The complex interplay between bulk oxygen and transition-metal redox is analysed, and it is demonstrated that Ni is fully oxidised to Ni^{4+} in one compound but not the other.

The structure of the disordered rocksalt Li_2MnO_2F is solved using a combination of neutron pair distribution function (PDF) and neutron diffraction, simultaneously fit using a Reverse Monte Carlo (RMC) approach. The capacity fade for the same material is investigated and found to be initially based on a large charge-transfer resistance, associated with the slow O redox kinetics on discharge.

Contents

List of Acronyms and Abbreviations **xiv**

List of Symbols and Operators **xviii**

1 Introduction **1**

1.1 The Development of Secondary Lithium Ion Batteries 1

1.2 The Cathode Challenge 2

1.3 Oxygen Redox and Lithium-Rich Cathode Materials 4

1.3.1 Structures of Layered Stoichiometric and Lithium-Rich Materials . 4

1.3.2 The Structure-Electrochemistry Relationship of Oxygen Redox . . 6

1.3.2.1 The Nature of Oxidised Oxygen Species 9

1.3.3 Challenges with 3d Lithium-Rich Cathode Materials 11

1.3.3.1 First-Cycle Voltage Hysteresis 11

1.3.3.2 Voltage Fade with Cycle Life 12

1.4 Disordered Rocksalt Cathode Materials 12

1.4.1 Structures of Rocksalt Cathode Materials 13

1.4.2 Lithium Diffusion in Rocksalts and Percolation Theory 13

1.4.3 The Redox Chemistry of Disordered Rocksalts 15

1.4.4 Disordered Lithium Oxyfluoride Rocksalts 16

1.4.5 Present Challenges with Disordered Rocksalt Cathodes 17

1.5 Thesis Outline and Objectives 18

2 Theory and Methods **20**

2.1 Working Principle of a Cell and Electrochemical Testing 20

2.1.1 Cell Voltage 22

2.1.2 Galvanostatic Cycling 23

2.1.3 Energy Stored Within a Cell 24

2.1.3.1 Influence of Current Flow 26

2.1.4 *Operando* Electrochemical Mass Spectrometry (OEMS) 26

2.1.5 Electrochemical Impedance Spectroscopy (EIS) 27

2.2 Synthesis of Cathode Materials 30

2.2.1 Solid-State Synthesis 30

2.2.1.1 Resorcinol Formaldehyde Gel-Assisted Solid State Synthesis 30

2.2.2 Mechanochemical Synthesis 31

2.3 Electrode Preparation and Cell Assembly 31

2.3.1 Composite Cathode Preparation 31

2.3.2 Coin Cell Assembly 32

2.3.3 Three-Electrode Pouch Cell Assembly 33

2.4 Total Scattering and Diffraction Analysis 34

2.4.1 Diffraction Analysis and Long-Range Order 35

2.4.1.1 Rietveld Refinement 38

2.4.2 Total Scattering and Local Structure Analysis 40

2.4.3 Reverse Monte Carlo Fitting 43

2.4.3.1 Total Scattering Function Convolution 45

2.4.4 Practical Aspects of Scattering Experiments 46

2.5 Transmission Electron Microscopy (TEM) 46

2.6 X-ray Absorption Spectroscopy (XAS) 47

2.6.1 X-ray Absorption Near Edge Structure (XANES) 50

2.6.1.1 High-Energy-Resolution Fluorescence-Detected X-ray Absorption Near Edge Structure (HERFD-XANES) . . 52
2.6.2 Extended X-ray Absorption Fine Structure (EXAFS) 53
2.7 X-ray Emission Spectroscopy (XES) 54
2.7.1 Chemical Sensitivity of the K_α Fluorescence Lines 55
2.8 Resonant Inelastic X-ray Scattering (RIXS) 57

3 Design of an X-ray-Transparent *Operando* Cell for the Study of Lithium-Rich Cathodes 59

3.1 Introduction 59
3.2 Requirements 62
3.3 Design Description 64
3.4 Component and Material Selection 70
3.4.1 Window Selection 70
3.4.1.1 Structural and Electrical Properties 70
3.4.1.2 X-ray Transparency 72
3.4.1.3 Selected Components 73
3.4.2 Spring Selection 73
3.4.3 Base Material Selection 75
3.4.4 Lid and Spacer Materials Selection 75
3.4.5 Insulating Materials Selection 76
3.4.6 Cell Dimensioning 76
3.4.7 Fastening and Sealing Mechanism 77
3.5 Design Evaluation and Verification 77
3.5.1 Electrochemical Performance 77
3.5.2 X-ray Transmission and Illuminated Window Area 78
3.5.3 Hermetic Sealing 81
3.5.4 Dimensions, Handling, and Practical Considerations 81
3.6 Summary and Discussion 82

4 First-Cycle Transition Metal Oxidation State Changes in Layered Lithium-Rich Compounds **85**

4.1 Introduction . . . 85

4.2 Experimental . . . 88

4.3 Structural Characterisation . . . 92

4.4 Transition Metal Oxidation States Probed via HERFD-XANES and XES . 97

4.4.1 Nickel Oxidation States . . . 97

4.4.2 Cobalt Oxidation States . . . 104

4.4.3 Manganese Oxidation States . . . 109

4.5 Summary and Discussion . . . 112

5 The Structure of Pristine Disordered Rocksalt Li_2MnO_2F **115**

5.1 Introduction . . . 115

5.2 Experimental . . . 117

5.3 Long-Range Order . . . 122

5.4 Morphology, Short-Range Order, and Local Structure . . . 124

5.5 Combined Reverse Monte-Carlo Refinement of Neutron PDF and Diffraction Patterns . . . 129

5.5.1 Fit Parameters and Constraints . . . 129

5.5.2 Fit Results . . . 130

5.5.3 Percolation Network Analysis . . . 135

5.5.4 Oxygen Redox Environments in Li_2MnO_2F . . . 136

5.6 Summary and Discussion . . . 138

6 Voltage and Capacity Fade of Li_2MnO_2F **140**

6.1 Introduction . . . 140

6.2 Experimental . . . 141

6.3 Cycle-Dependent Morphology and Local Structure Changes . . . 146

6.4 Cycle-Dependent Electrochemical Characterisation . . . 153

6.5 Summary and Discussion 160

7 Summary and Outlook **163**

A Appendix **167**

A.1 *Operando* Cell X-ray Transmission for the 3d TM K Edges. 167

A.2 First-Cycle *Operando* X-ray Diffraction Patterns And Fit Details for $Li_{1.2}Ni_{0.2}Mn_{0.6}O_2$ and $Li_{1.2}Ni_{0.13}Co_{0.13}Mn_{0.54}O_2$ 167

A.3 Influence of Carbon and Binder on X-ray PDFs 174

A.4 X-ray PDF Fit Details for Multi-Cycled Li_2MnO_2F Cathodes 174

A.5 Neutron PDF Fit Details for Multi-Cycled Li_2MnO_2F 178

A.6 Impedance Spectra and Fit Parameters for Multi-Cycled Li_2MnO_2F 180

Bibliography **184**

List of Figures

1.1 Structural Overview: Layered and Lithium-Rich Layered Cathodes. 5

1.2 Voltage Profiles of $LiCoO_2$ and $Li_{1.2}Ni_{0.13}Co_{0.13}Mn_{0.54}O_2$. 6

1.3 Electronic States in Stoichiometric and Lithium-Rich Cathode Materials. . 9

1.4 RIXS Maps of Cycled Lithium-Rich Materials. 10

1.5 The Structure of Rocksalt Compounds. 13

1.6 Lithium Percolation Mechanism in Rocksalt Compounds. 14

1.7 Voltage Profile and Cycle-Dependent Capacities for $Na_{1.3}Nb_{0.3}Mn_{0.4}O_2$. . . 17

2.1 Working Principle of a Li Ion Battery. 21

2.2 Drawing: Coin Cell - Exploded View. 33

2.3 Drawing: Three-Electrode Cell Stack - Exploded View. 34

2.4 Scattering Geometry Underlying Bragg's Law. 35

2.5 X-ray Atomic Form Factors. 37

2.6 X-ray Absorption Edges for Pb. 47

2.7 Dipole-Allowed Electronic Transitions in 3d Transition Metals. 49

2.8 Components of an XAS Spectrum. 51

2.9 HERFD XANES vs. Transmission XANES Spectra. 52

2.10 Johann-Type Spectrometer. 53

2.11 XES Data Analysis Techniques. 56

2.12 RIXS 3D Surface Plot. 57

2.13 RIXS 2D Map. 58

3.1 *Operando* Coin Cell - Exploded View. 61
3.2 Pictures: *Operando* Cell. 65
3.3 Drawing: *Operando* Cell - Assembled State. 65
3.4 Drawing: *Operando* Cell Lid. 67
3.5 Drawing: *Operando* Cell Base. 67
3.6 Drawing: *Operando* Cell Spacer. 68
3.7 Drawing: *Operando* Cell Assembly Process. 69
3.8 X-ray Mass Attenuation Coefficients of Selected Elements. 72
3.9 Coin Cell Spring Constant Determination. 74
3.10 *Operando* Cell Electrochemical Performance. 78
3.11 *Operando* Cell Beam Angle-Dependent Attenuation. 79
3.12 *Operando* Cell Seal Demonstration. 81
3.13 Picture: *Operando* Cell in Transmission Mode. 83

4.1 Voltage Profile of $Li_{1.2}Ni_{0.13}Co_{0.13}Mn_{0.54}O_2$: TM and O Contributions. . . . 85
4.2 First-Cycle Unit Cell Parameters of $Li_{1.2}Ni_{0.2}Mn_{0.6}O_2$ and $Li_{1.2}Ni_{0.13}Co_{0.13}Mn_{0.54}O_2$. 92
4.3 *Operando* TM K Edge EXAFS of $Li_{1.2}Ni_{0.2}Mn_{0.6}O_2$. 93
4.4 *Operando* TM K Edge EXAFS of $Li_{1.2}Ni_{0.13}Co_{0.13}Mn_{0.54}O_2$. 95
4.5 Ni K Edge EXAFS Peak Shift Evolution During First Charge in $Li_{1.2}Ni_{0.2}Mn_{0.6}O_2$ and $Li_{1.2}Ni_{0.13}Co_{0.13}Mn_{0.54}O_2$. 96
4.6 Ni K Edge HERFD-XANES Spectra for Pristine $Li_{1.2}Ni_{0.13}Co_{0.13}Mn_{0.54}O_2$ and Reference Compounds. 97
4.7 First-Cycle *Operando* Ni K Edge HERFD-XANES Spectra for $Li_{1.2}Ni_{0.2}Mn_{0.6}O_2$ and $Li_{1.2}Ni_{0.13}Co_{0.13}Mn_{0.54}O_2$. 99
4.8 Gaussian Fits of Ni K Pre-Edges in $Li_{1.2}Ni_{0.2}Mn_{0.6}O_2$ and $Li_{1.2}Ni_{0.13}Co_{0.13}Mn_{0.54}O_2$. 101
4.9 First-Cycle *Operando* Ni K_α XES for $Li_{1.2}Ni_{0.2}Mn_{0.6}O_2$ and $Li_{1.2}Ni_{0.13}Co_{0.13}Mn_{0.54}O_2$. 103

4.10 Co K Edge HERFD-XANES Spectra for Pristine $Li_{1.2}Ni_{0.13}Co_{0.13}Mn_{0.54}O_2$ and Reference Compounds. 105
4.11 First-Cycle *Operando* Co K Edge HERFD-XANES for $Li_{1.2}Ni_{0.13}Co_{0.13}Mn_{0.54}O_2$. 105
4.12 *Operando* Co K Edge HERFD-XANES: Reverse Edge Shifts During TM Redox in $Li_{1.2}Ni_{0.13}Co_{0.13}Mn_{0.54}O_2$. 107
4.13 First-Cycle *Operando* Co K_α XES for $Li_{1.2}Ni_{0.13}Co_{0.13}Mn_{0.54}O_2$. 108
4.14 Mn K Edge HERFD-XANES Spectra for Pristine $Li_{1.2}Ni_{0.2}Mn_{0.6}O_2$, $Li_{1.2}Ni_{0.13}Co_{0.13}Mn_{0.54}O_2$, and Reference Compounds. 109
4.15 First-Cycle *Operando* Mn K Edge HERFD-XANES for $Li_{1.2}Ni_{0.2}Mn_{0.6}O_2$ and $Li_{1.2}Ni_{0.13}Co_{0.13}Mn_{0.54}O_2$. 110
4.16 First-Cycle Mn *Operando* K_α XES for $Li_{1.2}Ni_{0.2}Mn_{0.6}O_2$ and $Li_{1.2}Ni_{0.13}Co_{0.13}Mn_{0.54}O_2$. 111

5.1 Statistically Expected Numbers of Collinear Li-O-Li Configurations in Layered and Rocksalt Materials. 116
5.2 Structural Analysis Algorithm for RMC-Fit Disordered Rocksalt Structures. 121
5.3 XRD Pattern and Rietveld Fit for Pristine Li_2MnO_2F. 123
5.4 Neutron Diffraction Pattern and Rietveld Fit for Li_2MnO_2F. 124
5.5 TEM Images: Morphology and Crystallinity of Li_2MnO_2F. 125
5.6 Electron PDF of Pristine Li_2MnO_2F. 126
5.7 Neutron PDF of Li_2MnO_2F. 127
5.8 Mn K Edge XANES Spectra for Pristine Li_2MnO_2F and Reference Compounds. 129
5.10 Cross-Section of a RMC-Fit Structure of Li_2MnO_2F. 130
5.9 RMC Fit of Neutron PDF and Diffraction for Pristine Li_2MnO_2F. 131
5.11 Bond Distances Observed for Pristine Li_2MnO_2F. 132
5.12 Partial Pair Correlation Function for Pristine Li_2MnO_2F. 133
5.13 Cation Coordination Statistics in Li_2MnO_2F. 134

5.14 Percolation Network in Li_2MnO_2F. 135
5.15 Li-O-Li Bond Angle Distribution in Li_2MnO_2F. 136
5.16 Oxygen Coordination Environments in Pristine Li_2MnO_2F. 137

6.1 Voltage Profile and Capacity Retention of Li_2MnO_2F. 141
6.2 Drawing: Binder-Free Cell for Electrochemically Delithiating Neutron Samples - Exploded View. 145
6.3 TEM Images: Morphology and Crystallinity of Cycled Li_2MnO_2F. 147
6.4 *Ex-situ* X-ray PDF of Cycled Li_2MnO_2F. 149
6.5 *Ex-situ* Neutron PDF of Cycled Li_2MnO_2F. 150
6.6 *Ex-situ* Mn K edge EXAFS of Pristine and Cycled Li_2MnO_2F. 151
6.7 First-Cycle *Operando* Mn K Edge EXAFS for Li_2MnO_2F. 152
6.8 First-Cycle *Operando* Mn K Edge XANES for Li_2MnO_2F. 153
6.9 Cycle-Dependent Three-Electrode Electrochemistry of Li_2MnO_2F. 154
6.10 Cycle-Dependent Impedance of Discharged Li_2MnO_2F at OCV. 156
6.11 Total Resistances Observed for Discharged Li_2MnO_2F Cathodes. 158
6.12 Cycle-Dependent Fitted Resistances and Capacitances Obtained via EIS for Li_2MnO_2F Cathodes. 159

A.1 *Operando* XRD of $Li_{1.2}Ni_{0.2}Mn_{0.6}O_2$. 169
A.2 *Operando* XRD of $Li_{1.2}Ni_{0.13}Co_{0.13}Mn_{0.54}O_2$. 170
A.3 Influence of Binder and Carbon on Cathode X-ray PDF. 174
A.4 *Ex-situ* Neutron PDF of First Cycle Discharged Li_2MnO_2F. 178
A.5 *Ex-situ* Neutron PDF of Five Cycle Discharged Li_2MnO_2F. 179
A.6 *Ex-situ* Neutron PDF of 30 Cycle Discharged Li_2MnO_2F. 179
A.7 Cycle-Dependent Impedance of Li_2MnO_2F at 2.0 V Voltage Hold. 180
A.8 Cycle-Dependent Impedance of Li_2MnO_2F at 4.8 V Voltage Hold. 181

List of Tables

2.1 Impedance Behaviour of Common Equivalent Circuit Elements 29

3.1 Part List: *Operando* Cell. 66

3.2 Physical Properties of *Operando* Cell Window Materials. 71

3.3 X-ray Transmission Properties of Different *Operando* Cell Windows. 73

3.4 Mechanical and Electrical Properties of *Operando* Cell Materials 75

3.5 Requirement Verification Overview 78

3.6 *Operando* Cell Electrochemical Performance Verification 79

5.1 Warren-Cowley Parameters for Li_2MnO_2F. 134

6.1 Li_2MnO_2F: Multi-Cycled Neutron PDF Lattice Parameters. 150

A.1 *Operando* Cell X-ray Transmission. 167

A.2 Common XRD Rietveld Refinement Parameters for Lithium-Rich Layered Materials. 171

A.3 Refined Structure Parameters as Obtained via XRD for $Li_{1.2}Ni_{0.2}Mn_{0.6}O_2$. 172

A.4 Refined Structure Parameters as Obtained via XRD for $Li_{1.2}Ni_{0.13}Co_{0.13}Mn_{0.54}O_2$. 173

A.5 Structure Fit Parameters for *Ex-situ* X-ray PDF of Pristine Li_2MnO_2F. . . . 174

A.6 Structure Fit Parameters for *Ex-situ* X-ray PDF of First-Cycle Discharged Li_2MnO_2F. 175

A.7 Structure Fit Parameters for *Ex-situ* X-ray PDF of Second-Cycle Discharged Li_2MnO_2F. 175

A.8 Structure Fit Parameters for *Ex-situ* X-ray PDF of Fifth-Cycle Discharged Li_2MnO_2F. 175
A.9 Structure Fit Parameters for *Ex-situ* X-ray PDF of Tenth-Cycle Discharged Li_2MnO_2F. 175
A.10 Structure Fit Parameters for *Ex-situ* X-ray PDF of Twentieth-Cycle Discharged Li_2MnO_2F. 176
A.11 Structure Fit Parameters for *Ex-situ* X-ray PDF of First-Cycle Charged Li_2MnO_2F. 176
A.12 Structure Fit Parameters for *Ex-situ* X-ray PDF of Second-Cycle Charged Li_2MnO_2F. 176
A.13 Structure Fit Parameters for *Ex-situ* X-ray PDF of Fifth-Cycle Charged Li_2MnO_2F. 176
A.14 Structure Fit Parameters for *Ex-situ* X-ray PDF of Tenth-Cycle Charged Li_2MnO_2F. 177
A.15 Structure Fit Parameters for *Ex-situ* X-ray PDF of Twentieth-Cycle Charged Li_2MnO_2F. 177
A.16 Cycle-Dependent Impedance Fit Parameters of Li_2MnO_2F at OCV. 182
A.17 Cycle-Dependent Impedance Fit Parameters of Li_2MnO_2F at 2.0 V. 182
A.18 Cycle-Dependent Impedance Fit Parameters of Li_2MnO_2F at 4.8 V. 183

List of Acronyms and Abbreviations

a.u.	Arbitrary unit
AC	Alternating current
AM	Active material
AO	Actual outcome
APS	Advanced Photon Source
BDD	Boron-doped diamond
CAD	Computer-aided design
CPE	Constant phase element
Cy	Cycle
DC	Direct current
DFT	Density functional theory
DMC	Dimethyl carbonate
DOS	Density of states
EC	Ethylene carbonate
EIS	Electrochemical impedance spectroscopy
EO	Expected outcome
ESRF	European Synchrotron Radiation Facility
EXAFS	Extended X-ray absorption fine structure
FKM	Fluorocarbon elastomer
FT.	Fourier transform

FWHM	Full width at half maximum
FYS	Flexural yield strength
GC	Glassy carbon
HERFD-XANES	High energy-resolution fluorescence-detected XANES
hs	High spin
IAD	Integrated absolute difference
Int	Intensity
JT	Jahn-Teller effect
LCO	$LiCoO_2$
Li-rich NM	$Li_{1.2}Ni_{0.2}Mn_{0.6}O_2$
Li-rich NMC	$Li_{1.2}Ni_{0.13}Co_{0.13}Mn_{0.54}O_2$
LiB	Lithium ion battery
ls	Low spin
MOC	Means of compliance
NIST	National Institute of Standards and Technology
NMP	N-Methyl-2-pyrrolidone
OCV	Open circuit voltage
OEMS	*Operando* electrochemical mass spectrometry
PDF	Pair distribution function
pDOS	Projected density of states
PEEK	Polyether ether ketone
PFY	Partial fluorescence yield
PI	Polyimide
PID controller	Proportional–integral–derivative controller
PTFE	Polytetrafluoroethylene
PVDF	Polyvinylidene difluoride
Req.	Requirement
RIXS	Resonant inelastic X-ray scattering

RMC	Reverse Monte Carlo
SAED	Selected area electron diffraction
SEI	Solid electrolyte interphase
SOC	State of charge
SQUID	Superconducting quantum interference device magnetometry
SS	Stainless steel
STXM	Scanning transmission X-ray microscopy
SXAS	Soft X-ray absorption spectroscopy, usually with energies <5 keV
TFY	Total fluorescence yield
TM	Transition metal
TYS	Tensile yield strength
XANES	X-ray absorption near-edge structure
XAS	X-ray absorption spectroscopy
XES	X-ray emission spectroscopy
XRD	X-ray diffraction

List of Symbols and Operators

C	Capacitance
D_f	Degree of freedom
E	Energy
F	Force
$F(q)$	Reduced total structure function
F_{hkl}	Structure factor
$G(r)$	Reduced pair distribution function, "PDF"
I	Current
L	Inductance
L_p	Path pength
N	Number
Q	Charge, capacity
Q_{th}	Theoretical capacity
R	Resistance
S	Total spin
$S(q)$	Reduced scattering function
T	Temperature
U	Voltage
U_{iso}	Isotropic atomic displacement factor
U_{oc}	Open circuit potential

V Volume

X Reactance

Y Young's modulus

Δ Difference, change

$\Rightarrow$ Implies

α^{kl} Warren-Cowley parameter for species l surrounding species k

$\approx$ Equals approximately

δ Dirac delta function

ℓ Orbital angular momentum quantum number

γ Conductivity

λ Wavelength

$\langle B \rangle$ Arithmetic mean of quantity B

$|B|$ Absolute value or magnitude of quantity B

$\longrightarrow$ Approaches

$\mathbf{a}, \mathbf{b}, \mathbf{c}$ Lattice vectors

a, b, c Lattice parameters, e.g. $a = |\mathbf{a}|$

$\mathcal{F}$ Faraday constant, $\mathcal{F} \approx 96485.332$ Cmol^{-1}

e Elementary charge, $e = 1.602176634 \cdot 10^{-19}$ C

$\hbar$ Planck's constant, $\hbar = 6.62607015 \cdot 10^{34}$ Js

μ Chemical potential; Absorption coefficient (context-dependent)

ν Frequency

ω Angular frequency

ϕ Phase angle

$\propto$ Proportional

μ/ρ Mass attenuation coefficient, absorption per volumetric mass density

ρ Volumetric mass density

$\rightarrow$ Electronic transition, e.g. $\phi \rightarrow \phi'$: Transition from state ϕ to state ϕ'

$\widetilde{E}$ Specific energy (energy per unit mass)

$\widetilde{I}$	Specific current (current per unit mass)
$\widetilde{Q}$	Specific capacity (charge per unit mass)
b	Neutron scattering length; Lattice parameter (context-dependent)
e	Euler's number, $e \approx 2.71828$
$g_{kl}(r)$	Pair correlation function between k and l
h	Thickness
i	Intensity
j	Imaginary unit, $j = \sqrt{-1}$
k	Spring constant
l	Length
m	Mass
n	Mole; Principal quantum number; Number (context-dependent)
p	Pressure
q	Absolute value of the scattering vector (λ-corrected scattering angle)
r	Radius, distance
t	Time
w	Width
x	Cartesian coordinate x; displacement (context-dependent)
x, y, z	Cartesian coordinates
#	Number, counts
Å	Angstrom
Z	Atomic number
°C	Degree Celsius
°	Degree
$\boldsymbol{Z}$	Impedance
~	Approximately
µ	Micro
Ah	Ampere hour

C	Coulomb
e^-	Electron
eV	Electron volt
G	Giga
g	Gram
h	Hour
Hz	Hertz, Hz = s^{-1}
J	Joule
k	Kilo
L	Litre
m	Metre; Milli (context-dependent)
m%	Percentage by mass
min	Minute
mol	Mole
Pa	Pascal
ppm	Parts per million
s	Second
V	Volt

Chapter 1

Introduction

The electrochemical storage of energy has revolutionised the way we live, enabling portable electronics like smartphones and mobile computers, and is a key technology for the electrification of transport. Consumer demand for battery-powered applications drives challenging requirements for ever increasing specific energy and power in rechargeable batteries and continues to fuel a wealth of research in the field. At present, cathodes[†] are the active material with the highest need for increased performance and where the least promising solutions are available. This thesis investigates different means of increasing the amount of energy stored in cathodes, by studying materials with high-voltage, high-capacity redox couples based on lattice oxygen.

1.1 The Development of Secondary Lithium Ion Batteries

Electricity was first stored physically in the form of the Leyden jar in the middle of the 18th century.[1] These early capacitors, however, could not store significant amounts of charge. At the turn of the 19th century, Alessandro Volta discovered the eponymous voltaic pile, a primary (non-rechargeable) battery, which enabled the electrochemical generation of large

[†]In this thesis the battery convention for the terms 'cathode' and 'anode' is used, which differs from the strict electrochemical definition. Cathode is used for the electrode that accepts electrons during discharge, regardless of whether the cell is charging or discharging. The anode is similarly defined as the electrode that releases electrons during discharge.

amounts of electricity, revolutionising the scientific world.[2] Reversible electrochemical charge storage was first demonstrated by Ritter almost immediately afterwards, but it took until the middle of the 19th century for the development of the first true secondary battery, based on lead-acid chemistry.[3–6] The 20th century saw the discovery of the nickel-cadmium (NiCd) battery, as well as nickel-metal-hydride (NiMH) cells.[7] In the 1980s, Oxford's Goodenough group discovered the $LiCoO_2$ (LCO) intercalation cathode, after reversible Li intercalation into transition metal (TM) oxides and sulfides had been demonstrated by Wittingham.[8–10] Following the discovery of the graphite anode, the $Li_{1-x}CoO_2/Li_xC_6$ lithium ion battery (LiB) was patented by Sony in 1991.[11–15] The invention was deemed so important that it was celebrated with the award of the 2019 Nobel Prize in Chemistry to some of the people critical for its development.[16]

1.2 The Cathode Challenge

LCO cathodes are still popular today and exhibit specific capacities of ~160 $mAhg^{-1}$ at ~4.0 V (vs. Li^+/Li). [‡],[17,18] Several factors, however, including the detrimental effects of Co on human health, cost, as well as ethical concerns regarding its sourcing, have lead to numerous derivatives with reduced Co content, whose general stoichiometry can be summarised by $LiCo_iNi_jMn_kAl_lO_2$ ($i + j + k + l = 1$).[18,19] Some of the most widely used cathodes are $LiNi_{0.33}Mn_{0.33}Co_{0.33}O_2$ (NMC333 or NMC111), $LiNi_{0.6}Mn_{0.2}Co_{0.2}O_2$ (NMC622), $LiNi_{0.8}Mn_{0.1}Co_{0.1}O_2$ (NMC811), and $LiNi_{0.8}Co_{0.15}Al_{0.05}O_2$ (NCA), which outperform LCO in various aspects.[17,18] Some of these materials reach specific capacities exceeding 200 $mAhg^{-1}$, at average voltages of ~3.8 - 4.1 V.[17,18]

These capacities compare unfavourably to the common anode material graphite, with a specific capacity of 372 $mAhg^{-1}$ and a suitably low voltage of ~0.3 V. [§],[17,18] Li metal has a

[‡]Most work cited and performed in this thesis uses *half cells*, in which the Li metal redox couple Li^+/Li is used as a counter electrode. If not mentioned otherwise, voltages given assume this counter electrode.

[§]The lower limit for redox couples in Li ion batteries is the voltage of the Li^+/Li (Lithium metal) redox couple, set at 0 V.

specific capacity of 3860 $mAhg^{-1}$, and secondary cells with these anodes are commercially available, albeit with limited use cases due to slow charging speeds. Silicon, with a theoretical capacity exceeding 3000 $mAhg^{-1}$, promises similar amounts of charge stored in conjunction with high charging rates, and mixed Graphite/Si anodes with capacities ~500 $mAhg^{-1}$ are used in some commercial cells.[17] While these technologies still suffer from drawbacks, preventing the use of their full potentials, they offer promising solutions for anodes that are currently not available for cathodes.

As a result, cathode materials with increased capacities and operating at high average voltages are required to significantly improve the specific energy of cells in the long run. Commercially used materials are mainly TM oxides that reversibly intercalate Li ions, where charge is stored via reversible reduction-oxidation (redox) reactions on the TM ions. These charge-compensate for the removal and insertion of Li via changes in oxidation state.[18] The capacity of the materials is therefore limited by the number of stable, accessible TM oxidation states, and high capacity cathodes require elements with multivalent redox such as Ni^{4+}/Ni^{2+}. In general, the higher the oxidation state of a TM, the higher the redox voltage, as electrons are removed from energetically lower states.

The voltage, however, cannot be increased arbitrarily, as it is limited by the thermodynamic and kinetic stability of all active and passive components in the cell, forming the so-called electrochemical stability window. Here the predominant, limiting factor is usually the electrolyte. It is composed of a Li salt, such as $LiPF_6$, dissolved in a mixture of organic solvents, such as ethylene carbonate (EC) and dimethyl carbonate (DMC) and oxidised at potentials exceeding ~4.5 V. The voltage window limits the accessible TM oxidation states and hence the amount of charge that can be stored on the cathode. Other factors, such as the structural stability of highly delithiated compounds, pose additional constraints. TMs furthermore have high atomic masses, decreasing the specific capacity.

Cathodes can be separated into two groups, single and two-phase reaction types. In single-phase materials, such as LCO and its derivatives, the composition of the entire cathode varies gradually with the Li content, and the voltage changes accordingly. This is based on changes in the reaction energy, as Li ordering in the material changes the free energies of formation, resulting in a sloping voltage profile (section 2.1.2). In two-phase materials, such as $LiFePO_4$ (LFP), a fraction of the cathode, proportional to the passed charge, is directly reacted to the final reaction product. As the same reaction occurs at all states of charge, these compounds exhibit a flat voltage plateau, delivering their capacity at a constant voltage. LFP, however, only exhibits capacities of ~160 $mAhg^{-1}$ at an equilibrium voltage of ~3.4 V, limiting the stored energy.[18,20]

An ideal cathode material would combine all of these points and exhibit a high-capacity, two-phase plateau at the top of the electrolyte stability window, based on a low-mass redox couple.

1.3 Oxygen Redox and Lithium-Rich Cathode Materials

Recent work has shown that lattice oxygen, in specific coordination environments, can act as a redox couple and exhibits a voltage plateau at ~4.5 V, sparking widespread research effort to understand the processes underlying the phenomenon.[21–25] The following sections give an overview of the history and current status of the field, after a brief discussion of the structures of layered cathodes.

1.3.1 Structures of Layered Stoichiometric and Lithium-Rich Materials

Stoichiometric layered Li ion cathode materials, such as $Li[Co]O_2$ (LCO), have a ratio of Li:TM = 1, and Li and TM ions form separate, alternating layers (fig. 1.1). The square brackets are used here to indicate cations in the TM layer. If it is only occupied by one

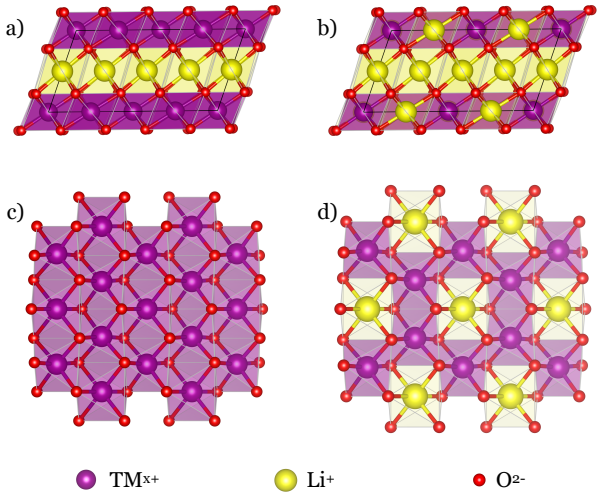


Figure 1.1: View along [110]: Layers formed by Li and TM in a) a stoichiometric layered cathode material with Li:TM = 1, e.g. Li[Co]O_2 and b) a Li-rich layered cathode with Li:TM = 2, e.g. Li[$Li_{0.33}$ $Mn_{0.66}$]O_2.
View of the TM layer along [001] for c) stoichiometric materials and d) Li-rich materials. The size differences between the different cations create a honeycomb ordering in the latter.

species, such as in LCO, the structure is described as an α-$NaFeO_2$ type, with a R$\bar{3}$m space group, where oxygen forms a cubic close-packed array and the different cation species form separate layers in the octahedral sites.[26,27] Each cation is octahedrally coordinated by oxygen and, similarly, each oxygen is coordinated by three Li in one layer and three TMs in another .

In Li-rich materials, whose distinct electrochemistry will be discussed in the next section, part of the TMs are substituted with Li ions and the ratio Li:TM > 1. Differences in the cation ionic radii result in a $\sqrt{3}\ a_{hex}$ x $\sqrt{3}\ b_{hex}$ superstructure, called honeycomb ordering (fig. 1.1).[21,22,28] Here, larger ions (e.g. Li^+, Ni^{2+}) are preferentially surrounded by six smaller ones (e.g. Co^{3+}, Mn^{4+}), to reduce Coulomb repulsion.[28] To form a perfect honeycomb ordering in the entire compound a ratio of = 2:1 is required, and typical materials, such as Li_2MnO_3 (Li[$Li_{0.33}$ $Mn_{0.66}$]O_2), crystallise in the space group C2/m.

Honeycomb ordering is also observed in compounds whose stoichiometry does not correspond to a perfect superstructure (2 > Li:TM > 1), as e.g. in $Li_{1.2}Ni_{0.2}Mn_{0.6}O_2$, and

the materials are assumed to have partial ordering. In practice, the compounds are often treated as if they had either perfect or no ordering, and indexed with C2/m or R$\bar{3}$m.[28,29]

1.3.2 The Structure-Electrochemistry Relationship of Oxygen Redox

Capacities exceeding what is expected from TM redox, based on what would be later identified as oxygen redox activity, were first observed in layered TM oxides in the early 2000s.[23,24,30,31] It was found that compounds with a ratio of Li:TM ≥ 1, as in the series $Li_{(4-2x)/3}Ni_xMn_{(2-x)/3}O_2$ ($0 < x \leq 0.5$) or in $Li_{1.2}Cr_{0.4}Mn_{0.4}O_2$, exhibited a large, irreversible 'excess' capacity when charged to high potentials, as well as discharge capacities greater than expected for pure TM redox.[21–24,30,31] Previously, in the 1990s, structurally similar solid solutions between $LiCoO_2$ (Li:TM = 1) and Li_2MnO_3 ($Li_{1.33}Mn_{0.66}O2$; Li:TM = 2) had been reported, but the compounds were not delithiated sufficiently to observe these anomalous capacities.[32]

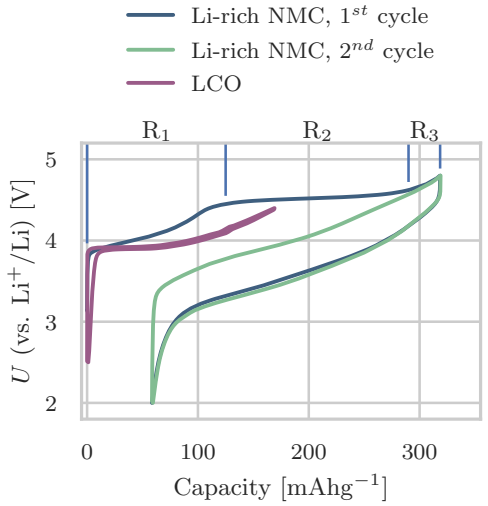


Figure 1.2: Voltage profiles for LCO and $Li_{1.2}Ni_{0.13}Co_{0.13}Mn_{0.54}O_2$ (Li-rich NMC), with the three regions of the first charge cycle (R_1 - R_3) indicated at the top. The expected TM redox capacity for Li-rich NMC is 123 $mAhg^{-1}$.

All of these compounds were found to have similar voltage profiles on first charge, that can be split into three sections: regions 1 - 3 (R_1 - R_3; fig. 1.2). Region 1 is a sloping profile up to ~4.5 V, followed by region 2, a plateau between ~4.5 - 4.6 V, and region 3, the section before the upper cutoff voltage is reached.[21,22] On discharge, as well as on subsequent cycles, this distinct separation is lost, and a sloping voltage profile with large hysteresis is observed.

A first explanation for the excess charge capacity of Li-rich materials was a combined process of oxygen loss from the lattice (O loss), which was observed along the R2 plateau via *operando* electrochemical mass spectrometry (OEMS), and the simultaneous migration of TM ions into the bulk of the structure.[33–36] This process, called densification, was supported by observations that Li was extracted from both the Li and TM layers, creating large amounts of vacancies, which enable TM diffusion within the structure.[36,37] On discharge, a reduction of Mn^{4+} ions was proposed, to charge-compensate and allow for the large, reversible capacity.[33–36] This theory, however, was not able to explain all observed phenomena: The mass loss from the electrodes, for example, was not sufficient to explain all O loss, and the change in Mn oxidation state, obtained via *operando* X-ray K edge absorption near-edge structure (XANES), was not sufficient to explain the discharge capacity.[38,39] These factors lead to the assumption that oxygen participates reversibly in the redox processes (O redox).[39] A first theory was based on the cyclic formation of lithium carbonate, via the reduction of emitted O_2 to O_2^- on discharge, and a subsequent reaction with the electrolyte.[40] This model, however, could not explain how these electrodes are able to exhibit 'excess' capacities for 100s of cycles.

Irreversible O loss and reversible O redox were merged into a single theory by the observation that different charge compensation mechanisms occur at the surface and in the bulk of cathode particles on first charge, based on electrochemical experiments using electrodes with varying particle sizes.[41,42] At the surface, O loss occurs and O_2 is evolved in conjunction with densification, while reversible O redox occurs in the bulk.[42] This was further supported by the observation of changes in O K edge soft X-ray absorption spectroscopy (SXAS) spectra, which varied between the surface and bulk, and where a reversible increase in spectral area was observed in region 2, indicating an increase in oxidation state of the oxygen.[43]

This theory was significantly advanced by quantifying the amount of O loss via OEMS using ^{18}O isotope-labelled $Li_{1.2}Ni_{0.2}Mn_{0.6}O_2$ (Li-rich NM) and $Li_{1.2}Ni_{0.13}Co_{0.13}Mn_{0.54}O_2$ (Li-rich NMC), two well-studied Li-rich compounds.[21,22] It was shown that only about 25 % of the first-charge excess capacity arises from O loss, where the majority of O_2 is released at the end of charge in region 3, with the remainder based on reversible O redox. The authors observed a spectral feature at ~531 eV in the O K edge across the plateau, and it was shown that O K edge resonant inelastic X-ray spectroscopy (RIXS) spectra exhibited a new emission feature at ~524 eV when excited at this frequency (fig. 1.4). This indicated a localised state on the O atoms, which the authors assigned to holes on the O, and the feature has become known as the *fingerprint* of O redox. The authors proposed that, due to the excess Li, O atoms coordinated by one Li^+ and two Mn^{4+} in the TM layer (and three more Li^+ in the Li layer), would be in the most ionic environment, with the least hybridisation between O 2p and TM 3d states. These O ions would therefore have the energetically highest O 2p states in the material, and would be oxidised first.[21,22]

This result was independently reproduced by a theoretical study, at the same time.[44] Using *ab initio* density functional theory (DFT) calculations, it was shown that O ions, collinearly coordinated by two Li^+, showed a significantly increased projected density of states (pDOS) close to the Fermi level in $LiNiO_2$ (fig. 1.3). The isosurfaces of this pDOS take the shape of an O 2p orbital, and the authors argued that the poor hybridisation between the Li 2s and the O 2p states results in very little stabilisation, raising the orbital to an energy comparable with the TM 3d electrons.[44]

Theory and experiment both suggested that the factor driving O redox activity are collinear Li-O-Li coordination geometries, creating bands with majority O 2p character. The extent of the overlap between TM bands, and those with O 2p character, likely varies between compounds and will be investigated in this thesis.

The concept of unhybridised O 2p states has been expanded from 3d Li-rich materials to

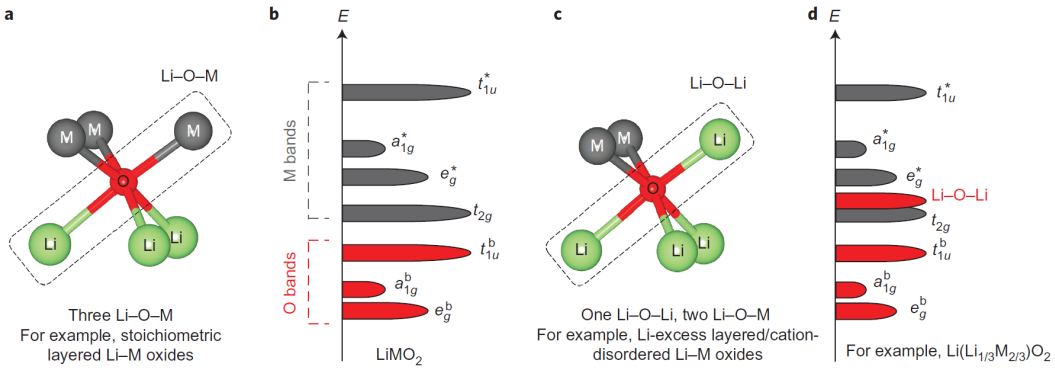


Figure 1.3: Coordination environment-dependent electronic states in stoichiometric and Li-rich cathode materials. In stoichiometric materials (a, b) all O 2p states are hybridised with TM states, resulting in an energetic stabilisation which renders them electrochemically inaccessible. In Li-rich materials (c, d), the collinear Li-O-Li coordination results in almost unhybridised, high-energy O 2p orbitals. The Fermi level lies between e_g^* and t_{2g}, close to the energy of these states, making them accessible.
Reprinted by permission from Springer Nature [44]. Copyright (2016).

other compounds, and O redox has been demonstrated in Na ion cathodes, structures where the low orbital overlap arises from Mg^{2+} substitutions, as well as in 4d and 5d TM compounds.[25,45–56] 3d Na cathode materials are of particular interest, as the structures are very similar to 3d Li-rich compounds, especially at high levels of alkali deintercalation.[25,49,51,54]

1.3.2.1 The Nature of Oxidised Oxygen Species

The nature of the oxidised oxygen species in 3d TM compounds has been a much-discussed topic. It was initially assumed to be based on highly localised holes on the oxidised O species, due to the observation of new features in O K edge SXAS and RIXS.[21,22] Extensive discussion has evolved around the hypothesis that, instead, dimerised, peroxo-like O species, are formed, as they are assumed to occur in 4d and 5d Li-rich compounds.[52,58–61] However, evidence for these is sparse in 3d systems.[21,22]

Recent work used high-resolution RIXS to identify molecular O_2 as the product of O oxidation in desodiated, honeycomb-ordered $Na_{0.75}[Li_{0.25}\ Mn_{0.75}]O_2$, using the vibrational

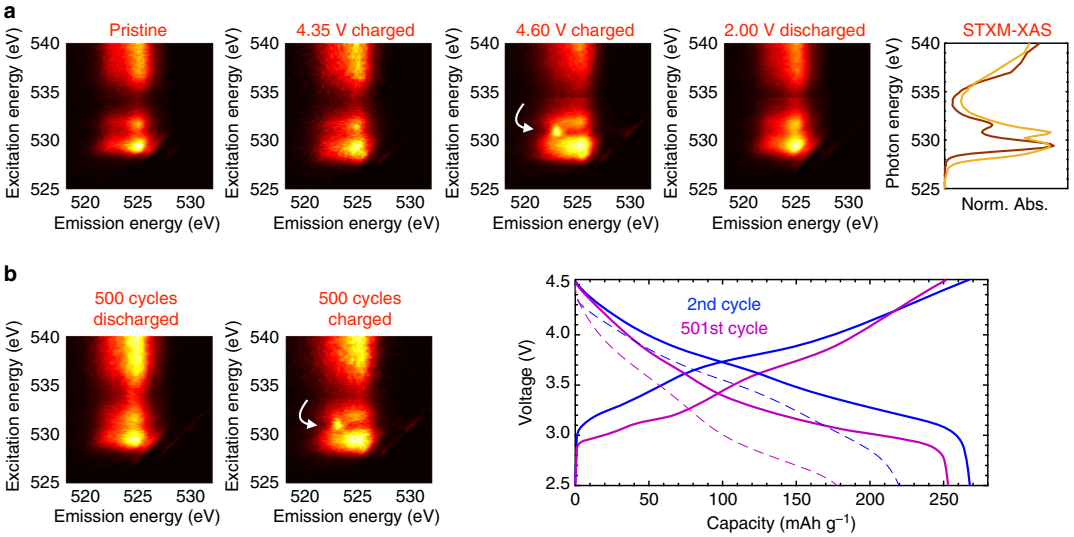


Figure 1.4: a) Left four: RIXS maps obtained for $Li_{1.17}Ni_{0.21}Co_{0.08}Mn_{0.54}O_2$ at different points during the first cycle. At 4.6 V the O redox emission feature is visible (arrow). Far Right: STXM-XAS of the O K edge obtained for a pristine (ochre) and fully charged (yellow) cathode.
b) Left two: RIXS maps of the discharged and charged compound after 500 cycles, the latter showing the O redox emission feature (arrow). Right: Voltage profiles for the 2nd and 500th cycles. Solid lines: Quasi OCV (C/68); Dashed lines: 2C.
Reproduced, with permission, from [57] under a Creative Commons CC BY license. Copyright (2017), the Authors.

frequencies of high-resolution data in conjunction with DFT to rule out peroxides and other oxidised forms of O^{2-}.[25] The same authors identified mixed O_2 and localised hole formation in the stoichiometrically close compound $Na_{0.6}[Li_{0.2}\ Mn_{0.8}]O_2$, which has a ribbon-like ordering in the TM layer, assigning the behaviour to the different superstructure preventing in-plane Mn migration and extensive O dimerisation.[25]

After it was initially assumed that O redox activity persists only for a few cycles, it has been shown that the characteristic RIXS feature is still observed after 500 cycles, demonstrating that O redox is highly reversible (fig. 1.4).[57]

1.3.3 Challenges with 3d Lithium-Rich Cathode Materials

At present, several fundamental problems remain with Li-rich compounds that prevent their commercialisation.

1.3.3.1 First-Cycle Voltage Hysteresis

The significant voltage hysteresis observed in 3d Li-rich materials during the first cycle is one of the factors preventing their use in practical applications. It only occurs after charging beyond region 1, and it was long assumed that this is linked to the reversible out-of-plane movement of TM ions into the Li layer, changing the site energies for Li upon re-intercalation.[47,57,62–64] Recent work, however, has demonstrated convincingly that it is instead based on the loss of the honeycomb superstructure through in-plane TM migration.[25] Across the plateau, oxidised O species combine and form O_2, restructuring the TM layer in the process. On discharge the O-O bonds are broken, but the restructured TM layer has changed the local O coordination environment, resulting in the lower reinsertion voltage.

This restructuring is not observed in ribbon-ordered $Na_{0.6}[Li_{0.2}Mn_{0.8}]O_2$, whose superstructure is retained on charge and discharge.[25]This results in a much reduced

difference between the local environments during Li extraction and reinsertion, and some of the voltage plateau is maintained on discharge. These encouraging results give a more unified view of the relationship between structural changes and O redox in 3d compounds and present a clear way forward for this class of materials.

1.3.3.2 Voltage Fade with Cycle Life

The second challenge associated with Li-rich compounds is voltage fading, a reduction of the average discharge open circuit voltage (OCV) with increasing cycle number (fig. 1.4). This effect has been linked to the aforementioned high TM mobility in the delithiated compounds, particularly to an irreversible migration of TMs into the Li layer.[65–67] After 50 cycles, a two- to threefold increase in Ni concentration is observed at the surface of some Li-rich compounds, as well as the local formation of a rocksalt-like structure, both of which were linked to Mn migration into the bulk of the particles, where it occupies sites in the Li layer (densification).[68,69] Computational evidence suggests that oxygen vacancies in the immediate coordination sphere of a TM destabilise it, creating a driving force for migration into sites with six coordinating oxygens. This presents an intuitive theory for the causal link between O loss and the structural rearrangement.[69]

1.4 Disordered Rocksalt Cathode Materials

Most Li ion cathode materials, such as the previously discussed layered compounds, as well as olivines and spinels, have highly regular structures, and it was long assumed that the strict ordering was required for electrochemical performance. This was mainly based on the poor performance of disordered LiTMO$_2$ compounds (TM = Ti, Fe, Co, Mn, Ni), prepared via high-energy ball milling, compared to their stoichiometrically identical, layered polymorphs.[70] A reduced performance is also observed in layered compounds after TM migration into the Li layer, where rocksalt-like structures are formed locally, further supporting the assumption.[71–74]

The low electrochemical performance was rationalised by a lack of Li diffusion channels, resulting in low ion mobility and hence poor performance.[75] Recent work, however, has shown that electrochemically active materials can be synthesised by increasing the relative amount of Li in the structure, and promising candidates for high-performance materials have been reported, some of which exhibit capacities exceeding 400 $mAhg^{-1}$.[75–79] Similar to layered materials, compounds with 4d TMs, as well as Na as the mobile ion, have been reported.[75,80–84]

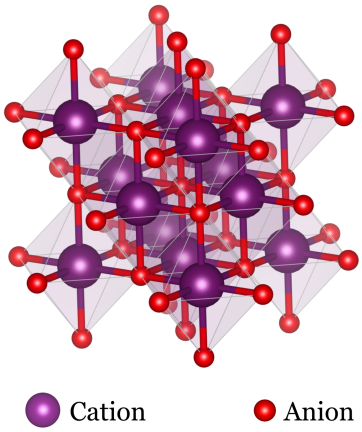


Figure 1.5: The rocksalt structure. Similarities to the structures of layered compounds are evident through the distinct layers.

1.4.1 Structures of Rocksalt Cathode Materials

Ordered rocksalt materials have a sodium chloride structure (space group $Fm\bar{3}m$), in which a cubic close-packed anion lattice is interpenetrated by a cubic close-packed cation lattice (fig. 1.5). Each ion is coordinated by six counterions, creating an octahedral first shell. The structure is very similar to the ones of layered TM oxides, which can be seen as ordered derivatives, in which the TM and alkali layer ions occupy distinct positions.

In disordered rocksalts, multiple kinds of anions and/or cations are present, which populate their respective sites without distinct long-range order.[70,75]

1.4.2 Lithium Diffusion in Rocksalts and Percolation Theory

The movement of Li ions in rocksalt materials is based on 'hopping' from one octahedral site to another, via an energetically unfavourable tetrahedral intermediate state (o-t-o diffusion; fig. 1.6).[75] The tetrahedral site is face-sharing with four octahedral sites in total, two of which are the empty starting and final sites, and the remaining two can either be empty or occupied by other cations. The energy of the intermediate state is dominated by

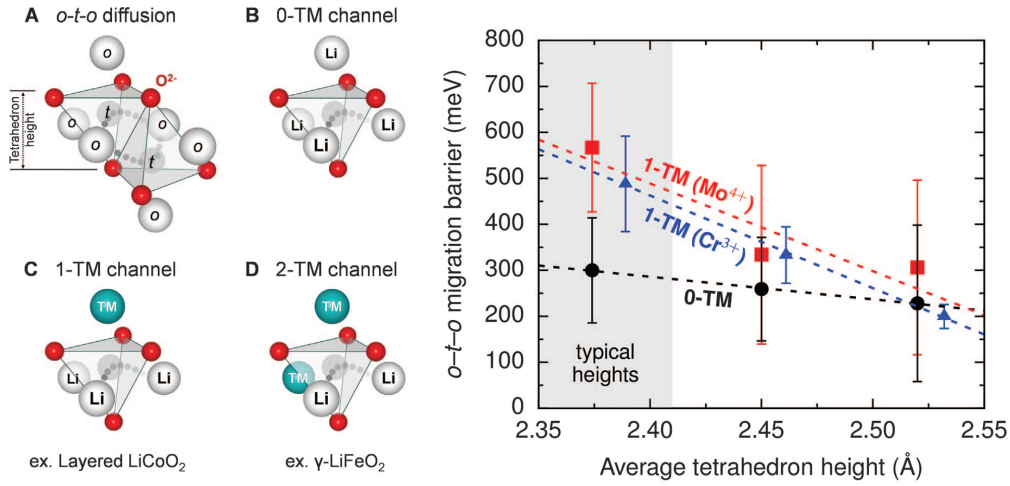


Figure 1.6: Left: Overview of different coordination environments around an intermediate tetrahedral site during Li diffusion between two octahedral sites in Li ion rocksalts, with varying numbers of adjacent TM ions.
Right: Migration energy barriers for Li^+ in in $Li_{1.211}Mo_{0.467}Cr_{0.3}O_2$, calculated as a function of the intermediate site's tetrahedron height, for the O-TM and 1-TM cases.
From [75] / Reprinted with permission from AAAS.

the Coulomb repulsion arising from the occupants of these two sites, and thus their charge and distance to the diffusing Li^+ (repulsive force $\propto {}^{Q_1}/_{r_1^2} + {}^{Q_2}/_{r_2^2}$). The cation species, as well as the lattice spacing, are therefore the major factors governing diffusion speed in rocksalt compounds.

In fully lithiated rocksalts, where no cation vacancies are present, there are three possibilities for occupying the two variable octahedral sites: 1. with a TM each ('2-TM'), 2. with one TM and one Li ('1-TM'), and 3. with two Li ('0-TM'), in decreasing order of energy penalty (fig. 1.6).[75] The 1-TM case is found in stoichiometric layered cathodes, which exhibit good rate performance based on the low Coulomb repulsion arising from only one multivalent TM ion.[85]

In rocksalts, however, smaller lattice spacings are found, making 1-TM channels energetically unfavourable, and 0-TM channels are required for Li mobility. This requires an increased Li:TM ratio, in order to establish cross-connected channels of 0-TM tetrahedral sites, creating a percolation network.[75,85] The exact amount of required 'excess' Li varies with the degree of cation disorder, and for fully disordered rocksalts a Li:TM ratio ~1.2

($Li_{1.09}TM_{0.91}O_2$) has been calculated.[75]

The percolation network model is a coherent explanation for bulk diffusion behaviour in these materials, as it explains why fully disordered, stoichiometric compounds show low electrochemical activity,[70] why disorder upon cycling reduces electrochemical performance in stoichiometric layered compounds,[71–74] and why highly lithiated compounds such as layered $Li_{1.211}Mo_{0.467}Cr_{0.3}O_2$ (Li:TM ~1.6) are able to disorder over the first few cycles without losing significant capacity.[75]

Some compounds, however, appear to violate the percolation network explanation. For example, approximately 80 % theoretical capacity has been observed for tens of cycles in the stoichiometric rocksalt $LiMnO_2$ and $NaMnO_2$.[79] These materials are synthesised via high-energy ball milling and have low surface areas, consisting of fused nanosized domains. It is assumed that the resulting large amounts of grain boundaries enable facile ion movement, and diffusion distances for o-t-o hopping in the bulk are sufficiently small.[79] Grain boundary diffusion is well-known from other fields and offers a reasonable explanation for this apparent violation of the previously discussed structure-mobility-relationship, while showing that several approaches for synthesising electrochemically active rocksalts are available.[86]

1.4.3 The Redox Chemistry of Disordered Rocksalts

Disordered rocksalt structures allow for the synthesis of compounds with significantly less order, as well as larger differences in ionic radii and valences.[84,85,87] For example, ions with d^0 valence can easily be incorporated, and accommodate large distortions of their coordination environments.[87] This is based on their low bond directionality, compared to ions with partially occupied d shells, where the incomplete orbital occupation results a non-centrosymmetric electron distribution and preferential bonding in certain directions.[87] While d^0 ions do not store charge and have low electronic conductivities,

their high tolerance for distortion allows for the synthesis of compounds with multivalent redox couples.[84,87] $Li_2Mn_{0.66}Nb_{0.33}O_2F$ (Nb^{5+}, d^0) and $Li_2Mn_{0.5}Ti_{0.5}O_2F$ (Ti^{4+}, d^0), for example, exhibit capacities of ~300 $mAhg^{-1}$, based on Mn^{4+}/Mn^{2+} redox.[84,87]

Disordered compounds are not limited to TM redox, and the structure-redox relationship between collinear Li-O-Li configurations and O redox, applies equally.[21,22,44,51,88] Several alkali-rich compounds with 'excess' capacities have been reported, and the characteristic O redox features in SXAS and RIXS have been observed.[80,88] The distinct voltage plateaus of layered Li-rich compounds are not present, although several compounds exhibit different voltage profiles for the first and subsequent cycles (fig. 1.7).[80,84] This is likely due to the multitude of local environments, which create a distribution of Li extraction and insertion voltages. The varying environments can be assumed to create redox-active O 2p states with a range of energies, resulting in an increased overlap of bands with TM and O character. Charge compensation is therefore likely based on both redox processes occurring simultaneously over a broad range of voltages.

1.4.4 Disordered Lithium Oxyfluoride Rocksalts

The partial replacement of O^{2-} with F^- has been shown to increase the insertion voltage in Li ion cathodes, based on the inductive effect arising from the highly electronegative fluorine.[18,84,89–92] The substitution with monovalent F^- also allows for the reduction of the average TM oxidation state in the pristine material, and therefore an increase in TM redox capacity. The effect can be observed in materials like Li_2VO_3 and Li_2VO_2F.[78,92] While Li_2VO_3 is limited to the V^{5+}/V^{4+} redox couple, and has a theoretical TM capacity of 238 $mAhg^{-1}$, Li_2VO_2F employs a V^{5+}/V^{3+} redox couple with 463 $mAhg^{-1}$. Experimentally, ~250 $mAhg^{-1}$ and ~320 $mAhg^{-1}$, respectively, are observed on first charge.[78,92] In addition to the larger capacity, the oxyfluoride shows significantly improved kinetics, based on the lower repulstion arising from the lower average charge of the V ions, as well as a higher discharge voltage.[78,92] Other compounds, such as $Li_2V_xCr_{1-x}O_2F$ (x = 0, 0.2, 0.5, 0.8; > 300

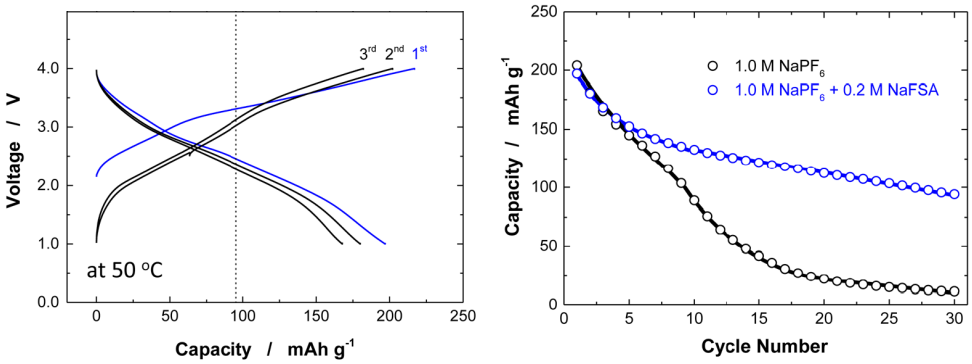


Figure 1.7: Voltage profile and cycle-dependent capacities for $Na_{1.3}Nb_{0.3}Mn_{0.4}O_2$.
Left: Voltage profiles obtained for the first three cycles, with the dashed line at ~95 $mAhg^{-1}$ indicating the TM redox capacity.
Right: Discharge capacity as a function of cycle number, with and without the electrolyte additive NaFSA.
Reprinted (adapted) with permission from [80]. Copyright (2017), American Chemical Society.

- 400 $mAhg^{-1}$),[93] LiNiOF (~200 $mAhg^{-1}$),[94] and Li_2MoO_2F (~300 $mAhg^{-1}$),[95] also exhibit high capacities, based on multi-valence TM redox.

Recently, the Li-rich 3d compound Li_2MnO_2F was reported, which exhibits a capacity of up to 300 $mAhg^{-1}$ at an average voltage of ~3.4 V.[88] Charge compensation is based on combined Mn^{4+}/Mn^{3+} TM redox, as well as highly reversible O redox.[88] The material is a promising candidate for addressing the cathode challenge and is investigated in detail in this thesis.[88]

1.4.5 Present Challenges with Disordered Rocksalt Cathodes

The disordered rocksalt and oxyfluoride space is not very well explored, and many aspects have not been investigated in much detail. The local structure-electrochemistry relationship of this class of materials is not well understood, particularly with regards to O redox. Investigating the structures of disordered rocksalts is challenging, as the conventional long-range probe XRD yields limited results, and advanced characterisation techniques, such as pair distribution function analysis (PDF), are required.[77–79,84,88,92]

Additionally, a rapid capacity fade observed in these compounds (fig. 1.7), which needs to

be understood and solved before commercial applications are possible.[78,80,84,88,92,93,96] The current understanding suggests a surface phenomenon, as carbonate species are observed on the cathodes on discharge, and electrolyte additives have been shown to improve performance in some compounds (fig. 1.7).[80,88] However, while cyclic performance was improved, the fading is still very high and potentially based on a bulk process, such as TM migration or local structural changes.

1.5 Thesis Outline and Objectives

In order to address some of the fundamental challenges associated with O redox in layered and disordered rocksalt compounds, this thesis aims to contribute to the following points:

1. Chapter 3 addresses the difficulty of reliably performing synchrotron hard X-ray *operando* experiments with Li-rich compounds, which are required to study the crystal and electronic structure. A novel *operando* cell, designed for this purpose, is presented and the design discussed.

2. Chapter 4 investigates the contribution of TM redox, and its interplay with O redox, in the layered Li-rich materials $Li_{1.2}Ni_{0.2}Mn_{0.6}O_2$ and $Li_{1.2}Ni_{0.13}Co_{0.13}Mn_{0.54}O_2$. There is significant debate about the oxidation states of Ni in both compounds, which are studied using bulk-sensitive techniques. *Operando* K_α-detected 3d TM K edge XANES and *operando* K_α X-ray emission spectroscopy (XES) are combined with several structural probes to show that Ni is fully oxidised in $Li_{1.2}Ni_{0.13}Co_{0.13}Mn_{0.54}O_2$ and not in $Li_{1.2}Ni_{0.2}Mn_{0.6}O_2$.

3. Chapter 5 addresses the structure-electrochemistry relationship of disordered rocksalts, using Li_2MnO_2F as a model compound. The previously unknown local structure of the material is analysed using a combination of neutron diffraction, neutron pair distribution function (PDF), and Reverse Monte Carlo (RMC) fitting. The obtained structural model shows that O environments are not statistically distributed in the material, with significant influence on O redox.

4. Chapter 6 investigates the capacity fade observed in Li_2MnO_2F. A variety of *ex-situ* and *operando* structural and electrochemical probes, such as neutron PDF and electrochemical impedance spectroscopy (EIS), are used to analyse bulk and surface changes and identify the origin of the behaviour. It is found that a significant increase in charge-transfer resistance over the first ten cycles creates an asymmetry in the cathode internal resistance between charge and discharge, preventing full reinsertion of Li.

Chapter 2

Theory and Methods

This chapter outlines the techniques used in this thesis, as well as the theory underlying them. Due to the breadth of the battery field, the descriptions are not exhaustive, but aim to give an overview.

2.1 Working Principle of a Cell and Electrochemical Testing

A typical lithium ion battery (LiB) consists of two electrodes, linked by an electronically insulating, ionically conductive compound called electrolyte (fig. 2.1). The electrolyte, usually a Li salt dissolved in organic solvents, is soaked into a glass fibre fleece or polymer film, called separator. The two electrodes are additionally connected to an external electronic conductor containing a load, completing the circuit. Through a suitably chosen load resistance, the amount of exchanged electrons can be controlled. Charge neutrality requires that for each electron that moves through the circuit an equivalent amount of charge, in the form of Li ions, is exchanged between the electrodes through the electrolyte. In a LiB, the electrode materials can reversibly take-up and release Li ions, and the compositions and reaction speed can therefore be controlled via control of the flow of electrons.

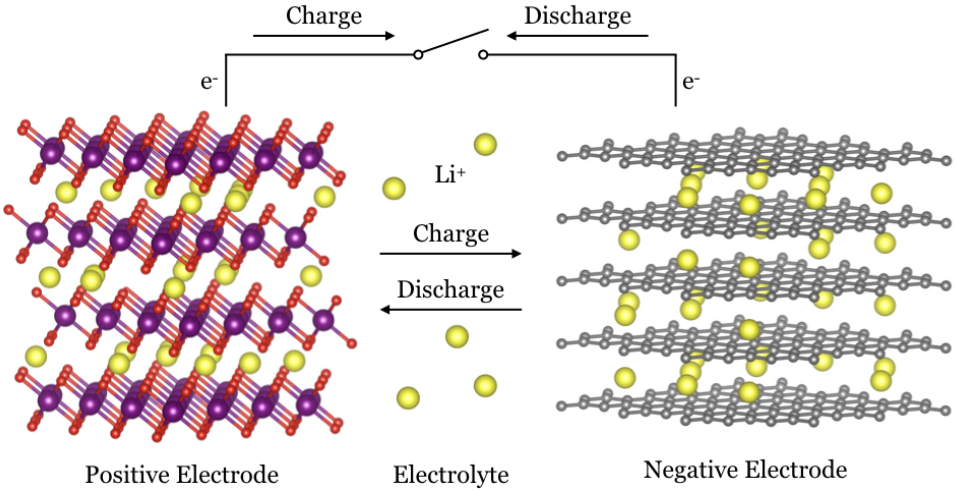


Figure 2.1: Working principle of a LiB, consisting of a layered positive electrode, and a graphite negative electrode. The direction of electron flow is indicated with arrows for the charge and discharge.

The reactions of a cell can be separated into two half cell reactions, one of which occurs at each of the electrodes. Again, charge neutrality requires that the oxidation reaction (anodic process), which occurs on one of the electrodes and releases electrons into the circuit, is accompanied by an equal reduction reaction (cathodic process) on the second. It is convention to label the electrode, at which the reduction reaction occurs on discharge, the cathode, or positive electrode, regardless of the direction of current flow. Similarly, the other electrode is called the anode, or negative electrode. This deviates from the exact electrochemical definition, where anode and cathode are used to describe the electrodes at which the reduction and oxidation reactions occur, respectively, and which change based on the direction of current flow.

For an LCO/graphite cell, the half- and full-cell reactions are as follows:

$$\mathrm{LiCo^{3+}O_2} \underset{\text{Discharge (Reduction)}}{\overset{\text{Charge (Oxidation)}}{\rightleftharpoons}} \mathrm{Li_{1-x}Co^{3+x}O_2} + x\mathrm{Li^+} + x\mathrm{e^-} \quad \text{Cathode reaction}$$

$$\mathrm{C_6} + x\mathrm{Li^+} + x\mathrm{e^-} \underset{\text{Discharge (Oxidation)}}{\overset{\text{Charge (Reduction)}}{\rightleftharpoons}} \mathrm{Li_xC_6} \quad \text{Anode reaction}$$

$$\mathrm{LiCoO_2} + \mathrm{C_6} \underset{\text{Discharge}}{\overset{\text{Charge}}{\rightleftharpoons}} \mathrm{Li_{1-x}CoO_2} + \mathrm{Li_xC_6} \quad \text{Full cell reaction}$$

2.1.1 Cell Voltage

During discharge the chemical reactions progresses spontaneously, at a voltage determined by the Gibbs free energy of the reaction:

$$\Delta G_r = G_{f,\,products} - G_{f,\,reactants} \tag{2.1}$$

$$= -n_e \mathcal{F} U_{oc} \tag{2.2}$$

where ΔG_r is the Gibbs free energy of reaction, $G_{f,i}$ is the sum of the Gibbs free energies of formation, n_e are the moles of electrons exchanged, $\mathcal{F}$ is the Faraday constant (~ 96485 $Cmol^{-1}$), and U_{oc} is the cell open circuit potential.

The relationship can also be expressed in the form of chemical potentials μ, which describe the change of the Gibbs free energy with the number of a given species' particles N, with all other factors kept constant:

$$\mu_k = \left(\frac{\partial G}{\partial N_k}\right)_{p,T,N_{l\neq k}} \tag{2.3}$$

where p is the pressure and T is the temperature.
The cell open circuit voltage then arises from the difference in chemical potential of the species in the anode μ_a and the cathode μ_c:

$$U_{oc} = \frac{\mu_a - \mu_c}{e} \tag{2.4}$$

where e is the elementary charge (~$1.602 \cdot 10^{-19}$ C).

The shape of the voltage profile, a plot of the measured cell voltage U vs. time t (or a related quantity), therefore contains information on the reaction, owing to the causal relationship between voltage and composition.

The concept can be expanded using Gibbs' phase rule, which describes the relationship between the degrees of freedom D_f of a system's intensive quantities (e.g. p, T, or μ and U_{oc}), and the number of phases P:

$$D_f = C - P + 2 \tag{2.5}$$

where C is the number of independent components in the system used to form the phases (e.g. in this case a Li ion and a host). D_f describes how many intensive quantities can vary independently, and for isobaric, isothermal conditions (which are found for all experiments performed in this thesis), the rule simplifies to:

$$D_f = C - P \tag{2.6}$$

In an electrode $C = 2$, as the system is comprised of the host and an ion. When the composition of an electrode changes as a solid solution (incremental, homogeneous change of the entirety of the active material), $P = 1 \rightarrow D_f = 1$, and the remaining degree of freedom allows U_{oc} to vary. This results in a sloping voltage profile. If a two-phase system is present, $P = 2 \rightarrow D_f = 0$, and a voltage plateau is observed.

2.1.2 Galvanostatic Cycling

The most commonly used form of passing charge in fundamental battery chemistry research is galvanostatic cycling, where a constant current I is applied to the cell, and the voltage is allowed to vary freely within pre-set bounds.

For easier comparison, I is often reported as an intensive quantity $\widetilde{I}$, which is normalised to the active mass (unit: mAg^{-1}).

The amount of Li (de)intercalation in the electrodes is directly proportional to the amount of current passed, according to Faraday's law of electrolysis, and the stoichiometry can therefore be controlled electrochemically. The specific capacity passed $\widetilde{Q}$, which describes the amount of charge Q passed per unit mass of active material, is defined as:

$$\widetilde{Q} = \int_{t_0}^{t} \widetilde{I}(t)dt \tag{2.7}$$

and simplifies to

$$\widetilde{Q} = \widetilde{I}\Delta t. \tag{2.8}$$

as the current is constant.

The theoretical capacity Q_{th} of a material is related to the amount electrons that can be extracted from it, or the amount of ions it can exchange, whichever is limiting:

$$Q_{th} = \frac{n_{th}\mathcal{F}}{3.6M} \ [\text{mAhg}^{-1}] \tag{2.9}$$

where n_{th} is the fraction of moles of electrons or ions per mole of compound (dimensionless), M is the molar mass, and 3.6 is a factor arising from the the conversion from coulomb to milliampere hours (mAh), a commonly used unit in battery chemistry research. As both electrons and Li^+ have the same magnitude of charge, the number of electrons is equal to the number of Li ions extracted for LiBs.

2.1.3 Energy Stored Within a Cell

For a given amount of charge, the released chemical energy, or work done, per unit mass $\widetilde{E}$ is defined by the cell reaction:

$$E = \Delta G_r \tag{2.10}$$

$$\widetilde{E} = \widetilde{Q}U \tag{2.11}$$

$$= \int_{t_0}^{t} \widetilde{I}(t)U(t)dt \tag{2.12}$$

$$= \widetilde{I} \int_{t_0}^{t} U(t)dt \tag{2.13}$$

$$\approx \widetilde{I} \sum_{k}^{n-1} \frac{U_{k+1} + U_k}{2}(t_{k+1} - t_k) \tag{2.14}$$

where the last equation factors in that experimental data is sampled at a finite rate.

As evident from the relationship, two related properties directly influence the energy stored in a cathode: First, the amount of charge Q that is available, mainly limited by the amount of (accessible) Li^+ in the material, due to the voltage window and irreversible structure changes. It can, however, also be based on the available number of electrons, which depends on the redox reactions and therefore ultimately on the stable oxidation states of the redox couples (e.g. Ni^{4+}/Ni^{2+}). Second, the voltage is crucial, as the stored energy is directly proportional to it, and high-voltage redox reactions are therefore desired.

These factors can be visualised as a plot of $^{dQ}/_{dU}$ vs. U, called differential capacity. Extrema in this plot correspond to the voltages of redox reactions, and the peak area corresponds to the amount of charge passed. Positive values correspond to oxidation reactions on the working electrode, whilst negative values indicate reduction processes. A fully reversible electrochemical system at OCV would be symmetrical with regards to the abscissa, and deviations from this symmetry contain additional information on thermodynamic limitations, e.g. hysteresis, as well as rate effects caused by the current.

2.1.3.1 Influence of Current Flow

The magnitude of the current used to charge and discharge a cell has an influence on the observed electrochemical behaviour. This is due to the internal resistance of the cell, which arises from the ohmic contributions of the individual components, as well as their reactances, which are mainly based on polarisation effects and concentration gradients due to the movement of ions.

The magnitude of the voltage drop ΔU is proportional to the product of the effective resistance R_e and the applied current, according to Ohm's law, and called overpotential:

$$\Delta U = R_e I \tag{2.15}$$

where the sign of the current is positive during charge and negative during discharge. This results in a difference of the observed cell voltage U from U_{OC}, as described by:

$$U = U_{OC} + \Delta U \tag{2.16}$$

Large overpotentials cause U to reach the voltage limits more quickly, and hence limit the amount of ions that can be extracted or inserted. As a result, low currents are used most frequently in fundamental cathode research. The value is sometimes presented as a so-called C rate, the inverse of the number of hours required for a full (dis)charge (e.g. a 2 C discharge indicates a full discharge in 30 min).

2.1.4 *Operando* Electrochemical Mass Spectrometry (OEMS)

Operando Electrochemical Mass Spectrometry (OEMS) is an experimental technique that allows for the identification and quantification of gases emitted by an electrochemical system during cycling. It is based on an electrochemical cell that is subject to a constant stream of an inert gas, e.g. Ar, which is fed into a mass spectrometer. There the gas is ionised, and the ions are separated and analysed according to their mass-to-charge ratio $^{m}/_{z}$, e.g. via a time-of-flight

analyser. Gasses evolved by the cell can then be identified according to their $^{m}/_{z}$, quantified by the amount of counts, and correlated with the electrochemical processes.

2.1.5 Electrochemical Impedance Spectroscopy (EIS)

Electrochemical impedance spectroscopy (EIS) is a powerful, non-destructive technique for studying electrochemical systems. It is based on probing the frequency-dependent opposition to current flow, called impedance $\boldsymbol{Z}(\nu)$, and correlating it with physical and electrochemical processes.

Experimentally, this is achieved by sending a variable-frequency alternating current (AC) signal of either constant voltage or constant current amplitude through the system and recording the corresponding response.[97]

$\boldsymbol{Z}$ can be seen as an extension of Ohm's law to the frequency space, where $\boldsymbol{Z}$ is the quotient of voltage $U(\nu)$ and current $I(\nu)$. Using a sinusoidally varying voltage as an input signal the relationship can be expressed as:[97]

$$\boldsymbol{Z} = \frac{U(\omega)}{I(\omega)} \tag{2.17}$$

$$= \frac{U_0 \sin(\omega t)}{I_0 \sin(\omega t - \phi)} \tag{2.18}$$

$$= Z_0 \frac{\sin(\omega t)}{\sin(\omega t - \phi)} \tag{2.19}$$

where $\omega = 2\pi\nu$ is the angular frequency and ϕ the phase shift of the response. According to Euler's formula this expression can also be represented using complex exponentials:

$$\boldsymbol{Z} = Z_0 \frac{e^{j\omega t}}{e^{j(\omega t - \phi)}} \tag{2.20}$$

$$= Z_0 e^{j\phi} \tag{2.21}$$

$$= Z_0 \left(\cos\phi + j \sin\phi\right) \tag{2.22}$$

$$= \sqrt{R^2 + X^2} \tag{2.23}$$

where $j = \sqrt{-1}$ is the imaginary unit, R is the (frequency-independent) ohmic resistance, and X is the (frequency-dependent) reactance.
$\boldsymbol{Z}$ can be represented in two ways: Either as two plots of Z vs. ν and ϕ vs. ν, called Bode plot, or as as plot of $Z_0 \cos\phi$ vs. $Z_0 \sin\phi$, called a Nyquist plot.[97]

Individual parts of an electrochemical system exhibit different responses as a function of AC frequency, and often behave close to ideal physical components such as resistors, inductors, and capacitors (tab. 2.1). E.g. the solid electrolyte interphase (SEI) between the anode and the electrolyte, as well as electrochemical double layers, behave close to ideal capacitors, which cause a phase shift of ϕ = -90° between $I(t)$ and $U(t)$. For Li ion batteries, usually 0° > ϕ > -90° is found, owing predominantly to geometric effects such as electrode porosity, and constant phase elements (CPEs) can be used to account for these effects and fit the data accurately (see tab. 2.1).

Inductors cause a positive phase shift of ϕ = 90°. Their effects are often small in battery cells and of lower interest to electrochemical research, as they arise predominantly from the metallic components such as current collectors and are usually observed in the high frequency region of a spectrum, which are less important for DC sources like batteries.

Diffusion processes cause phase shifts of ϕ = -45°, and the effects are often described using Warburg elements. Concentration gradients take comparatively long to build-up, and

Table 2.1: Impedance Behaviour of Common Equivalent Circuit Elements

Electrochemical System Component	Equivalent Circuit Element	Impedance Behaviour	ϕ [°]
Electrolyte & current collector resistance, charge-transfer processes	Resistor	$\boldsymbol{Z} = R$	0
Ideal double-layers, surface-layers, interfaces	Capacitor	$\boldsymbol{Z} = {}^{1}/_{j\omega C}$	- 90
Real double-layers, surface-layers, interfaces	Constant Phase Element	$\boldsymbol{Z} = {}^{1}/_{(j\omega)^{\alpha} Y_c}$	0 > ϕ > -90
Wires, current collectors, etc.	Inductor	$\boldsymbol{Z} = j\omega L$	90
Diffusion in electrodes, etc.	Warburg Element	$\boldsymbol{Z} = (1 - j)\sigma\sqrt{\omega}$	-45

R is the ohmic resistance, C is the capacitance, Y_c is the capacitance for a constant phase element (no direct physical meaning), α is a coefficient < 1, L is the inductance, and $\sigma \propto {}^{1}/\sqrt{D}$ is the Warburg coefficient, related to the system's diffusion coefficient D.

Warburg impedance effects are observed at low frequencies, usually < 1 Hz.

Lastly, ohmic resistances, which are frequency independent and do not exhibit a phase shift, arise from constituents such as the electrolyte or the current collectors, as well as resistances at interfaces, e.g. the charge-transfer resistance.

Using these components, an equivalent circuit, based on reasonable assumptions about the electrochemical system, can be fitted to the data.[97] The values for the fitted properties, e.g. resistances and capacitances, contain information about the studied system. A prerequisite for this is that a causal relationship exists between the input and output signals, which requires the system to be in a stable state for the duration of the experiment, and its response to be linear, as well as proportional to the input quantity. This requires stringent experimental conditions, such temperature control and suitable relaxation times of the electrochemical system before measurements, as well as sufficiently small input signals.

2.2 Synthesis of Cathode Materials

Li ion cathode materials can be prepared in a variety of ways, ranging from wet-chemistry techniques, e.g. hydrothermal synthesis, and solution-assisted approaches, such as co-precipitation and spray pyrolysis, to powder-based mechanochemical and high-temperature solid-state methods.[19,98,99]

The technique, as well as the exact synthesis conditions, greatly influence the electrochemical performance of the resulting material, as they control factors such as phase composition and purity, TM oxidation states, cation mixing, bulk and surface defects, and particle size distribution, amongst others.[19,98,100]

2.2.1 Solid-State Synthesis

For the solid-state synthesis of layered 3d TM cathodes, precursors based on metal oxides, carbonates, organic salts, and other compounds that decompose at elevated temperature, are usually used.[19,99] The powders are intimately mixed, e.g. using mortar and pestle or via ball milling, and pressed into pellets using several GPa of pressure, which increases the contact area between adjacent particles, reducing the diffusion lengths and facilitating a quicker reaction.[99] The precursors are then reacted at elevated temperatures ranging from several hundred degrees Celsius to above 1000 °C, under a variety of atmospheres (e.g. air, vacuum, O_2, H_2, etc.).

2.2.1.1 Resorcinol Formaldehyde Gel-Assisted Solid State Synthesis

In this thesis resorcinol formaldehyde gel-assisted synthesis (RF-gel), a solution-assisted solid-state approach, was used. The technique relies on creating a precursor powder via the combustion of a gel, formed from a solution containing stoichiometric amounts of Li and TM ions. The solidified gel traps the ions, and subsequent drying and combustion of the organic framework creates an intimately mixed metal oxide powder, which is reacted at

elevated temperatures in a second step.[101] Due to the nanoscale mixing of the ions, phase-pure powders can be synthesised without a pellet-pressing step.

2.2.2 Mechanochemical Synthesis

Mechanochemical synthesis is a collective term describing techniques that enable chemical reactions through externally introduced mechanical stress.[102] The reactants are usually loaded into a ball mill jar, comprised of a hard, abrasion resistant material such as ZrO_2, along with several balls of the same material. Energy is then introduced to the system by spinning or vibrating the jar at high speeds, e.g. in a planetary mill, resulting in a reduction of the particle size and intimate mixing, as well as high mechanical stress and localised heating, due to the high-speed impacts of the balls.[102] These extreme local conditions enable the synthesis of many compounds, some of which are metastable and not accessible using traditional heat-based synthesis routes. Process variables such as rotation speed and milling time, as well as size and density of the milling media, are available to control the synthesis conditions.

2.3 Electrode Preparation and Cell Assembly

In order to study the electrochemical behaviour of cathode materials, charge needs to be passed between it and a counter electrode in a controlled and reproducible manner. Cathode materials are electronic semiconductors or insulators and composite electrodes, comprised of the cathode active material (AM), a conductive additive, such as carbon black, and a polymer binder, that ensures structural stability, are used to increase the conductivity.[103–106]

2.3.1 Composite Cathode Preparation

Industrially, cathodes are usually prepared by casting, where the AM and conductive additives are suspended in a solution of the binder and a solvent like N-Methyl-2-pyrrolidone (NMP), creating a slurry, called ink. This ink is then coated onto a current

collector foil (e.g. Al) and the NMP evaporated, creating electrode sheets. A calendering step, in which the electrode is compressed between roller presses, is used to increase the contact area between the AM and the conductive additive, as well as control the porosity. The sheets are then cut to size and assembled into cells.
A similar process can be used in laboratory settings, where the ink is applied to the current collector using e.g. a doctor blade. These electrodes show excellent electrochemical performance, due to the intimate contact between AM and conductive additive.

For many analysis techniques, however, the presence of an Al current collector can be detrimental (e.g. diffraction experiments where additional reflections are introduced), and free-standing electrodes are desirable, which can be prepared using polytetrafluoroethylene (PTFE) as a binder. For cathodes used in this thesis this technique was used throughout. First, AM and carbon black were mixed for ten minutes using a mortar and pestle. Second, the PTFE was added to the mixture, and ground for five minutes. The resulting flakes were folded onto one other and sheared between the mortar and pestle for an additional five minutes. The resulting cathode was calendared using a roller press to a thickness of ~100 μm, and discs with ∅ 6 mm were cut using a hollow punch.

2.3.2 Coin Cell Assembly

Coin cells are the most popular cell format for the study of fundamental LiB electrode processes, as they are easy to assemble, hermetically sealed, and have an almost ideal, parallel electrode geometry, where both cathode and anode pellets are compressed between oversized current collectors (fig. 2.2). This prevents geometric factors, such as the number and position of tabs, from influencing the electrochemical response of the system.

Coin cell dimensions are standardised for 'watch batteries' in IEC 60086-3, and most available cells follow this same convention. For larger cells, the standard establishes a four digit system, where the first two describe the approximate diameter of the cell in millimetres,

and the second two give the thickness in 0.1 mm increments. In this thesis 2325 coin cells, with a diameter ∅ of 23 mm and a thickness h of 2.5 mm, as well as 2032 (∅ 20 mm, h 3.2 mm), were used.

During assembly (fig. 2.2), a cathode pellet (7) is placed inside the can (8) and covered with a glass fibre or polymer separator (6). The separator is soaked with electrolyte, a Li metal disc (5) is placed on top of it, and covered with a stainless steel spacer (4) and a spring (3). A polypropylene gasket (2) is fitted around the lip of the lid (1) and the assembly placed on top of the spring (3). The whole cell is then hermetically sealed, in a dedicated tool, by partially crimping the top of the can (8) around the gasket (2), without electronically contacting the lid (1).

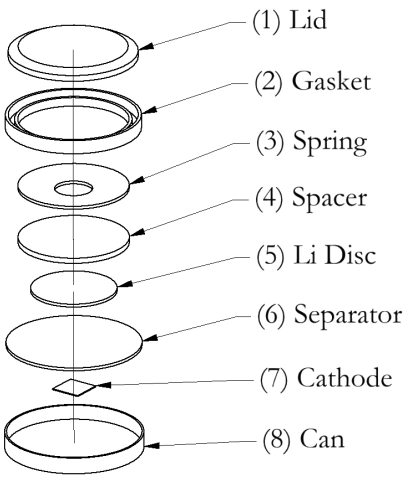


Figure 2.2: Exploded view of a coin cell.

To remove the cathode after cycling, e.g. for *ex-situ* analysis, the cells can be opened using a dedicated decrimping tool that prevents short circuiting.

2.3.3 Three-Electrode Pouch Cell Assembly

Coin cells are limited to two-electrode experiments, owing to their architecture, and the collected electrochemical data is a combination of the responses of the anode and cathode. In order to separate the effects of the individual electrodes on the total cell properties, a three electrode set-up is required, where a reference is placed in between the working and counter electrodes.

This can be achieved with pouch cells, using a cell stack as depicted in fig 2.3. L-shaped

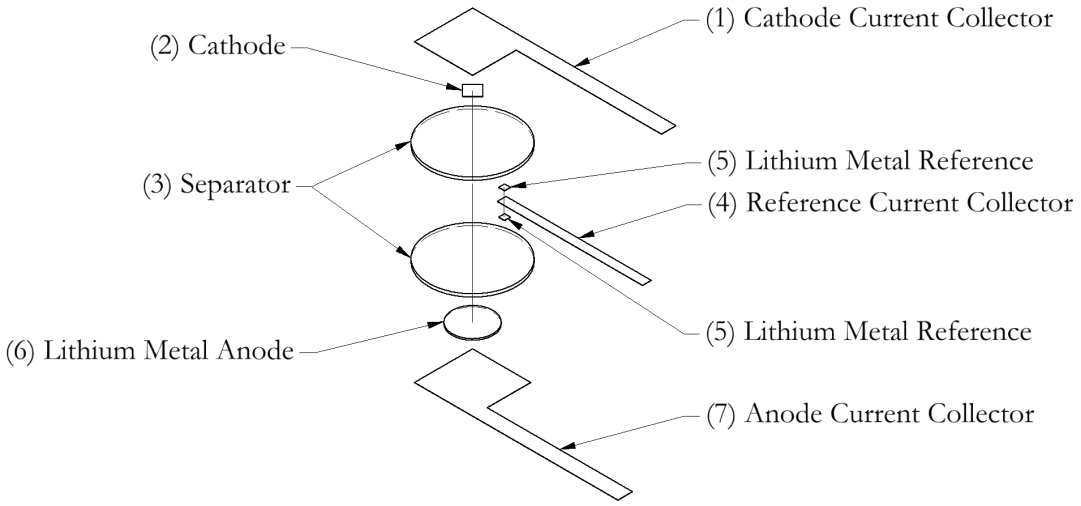


Figure 2.3: Exploded view of a three-electrode cell stack, which is sealed inside an aluminium laminate pouch for electrochemical testing.

current collectors (1, 7) are used to connect the cathode (2) and Li metal anode (6) to the external circuit. In between, a small Li metal reference electrode (5), on a thin current collector (4), is compressed between two glass fibre separators. The reference electrode assembly is arranged in such a way that it is as close as possible to the anode and cathode, but not in between, in order not to disturb the flow of ions. Similarly, it is placed in a manner that the Li pellet is equidistant to both cathode and anode.

Electrolyte is added to the separators, and the whole stack is vacuum-sealed inside of an aluminium laminated pouch, with the three current collectors protruding from the seal. The pouch can then be clamped between two rigid surfaces, to provide stack pressure.

2.4 Total Scattering and Diffraction Analysis

Condensed matter is comprised of atoms, with bond distances of approximately the same order of magnitude as the wavelengths of X-ray, neutron, and electron radiation. As a result, the waves of these particles create interference patterns after scattering on the atoms, and the resulting intensity variations contain information that can be used to analyse the local and

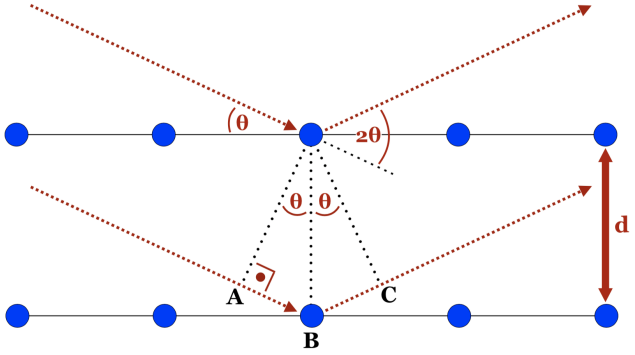


Figure 2.4: The scattering geometry underlying Bragg's law for two planes of atoms with a separation of distance d.

average structures of materials. The following sections outline the techniques used in this thesis.

2.4.1 Diffraction Analysis and Long-Range Order

Crystalline solids contain regular arrays of atoms or ions. This order can be described using the planes generated by the regular arrangement, which are described by the Miller indices hkl. These are defined as the reciprocal values of a plane's intersects with the lattice vectors of the unit cell **a, b, c**, e.g. the (215) plane has intersects at 0.5 **a**, 1.0 **b**, and 0.2 **c**.
The waves scattered by a set of (geometrically equivalent) planes $\{hkl\}$ interfere destructively, unless the path difference between waves scattered by two adjacent planes is an integer multiple of the wavelength, as described by Bragg's law (fig. 2.4):[107,108]

$$\begin{aligned} n\lambda &= \overline{AB} + \overline{BC} \\ &= 2\overline{AB} \\ &= 2d_{hkl}\sin(\theta) \end{aligned} \tag{2.24}$$

where n is an integer, λ is the wavelength, the points A, B, C are defined in fig. 2.4, d_{hkl} is the lattice spacing for the set of planes $\{hkl\}$, and θ the incident angle.

The constructive interference can be detected as a sharp increase in the intensity of scattered

radiation, termed reflection, and a set of reflections in a diffraction pattern can be used to determine the lattice spacings and symmetry of the underlying crystal structure.
For single crystals, the reflections are visible as distinct spots, whereas the random crystallite orientations in a powder sample cause the radiation to be scattered statistically, creating rings of diffracted radiation. A 2D powder diffractogram is a slice through these cones, with the intensity of the cones i recorded on the ordinate.

The scattering angle between the incoming and reflected beam is at an angle of 2θ (fig. 2.4), and the intensity variation is usually reported as a plot of i vs. 2θ. This makes direct comparison of data collected using different wavelengths difficult, as the scattering angles vary. A wavelength-independent quantity is the absolute value of the scattering vector q:

$$q = \frac{4\pi sin\,(\theta)}{\lambda} \quad [\text{Å}^{-1}] \tag{2.25}$$

Using q instead of 2θ, data collected using different kinds of radiation can be compared directly, and it is used exclusively in this thesis.

The positions of the Bragg reflections in a diffractogram contain information on the unit cell size and space group (symmetry), but not on the kinds of elements populating it. This information is contained in the intensity of the reflections, which depends on the species' scattering properties:.
The intensity i_{hkl} of a reflection, corresponding to a set of planes $\{hkl\}$, is related to the structure factor F_{hkl}:

$$i_{hkl} \propto |F_{hkl}|^2 \tag{2.26}$$

where F_{hkl} is defined as:

$$F_{hkl} = \sum_m f_m e^{2\pi j(hx_m + ky_m + lz_m)} \tag{2.27}$$

where f_m is the atomic form factor of atom m. x_m, y_m, z_m are the corresponding real-space coordinates, and hkl are the Miller indices.

For electrons, f describes the q-dependent scattering power of atoms and ions, as a multiple of the scattering power of a single electron (fig. 2.5). This is due to the oscillating electric field of an X-ray interacting with the atom's electrons, and their number is therefore directly proportional to the scattering amplitude. At $q = 0$, $f = Z$, provided the atom is not ionised. A similar relationship with a strong q-dependence exists for electron radiation. Neutrons interact with the nucleus of atoms via the strong nuclear force, and the neutron equivalent of f, the scattering length b, shows no q-dependence, as well as no Z-dependent trend, varying significantly between adjacent elements and even isotopes. The diffractograms for the same compound, collected using multiple kinds of radiation, can hence look very different.

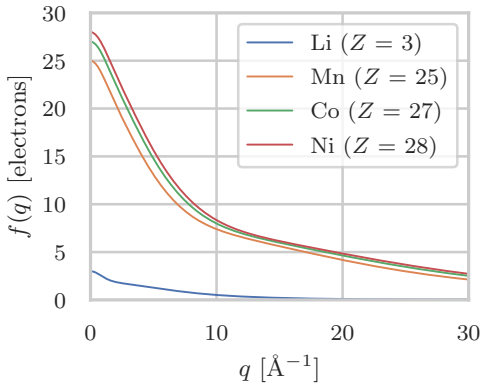


Figure 2.5: X-ray atomic form factors f for elements commonly used in Li ion batteries.[109]

A final property of a diffractogram is the shape and width of the reflections. As diffraction experiments are not conducted at absolute zero temperature, the thermal motion of atoms around their mean positions causes broadening. Additionally, the instrument has a contribution, as well, as e.g. the wavelength of the radiation is not perfectly monochromatic and has a spread around an average energy.

Two other important sources are the size of the crystallites in the sample, as well as lattice strain. For crystallite sizes below ~100 nm, the peak width increases according to the Scherrer equation:[110]

$$\beta_{ps} = \frac{K\lambda}{\tau \cos\theta} \tag{2.28}$$

where β_{ps} is the broadening, K is a constant ~1, and τ is the crystallite size, also called domain size.

Microstrain also causes peak broadening, as it changes the lattice spacings:

$$\beta_{\epsilon} = 4\epsilon \tan\theta \tag{2.29}$$

where β_{ϵ} is the strain broadening, and ϵ the lattice microstrain.

In practice, many factors influencing a diffraction pattern, such as details of the the instrument geometry and broadening, are determined through the use of a standard with known properties, and fixed for the data processing of unknown samples. This way parameters, such as the unit cell dimensions and site occupancies, can be obtained. Especially more sensitive contributions, such as peak broadening, require careful calibration of the instrument's effects. The different types of broadening can then be separated, based on their different q-dependence, provided sufficient reflections are present.

2.4.1.1 Rietveld Refinement

Rietveld refinement is a methodology for iteratively fitting a structure to a diffraction pattern using a least-squares method. In this approach, a reasonable guess for a structure is used as a starting point, and its peak positions, intensities, and broadening are calculated using the equations outlined in the previous section. The resulting pattern is added to a background, usually described by a polynomial, which attributes for the diffuse (non-Bragg) scattering of the sample.

The calculated result is then compared with the experimental pattern, and, via variation of parameters such as unit cell parameters or site occupancies, improved using a least-squares algorithm.

The algorithm minimises

$$\Delta = \sum_m w_m (i_{c,m} - i_{e,m})^2 \tag{2.30}$$

where w_m is a weighting factor, i_m is the intensity at q_m, the indices c and e describe calculated and experimental values, respectively, and m runs over the data points of the sample.[111,112]

A common way to quantify the discrepancy between the calculated and experimental data is the weighted profile factor R_{wp}:[111]

$$R_{wp}^2 = \frac{\sum_m w_m (i_{c,m} - i_{e,m})^2}{\sum_m w_m i_{e,m}^2} \tag{2.31}$$

$$= \frac{\Delta}{\sum_m w_m i_{e,m}^2} \tag{2.32}$$

The 'goodness of fit' as determined by R_{wp} depends largely on which parts of the data are taken into account. A large amount of well-fit background reduces R_{wp} but does not directly improve the fit's information, as the data at the sharp reflections is significantly more important.

An ideal value for R_{wp}, taking into account the number of data points, is called the expected R-factor R_{exp}:[111]

$$R_{exp}^2 = \frac{N - P}{\sum_m w_m i_{e,m}^2} \tag{2.33}$$

where N is the total number of data points, and P is the number of fit parameters. This enables the use of a relative measure of 'goodness-of-fit' chi-squared (χ^2):[112]

$$\chi^2 = \left(\frac{R_{wp}}{R_{exp}} \right)^2 \tag{2.34}$$

with values $\chi^2 \geq 1$, and $\chi^2 = 1$ for the best possible fit.

Using this iterative approach, in conjunction with a chemically reasonable starting model, the average, long-range structure of a compound can be determined with high precision.

2.4.2 Total Scattering and Local Structure Analysis

Bragg diffraction analysis is a powerful tool for understanding the long-range structure of solids, but the technique is limited to solving the average structure, as the diffraction peaks arise from the constructive interference of many planes of atoms. The background surrounding the Bragg reflections, which arises from diffuse scattering, is not analysed explicitly but fitted with e.g. a polynomial, and the information contained within it is ignored. Pair distribution function (PDF) analysis treats all parts of the scattering data equally and explicitly includes the diffuse 'background' scattering. The technique can therefore be used to analyse the structure of matter without long-range order, including gasses, liquids, and amorphous solids.[113,114]

Experimentally, the setup is similar to diffraction experiments, however more care needs to be taken to minimise unwanted contributions. As for diffraction, the total scattering intensity $i(q)$ is collected,† however to much larger values of q (large scattering angles). It therefore contains the Bragg reflections, as well large regions of almost featureless diffuse scattering. A value of q ~8 Å^{-1} is the maximum achievable on a laboratory diffractometer using Cu-K$_\alpha$ radiation, whereas $q \geq 20$ Å^{-1} is required for PDF, to obtain a sufficient resolution, and experiments are often performed with high-energy synchrotron radiation.

Using $i(q)$, the reduced scattering function $S(q)$ is derived via normalisation:

$$S(q) = \frac{i(q)}{N\langle f(q)\rangle^2} + \frac{\langle f(q)\rangle^2 - \langle f^2(q)\rangle}{\langle f(q)\rangle^2} \tag{2.35}$$

where N is the number of scatterers and $\langle f(q)\rangle$ is the arithmetic mean of the form factors

†As only powdered samples are used in this thesis, and the properties are hence isotropic, $q = |\mathbf{q}|$, where $\mathbf{q}$ is the scattering vector, is used to present the scattering-angle-dependence of all properties in this thesis. The equations are therefore not valid for single-crystal total scattering.

$f(q)$, which are defined as in 2.4.1. This has the effect that $\langle S(q) \rangle = 1$.

To increase the contribution from the high-q region, where the information of the diffuse scattering is predominantly contained, the reduced total structure function $F(q)$ is calculated:

$$F(q) = q\,(S\,(q) - 1) \tag{2.36}$$

$F(q)$ is a normalised, scaled version of the total scattering $i(q)$ obtained experimentally. As it is still defined as a function of reciprocal / q-space, its interpretation is not intuitive and a transformation into real space is achieved via a sine Fourier transform, resulting in the reduced pair distribution function $G(r)$: [‡]

$$G(r) = \frac{2}{\pi} \int_0^\infty F(q) sin(qr) dq \tag{2.37}$$

$$= \frac{2}{\pi} \int_{q_{min}}^{q_{max}} F(q) sin(qr) dq \tag{2.38}$$

$$\approx \frac{2}{\pi} \sum_m^{N-1} F_{q,m} \sin\left(\frac{2\pi m}{N} r\right) \tag{2.39}$$

where r is the real-space radius, q_{min} and q_{max} are the extrema of the collected data, and the last equation factors in the discrete nature of the data with N sample points, with $F_{q,m}$ as the m^{th} sample of $F(q)$, and making use of the implied periodicity of a discrete Fourier transform.

$G(r)$ oscillates around the abscissa and $G(r) \longrightarrow 0$ as $r \longrightarrow 0$ with a slope of $-4\pi\rho_0$, where $\rho_0 = N_A/V$ is the average number density of the material (atoms per unit cell [# Å^{-3}]). In a perfect crystal, this oscillation continues as $r \longrightarrow \infty$, but in real systems it approaches zero due to the finite size of the scattering domains. The function hence contains information

[‡]In literature, the acronym PDF is used as an umbrella term for several forms of correlation functions based on Fourier-transformed total scattering data. In this thesis, and if not otherwise specified, PDF refers to $G(r)$ as defined here.

on the dimensions of the studied material, e.g. crystallite size.

As $G(r)$ is obtained directly from the Fourier transform of the data, measurement uncertainties are not a function of r, and hence errors during fitting (the difference between a calculated and experimentally observed $G(r)$) are indicative of the validity of a structural model at a certain region.[115] $G(r)$ is therefore very useful to interpreting fit quality and used for all data fitting in this thesis, although the quantity is not directly physically meaningful.

Several directly physically significant correlation functions, however, can be derived, including $g(r)$, which gives the probability of finding two atoms separated by a distance of r:

$$g(r) = \frac{G(r)}{4\pi r \rho_0} + 1 \tag{2.40}$$

An second, important function is the radial distribution function $R(r)$:

$$R(r) = 4\pi r^2 \rho_0 g(r). \tag{2.41}$$

which is closely related to the structure of a material, as its integral gives the number of atoms N_A within a certain distance window:

$$N_A = \int_{r1}^{r2} R(r) dr. \tag{2.42}$$

$R(r)$ is can also be calculated for a given structure model via:

$$R(r) = \frac{1}{N} \sum_m \sum_n \frac{f_m^* f_n}{\langle f \rangle^2} \delta(r - r_{mn}) \tag{2.43}$$

where the atomic form factors f_i are defined as in sec. 2.4.1, N is the number of atoms, $\delta(r - r_{mn})$ is a Dirac delta function located at the distance r_{mn} between atoms m and n, and the indices run over all atoms in the structure.

Further information about the structure is contained in the pair correlation functions g_{mn} between different atomic pairs in the structure:

$$g_{mn}(r) = \frac{1}{N_m}\frac{1}{N_n}\sum_{m}^{N_m}\sum_{n}^{N_n}\delta(r - r_{mn}) \tag{2.44}$$

where the indices m, n only run over the two species of interest. These functions can be used to show the relationships (correlations) between different kinds of atoms in a structure, which is particularly important for complex structures (e.g. disordered rocksalts), where a simple unit cell is not sufficient to fully describe the material.

Lastly, the reduced scattering function $S(q)$ can be recovered from the real-space data via an inverse transformation:

$$S(q) = \frac{1}{q}\int_0^\infty G(r)\sin(qr)\,dr + 1 \tag{2.45}$$

As can be seen, $R(r)$ and therefore $G(r)$, as well as $S(q)$, are accessible through both experiment and structural models. Experimental PDF data can hence be fit using an iterative approach similar to Rietveld refinement (sec. 2.4.1.1).

2.4.3 Reverse Monte Carlo Fitting

"Monte Carlo" is an umbrella term for methods that are based on random sampling to generate an approximate solution for a given problem.[116] The general principle lies in calculating a state or a property, which is a function of variables, before and after a random change is made. If, after comparing the outcomes of the two states, the new one shows an improvement in a predetermined metric, the move is accepted. Otherwise it is accepted only with a certain, finite probability < 1. Over time, this results in a map of a property or state vs. the variables. As moves with a detrimental effect are also accepted, albeit with a

lower frequency, these algorithms can find global minima, and do not terminate at the first local minimum.

An example is the internal energy of a solid, which varies as a function of the atomic coordinates. Using a Monte Carlo approach, the energy can be calculated while the atomic positions are varied. Over time, a surface of the internal energy vs. different atomic arrangements is generated, that is guided towards the global minimum by the different probabilities of accepting moves that do and do not lower the energy. Choosing appropriate parameters for the magnitude of the random moves ensures that the algorithm runs in a stable fashion.

Reverse Monte Carlo (RMC) methods are similarly based on random moves, however using experimental data to guide the algorithm. The calculated values are compared to a dataset, e.g. scattering data, and moves which improve the fit are accepted with a higher probability than those that do not.[117]

For PDF data, a first guess for the structure is made, usually in the form of a supercell derived from a Rietveld refinement. The size of the supercell, often called box, is then based on the correct unit cell parameters of the average structure, and the atoms within represent the average atomic configuration. The algorithm then calculates the PDF for this cell, using the equations derived in the previous section, and compares it to one or several experimental datasets.[118] The goodness of fit, χ^2_k, is then determined via:[118,119]

$$\chi^2 = \sum_m \frac{(y_{c,m} - y_{e,m})^2}{\sigma_m^2} \tag{2.46}$$

where $y_{c,l}$ and $y_{e,l}$ are the calculated and experimental value at the m^{th} datapoint. The parameter σ_m can be the standard error, or, as in the case of the software used in this work, a manually set variable, used to weight the contribution of different data.

The total goodness-of-fit χ^2_T is then calculated via:[118,119]

$$\chi_T^2 = \sum_n \chi_n^2 \tag{2.47}$$

where n runs over all datasets used.

For each of these iterations, a random change to the structure is made, e.g. by moving an atom, or swapping two, and the difference between the previous $\chi^2_{T,old}$ and the new $\chi^2_{T,new}$ is calculated. For the software used in this thesis, the probability of a move being accepted (p_{acc}), is given by:[118,119]

$$p_{acc} = \begin{cases} 1, & \text{if } \chi^2_{T,new} \leq \chi^2_{T,old} \\ e^{-\frac{\chi^2_{T,new} - \chi^2_{T,old}}{2}}, & \text{if } \chi^2_{T,new} > \chi^2_{T,old} \end{cases} \tag{2.48}$$

As in conventional Monte Carlo techniques, this fit-dependent acceptance of the change allows the RMC algorithm to converge towards the global minimum of χ^2_T.

Due to the random movements of the atoms, RMC methods tend to converge towards the most highly disordered structures.[118] These are not necessarily physically or chemically meaningful, and additional constraints are usually required to guide the calculation. This can be achieved by including data that are biased towards the long-range order, e.g. $S(q)$ or Bragg diffraction data, requiring moves to fulfill both local and long-range criteria. In this work the algorithm implemented in the RMCprofile package (Version 6.7.0) was used, which was created for this purpose.[118,119]

2.4.3.1 Total Scattering Function Convolution

The supercell used for the optimisation via RMC is of a finite size, as a compromise between model accuracy and calculation time, which is accounted for by introducing periodic boundary conditions at its ends. This periodicity implies that the correlation functions, such as $G(r)$, can only be calculated to a maximum of half of the shortest length of the

cell, and the calculated real space data is therefore truncated at this point. Mathematically, this is achieved by multiplying $G(r)$ with a step function, the Fourier transform of which is a sinc function. $S(q)$ is calculated as the Fourier transform of $G(r)$, and therefore in turn convolved with a sinc function. To enable a direct comparison, the experimental $S(q)_e$ needs to be convolved similarly, resulting in an 'unphysical' appearance of the fit $S(q)$ data.

2.4.4 Practical Aspects of Scattering Experiments

A direct result of the strong interactions between X-rays and matter is that only small amounts of sample, on the order of milligrams, are needed to collect an $i(q)$ pattern with a good signal-to-noise ratio. Due to the X-ray form factors, light elements, such as Li, are hard to detect using X-ray-based techniques, as their scattering power is low. Additionally, elements with similar atomic numbers, such as the 3d TMs, are hard to distinguish. The strong q-dependence of the scattering factors also requires significant data collection times for PDF experiments, to achieve sufficient counting statistics in the high-q regions.

As the neutron scattering length b does not scale as a function of Z, techniques based on this radiation are powerful tools for distinguishing between different TMs, and particularly to identify positions occupied by Li. b is also constant with q, resulting in good counting statistics in the high-q region. The weak interaction between the electrically neutral neutrons and the atoms, however, requires significantly larger sample masses of several 100s of milligrams, as well as collection times of several hours, to obtain sufficient signal-to-noise.

2.5 Transmission Electron Microscopy (TEM)

Transmission electron microscopy (TEM) is a technique in which the transmission of an electron beam through a very thin sample is used to analyse the local morphology and structure.[120] A focussed beam of high-energy electrons is accelerated through an electric field and directed onto the sample surface. Part of it is transmitted and hits a phosphor

screen or a charge-coupled device (CCD) camera, where an image is formed.

As electrons are charged particles, a strong interaction occurs between the electrons of the beam and the charges of the nuclei and electrons in the process. The amount of absorption therefore mainly depends on the number of protons and electrons in the beam path, and hence Z, as well as the sample thickness.

Due to the low wavelengths of the accelerated electrons, a higher resolution can be achieved compared to light microscopy, and in high-resolution instruments individual columns of atoms can be observed.

During the interaction between the electrons and the charges in the materiale, part of the electrons are scattered, creating a diffraction pattern. These patterns contain information on the average local crystal structure, as outlined previously (sec. 2.4.1).[120] The combination of both direct observation of the local structure, and the average structure from diffraction, can then be used to characterise the local environments.

2.6 X-ray Absorption Spectroscopy (XAS)

X-ray absorption spectroscopy (XAS) entails a wide range of techniques that use the absorption of X-rays of varying energy to study materials, based on the fact that elements absorb radiation at characteristic energies within the X-ray regime. Increases in X-ray absorption, due to transitions of bound electrons into unoccupied states and the continuum, are used to probe an element's unoccupied density of states, as well as its coordination environment. Synchrotron radiation has made these powerful

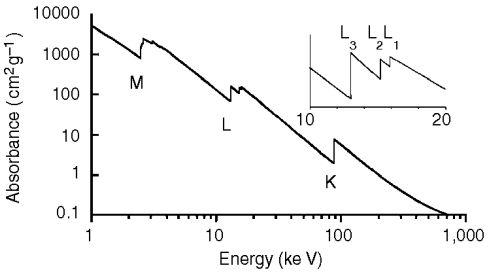


Figure 2.6: The X-ray absorption spectrum for Pb. Three absorption edges are visible, based on excitations from different energy levels within the atom.
Reprinted from [121], Copyright (2003), with permission from Elsevier.

techniques common in battery research, as high-brightness sources of monochromated X-ray radiation are accessible with moderate experimental effort.

When a sample is subject to a beam of X-rays, whose energy is varied, sudden increases in the absorption are observed at certain, element-specific energies (fig. 2.6). Each rise in absorption occurs as a photon is absorbed by an electron, which requires the photon energy to be equal to the energy of the electronic transition from a bound to an unoccupied state:

$$\hbar\nu = E_{b\to u} \tag{2.49}$$

where $\hbar$ is Planck's constant (~$6.626 \cdot 10^{-34}$ Js), ν is the photon's frequency, $E_{b\to u}$ is the energy difference between two states. In addition to the minimum energy, the transitions are also constrained by the selection rules, most importantly the dipole rule for the change of angular quantum number ℓ: $\Delta\ell = \pm 1$. Due to this, allowed transitions occur between adjacent shells, e.g. s → p and p → d, and these processes have high absorption intensities (fig. 2.7). Electric quadrupole transitions, where $\Delta\ell = 0, \pm 2$, occur as well, however with much lower intensities, as they have a relative probability of occurring $\lessapprox$ 0.1 %, compared to the dipole transitions.[122,123]

The naming convention of the transitions is based on the principal quantum number n of the initial state of the electron, where the K, L, M transitions correspond to excitations from n = 1, 2, 3, respectively (fig. 2.7).[124] The energies of the K and L transitions vary significantly between different elements, but vary only by a few eV for different compounds of a given element, making XAS an element-specific probe.

In solids, the individual atomic orbitals are replaced by a band structure, but the same principles apply, and XAS can be used to excite electrons into the unoccupied DOS of the correct character (e.g. the contribution from the d-states) in hybridised orbitals.

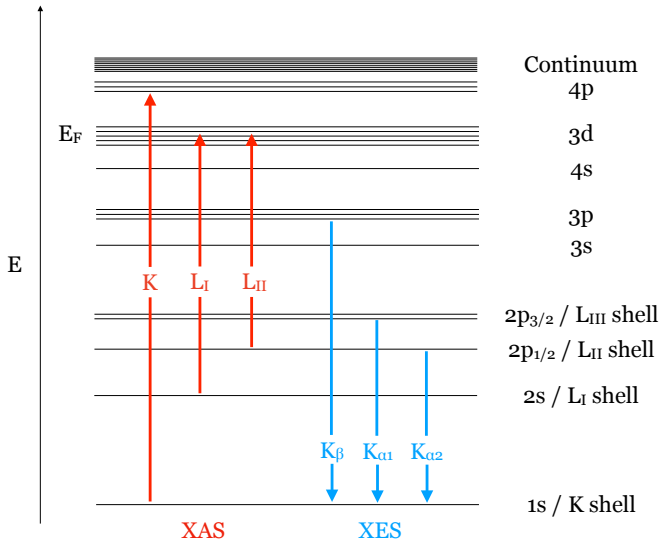


Figure 2.7: Simplified electron shells and relevant dipole-allowed electronic transitions in 3d TMs. Absorption processes in red, emission in blue.

The absorption of X-rays follows the Beer-Lambert law:

$$i(E) = i_0(E)e^{-\mu(E)x} \rightarrow \mu(E) \propto \ln\left(\frac{i(E)}{i_0(E)}\right) \tag{2.50}$$

where i is the intensity after passing through the sample, i_0 is the initial intensity, E is the X-ray energy, μ is the absorption coefficient, and x the distance travelled through the solid by the X-ray.

The probability of an excitation occurring into a certain final state is proportionate to the empty DOS at that energy, according to Fermi's golden rule:

$$\mu\left(E\right) \propto \sum_f |\langle \Psi_i | \nabla | \Psi_f \rangle| \delta\left(E_f - E_i + h\nu\right) \tag{2.51}$$

where Ψ_i is the initial state, Ψ_f is the final state, ∇ is the dipole operator, δ is a Dirac delta function, and E_i and E_f are the energies of the initial and final state, respectively.

A plot of $\mu(E)$ vs. E hence contains information on the energetic position and magnitude of the unoccupied DOS, which is, in turn, strongly related to the oxidation state of the element and bond lengths to surrounding atoms.

Experimentally, $i_0(E)$ is often detected using an ionisation chamber, through which the incoming X-ray beam is routed, and $i(E)$ either the same way, or using a suitable proxy quantity. These are usually based on the fluorescence or electrons emitted by the sample upon relaxation from the excited state. Frequently used techniques are total fluorescence yield (TFY), where all radiation emitted from the sample is detected, partial fluorescence yield (PFY), where only a certain energy range is monitored, and total electron yield, where the total number of ejected electrons is quantified.[125]

The raw $\mu(E)$ obtained this way consists of a downward-sloping region before the rising edge, the edge itself, and following oscillations, arising from interactions with neighbouring atoms, that decay with increasing energy (fig. 2.6). In order to regularise the data, and make them comparable to other spectra, they are processed. The influence of lower-energy edges is removed by fitting a first order polynomial to the pre-edge region, extrapolating it across the whole spectrum, and subtracting it. Normalisation is achieved by fitting a second-order polynomial to the high-energy region, extrapolating it to the low-energy region including the edge, and dividing all data by the function.[126]
The result of the processing is a flat, normalised spectrum, which exhibits distinct features, that are the basis for several analysis techniques, that will be discussed in the following (fig. 2.8).

2.6.1 X-ray Absorption Near Edge Structure (XANES)

X-ray Absorption Near Edge Structure (XANES) is a powerful XAS technique that focusses on the region in the immediate vicinity of the edge (fig. 2.8). The edge itself is usually defined as the maximum of the first derivative of the XAS spectrum, while the absorption maximum is called the white line. For 3d TMs, the XANES region is based on 1s $\rightarrow$ 4p transitions, which extend up to ~50 eV above the edge, and with the shape defined by the coordination environment and oxidation state of the element.

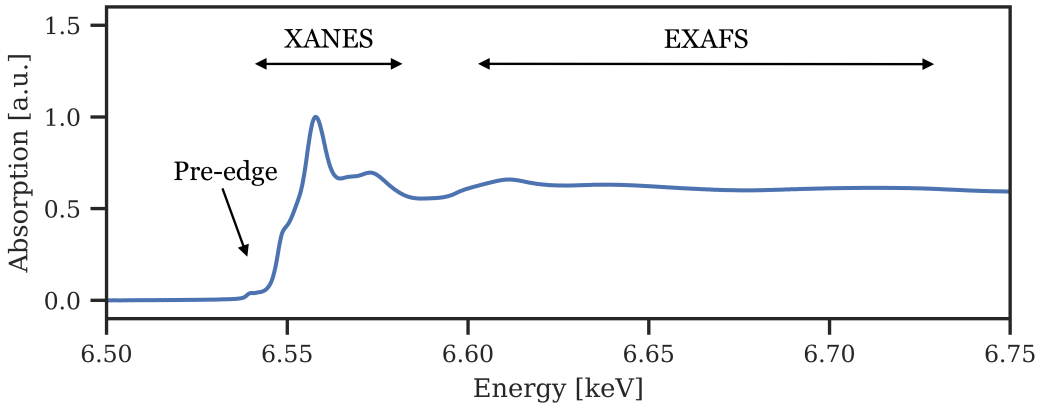


Figure 2.8: Normalised Mn K edge XAS spectrum of Li_2MnO_2F, obtained on beamline B18 (Diamond Light Source). The white line energy is ~6.558 keV and XAS techniques and their energies are shown.

Changes of the oxidation state manifest as shifts of the absorption energy, which can be explained intuitively by the approximation that a change in number of electrons results in a change in shielding of the nucleus' attraction on the remaining negative charges. As a result, an increase in oxidation state results in a stronger Coulomb attraction, causing an upward shift of the edge energy. This correlation is not perfect, and other effects, such as bond lengths and -angles, as well as ligand number and charge, can influence the XANES spectrum significantly.[127] In calculations made for MnO_6 octahedrons with fixed electronic structure but varying bond lengths, shifts of up to 5 eV were observed.[127] Ultimately, the charge density present around the probed ion determines the shielding, which can be heavily influenced by the kind of ligands and their inductive effects.

The pre-edge in 3d TM K edge XANES is observed at energies immediately above the Fermi energy and below the main edge (fig. 2.8). It is comprised of quadrupole-allowed 1s → 3d excitations, as well as dipole-allowed excitations into hybridised 3d/4p states, that arise when no inversion symmetry is present around the TM (e.g. tetrahedral complexes).[128] In Mn complexes, the shift of the K pre-edge energy has been linked directly to changes in charge density, and is a better indicator of the oxidation state, compared to the rising K edge.[127–129] In practice, 'fingerprinting' is a commonly used approach to qualitatively study both the

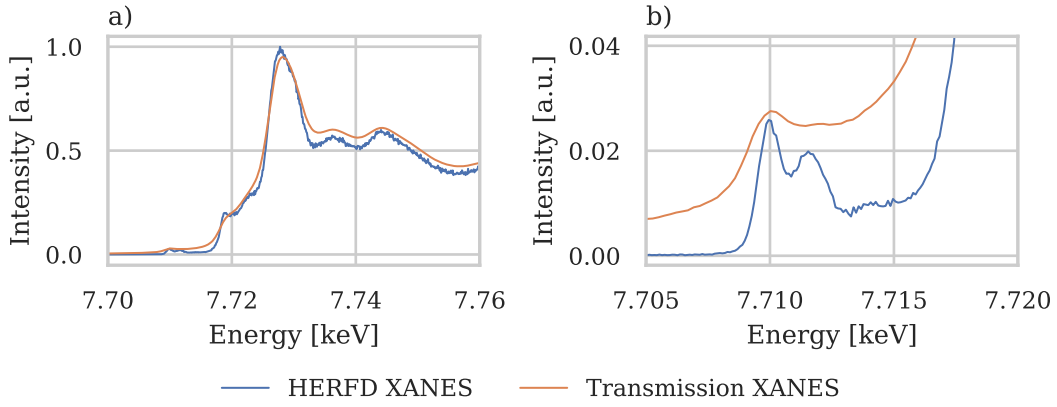


Figure 2.9: Comparison of HERFD XANES and Transmission XANES for the Co K edge in $Li_{1.2}Ni_{0.13}Co_{0.13}Mn_{0.54}O_2$, measured on beamline ID26 (ESRF) and B18 (Diamond Light Source), respectively, for a) the K edge and b) the pre-edge region.

K edge XANES region, as well as the pre-edges, in which spectra are compared to ones of structurally well-characterised references, with known oxidation states and coordination environments. Through direct comparison, the coordination geometry is then deduced from peak shapes and intensities, and the oxidation state inferred from the peak positions of the K edge and pre-edge region.[130]

2.6.1.1 High-Energy-Resolution Fluorescence-Detected X-ray Absorption Near Edge Structure (HERFD-XANES)

Conventional transmission or TFY XANES is subject to lifetime broadening of the core hole, which smears out the features, particularly in the pre-edge region.[130] In the 1970s, first experiments showed that by measuring the PFY in a narrow energy range, similar to the lifetime broadening, the effect could be significantly reduced. This approach, called high-energy-resolution fluorescence-detected XANES (HERFD-XANES), results in spectra with much more clearly resolved features (fig. 2.9).[131]

Experimentally, the technique requires specially set-up beamlines, where Bragg diffraction from perfect crystals is used to select a narrow energy range of the fluorescent radiation emitted by the sample. This can be accomplished using a Johann-type spectrometer, where

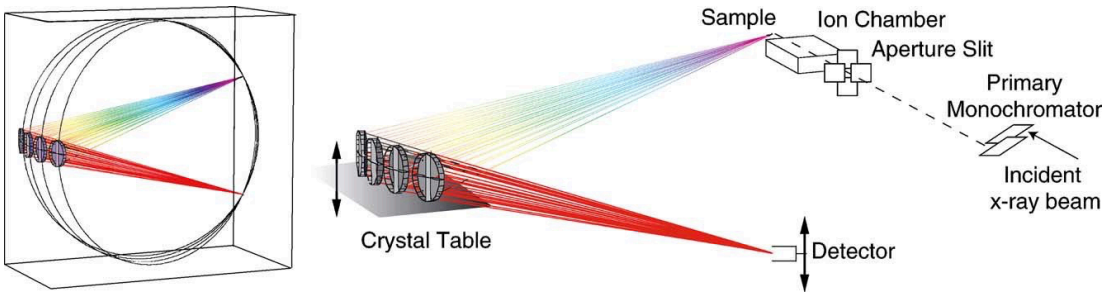


Figure 2.10: Schematic of a Johann-type spectrometer for HERFD XANES, XES, and RIXS.
Reprinted from [122], Copyright (2005), with permission from Elsevier.

spherically-bent crystals are used to focus the fluorescent radiation onto a photodiode (fig. 2.10).[122,130,132] Usually part of a strong emission line, such as the maximum of the K_α or K_β line, is used, in order to obtain good counting statistics (fig. 2.7).[129,130]

2.6.2 Extended X-ray Absorption Fine Structure (EXAFS)

At energies above the XANES region, oscillations are observed in XAS spectra (fig. 2.8). These oscillations are causally related to the scatterers surrounding the center atom, and hence the coordination environment, and form the basis for extended X-ray absorption fine structure (EXAFS).

When core electrons are excited into the continuum, where they are not bound to the nucleus, an electron wave is emitted radially from the atom. This wave is scattered by the surrounding atoms' electrons, and the wave functions of the outgoing and backscattered electron waves overlap, creating an interference pattern. The electron's wavelength λ_e, and hence the interference pattern, is a function of the photoelectron's energy:

$$\lambda_e = \frac{\hbar}{\sqrt{2m_e E_e}} \tag{2.52}$$

where $\hbar$ is Planck's constant, and m_e and E_e are the mass and energy of the electron, respectively.

The absorption coefficient μ is a function of the magnitude of the electron's final state wave function, as shown in eq. 2.51, which varies due to the interference with the backscattered waves, resulting in differences in $\mu(E)$.

The EXAFS $\chi(E)$ can then be represented as:

$$\chi(E) = \frac{\mu(E) - \mu_0(E)}{\mu_0(E)} \tag{2.53}$$

where $\mu_0(E)$ is the theoretical absorption coefficient without the influence of surrounding scatterers, and approximated using a spline fit to the high-energy range where the oscillations have decayed, and extrapolated into the EXAFS region. $\chi(E)$ is usually plotted as a function of $k = {}^{2\pi}/_{\lambda}$ [Å^{-1}]. $\chi(k)$ is then often weighted with k^2 or k^3, in order to increase intensity in the high-k region. The resulting function is then Fourier transformed, resulting in a real-space radial distribution function $|\chi(r)|$, containing information on the number and scattering power of the surrounding atoms.

2.7 X-ray Emission Spectroscopy (XES)

In addition to XAS, the emission of fluorescent radiation, released during the relaxation of electrons from excited states, can be used to study the electronic structure of materials (fig. 2.7). Akin to the K absorption edges, the K fluorescence energies are element specific, and can be used to probe the electronic structure.[122] (Non-resonant) X-ray emission spectroscopy (XES) makes use of this fact, and is a powerful technique to gain information on the spin state of a TM.

In K fluorescence spectroscopy, a 1s electron is excited to the continuum via photoionisation, using a similar experimental set-up as described for HERFD-XANES (fig. 2.10). However, instead of scanning through a range of energies, and monitoring at a fixed emission energy, the excitation energy is kept constant and the emission energy is scanned.[122] For 3d TMs this results in an initial $3d^n \rightarrow 1s^1 3d^n$ excitation, where the excited state decays through an electron transitioning from a higher shell and filling the energetically unfavourable 1s core

hole. The energy difference between the final and excited state is emitted as fluorescent X-ray radiation that can be detected.

Fluorescence is based on electronic transitions and therefore subject to the same selection rules as outlined for XAS (sec. 2.6). The transitions 2p → 1s (K_α lines, final state $2p^5 3d^n$) and 3p → 1s (K_β lines, final state $3p^5 3^n$) are dipole allowed, and have high-intensities with a ratio of ~8:1 between the two (fig. 2.7).[122,133] As the wave functions of the 3p and 2p states overlap significantly with those of the 3d states, these emission lines have a strong chemical sensitivity in 3d TMs, and can be used to study the valence states.[134] Fluorescence from the 3d states directly (final state $3d^{n-1}$) is observed, as well, and the features are called the K_β satellite lines.[122] These contain direct information on the valence and ligand states, however the intensities are 50 - 100x lower than those of the K_α lines, due to their quadrupole nature.[133]

Due to concerns about beam damage during *operando* experiments, K_α fluorescence was chosen in this thesis, as the high intensity results in lower collection times and hence lower sample exposure, and will be discussed exclusively in the following. It should be mentioned, however, that the K_β main and satellite lines should be an equal, if not more suitable, probe.

2.7.1 Chemical Sensitivity of the K_α Fluorescence Lines

The K_α emission lines are split into the $K_{\alpha 1}$ and $K_{\alpha 2}$ lines, due to spin-orbit coupling of the 2p states. The changes to the $K_{\alpha 1}$ line upon delithiation are mainly influenced by the spin-orbit-coupling, but also by the exchange interaction between the 2p core hole and the net spin in the 3d valence states.[122] The relationship is given by:

$$\Delta E_{xc} \propto S_{3d}^{eff} \alpha \tag{2.54}$$

where ΔE_{xc} is the exchange energy splitting, which broadens the $K_{\alpha 1}$ line, S_{3d}^{eff} is the effective spin in the 3d states acting on the 2p electrons, and α is the atomic exchange

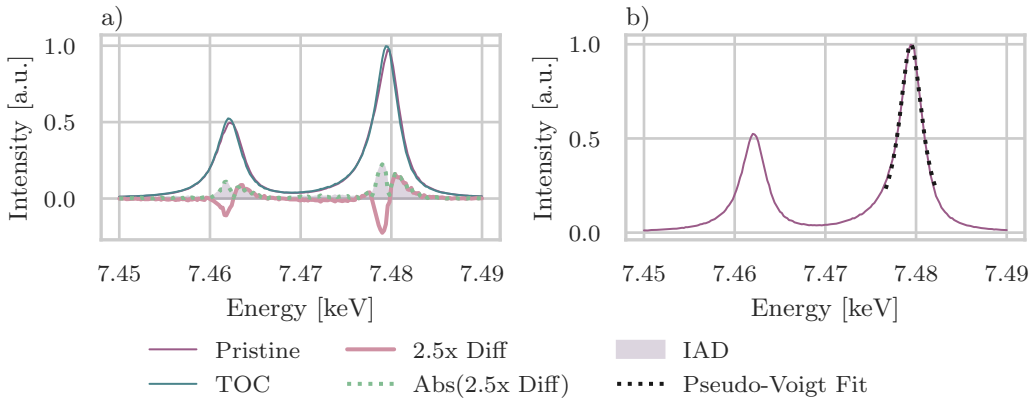


Figure 2.11: K_α XES spectrum for Ni in $Li_{1.2}Ni_{0.2}Mn_{0.6}O_2$, showing the $K_{\alpha 1}$ (7.479 keV) and $K_{\alpha 2}$ (7.462 eV) peaks.
a) IAD calculated between the pristine compound ('Pristine'), and a spectrum collected at the top of charge ('TOC'); b) FWHM determination using a pseudo-Voigt function to fit the the $K_{\alpha 1}$ emission line of a spectrum collected at TOC.

parameter that arises directly from the exchange integrals.[122] In 3d TMs, the $K_{\alpha 1}$ line is usually dominated by the 2p-3d exchange interaction, and, as a good approximation, a near-linear relationship exists between its full width at half maximum (FWHM) and the TM spin state.[122,135,136] The effective spin is usually calculated using e.g. DFT, and lower than the absolute spin of the d electrons. If, however, the spin states of the pristine compounds are known, changes can be tracked using the changes in $K_{\alpha 1}$ FWHM, provided that the coordination environment does not change significantly.

In addition to the FWHM, the changes in spin can also be analysed using the integrated absolute difference (IAD) between a spectrum and a reference.[136,137] This data reduction technique tracks the total changes between the two spectra by calculating the area of the absolute value of the difference (fig. 2.11). As it is based on the whole spectrum, it is less affected by the resolution of the data, and a low-noise complement to the FWHM. Using these two metrics, changes of the spin state, which is directly influenced by the oxidation state of the metal center, can be tracked, making it a powerful tool for the study of 3d TM cathodes.

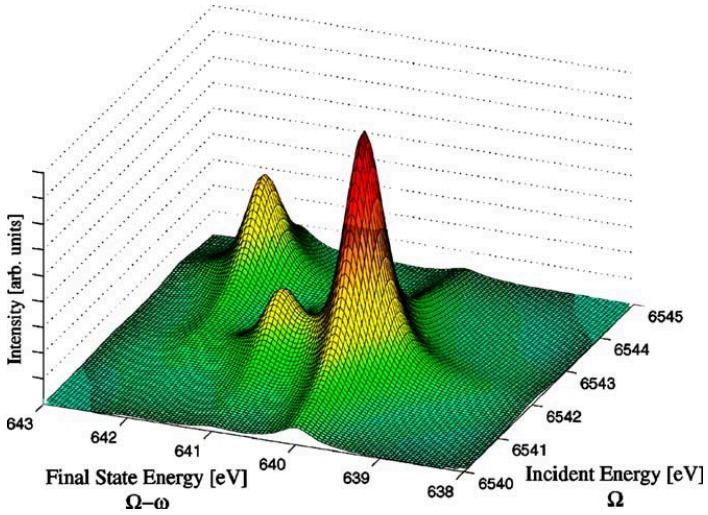


Figure 2.12: Surface plot of a Mn K pre-edge RIXS plane, showing the incident (absorption) energy, as well as the final state energy, corresponding to the energy transfer between the absorbed and emitted photon.
Reprinted from [122], Copyright (2005), with permission from Elsevier.

2.8 Resonant Inelastic X-ray Scattering (RIXS)

Resonant inelastic X-ray scattering (RIXS) can be viewed as a combination of XAS and XES, with the difference that the incident energy is scanned through the absorption edge, and an emission spectrum is collected at each point. Contrary to conventional, non-resonant XES, where the electrons are excited into the continuum, the electrons are excited into bound states (resonance), and the element is not ionised.[122] For 3d TMs, an electron can be excited into the unoccupied 3d states just above the Fermi level, followed by the relaxation of a 3d electron from the valence band.[122] The energy difference between the absorbed and emitted photons then corresponds to a d-d excitation, and contains information on the electronic structure of the valence band. Similarly, the core-hole in the excited state can lead to further excitations in the material, to reduce the energy of the intermediate state, followed by a decay of the excited electron back to the initial energy level, and leaving the atom in an excited state (indirect RIXS).

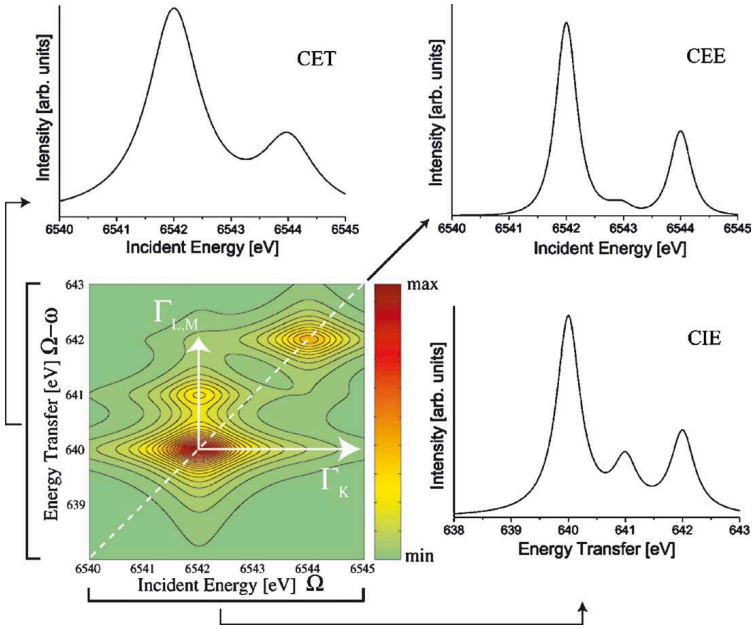


Figure 2.13: Mn K pre-edge RIXS map of the surface in fig. 2.12, showing the relationship with other types of spectroscopy. Constant energy transfer (CET) shows all states that contribute to a final state, whereas the constant incident energy (CIE) shows all final states that arise from an excitation at this energy. Constant emission energy (CEE) is similar to HERFD XANES, as only a single energy is monitored.
Reprinted from [122], Copyright (2005), with permission from Elsevier.

By scanning across the absorption and excitation energies, a 3D RIXS map is generated, which shows the relationship between all resonant (unoccupied DOS) and final states after X-ray photon emission (figs. 2.12, 2.13).[122] This way the electronic structure can be characterised with great detail and high energy resolution, at the expense of long collection times.

RIXS can be used at all absorption edges, and hence with a variety of energies. It has been extensively used to study the O K edge in the soft X-ray regime, where the characteristic final state is used to identify O redox in Li-rich materials.[21,22,25,57] Similarly, hard X-ray RIXS can be used to study the electronic structure of 3d TMs using the K edges, where the 3d states can be characterised with more detail than it is possible with HERFD-XANES (fig. 2.13).[122,138]

Chapter 3

Design of an X-ray-Transparent *Operando* Cell for the Study of Lithium-Rich Cathodes

3.1 Introduction

Operando characterisation refers to methods where a system is probed at the same time as it is changing. In the case of battery cathodes, an attribute, e.g. the lattice spacings, is analysed while the electrode is subject to a controlled electrochemical redox-process. The advantages over *ex-situ* approaches include the elimination of cell-to-cell variation and error sources, such as unwanted reactions due to short circuiting during cell opening, exposure to H_2O or O_2, or the relaxation of metastable species. Additionally, system dynamics, which are otherwise hard to investigate, can be studied directly.

Operando experiments are based on the implicit assumption that the cell reaction occurring in the system under study is the same as in a 'real' reference system, e.g. a coin cell, and that the probing of the system does not alter it. This can not always be assumed to be true, and

it has been shown that variations in stack pressure† across an electrode surface influence the uniformity of the cell reaction at a local scale, resulting in differences in the local state of charge (SOC).[139] These deviations are almost impossible to detect through the cell voltage curve, but can falsify results obtained e.g. via spectroscopy or structural probes, and stack pressure homogeneity needs to be tightly controlled.

For X-ray-based techniques the interaction between the beam and the sample is another potential error source that can influence the outcome of the experiment, particularly when the beam energy matches or slightly exceeds an absorption edge energy.[139] The impact can be reduced for structural experiments, e.g. XRD or PDF, through the use of very high-energy X-rays, but for X-ray spectroscopy, where the techniques inherently require strong interaction, care needs to be taken to reduce the exposure time to a minimum.

A direct result of these factors is that well-controlled experimental setups, which reproduce the conditions of the reference system and allow for rapid data collection, are crucial to obtaining reliable results. This is particularly difficult for layered Li-rich materials, as the compounds tend to exhibit slow kinetics and require significant stack pressure on charging to delithiate the structures sufficiently to observe O redox.[55,140–142] A lack of stack pressure often manifests as a reduced capacity across the voltage plateau in region 2, limiting the amount of information that can be extracted from the experiment. Strong compression, however, is difficult to combine with the requirement for X-ray transparency, as rigid compression surfaces tend to be thick or made of strongly absorbing materials. This is particularly true for the low energies required for 3d TM K edge spectroscopy and Cu K_α based XRD, which are in the range of 5 - 10 keV.[124]

†Stack pressure is the compression of the cathode - separator - anode stack in a cell, which is controlled via a compression spring in coin cells. It controls the contact surface between cell components, as well as individual electrode particles and the conductive additives, and hence directly influences the contact resistance.

X-ray absorption increases with atomic number Z and the thickness of a system. In the widely-used experiment setups based on modified coin cells, transparency is usually achieved through thin windows of a low-Z material, such as polyimide or aluminium.[139,143–147] These foils, however, can bulge outward under load, resulting in a lack of stack pressure. In the case of polyimide, the material is also non-conductive, which increases the electronic resistance and can lead to additional reaction inhomogeneity with increasing size of the window, as electrons have to flow laterally through the cathode pellet. The effect is less pronounced in cathodes with good kinetics, such as LFP, and can be reduced through the use of cast electrodes, where the Al foil increases conductivity or coating with conductive additives.[145–147] Oftentimes, however, this is usually not sufficient to fully overcome the sluggish reaction kinetics of O redox.[140]

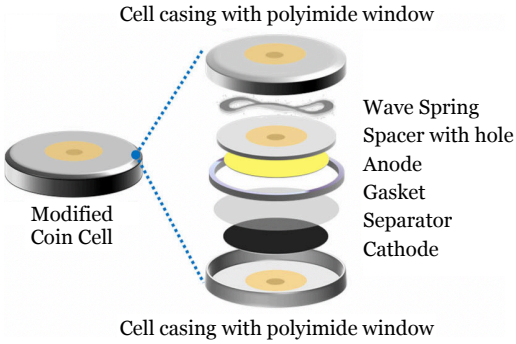


Figure 3.1: Exploded view of a coin cell, modified for *operando* experiments.
Adapted, with permission, from [143] under a Creative Commons CC BY license. Copyright (2018), the Authors.

Good results have been reported with beryllium windows, where the low absorption of the light element enables windows of considerable thickness and stiffness, and full capacities can be achieved.[148] The downsides include the element's toxicity, as well as the fact that it is oxidised at high potentials.[143]

Coin cell-based setups, in general, require additional peripheral equipment, such as crimping tools, during assembly, which is not always available at synchrotron facilities and poses an additional constraint. Coin cells have to be prepared in advance, and are therefore hard to troubleshoot should problems arise.

Setups using modified pouch cells with polyimide windows have been reported.[143] The

same stack-pressure problems, however, can be expected to be present, as well as difficulties with rapid assembly, rendering them less suitable for fundamental research.

The most advanced setup reported to date is the AMPIX cell, developed at the Argonne National Laboratory.[149] It can be assembled in a glovebox with hand tools and features stiff glassy carbon windows, which result in good stack pressure and reaction homogeneity.[139] The cell, however, combines the mechanism for applying stack pressure with the cell's sealing mechanism, compressing the stack and seal between the same two rigid parts, and pressure control is thus achieved via the total thickness of the stack components. This requires very precise tolerancing of the thicknesses of the cathode, anode, and separator, in order not to break the windows but achieve sufficient compression, creating a particular problem for Li-rich materials. Additional preparation time for trial-and-error is therefore required, which is often not available during synchrotron experiments.

Owing to the discussed factors, an *operando* cell, purpose-built for Li-rich cathodes, is presented in the following. It takes the learnings from the previously described solutions into account and combines excellent X-ray transparency at the energies required for 3d TM X-ray spectroscopy with ease of assembly, and a reliable mechanism for stack compression and sealing.

3.2 Requirements

In order to assist the design process of the *operando* cell, and establish measurable attributes and behaviours that can be verified via tests and calculations, the following requirements were created.

The *operando* cell shall:

1. Have no more than ± 5 % difference in first charge and discharge capacities, at a rate

of 50 mAg^{-1}, compared to a coin cell reference value of 330 $mAhg^{-1}$ for charge, and 250 $mAhg^{-1}$ for discharge, respectively, using a $Li_{1.2}Ni_{0.13}Co_{0.13}Mn_{0.54}O_2$ cathode pellet (80 % active material, 10 % carbon-based conductive additive, 10 % binder).

Rationale: The first cycle capacities observed in coin cells vary slightly, mainly due to the accuracy of the balance used to measure the mass of the cathode pellet. $Li_{1.2}Ni_{0.13}Co_{0.13}Mn_{0.54}O_2$ is a widely used, well-studied compound, and literature values of the capacity at 50 mAg^{-1} are ~330 $mAhg^{-1}$ and ~250 $mAhg^{-1}$ for charge and discharge, respectively.[22,42]

2. Have an attenuation of ≤ 90 %, excluding contributions from the cell stack, for X-rays with energies ≥ 6.54 keV (Mn K edge), throughout all operational modes.

   Rationale: In order to enable rapid data acquisition, the cell attenuation needs to be as low as possible. The attenuation length of X-rays increases with energy, and Mn has the lowest energy (6.54 keV) out of the set of TMs relevant to this thesis: {Mn, Fe, Co, Ni}.[124] Ti and V are sometimes used in Li-rich materials, but as these elements are not used here, and their very low K edge energies would pose a significant constraint.[92,124,150–153]

3. Be able to be used in transmission geometry with scattering angles of ≥ 50° and with signal attenuation as defined in requirement 2.

   Rationale: Some X-ray probes, such as XRD and PDF, can be performed in transmission mode and can be based on low-energy radiation such as Cu K_α. Obtaining a good signal-to-noise ratio requires sufficient signal intensity at high scattering angles.

4. Be able to be used in reflection geometry with an angle ≥ 100° between the incident and reflected beam and with signal attenuation as defined in requirement 2.

   Rationale: Many X-ray techniques, such as XRD and TFY XAS can be performed in reflection mode, and can be based on low-energy radiation such as Cu K_α. Obtaining a good signal-to-noise ratio requires sufficient signal intensity at high angles.

5. Enable the illumination of an area of ≥ 5 mm^2 of cathode material with the X-ray beam, in both transmission and reflection geometry.

Rationale: As beam damage can occur, several sampling locations need to be available in one cell, in order to take multiple samples during one experiment. Assuming a beam cross section of 0.5 x 0.5 mm, a 5 mm^2 area enables 20 samples to be taken.

6. Be hermetically sealed for ≥ 22 h at standard ambient temperature and pressure in air after assembly.

   Rationale: In order not to change the electrode materials, and to enable stable electrochemical reactions in ambient conditions, the cell needs to minimise ingress of H_2O and O_2. Assuming capacities of 330 $mAhg^{-1}$ and 250 $mAhg^{-1}$ for the first charge and discharge, as well as 250 $mAhg^{-1}$ for both charge and discharge of the second cycle, a total capacity of 1080 $mAhg^{-1}$ needs to be passed. At a rate of 50 mAg^{-1} this requires 21.6 h, rounded to 22 h, for which time H_2O or O_2 shall not influence the reactions.

7. Be reusable and able to be assembled inside of a glovebox with hand tools in ≤ 15 min.

   Rationale: Gloveboxes or dry rooms are required for the assembly of battery cells, to reduce H_2O (and O_2) exposure. Gloveboxes are widely available at synchrotrons. With hand tools, which can be provided by the user, the cell can be assembled and re-assembled on site without the need for complex equipment.

8. Have no dimension exceeding 50 mm in the assembled state.

   Rationale: The size needs to be small enough to fit at least one cell onto synchrotron beamline stages.

3.3 Design Description

This section gives an overview of the basic design of the cell. In fig. 3.2 pictures of the cell are depicted, and in fig. 3.3 an overview drawing is presented. A complete list of parts with details and reference numbers, indicating parts in the following drawings and throughout the chapter, can be found in table 3.1.



Figure 3.2: Pictures of the *operando* cell. Left: Closed cell after assembly. Right: Cell components.

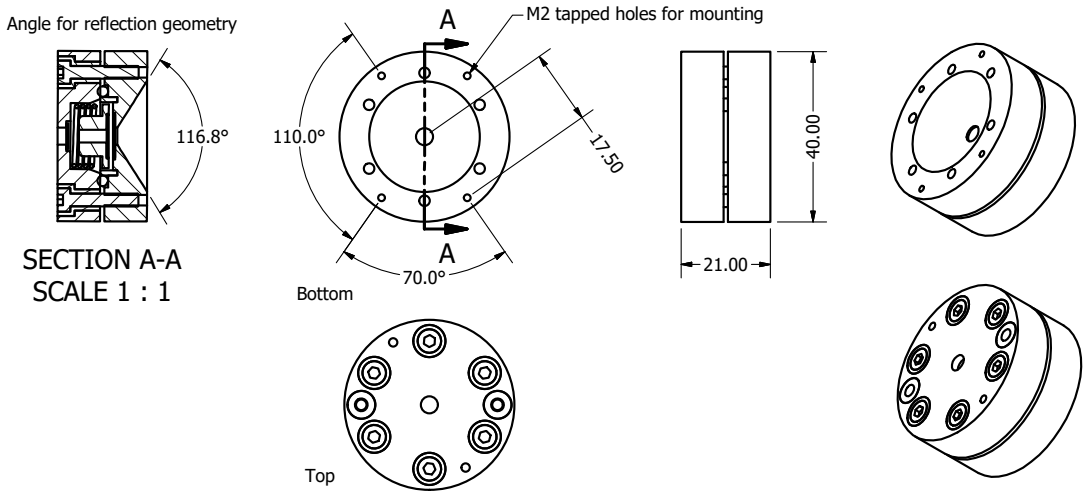


Figure 3.3: Drawing of the *operando* cell after assembly. Dimensions in mm.

Table 3.1: Description and Part List: *Operando* Cell Parts

#	Part or Feature	Details
(1)	Cell Lid	Stainless steel (AISI 316L)
(2)	Window, Lid	Glassy carbon, ∅ 5.0 mm, h 0.1 mm
(3)	Insulating Sleeve	PEEK; Screw insulation
(4)	Insulating Sleeve	PEEK; Position pin insulation
(5)	Circular Pocket	Used for spring positioning & travel
(6)	Hole	∅ 2.0 mm, ↧ 6.0 mm; For banana plug, negative pole
(7)	Cell Base	Aluminium (7075 - T6)
(8)	Annular Insert	PEEK; Electronic separation between lid & base
(9)	Window, Base	Glassy Carbon, ∅ 10.0 mm, h 0.5 mm
(10)	Annular Foil Insert	Aluminium; Electrical contact to windows
(11)	Positioning Pin	Brass; Base & lid alignment
(12)	Tapped Holes	M3 thread, THRU; Cell clamping
(13)	Conical Pocket	Beam path
(14)	Tapped Hole	M2 thread, ↧ 3 mm; Mounting & positive pole
(15)	Copper Spacer Body	Copper (oxygen free)
(16)	Window	Glassy Carbon, ∅ 10.0 mm, h 0.5 mm
(17)	Boss, Spacer	Compression spring positioning
(18)	Cathode Pellet	Disc, ∅ 6.0 mm
(19)	Separator	-
(20)	Lithium Metal Disc	-
(21)	Compression Spring	Stainless steel
(22)	O-Ring	FKM
(23)	M3 Socket Head Screw	Cell clamping

The cell consists of a lid (sub)assembly, a base (sub)assembly, and a spacer (sub)assembly, which, together with additional components, such as a compression spring, are used to compress the cell stack.

The cell lid (1) (fig. 3.4) is made of 316L stainless steel (SS) and is fitted with a glassy carbon (GC) window (2) that is fixed into a pocket (5) with epoxy adhesive, hermetically sealing a ∅ 5 mm through-thickness hole that enables X-rays to penetrate. It has six counterbore holes along the outside perimeter, containing polyether ether ketone (PEEK) liners (3), which provide an electrically insulated opening for the screws (23). Two additional counterbore holes, lined with PEEK sleeves (4) provide paths for the positioning pins (11).

The base assembly contains the cell base (7), made from 7075 - T651 aluminium (fig. 3.5).

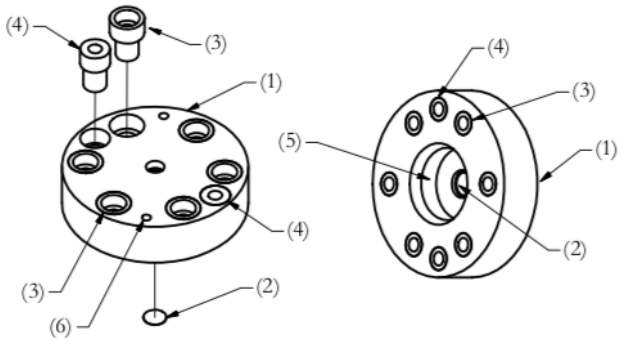


Figure 3.4: Left: *Operando* Cell lid assembly, top view, partially exploded; Right: Lid assembly, bottom view.

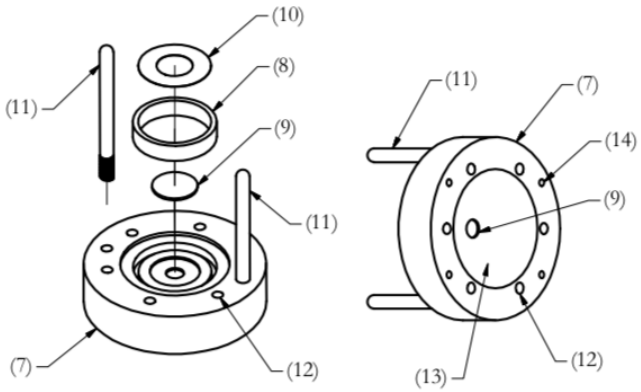


Figure 3.5: Left: *Operando* Cell base assembly, top view, partially exploded; Right: Base assembly, bottom view.

An annular insert (8), made from PEEK, is press-fit into a recess on the top face, separating the lid (1) and base (7) when the cell is assembled. A glassy carbon window (9) is fitted into a pocket using epoxy adhesive, creating a flat surface for the cell stack and hermetically sealing a ∅ 4 mm through thickness hole that is part of the beam path in transmission. An annular aluminium foil insert (10), with an 8 mm hole, covers a section of the top of the glassy carbon, ensuring conductivity between the base (7) and the window (9).

Six tapped holes (12) provide a means for mechanically connecting the lid (1) and base (7) via the screws (23). On the bottom face of the base, a conical pocket (13) provides a beam path for diffracted beams in transmission geometry, and incoming and reflected beams in reflection geometry.

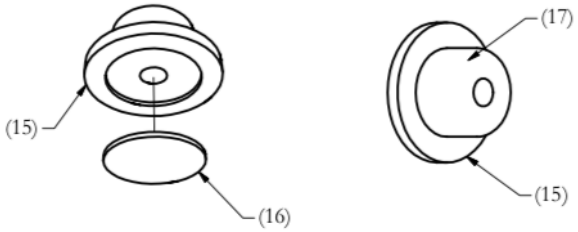


Figure 3.6: Left: *Operando* Cell cell spacer assembly, bottom view, exploded; Right: Spacer assembly, top view.

The copper spacer assembly is comprised of the copper body (15), fitted with a glassy carbon window (16), which covers a ∅ 4 mm axial hole, that provides a beam bath for a transmitted beam (fig. 3.6). In the assembled cell, the copper spacer (15) is located in the cavity formed by the base (7) and the annular insert (8), as well as the lid (1) (fig. 3.7). A boss (17) protrudes from the top face of the copper spacer (15), which holds the compression spring (21) in position.

During cell assembly, a cathode disk (18) is placed on top of the base window (9) in the circular pocket formed by the PEEK insert (8), and one or more glass fibre or polymer film separators (19) are stacked on top (fig. 3.7). A Li metal disc (20) is placed on top, electrolyte is added, and the stack is covered using the copper spacer (15). During these assembly steps, the separator (19) and the spacer (15) are held in place by the PEEK insert (8). A compression spring (21) is placed around the boss of the spacer (17), and an FKM O-ring (22) is placed around the PEEK insert (8). The lid assembly is lined up using the positioning pins (11), placed onto the spring (21), and lid and base assemblies are mechanically connected using the six socket head screws (23), directly compressing the O-ring (22) in the process. Simultaneously, the cell stack is compressed with the spring (21), resulting in a controlled application of force.

Optionally, during cell stack assembly, a small piece of polyimide foil (not shown) can be placed between the Li metal disc (20) and the copper spacer (15), to protect the window (16) from reacting with the Li. In this case, the Li metal anode (20) needs to have a larger

diameter than the polyimide foil, to establish an electrical connection with the copper spacer (15).

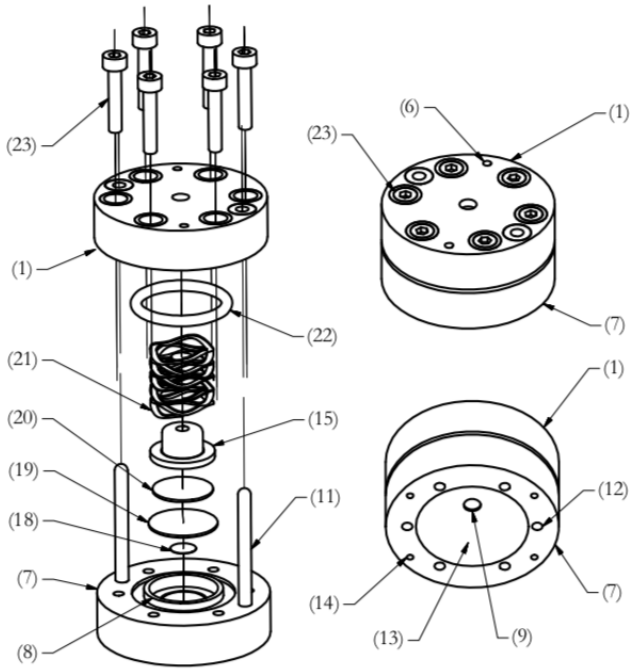


Figure 3.7: Left: *Operando* cell assembly, exploded view.
Top right: Closed cell, top view; Bottom right: Closed cell, bottom view.

Once the cell is closed (fig. 3.7) the positioning pins (11) can be unscrewed and removed. The cell is mounted using the mounting holes (14) on the bottom face of the base (7), which simultaneously serve as the electrical connection for the positive terminal, via small ring terminals. An electrical connection to the negative terminal is made by connecting a 2 mm banana connector to one of the holes (6) in the lid (1).

The cell can be used in transmission mode, where the beam enters through the window (2) in the lid (1), penetrates the window (16) in the copper spacer (15), pierces the cell stack (18, 19, 20) and exits through the window (9) in the base (7) and the conical opening (13). In reflection mode, the bean enters and exits through the window (9) in the base (7), where the conical opening (13) provides a path for beams at high incoming and exit angles.

3.4 Component and Material Selection

Components in battery cells are subject to reactive conditions, including highly oxidising and reducing environments at the cathode and anode, respectively, which greatly limits the number of suitable materials. Among the stable ones, strength and stiffness are important factors, in order to reduce deformation during compression of the cell. Electronic conductivity is equally important for components that act as current collectors, as well as X-ray transparency for those in the beam path.

3.4.1 Window Selection

The structural windows (9, 16), located in the base (7) and spacer (15), are among the most critical components of the cell. Mechanically, they need to be sufficiently strong and stiff, in order to provide stack pressure across a large, unsupported area with minimal bowing (reqs. 1. & 5.). The material also needs to be electrically conductive, for the window to act as a current collector, and electrochemically stable, to not influence the cell reaction (req. 1.).

The window (2) in the lid (1) is not loaded by the stack pressure and only has to withstand small pressure differences arising during sealing and gas production through electrochemical processes. It also does not act as a current collector, requiring no electrical conductivity.
Both outer windows (2, 9) have to be non-permeable to air and moisture, to seal the cell (req. 6.), and all windows (2, 9, 16) need to be sufficiently X-ray transparent (req. 2.).

3.4.1.1 Structural and Electrical Properties

The combination of these properties poses a significant challenge to the used materials. Candidates were selected based on attributes such as strength, stiffness, electrical conductivity, low toxicity, and commercial availability, in conjunction with a low-Z chemical composition, as it directly influences X-ray transparency. For this reason, aluminium was not selected.

Table 3.2: Physical properties of candidate materials for the window of the *operando* cell.

Material	Y [GPa]	FYS [MPa]	ρ [gcm^{-3}]	γ [Sm^{-1}]
Glassy carbon (GC)[156]	35	260	1.42	$2.22 \cdot 10^{4}$
Boron-doped diamond (BDD)[155,159]	1050	450	3.40	$5.26 \cdot 10^{2}$
Polyimide (PI)[157]	2.5	69*	1.42	$8.33 \cdot 10^{-16}$

*3 % elongation, for comparison with the brittle solids GC and BDD.
Y: Young's modulus; FYS: Flexural yield strength; ρ: Volumetric mass density; γ: Electrical conductivity.

In table 3.2 a selection of the mechanical, physical, and electrical properties of the selected candidate materials are presented.

Glassy carbon (GC), is an amorphous form of carbon that is used as an electrode material in electrochemistry and has been implemented in similar applications.[149,154] Circular discs of ∅ 10 mm, h 0.5 mm and ∅ 5 mm, h 0.1 mm, respectively, were commercially available off-the-shelf and selected for the analysis.[155] Boron-doped diamond (BDD) is crystalline, also used in electrochemistry, and small plates with dimensions 10 x 10 x 0.6 mm (l x w x h) were available.[156] Polyimide (PI), is frequently used as a window material, and is available as foils of various thicknesses that can easily be cut to size. For this analysis, a thickness of h 0.1 mm was considered.[157]

The data show that GC possesses a reasonably high mechanical strength, adequate stiffness, and is very conductive, compared to BDD, which is extremely strong and stiff, but is approximately two orders of magnitude less conductive.[155,158,159]
PI has the lowest strength and stiffness out of the three materials, and is an electrical insulator, making it not suitable for the windows with cell stack contact (9, 16).[157] From a structural point, it can, however, be used for the window (2) of the lid (1).

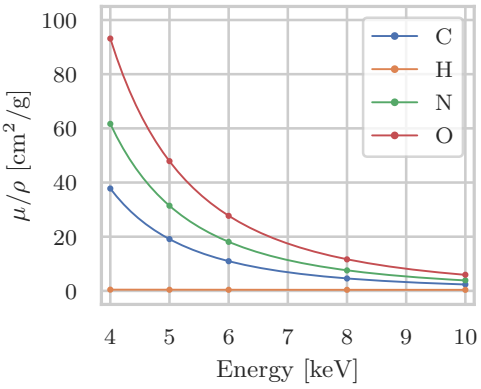


Figure 3.8: X-ray Mass Attenuation Coefficients μ/ρ of C, H, N, and O, plotted vs. X-ray energy and fit with power functions.[160,161]

3.4.1.2 X-ray Transparency

In order to study the X-ray absorption behaviour of these materials in an application-focussed manner, the energy-dependent X-ray attenuation was calculated for the commercially available parts, using tabulated values available from NIST (fig 3.8).[160,161] As the mass attenuation coefficients μ/ρ [cm^{2}g^{-1}] follow a power law at the energies of interest, a power function $\mu/\rho = aE^b + c$ was fit to the tabulated data and the coefficients obtained by evaluating the functions at the energies of the 3d TMs.

For polyimide the extinction coefficient was calculated using a mass-weighted linear combination of the mass attenuations of the individual elements, $\mu/\rho = \sum_i w_i(\mu/\rho)_i$, using the chemical formula $C_{22}H_{10}N_2O_5$.[157] For BDD the boron doping was neglected.

The transmission was then calculated via the Beer-Lambert law:

$$\frac{i}{i_0} = e^{-\mu h} \tag{3.1}$$

$$= e^{-(\mu/\rho\ \rho)h} \tag{3.2}$$

where the extinction coefficient μ is the product of the mass attenuation coefficient and the sample density, and h is the total sample thickness.

Table 3.3: 3d K edge energy-dependent transmission of different window candidates [%] .

Element	Sc	Ti	V	Cr	Mn	Fe	Co	Ni	Cu	Zn
E [keV]	4.49	4.97	5.47	5.99	6.54	7.11	7.71	8.33	8.98	9.66
0.6 mm BDD	1	2	5	11	18	26	35	44	52	59
0.5 mm GC	15	25	36	46	55	63	70	75	79	83
0.1 mm GC	69	76	81	86	89	91	93	94	96	96
0.1 mm PI	61	69	76	81	85	88	91	93	94	95

For all samples, the calculated transmission values at the K edge energies of all 3d TMs are listed in table 3.3. The data show that the h 0.5 mm GC discs are 1.5 - 15 x more X-ray-transparent, compared to BDD, largely due to the density difference between the two materials. Particularly at the minimally required energy of the Mn K edge (req. 2.), the GC disc is 3 x more transparent. There is only a small difference in transparency between GC and PI for the h 0.1 mm plates, which is mainly significant at lower energies.

3.4.1.3 Selected Components

Based on the high conductivity and transparency of GC, coupled with the materials adequate strength and stiffness, GC discs (∅ 10 mm, h 0.5 mm) were selected as parts for the structural windows (9, 16). Similarly, GC (∅ 5 mm, h 0.1 mm) was also chosen for the non-structural window (2) in the lid, due to its overall highest transparency.

3.4.2 Spring Selection

To accurately recreate the electrochemical performance of coin cells (req. 1.) the force exerted by the coin cell spring needs to be replicated in the *operando* cell.

To determine the applied reference force, the dimensions of coin cell parts and the cell stack components, as well as of crimped cells were accurately measured. The values were incorporated into a computer-aided design (CAD) model, and the deflection of the spring was derived as 0.3 - 0.35 mm. The force-displacement curve of ten coin cell wave springs was measured using a compression rig (Instron 3366), and the spring constant k was obtained via a fit of Hooke's law (fig. 3.9):

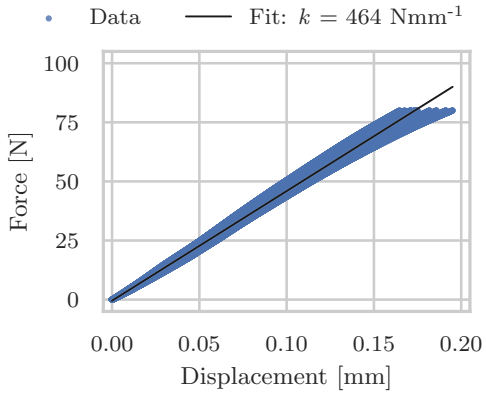


Figure 3.9: Spring constant k, as determined for commercially available wave springs used in 2332 coin cells.

$$F = kx \tag{3.3}$$

where x is the displacement and F the force.

Using the spring displacement from the CAD model, a force of 140 - 162 N was derived, which compares well to literature values of coin cell spring forces.[162]

The operando cell should apply a near-constant force across the cell stack, regardless of small thickness variations of the cell stack components. The error in force ΔF scales linearly with the error in spring displacement Δx according to:

$$\Delta F = \frac{dF}{dx}\Delta x \tag{3.4}$$

$$= k\Delta x \tag{3.5}$$

As a result, a spring with a minimised spring constant is required. As the force is frozen, the spring's length needs to be maximised. A stainless steel wave spring with a free length of 23.44 mm and k = 10.32 Nmm^{-1} was selected, as a compromise between the total cell thickness and force error, and using a material with good chemical stability. Using this spring, an average force of 159 N is applied when the cell is fully closed.[163]

3.4.3 Base Material Selection

During operation, the base (7) of the cell is in contact with the cathode and subject to highly oxidising potentials of up to 4.8 V in battery electrolyte, which it needs to withstand (req. 1.). This environment, in conjunction with cost and structural requirements, greatly limits the available materials, and leaves some stainless steels, aluminium alloys, and a selection of structural polymers, most notably polyether ether ketone (PEEK), as potential materials (tab. 3.4).[154]

Most steels, such as AISI 304, show high stability at potentials of up to 4.9 V, however the stability has been reported to vary greatly with the solvent, potentially reducing the flexibility of the cell.[154] Aluminium and its alloys readily passivate in electrolytes containing $LiPF_6$ and $LiBF_4$, making them one of the most stable and commonly used current collector materials for LiBs.[154] They also possess high strength and stiffness, as well as excellent conductivity. The mechanical attributes of PEEK, along with it's insulating nature, make it less suitable for this cell design, and 7075 - T651 Aluminium was ultimatly chosen for the base of the cell, based on the materials high strength, good stiffness, high conductivity, and corrosion resistance.[154,164–167]

Table 3.4: Mechanical and electrical properties of a selection of materials used for the *operando* cell.

Material	Y [GPa]	TYS [MPa]	γ [S m^{-1}]
PEEK[168]	4	110	$1.0 \cdot 10^{-17}$
7075 - T651 Aluminium[165–167]	72	460	$2.0 \cdot 10^{7}$
316 / 316 L Stainless Steel[169]	193	220	$1.4 \cdot 10^{6}$
Oxygen-free Copper[170]	117	70	$5.8 \cdot 10^{7}$

TYS: Tensile yield strength

3.4.4 Lid and Spacer Materials Selection

The lid (1) and copper spacer (15) are exposed to electrolyte at the potential of the battery anode, and hence need to be stable at low potentials (req. 1.). Li reacts spontaneously with aluminium and its alloys, which is therefore not suitable for these components. Stainless

steel, polymers, and copper are commonly used in similar applications and are potential candidates for the structural elements.[145,146,149]

For the structural lid (1), AISI 316L stainless steel was chosen, due to the materials high stiffness and corrosion resistance, as well as its better machinability and lower price compared to copper (tab. 3.4).[154] For the spacer body (15), copper was chosen, as it is in constant contact with the electrolyte, widely used as an anode current collector in commercial LiB cells, and has superiour electrical properties.

3.4.5 Insulating Materials Selection

All components which mechanically connect the lid and base assemblies, and therefore bridge two points that are at different potentials, need to be electrically insulating, to prevent short-circuiting of the cell (req. 1.). PEEK was chosen as a material, due to the material's high strength, chemical stability, and good machinability (tab. 3.4).[168]

3.4.6 Cell Dimensioning

The size of the cell is driven by several factors, including req. 8., which determines the maximum allowable size of the cell. Additionally, it needs to be easy to assemble (req. 7.), which requires a certain size for the individual parts to allow for handling inside of a glovebox. It also needs to accommodate the cell stack, spacer assembly, and the compression spring (21). A last factor is part interchangeability between coin cells and the *operando* cell, which allows use of the cell without much adaptation and reduces variability.

To enable this, the diameter of the separator (19) and copper spacer (15) were chosen to be 16 mm, the same size as comparable parts in coin cells. These parts then drive the size of the PEEK insert (8), which, in turn, determines the size of the sealing O-ring (22), as well as the screws (23), required for mechanically connecting the parts, compressing the spring (21), and clamping the O-ring (22) (subsec. 3.4.7). Ultimately, this resulted in a size of ∅ 40 mm, h 10 mm for both lid (1) and base (7).

3.4.7 Fastening and Sealing Mechanism

In order to close the cell and seal it hermetically (req. 6.), as well as compress the cell stack (req. 1.), a clamping force needs to be applied between the lid and base. This is achieved using six M3 socket head screws (23), which were selected as a size compromise between miniaturisation of the cell (req. 8.) and ease of assembly inside of a glovebox (req. 7.).

The force required for the compression of the spring (21) and O-ring (22) does not require this number of screws, as even M3 screws with property class 4.6 (ISO 898) can withstand a proof load of 1200 N each. The number was chosen, however, to evenly distribute the clamping force across the surface of the O-ring (22) and the screws are arranged in an equidistant hexagonal pattern for the same reason.

A fluoroelastomer O-ring (22) (FKM; 75 Shore A), deformed by 30 % when compressed, was selected to seal the cell, based on the material's high resistance to various chemicals, including battery electrolytes.[171] In the cell, the PEEK insert (8) acts as a spacer, maintaining 1 mm separation between lid (1) and base (7) and controlling the O-ring and spring compression, as well as ensuring that the cell cannot be overly compressed or short circuited after closing.

3.5 Design Evaluation and Verification

This section evaluates the *operando* cell, based on the requirements presented in sec. 3.2. An overview is presented in tab. 3.5, with details given in the following subsections.

3.5.1 Electrochemical Performance

In order to verify compliance with req. 1., galvanostatic voltage profiles using $Li_{1.2}Ni_{0.13}Co_{0.13}Mn_{0.54}O_2$ composite cathodes were collected at 50 mAg^{-1} between 2.0 - 4.8 V vs. Li metal. The profiles observed for charge and discharge are depicted in fig. 3.10, along with representative coin cell data. The absolute values for the charge and discharge

Table 3.5: Requirement verification overview with means of compliance and outcomes.

Req.	Description	MOC	EO	AO	Compl.	Details
1.	Electrochem. Capacity	Test	≤ 5 %	1.7 %	Yes	3.5.1
2.	Max. X-ray Attenuation	Analysis	≤ 90 %	87.6 %	Yes	3.5.2
3.	Operation: Transmission	Analysis	≥ 50°	55°	Yes	3.5.2
4.	Operation: Reflection	Analysis	≥ 100°	110°	Yes	3.5.2
5.	Illuminated Area	Analysis	≥ 5 mm²	7 mm²	Yes	3.5.2
6.	Hermetic Sealing	Test	≥ 22 h	22.5 h	Yes	3.5.3
7.	Assembly Time	Test	≤ 15 min	10 - 15 min	Yes	3.5.4
8.	Physical Size	Review	≤ 50 mm	40 mm	Yes	3.5.4

MOC: Means of compliance; EO: Expected outcome; AO: Actual outcome; Compl.: Compliance with the respective requirement.

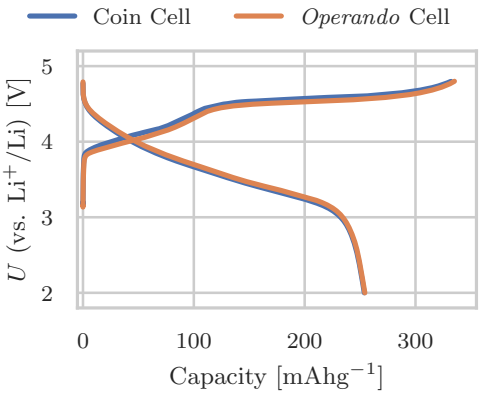


Figure 3.10: Voltage profiles obtained for $Li_{1.2}Ni_{0.13}Co_{0.13}Mn_{0.54}O_2$ in a coin cell reference, as well as the *operando* cell, at 50 mAg^{-1} and 30 °C.

capacities are listed in tab. 3.6. The data show that the cell complies with req. 1. Further evidence is given in chapter 3, where the cell is used extensively.

3.5.2 X-ray Transmission and Illuminated Window Area

In order to verify the requirements for X-ray transmission (reqs. 2., 3., 4.), the absorption was determined using calculations. The requirement for sufficient illuminated cathode area (req. 5.) was used as a boundary condition, to validate it simultaneously.

The transmission depends on the total distance the beam travels through absorbing materials and the beam paths and resulting absorptions were calculated using simple

Table 3.6: Charge and discharge capacities of the *operando* cell and ideal reference values.

	Reference [mAhg^{-1}]	*Operando* Cell [mAhg^{-1}]	Δ [mAhg^{-1}]	Δ [%]
Q_{charge}	330.0	335.1	5.1	1.5
$Q_{\text{discharge}}$	250.0	254.3	4.3	1.7

Δ: Difference between the results obtained for the *operando* cell and the reference values.

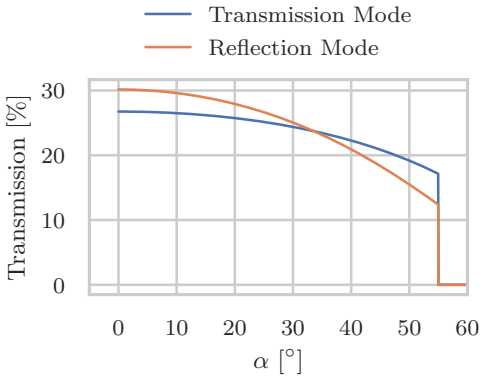


Figure 3.11: Angle-dependent transmission of the *operando* cell in transmission mode at the Mn K edge. α is defined as the angle between the beam(s) and the surface normal of the base window (2).

geometric assumptions and the methodology as discussed in subsec. 3.4.1.

The property influencing the absorption most significantly is the angle-dependent path length through the base window (2) L_p. It is part of the beam path in reflection and transmission mode, and varies based on the incident and/or exit angle.
L_p is defined as a function of the angle relative to the surface normal (α) and can be calculated via:

$$L_p = \frac{h}{cos\,(\alpha)} \tag{3.6}$$

where h is the thickness of the window.

For the calculation of the total absorption in each case, the individual total path lengths for reflection and transmission were derived. In transmission mode, the thicknesses of the spacer window (16) and the lid window (2) are added to $L_p(\alpha)$, while in reflection mode, where the angle of the reflected beam equals the one of the incident one, $L_p(\alpha)$ is doubled.

Using the previously presented design, where a circular area of 7 mm² (∅ 3 mm) can be illuminated with a maximum angle of 55° to the surface normal, as a constraint, the transmission was derived and is depicted in fig. 3.11 for 6.539 keV (Mn K edge). The transmission exceeds 10 % at all angles allowed by the geometry, namely ≤ 55° in transmission, and ≤ 110° in reflection, with a minimum of 12.4 %, observed at 110° in reflection mode. This verifies reqs. 2., 3., 4., and 5.

For completeness, the transmission values for a direct beam through the cell at all 3d TM K edges are given in the appendix (tab. A.1).

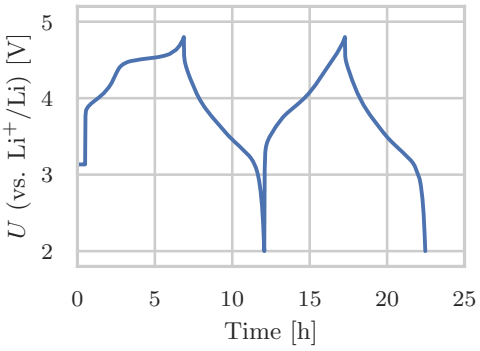


Figure 3.12: Voltage profile for the first two cycles of $Li_{1.2}Ni_{0.13}Co_{0.13}Mn_{0.54}O_2$, obtained in the *operando* cell at 50 mAg^{-1}.

3.5.3 Hermetic Sealing

In order to verify req. 6., it needs to be demonstrated that the cell remains hermetically sealed for at least 22 h. To verify the seal, the electrochemical performance was used as a proxy, due to its sensitivity to moisture. The voltage profile for the first two cycles of $Li_{1.2}Ni_{0.13}Co_{0.13}Mn_{0.54}O_2$ was obtained in air, after assembly of the cell in a glovebox (fig. 3.12). The total duration of the experiment lasted ~ 22.5 h, demonstrating compliance with the requirement.

3.5.4 Dimensions, Handling, and Practical Considerations

Req. 8. requires that no dimension of the cell exceeds 50 mm in the assembled state. After closing and removal of the positioning pins (11), the cell has the shape of a cylinder with ∅ 40.0 mm, h 21 mm. This verifies the requirement and enables the cell to easily fit onto beamlines (fig. 3.3).

Req. 7. requires assembly within 15 min with hand tools. The cell can be assembled with a 2.5 mm hex key and no additional tools apart from a pipette and tweezers. The total assembly time was benchmarked at five to ten minutes, depending on the user's experience. The cell is fully reusable, apart from the cell stack, and disassembly takes approximately five

minutes inside of a glovebox, where the cell can be cleaned with cotton buds and tissues before reassembly, resulting in a total reassembly time of 10-15 min.

3.6 Summary and Discussion

An *operando* electrochemical cell, transparent for X-rays with energies corresponding to the 3d TM K absorption edges, was designed and built. Owing to a long compression spring and rigid glassy carbon windows, the design reliably reproduces the stack pressure and electrochemistry observed in coin cells. The X-ray transparency of the windows enables the cell to be used for X-ray experiments in both transmission and reflection geometries. The scattering angle range is 0 - 55° in transmission, and 0 - 110° in reflection. At the Mn K absorption edge energy of 6.54 keV, the transmission exceeds 12.4 % at all scattering angles. The cell provides a reliable base for advanced X-ray based *operando* techniques for fundamental cathode research, including Li-rich materials, such as K edge XANES, K_α & K_β XES, and structural probes such as XRD, PDF, and EXAFS.

In practice, the cell has proven to be very performant, and data collection times in transmission, with glass fibre separators, were in the range of seconds for high-energy XRD experiments, and tens of seconds for transmission and reflection 3d K edge TM XAS. Given the reasonably low rates of up to C/5 employed during most experiments, even a high capacity resolution requires long wait periods between data acquisitions, and several cells can be used in parallel. Fig. 3.13 depicts three cells being used simultaneously for transmission XAS. Most synchrotron stages provide sufficient space, and, to date, a maximum of eight cells was used simultaneously for combined XRD/PDF experiments on beamline 11-ID-B at the Advanced Photon Source (APS), where data was collected for each cell every 40 min.

Use of the cell at synchrotron beamlines has resulted in several lessons learned. These are mainly related to the mass of the cell, which caused problems at a beamline, where the cells

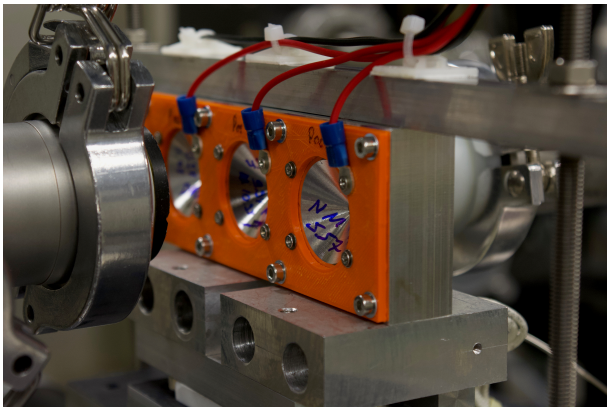


Figure 3.13: Three *operando* cells being used for transmission XAS on Beamline B18, Diamond Light Source.

had to be mounted on a horizontal beam. The setup needed the cell to protrude into the beam path, instead of being mounted on a vertical frame. The cell mass limited the number of cells that could be used in parallel, and a lighter design would have been beneficial. The mass could be revisited during a second design iteration, as it is mainly based on the selection of solid metals for the lid (1) and base (7). Several options are available, and e.g. a design incorporating a polymer body with metal inserts should be investigated.

Related to the cell mass is the choice of M3 screws, which improve the handling but come at the cost of additional mass, particularly due to the increased cell size required to fit them around the cell stack and O-ring (22). Smaller screws, potentially coupled with a fixture or jig to assist with assembly, could reduce the cell volume and mass.

Another lesson learned is the circular cross-section of the cell, which was initially chosen to enable easy manufacture on a lathe. CNC milling services, however, allow for cost efficient and quick manufacturing of more complex designs, and a cell with e.g. a rectangular cross section could be stacked more densely on a beam line stage, again increasing the number of cells in parallel.

These improvements would be particularly beneficial for low collection time structural probes, e.g. XRD, where tens of cells could be tested in parallel.

Lastly, through simple variations of the used materials in contact with the cell stack, the cell could be adapted for anode studies.

Chapter 4

First-Cycle Transition Metal Oxidation State Changes in Layered Lithium-Rich Compounds

4.1 Introduction

Li-rich layered compounds with a honeycomb superstructure, such as $Li_{1.2}Ni_{0.2}Mn_{0.6}O_2$ ('Li-rich NM') and $Li_{1.2}Ni_{0.13}Co_{0.13}Mn_{0.54}O_2$ ('Li-rich NMC'), exhibit combined TM and O redox.[21,22,25,44,55,57,140,141,172]

Owing to this, their first-cycle voltage profiles exhibit several distinct features (fig. 4.1). Region 1 is similar to the ones observed in stoichiometric, layered Li ion cathodes, and regularly assigned to TM redox.[21,22] The voltage plateau in region 2 is associated

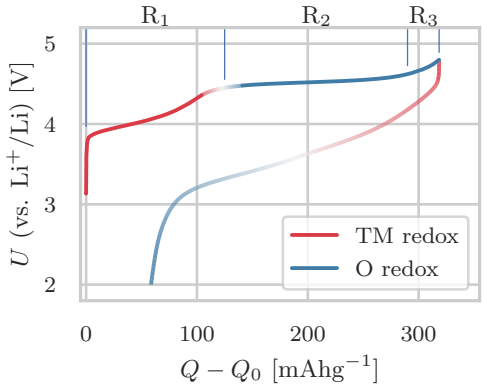


Figure 4.1: First-charge voltage profile for a Li-rich material, here $Li_{1.2}Ni_{0.13}Co_{0.13}Mn_{0.54}O_2$. Qualitatively coloured according to the present understanding of TM and O redox activity (see text).

with reversible O redox, while region 3 arises mainly due to O loss.[21,22] On discharge, the redox behaviour is less clearly separated, which is ascribed to structural changes during the first charge lowering the O redox potential.[25,57,140,141]

The exact interplay between TM and O redox is still being investigated. It is usually assumed that pure TM redox only occurs in region 1, and that the 'excess' capacity, observed in regions 2 and 3, is based on O redox and O loss, as the observed inflection points between regions 1 and 2 correlate well with the theoretical TM capacities.[21,22] TM and O bands, however, are expected to overlap and, at a certain point along the voltage profile, the phenomena should occur simultaneously.[25,52,141,173] Particularly the oxidation state of Ni is of high interest, due to the element's high voltage and specific capacity, arising from the Ni^{4+}/Ni^{2+} redox couple, as well as the metastable and nature of Ni^{4+} compounds.[174]

The majority of information on the TM and O oxidation states has been obtained using *ex-situ* 'soft' X-ray techniques with energies < 1 keV. These include TM L edge soft XAS (SXAS), which gives insight into the population of TM 3d orbitals, O K edge SXAS and RIXS, which contain information on the O 2p states, scanning transmission X-ray microscopy and nanoscale XAS (STXM-XAS), as well as X-ray photoelectron spectroscopy (XPS).[21,22,25,44,51,54,55,57,140,141,172,175] While these techniques are powerful tools for analysing the valence states, they require high vacuum conditions, due to the low energies of the X-rays and resulting short mean free paths, limiting the techniques to mainly *ex-situ* experiments. Some success has been reported for *operando* soft-XAS on NMC and LFP cathodes using solid polymer electrolytes,[176] liquid systems with windows of ~100 nm thickness,[177–179] as well as atmospheric-pressure XPS (APXPS).[180,181] None of these approaches, however, are suitable for Li-rich layered materials, owing to the sluggish O redox kinetics.[55,140–142]
Soft X-ray techniques also have low sample penetration depths of the order of 100 nm, making it harder to obtain truly bulk sensitive information, and the extracted information tends to contain a bias towards the surface.[124,182]

The 'hard' X-ray regime > 5 keV of the 3d TM K absorption edges, with absorption lengths of > 10 μm, makes them truly bulk sensitive and suitable for *operando* experiments, as the mean free path of the high-energy photons is long and setups do not require vacuum conditions. Ni, Co, and Mn K edge XANES has been used extensively to probe the oxidation states in Li-rich compounds, both *ex-situ* and *operando*.[21,22,31,39,62,144–146,148,183]

The K edges, however, are less sensitive to the oxidation states, as the dipole-allowed 1s → 4p transitions do not probe the valence states directly. As discussed in chapter 2, however, weak quadrupole-allowed 1s → 3d excitations occur at energies immediately below the edge and contain information on the energies and symmetry of the unoccupied valence states.[122,128–131] These can be studied using HERFD-XANES, owing to the highly resolved absorption peaks, as discussed in sec. 2.6.1.1. The technique has been used to study complexes, catalytic centres, as well as metal oxides, where it was used to characterise the coordination symmetry and oxidation states.[122,127–131]
Previous work has shown that assigning the pre-edge features is compex in TM oxides, as interactions with neighbouring TMs can feature heavily.[122,129,130] Nonetheless, the spectra contain valuable information on the electronic structure of the 3d states, and the energy and shape of the pre-edge peaks is usually well correlated with the oxidation states.[127,129]

The technique can be complemented with XES, due to the similar experimental setup, as discussed in sec. 2.7. In K_α XES, radiation from the 2p → 1s transition is detected, which occurs in the hard X-ray regime for 3d TMs. Due to spin-interactions between the TM 2p and 3d states, the line shape is a function of the spin in the 3d orbitals, and hence the oxidation state.[122]

HERFD-XANES and K_α XES bridge the gap between conventional hard and soft X-ray techniques, as they enable the direct observation of 3d states in the hard X-ray regime. This

makes these methods particularly suited for *operando* experiments. In the following, both techniques, along with XRD and EXAFS, are used *operando* to investigate the TM oxidation states in $Li_{1.2}Ni_{0.2}Mn_{0.6}O_2$ and $Li_{1.2}Ni_{0.13}Co_{0.13}Mn_{0.54}O_2$, using the electrochemical cell discussed in the previous chapter.

4.2 Experimental

Synthesis of Layered Materials $Li_{1.2}Ni_{0.2}Mn_{0.6}O_2$ and $Li_{1.2}Ni_{0.13}Co_{0.13}Mn_{0.54}O_2$ active materials (AM) were prepared using a sol-gel-assisted solid-state method as described in 2.2.1.1.[101] For 0.02 mol of final product, stoichiometric amounts of $LiCH_3COO \cdot 2H_2O$ (99 %, Alfa Aesar), $Ni(CH_3COO)_2 \cdot 4H_2O$ (98 %+, Alfa Aesar), $Mn(CH_3COO)_2 \cdot 4H_2O$ (≥ 99 %, Sigma Aldrich), $Co(CH_3COO)_2 \cdot 4H_2O$ (99 %, Alfa Aesar) were dissolved in 75 mL of distilled water with a 5 % molar excess of Li_2CO_3 (99.999 %, Acros Organics). This was added to a solution of 0.2 mol resorcinol (≥ 98 %, Sigma Aldrich), dissolved in 0.3 mol formaldehyde (37 m% in H_2O, Sigma Aldrich) and stirred for 30 min. Following, the solution was heated to 60 °C until a white gel was formed. This was dried at 90 °C for 12 h and then ground using mortar and pestle. The resulting powder was heated to 450 °C for 12 h (ramp: 5 °C/min), to burn off organic compounds, and subsequently reacted at 900 °C for 8 h in air (ramp: 10 °C/min).

Free-Standing Cathode Pellet Preparation Self-supporting cathode pellets with a ratio of 80 m% AM, 10 m% acetylene carbon black (99.9+ %, Alfa Aesar), and 10 m% PTFE (Imperial Chemical Industries Ltd.) were prepared as described in sec. 2.3.1.

***Operando* X-ray Diffraction** Powder X-ray diffraction (XRD) patterns were collected on beamline I11, Diamond Light Source, Didcot, UK, using *operando* cells in transmission mode. The cells were assembled in an argon-filled glovebox (O_2 & H_2O < 0.1 ppm), as described in sec. 3.3. Cathode pellets as described in the previous paragraph were used. Li metal with a thickness of ~125 µm was used as the anode, as well as dry LP30 electrolyte

(Sigma Aldrich / Merck), soaked into glass fibre separators (Whatman GF-D).

Six cells were simultaneously cycled galvanostatically between 2.0 - 4.8 V using a BioLogic MPG-2 battery cycler at a rate of 30 mAg^{-1} at a temperature of ~20 °C. XRD patterns were collected using a position-sensitive detector. An X-ray wavelength of 0.82496 Å was selected using a double-bounce Si(111) monochromator. Data was collected for 30 s per sample every 6 min. No beam damage was observed.

A background pattern, obtained for an assembled cell without cathode, was subtracted from the data. Structures were refined against each pattern using the Rietveld method as implemented in the GSAS-II scripting environment based on the Python 3 programming language.[184] Instrument parameters were obtained by fitting a silicon standard measured in a capillary. To analyse the structures, α-$NaFeO_2$-type structures (space group $R\bar{3}m$) were fit to the data, populated with Li according to the capacity. A background function, lattice parameters a and c, as well as the peak shape and isotropic displacement factors U_{iso} were refined. Fractional coordinates and site populations were not refined. The obtained fit quality was not exceptional, particularly for Li-rich NM, but was sufficient to extract the lattice parameters, as confirmed visually from the peak positions (see. A.2).

***Operando* EXAFS** *Operando* K edge EXAFS was collected on beamline B-18, Diamond Light Source, Didcot, UK, using *operando* cells in transmission mode. The cells were assembled in an argon-filled glovebox (O_2 & H_2O < 0.1 ppm), as described in sec. 3.3. Cathode pellets as described previously were used. Li metal with a thickness of ~125 µm was used as the anode, as well as dry LP30 electrolyte (Sigma Aldrich), soaked into glass fibre separators (Whatman GF-D).

Three cells were simultaneously cycled galvanostatically between 2.0 - 4.8 V using a BioLogic MPG-2 battery cycler at a temperature of ~30 °C. The temperature was controlled via two proportional–integral–derivative (PID)-controlled cartridge heaters connected to the bottom of an aluminium sample holder (pic. 3.13). The XANES energy was controlled using a Si(111) double-bounce monochromator, capable of scanning through the energy ranges of

all three TMs (Ni, Mn, Co). The energy was calibrated with a Mn foil, resulting in a slight shift of the edge positions for Ni and Co of about 0.2 eV.

For each sample, the TM edges were measured sequentially in transmission mode every 40 min. No beam damage was observed. Even still the beam was rastered across the area of the cathode, and each location only visited once. At each point five spectra were collected for each edge, and averaged for the subsequent analysis. Data processing was performed using the Athena package.[185] The pre-edge subtraction, data normalisation, and $\chi(E)$ extraction was performed as described in secs. 2.6 and 2.6.2. $\chi(k)$ was weighted by k^2 and Fourier transformed up to k = 12 Å^{-1} to obtain $|\chi(r)|$.

***Operando* HERFD-XANES & XES** *Operando* HERFD-XANES and XES spectra were collected on beamline ID26 at the European Synchrotron Radiation Facility (ESRF), Grenoble, France, using *operando* cells, which were assembled in an argon-filled glovebox (O_2 & H_2O < 0.5 ppm), as described in sec. 3.3. Cathode pellets, as described previously, were used. Li metal with a thickness of ~500 μm was used as the anode, and dry LP30 electrolyte (Sigma Aldrich / Merck), soaked into glass fibre separators (Whatman GF-D).

Two cells were cycled simultaneously and the temperature was kept at ~30 °C using a PID-controlled hot air blower connected to a thermocouple on the back of one of the cells. The cells were cycled galvanostatically between 2.0 - 4.8 V at a rate of 40 mAg^{-1} for Ni and Mn, and 45 mAg^{-1} for Co (due to time constraints) using a BioLogic SP-300 instrument.

Beam damage was assessed by repeatedly collecting Ni K edge spectra with an unattenuated beam on the same location. Minor damage was observed in the samples after exposure to the beam for several minutes, as evidenced by a minor shift of the K edges to lower energies. The beam-sample-interaction was also visible in the voltage profiles, where a reversible voltage increase was observed during beam exposure, particularly in regions linked with O redox.[21,22,140] Even though the damage appeared to be reversible, the beam was attenuated and rastered across the surface, and each position was used to acquire just one set of spectra.

For HERFD-XANES, the incident beam's wavelength was selected using a cryogenically-

cooled Si(311) crystal double bounce monochromator, and tuned through the respective TM K edge. The beam energy was calibrated using foils of the respective TMs for Ni and Co, and an Fe foil for Mn.

Data was collected using four spherically bent Si(531) crystals for Ni and Co, and Ge(333) crystals for Mn, arranged with the sample and an avalanche photodiode detector in a vertical Rowland geometry with a radius of 1 m. HERFD-XANES data were collected using the maximum of the respective $K_{\alpha 1}$ emission lines for detection, which were located at the following positions: Ni: 7.4799 keV, Co: 6.9319, Mn: 5.8992 keV. Spectra were collected alternately between the two cells every 40 mins. During dedicated pre-edge scans, a second scan of the full XANES region was performed, for normalisation of the pre-edge.

Data processing was performed using custom code written in Python 3. Due to the low background, resulting from the HERFD, no background subtraction was required. The collected spectra were normalised using the spectral area in the following ranges: Ni: 8.328 - 8.450 keV, Co: 7.700 - 7.770 keV, Mn: 6.530 - 6.630 keV.

XES spectra were collected for the $K_{\alpha 1}$ and $K_{\alpha 2}$ emission lines, using the following incident energies: Ni: 8.400 keV, Co: 7.785 eV, and Mn: 6.600 eV. Spectra were collected every 40 mins for each cell. The collected spectra were normalised by spectral area in the following ranges: Ni: 7.450 - 7.490 keV, Co: 6.901 - 6.945 keV, and Mn: 5.875 - 5.910 keV.

To probe the changes in local spin magnetic moment with changing lithium-content, the full width at half maximum (FWHM) of the TM $K_{\alpha 1}$ peaks was determined, as well as the integrated absolute difference (IAD), as described in sec. 2.7. Errors were estimated by applying the respective technique to two spectra obtained for the pristine compound. All calculations were performed using custom scripts based on Python 3.

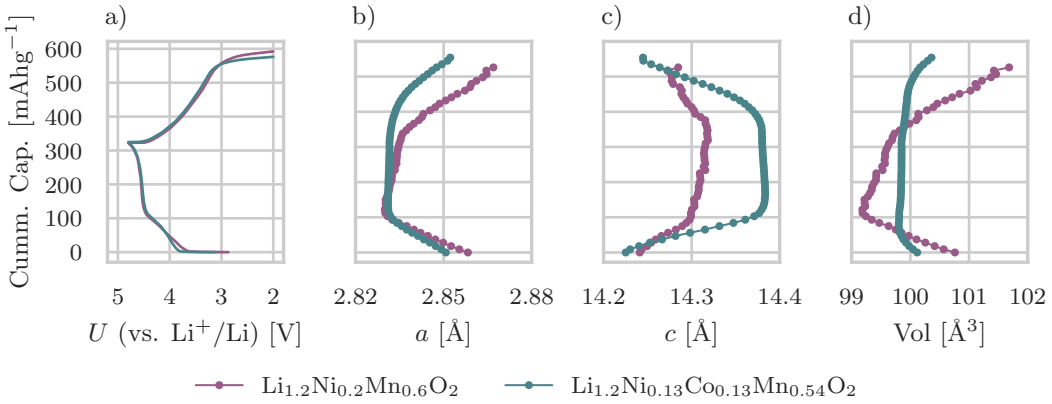


Figure 4.2: Unit cell parameters of Li-rich NM and Li-rich NMC obtained via *operando* XRD for the first cycles of the materials. a) Voltage profiles; b) Lattice parameter a; c) Lattice parameter c; d) Unit cell volume. Errors bars are smaller than data point symbols.

4.3 Structural Characterisation

The bond lengths surrounding a central atom have a direct impact on the spectra observed in XAS and XES. To understand the evolution of the long-range, average structures of the compounds, *operando* XRD was collected for Li-rich NM and Li-rich NMC. The patterns were found to correspond to previous reports and selected results of the Rietveld refinements are presented in fig. 4.2.[21,22] Details are presented in the appendix (sec. A.2).

The data show that the lattice parameters a and c are very similar in the pristine compounds, and vary only slightly in their aspect ratios. During delithiation, a contracts almost linearly in both compounds, and at the end of region 1 they have nearly identical a parameters. Across the plateau, a is maintained in Li-rich NMC, whereas in Li-rich NM it slightly contracts. For c a more pronounced change is observed in Li-rich NMC, compared to Li-rich NM. The parameter grows across region 1, and then stays largely constant in the former, while it continues to grow in the latter. On discharge, it shrinks continuously in both compounds. The influence of c on the unit cell volume, however, is small, and a dominates.

Interestingly, on discharge, lattice parameter changes are only observed after ~50 mAhg^{-1} of charge have been passed. The parameters revert to their original positions in Li-rich NMC,

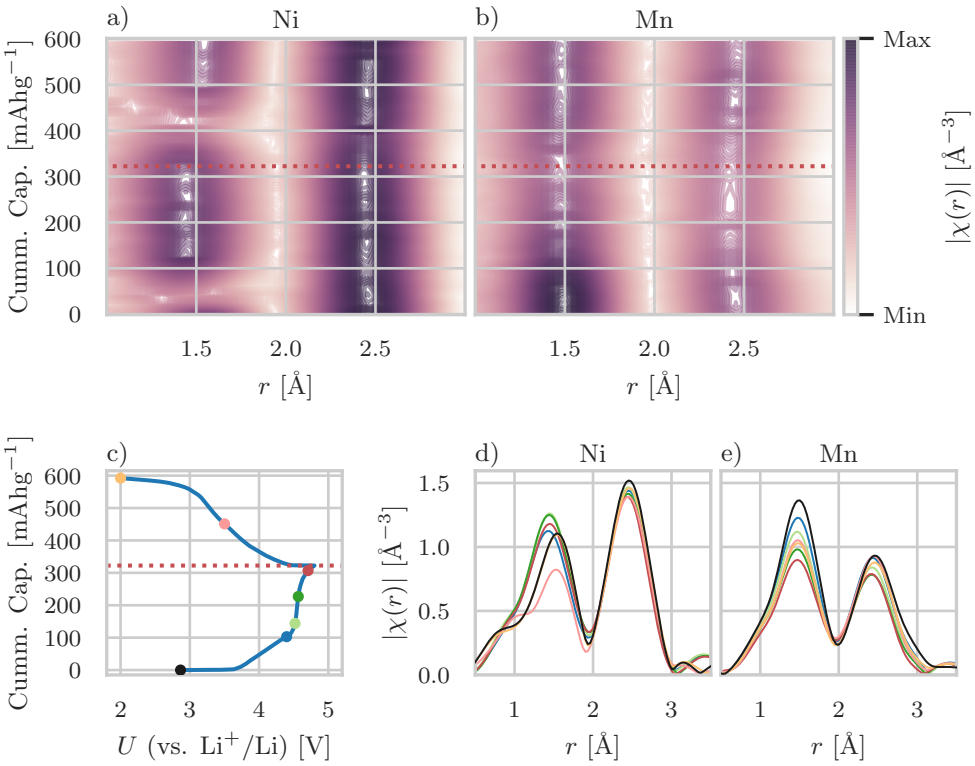


Figure 4.3: *Operando* TM K edge EXAFS of $Li_{1.2}Ni_{0.2}Mn_{0.6}O_2$. a & b) Contour plots of the EXAFS spectra for Ni and Mn, respectively, as a function of capacity. The red line indicates the top of charge; c) Corresponding voltage profile; d & e) Selected spectra for Ni and Mn, respectively. The plot colour corresponds to the capacity at which the data was obtained, as indicated by the coloured dots in the voltage profile.

whereas for Li-rich NM the final unit cell aspect ratio differs from the pristine compound. These effects are also visible in the respective unit cell volumes, where the changes are small for Li-rich NMC, while Li-rich NM shows a significant volumetric strain, and a large volume increase on discharge.

To investigate the local environments, *operando* EXAFS was collected for both compounds, and the data for Li-rich NM are depicted in fig. 4.3.

In the pristine material, a sharp peak is observed for the Ni-O bonds at approximately 1.5 Å. The contour plot shows a shift to lower values of the radius r on charging across region 1, along with a decrease in intensity. The intensity is recovered at the beginning of the plateau

and a well-defined peak persists until the top of charge. On discharge, a similar process is observed in reverse.
The Ni-metal (Ni-M) peak at approximately 2.5 Å does not change significantly during the first cycle, and only a slight shrinking on charge and expansion on discharge is observed, as expected from the lattice breathing due to Li extraction and reinsertion.

The Mn-O bond lengths stay very similar during the entire first cycle, however the peak intensity decreases significantly, and does not recover fully on discharge. The nearly constant peak position suggests no changes in Mn oxidation state, while the intensity changes suggest a reduction of order around the atom, potentially linked to O redox.[21,22,186]
The Mn-M peak has a lower intensity, compared to Ni-M, as expected from the honeycomb ordering of the TM layer, where a larger fraction of the weak scatterer Li is present in the second Mn coordination sphere.[21,22] Only small changes are observed across the first charge, similar to those of Ni, and the peak is almost fully recovered on discharge.

The EXAFS data for Li-rich NMC are depicted in fig. 4.4, and show a similar behaviour for Ni and Mn as observed for Li-rich NM.
The pristine spectrum for Co is very similar to that for Mn. On charge, the Co-O bond distances show a slight shift to lower r, indicating an increase in oxidation state, as well as a decrease in the peak intensity of approximately 50 % of what is observed for Mn. On discharge, the position, but not the intensity, is recovered. The Co-M peak intensity and position remains largely unchanged across the whole first cycle. The close resemblance to Mn is expected, as both elements occupy similar positions within the honeycomb.

A closer investigation of the evolution of both compounds' Ni-O peaks across region 1 is depicted in fig. 4.5. In Li-rich NM, the initial shift to lower r is accompanied by a splitting of the peak that is recovered towards the end of the region. The peak ratios indicate a contraction of four of the bonds, and an elongation of two others,

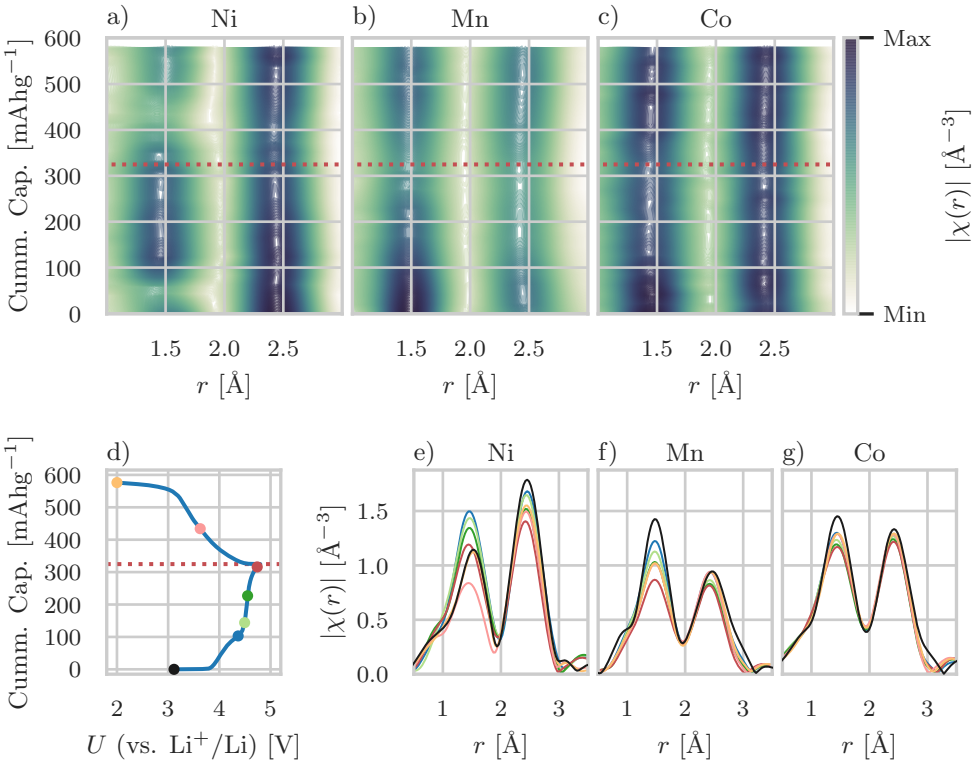


Figure 4.4: *Operando* TM K edge EXAFS of $Li_{1.2}Ni_{0.13}Co_{0.13}Mn_{0.54}O_2$. a, b, c) Contour plots of the EXAFS spectra for Ni and Mn, respectively, as a function of capacity. The red line indicates the top of charge; d) Corresponding voltage profile; e,f,g) Selected spectra for Ni and Mn, respectively. The plot colour corresponds to the capacity at which the data was obtained, as indicated by the coloured dots in the voltage profile.

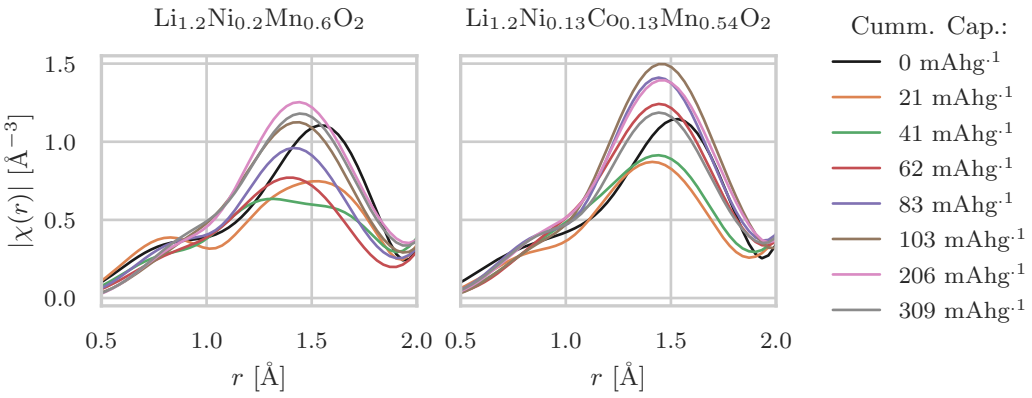


Figure 4.5: Detailed view of the Ni-O peak transformations in LI-rich NM and Li-rich NMC during the first charge. The peaks for the pristine compounds are almost identical, whereas the changes across region 1 differ. In Li-rich NM a splitting of the peak due to JT distortion is evident at 40 mAhg^{-1}, which is not observed to the same extent in Li-rich NMC.

suggesting Jahn-Teller effect (JT) activity. Similar observations have been reported for $LiNi_{0.33}Mn_{0.33}Co_{0.33}O_2$, where they were attributed to JT-active d^7 Ni^{3+} (d^7 low spin, S = 0.5), as well as for comparable Li-rich materials.[39,187] Similarly, Ni^{3+} was observed using magnetic measurements using superconducting quantum interference device magnetometry (SQUID) in partially delithiated $LiNi_{0.5}Mn_{0.5}O_2$.[188] Given the close structural similarity between these compounds and Li-rich NM, as well as the voltage and amount of charge removed, the presence of Ni^{3+} is a reasonable assumption.

Upon further delithiation, the growth of a sharp peak at lower r (~ 1.4 Å) is observed, that persists across regions 2 & 3. This suggests the formation of a JT-inactive species with a similar coordination sphere, but shorter bond lengths and hence higher oxidation state, indicating the presence of Ni^{4+}.[187,188]

In Li-rich NMC less peak splitting is observed. The transition phase is shorter and the 'final' low-r peak location is reached already after ~60 mAhg^{-1}, where its high intensity suggests an ordered environment. Interestingly, the peak intensity in Li-rich NMC decreases towards the end of region 2, accompanied by a slight shift to lower r, which is not observed in Li-rich NM. At the top of charge, both compounds exhibit essentially identical Ni-O peaks.

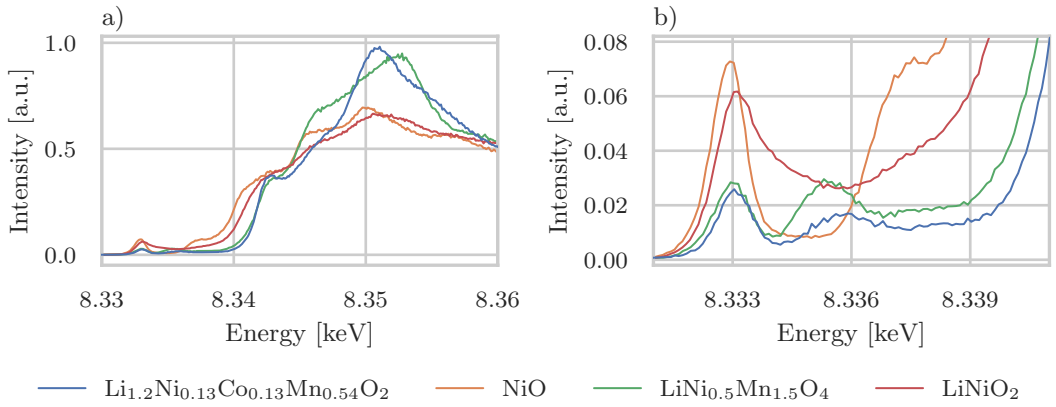


Figure 4.6: Ni K edge HERFD XANES spectra for Li-rich NMC and reference compounds. a) K edges; b) Pre-edge regions.

4.4 Transition Metal Oxidation States Probed via HERFD-XANES and XES

The structural probes give indirect evidence on the oxidation states of the TMs, particularly for Ni. In the following, results for a more direct investigation of the electronic structure via HERFD-XANES and XES are presented.

4.4.1 Nickel Oxidation States

Ni K edge HERFD-XANES spectra were collected for pristine Li-rich NM and Li-rich NMC, as well as several Ni^{2+} and Ni^{3+} standards, where the TMs are in similar octahedral coordination environments (fig. 4.6). As the observed K and pre-edges for the two materials of interest are virtually identical, only the spectrum for Li-rich NMC is discussed (see fig. 4.7).

The XANES regions of all four compounds show broadly similar features, with Li-rich NMC and $LiNi_{0.5}Mn_{1.5}O_4$ exhibiting the most similarity and almost identical rising edge

energies. The peak shapes of NiO (Ni^{2+}) and $LiNiO_2$ (Ni^{3+}) are very similar, although the edge for NiO is shifted to lower energies, as would be expected from the lower Ni oxidation state. Interestingly, the rising edge energies of Li-rich NMC and $LiNi_{0.5}Mn_{1.5}O_4$ are ~2 eV higher than NiO, even though all three compounds contain Ni^{2+}.

The pre-edges are less sensitive to the influences of the coordination environments, and two well-separated peaks, at 8,333.1 eV and 8,335.7 eV, respectively, are observed for Li-rich NMC. The one at lower energy matches well with the one observed for NiO, as well as the first peak of $LiNi_{0.5}Mn_{1.5}O_4$ and can be assigned to the expected quadrupole-allowed 1s → 3d excitations into the unfilled e_g orbitals of the d^8 Ni^{2+} (t_{2g}^6 e_g^2).[129] Noticeably, the energy of $LiNiO_2$ (Ni^{3+}) is only shifted by ~0.2 eV, compared to the Ni^{2+}compounds. Similar observations have been reported for Ni complexes, where both high-spin (hs) and low-spin (ls) Ni^{2+}, as well as Ni^{3+} (ls) exhibited similar peak energies.[122,189]

From the t_{2g}^6 e_g^2 configuration a twofold degenerated e_g state is expected, with no JT distortion, as supported by the EXAFS results, and hence only one peak should be observed. Additional peaks, shifted by ~2.5 - 3.5 eV, have also been reported for other 3d TM compounds (TM = Ti, Mn, Co), where the first peak arises from the local, quadrupole-allowed $1s_{TM}$ → $3d_{TM}$ transition, and the higher-energy peak was attributed to O-mediated transitions into states with mixed p-d-character.[129,190–193] These dipole-allowed transitions into bands with $4p_{TM}$-$2p_O$-$3d_{TM'}$ character result in an indirect $1s_{TM}$ → $3d_{TM'}$ transition, where $TM'$is an adjacent TM. The states on TM' are subject to a lower core-hole potential than the ones on TM, and are hence shifted to a higher energy.[190] This mixing is not possible in systems with inversion symmetry, but can occur if the symmetry is broken outside of the immediate coordination sphere. Breaking of the local inversion symmetry can be expected in Li-rich NM and Li-rich NMC through the inhomogeneous honeycomb ordering, as well in $LiNi_{0.5}Mn_{1.5}O_4$. Similarly, the rocksalt structure of NiO has no inversion symmetry and only a single peak is observed. The additional peaks can therefore be assigned

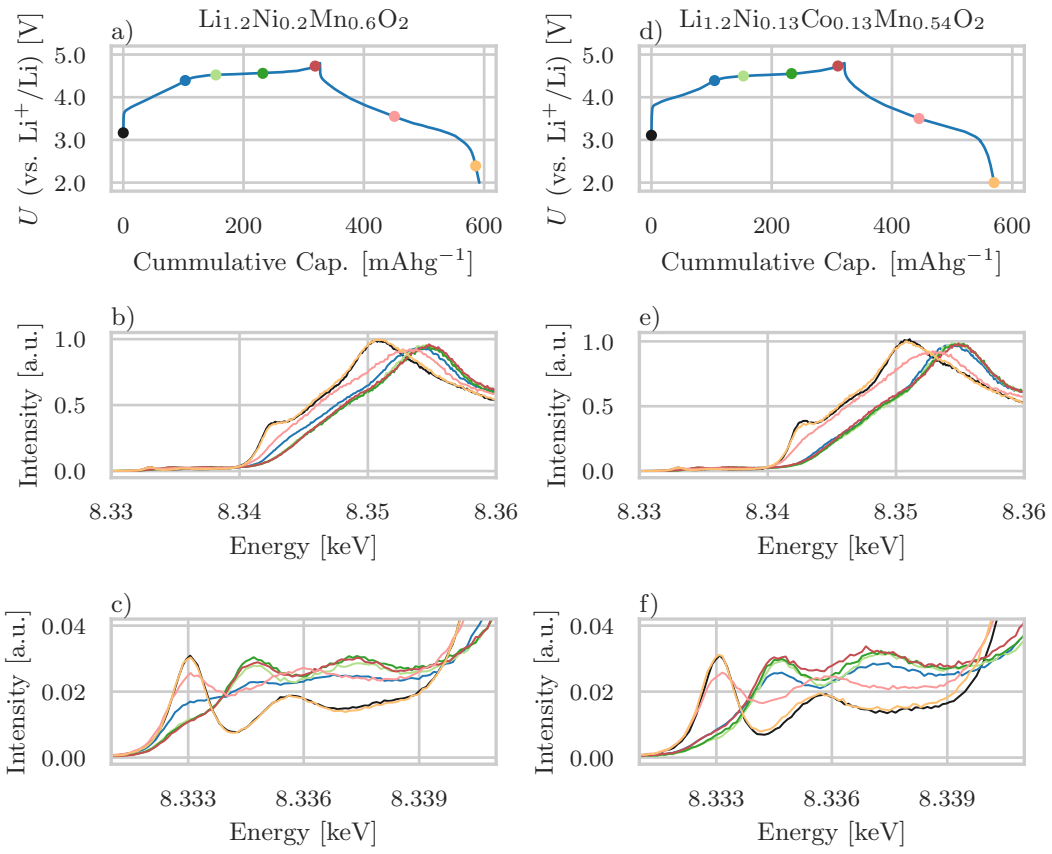


Figure 4.7: *Operando* Ni K edge HERFD-XANES for Li-rich NM and Li-rich NMC. a, d) Voltage profiles, with colour-coded dots indicating the capacities corresponding to the selected spectra. b, e) Ni K edge; c, f) Pre-edge region.

to non-local excitations.

In fig. 4.7 the *operando* HERFD-XANES spectra for the first cycles of Li-rich NM and Li-rich NMC are presented. The main edges of the compounds show a shift to higher energies during charge, in accordance with an electrostatic approximation. Interestingly, at the end of region 1, the main edge in Li-rich NMC has already shifted to its maximum, whereas for Li-rich NM this is only observed after an additional ~50 mAhg^{-1}. The positions are maintained until the top of charge, and, on discharge, the main edges shift gradually back to lower energies and the pristine spectra are recovered.

In the pre-edge spectra of Li-rich NMC, the quadrupole-allowed peak is shifted upwards by ~1.5 eV to ~8,334.6 eV through region 1, and is largely maintained across the plateau. At

the top of charge some intensity is recovered at 8,333.1 eV. The Li-rich NM pre-edge shifts more gradually, similar to what is observed for the main edge, and residual peak intensity at 8,333.1 eV remains in regions 2 and 3. On discharge, the spectra for both compounds gradually shift back and the pristine spectra are recovered.

The low-energy peak at 8,334.6 eV, observed for Li-rich NMC at ~230 $mAhg^{-1}$, can be assigned to Ni^{4+}, as a d^6 ls configuration ($t_{2g}^6\ e_g^0$) is the only JT-inactive possibility for the d orbitals to be populated with six (or seven) eletrons.[†] Almost pure Ni^{4+} can be assumed as almost no intensity remains at 8,333.1 eV. The previous observation that Ni^{2+} and Ni^{3+} ls species have approximately the same pre-edge energy, coupled with the signficant shift observed here, further supports this.[122,189]

Based on this assignment, the remainder of the spectra can then be interpreted: Ni is fully oxidised to Ni^{4+} in Li-rich NMC after region 1, and stays so across the plateau, while potentially being slightly reduced at the top of charge. Li-rich NM is never fully oxidised to Ni^{4+}, based on the residual intensity at 8,333.1 eV, that is observed throughout.

As spectra were collected every ~25 $mAhg^{-1}$, the oxidation state changes can be tracked across the entire first cycle. To achieve this, the main edge contribution was subtracted by fitting a Lorentzian function to the rising edges, and a series of Gaussians were fit to the pre-edge peaks. This allowed for a direct comparison between the low-energy peaks in the pristine and highly oxidised materials (fig. 4.8). In the example fits it can be seen that a trade-off between the first peak (blue), assigned to Ni^{2+}, and the second peak (orange), assigned to Ni^{4+}, is observed. Interestingly, the spectra required a third peak to fit the pre-edge, indicating another non-local excitation. These are known to occur in other TM oxides and are discussed in detail for Co later in this chapter.[129,190,194] Although the fitted area of the orange peak is quite noisy, owing to the neighbouring peaks, the intensity of the blue Gaussian can be used to track the amount of Ni^{2+}/Ni^{3+} in the material.

[†] d^7 hs: $t_{2g}^5\ e_g^2 \Rightarrow$ JT; d^7 ls: $t_{2g}^6\ e_g^1 \Rightarrow$ JT ; d^6 hs: $t_{2g}^4\ e_g^2 \Rightarrow$ JT; d^6 ls: $t_{2g}^6\ e_g^0 \not\Rightarrow$ JT.

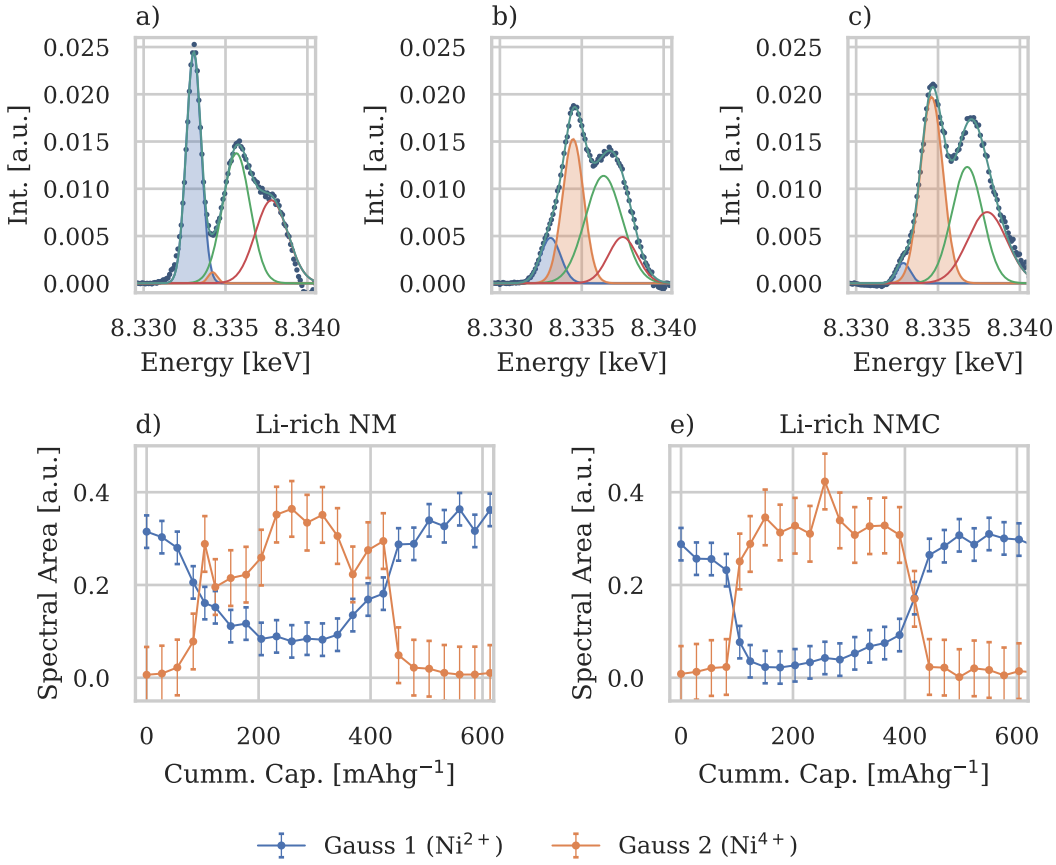


Figure 4.8: Gaussian fits of the *operando* Ni K pre-edges in Li-rich NM and Li-rich NMC. a-c) Example fits for Li-rich NMC obtained at 0 mAhg^{-1}, 105 mAhg^{-1}, and 150 mAhg^{-1}, respectively, showing the trade-off between the Gaussian peak 1 (blue), associated with the Ni^{2+} (and Ni^{3+}) species, and Gaussian peak 2 (orange), associated with the Ni^{4+} species; d) Spectral areas observed for the two peaks in Li-rich NM; e) Spectral areas observed for the two peaks in Li-rich NMC. Errors were estimated by fitting Gaussians to different spectra collected for the pristine compound.
Even though the fit datapoints are noisy, owing to the position of the Gaussian 2 peak in between several others, Gaussian 1 and Gaussian 2 always sum to approximately 0.35 a.u., and Gaussian 1 can be used to track the oxidation state.

The intensity of the Ni^{2+} peak quantifies the observations made so far, namely that Ni is oxidised more slowly in Li-rich NM, and only reaches ~$Ni^{3.5+}$ on average, while it is fully oxidised in Li-rich NMC. The data for the latter shows a sudden jump between 60 - 80 $mAhg^{-1}$, where Ni^{2+}/Ni^{3+} appears to rapidly be oxidised fully. This matches well with the observations made with EXAFS, where a lot less JT-active Ni^{3+} was observed for Li-rich NMC, as well as a sudden peak change between 40 - 80 $mAhg^{-1}$. Ni also appears to be reduced slightly across the plateau in Li-rich NMC, whilst the oxidation state is maintained in Li-rich NM until discharge, following the trend observed in EXAFS. In conjunction with the EXAFS data, it can be concluded that during the second half of the discharge Ni is fully reduced to Ni^{2+} in both compounds.

The spin states of the TMs, which gives insight into the population of the 3d states, was also probed using *operando* K_α XES. As discussed in sec. 2.7, the K_α line is primarily broadened due to exchange interaction between the 2p and 3d states, and a near linear relationship between the full width at half maximum (FWHM) of the peak and the TM spin state can be expected in 3d TM compounds.[122,135,195] As the coordination environments for Ni in both Li-rich NM and Li-rich NMC are very similar, the relative changes can be tracked.
A reduction of the total spin would suggest an increase in oxidation state from Ni^{2+} (t_{2g}^6 e_g^2, $S = 1$) towards Ni^{4+} (t_{2g}^6 e_g^0, $S = 0$), manifesting as a narrowing of the $K_{\alpha 1}$ peak at ~7.479 keV. This can be tracked via changes of the FWHM, as well as the IAD as a low-noise complement. The data are presented in fig. 4.9.

The FWHMs of the pristine compounds are very similar, suggesting similar spin states for Ni in both compounds, in accordance with the previous observations. On charging, similar trends as for the pre-edges are observed. The FWHM for Li-rich NM decreases gradually up to ~200 mAhg, where it is maintained until the top of charge. For Li-rich NMC, it is reduced up to 60 $mAhg^{-1}$, when it jumps to its minimum width. The FWHM of the

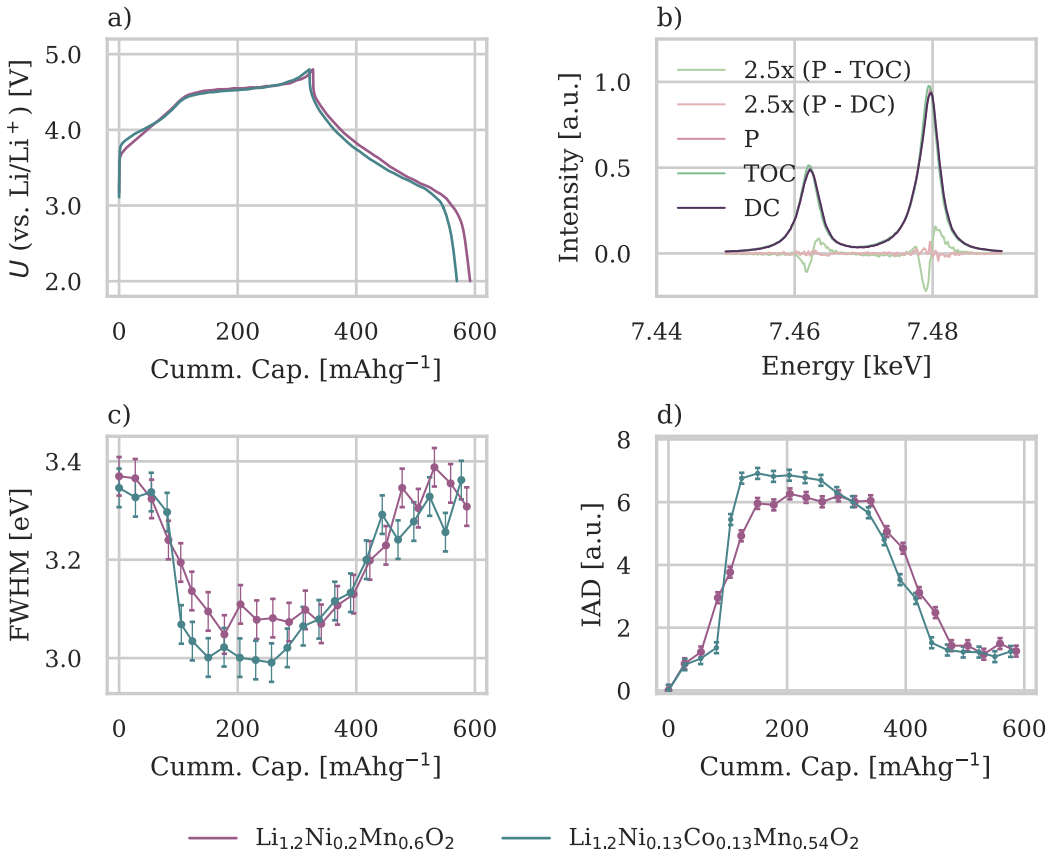


Figure 4.9: *Operando* Ni K_α XES for Li-rich NM and Li-rich NMC. a) Voltage profiles; b) Example XES spectra and differences, scaled by 2.5 for visibility. The letters indicate the state of charge: P: Pristine; TOC: Top-of-charge; DC: Discharged. c) FWHMs of the $K_{\alpha 1}$ emission lines; d) IADs of the K_α spectra.

compound begins to decrease after ~250 $mAhg^{-1}$, and the same values are observed for both compounds at the top of charge, similar to what was observed in EXAFS and the pre-edges. The total change of the Li-rich NM FWHM is only ~80 % of the change observed for Li-rich NMC. On discharge, the FWHM increases in both compounds and the pristine spectra are almost recovered. The IAD shows the same trends, and suggests that no Ni activity during the second half of the discharge.

The XES data corroborates the observations made previously. Although exact oxidation states cannot be deduced with the technique, the data show that Ni in Li-rich NM is only oxidised to approximately 80 % of the value observed in Li-rich NMC. Additionally, Ni is slightly reduced across the first-charge plateau in the latter.

4.4.2 Cobalt Oxidation States

The second redox-active TM in $Li_{1.2}Ni_{0.13}Co_{0.13}Mn_{0.54}O_2$ is Co. In fig. 4.10 HERFD-XANES spectra of the pristine compound, as well as several Co^{2+}/Co^{3+}standards, are presented.

The Co^{3+} compounds exhibit very similar K edges as Li-rich NMC, while the energy of the mixed Co^{2+}/Co^{3+} oxide Co_3O_4 is shifted to lower values. All edges share a lot of similarities, particularly among the layered Co^{3+} materials, as expected from the close structural relationship.

The pre-edge region for Li-rich NMC exhibits two peaks, at 7,709.9 eV and 7,711.5 eV, respectively, and is similar to those observed for stoichiometric NMC and LCO. These Co^{3+} compounds have a $3d^6$ ls (t_{2g}^6 e_g^0) electron configuration and only a single peak in the pre-edge region is expected.[129,188,190,196–198] However, similar to the observations made for Ni, the additional peak likely arises from non-local excitations. This has been previously observed in LCO, as well as the closely related $Na_{0.91}CoO_2$, and can be transferred onto the other layered compounds due to the structural similarity.[129,190,194,199,200]

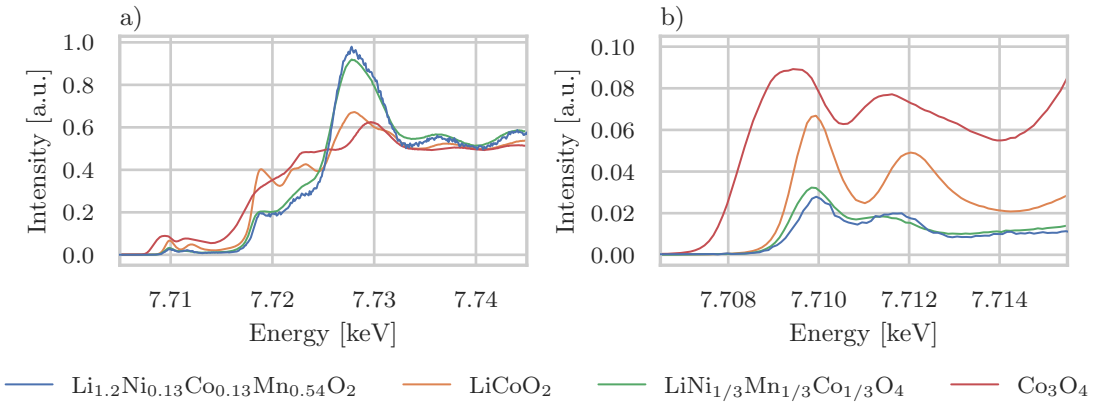


Figure 4.10: Co HERFD-XANES spectra for pristine Li-rich NMC and standards with similar coordination environments. a) Main edges; b) Pre edge region.

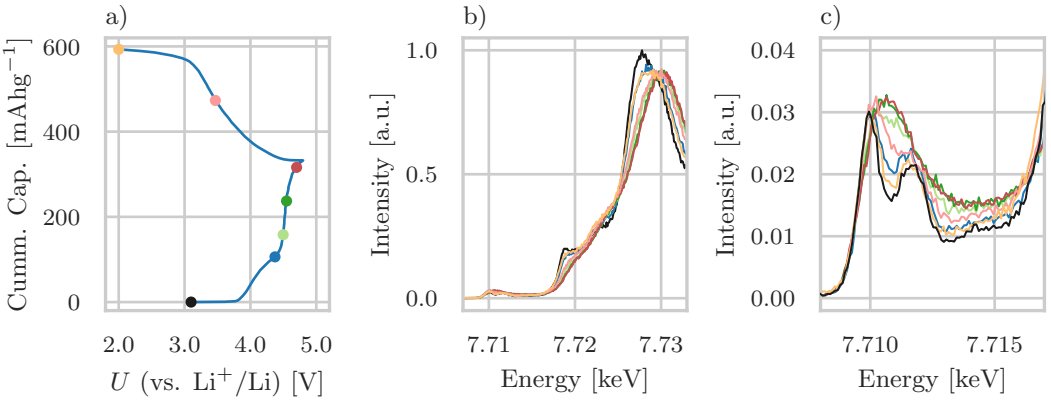


Figure 4.11: *Operando* Co K edge HERFD-XANES for Li-rich NMC. a) Voltage profile, with colour-coded dots indicating the capacities corresponding to the selected spectra; b) K edge spectra; c) Pre-edge region.

Interestingly, a third, smaller shoulder is visible in the pre-edge of Li-rich NMC, ~4.5 eV above the first peak (compare fig. 4.11 c), which is again assigned to a non-local excitation, as similar phenomena were previously observed in LCO.[194] There the different peaks are assigned to O-mediated transitions into hybridised states with 3d character arising from Co in adjacent layers at different positions, demonstrating the strong interactions in the material.[129,190,194]

In fig. 4.11 the *operando* Co K edge HERFD-XANES spectra for the first cycle are presented.

On charge, the main edge is shifted upwards in energy until approximately 50 $mAhg^{-1}$ into the plateau of region 2, where it persists until the top of charge. On discharge, the edge shifts back linearly. The pristine spectrum is never fully recovered.

In the pre-edge region, the intensity in the region between the two large pre-edge peaks gradually increases with increasing state of charge until a single, asymmetrical peak is observed, which is fully established midway through region 2 and persists until the top of charge. On discharge, the pre-edge changes are gradually recovered. The shift of the pre-edge towards higher energy suggests that Co is oxidised and continues to do so well into the fist-charge plateau.

Interestingly, during the charge in region 1, Co appears to be temporarily re-reduced, or at least not further oxidised. In fig. 4.12 a selection of the K and pre edge spectra for the region are depicted, showing a shift towards lower energies for the former, and a stagnation of the peak growth for the latter. These changes occur at the same point where a strong upward shift of the Ni pre edge, as well as a sudden increase in the Ni XES data, are observed, potentially indicating a charge transfer.

The changes of the Co pre-edge do not correspond to a change from a d^6 ls to a d^5 ls state, which is expected from an oxidation to Co^{4+}. For this, two separate peaks, arising from excitations into the t_{2g} and e_g states, should be observed. A similar peak shape was previously reported for $Na_{0.66}CoO_2$, whose average oxidation state of $Co^{3.34+}$ could suggest that Co is not fully oxidised upon charging in Li-rich NMC.[200] The asymmetry of the peak observed at the top of charge, however, suggests a contribution from several overlapping excitations, and non-local transitions, coupled with the finite energy resolution, might be covering the expected peaks. Significant intensity growth is observed at ~7,710.5 eV, potentially due to the expected transition into t_{2g} states. Similar spectra have been reported for calculations with small crystal field splitting, where the empty states in the t_{2g} and e_g orbitals overlap

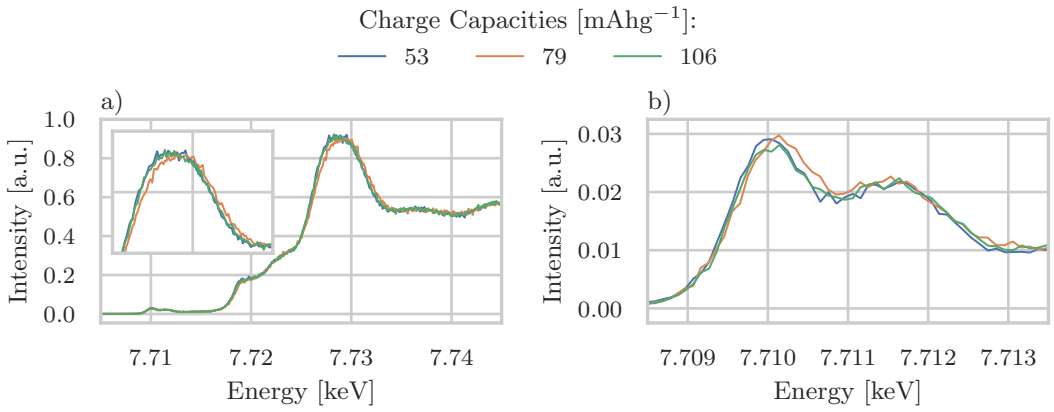


Figure 4.12: Observed shifts of the Co main and pre-edge during the TM redox region 1 Li-rich NMC. a) Main edge; b) Pre-edge region.

heavily.[129]

To study the system further, *operando* K_α XES was performed, and the results are depicted in fig. 4.13. Across region 1, and for an additional ~50 mAhg^{-1} into region 2, a reduction of the $K_{\alpha 1}$ FWHM is observed, that is subsequently maintained across the plateau. On discharge, the peak width increases, and the final width exceeds the one of the pristine compound. The IAD shows very similar changes, but the total difference is not recovered on discharge. During charge, at ~80 mAhg^{-1} and ~140 mAhg^{-1}, slight reductions of the IAD are observed, with the first occurring the same location as the temporary changes in XANES. The changes are also observed in the FWHM, but, due to the noisy data, they are not significant.

The reduction of the FWHM on charge suggests a reduction of the total spin in the 3d states. It can be reasonably assumed that Co is in a d^6 ls ($S = 0$) state in the pristine compound, due to the similarities with LCO and NMC, where this has been demonstrated.[129,188,190,196–198] Upon oxidation, the total spin therefore has to increase, as one electron is unpaired, assuming a d^5 ls state ($t_{2g}^5\ e_g^0$, $S = 1/2$) is reached on charge. As a first approximation, this increase in spin should result in an increase in FWHM, which is not observed.[122] Interestingly, the changes observed in XES are well correlated with the unit cell volume changes derived from

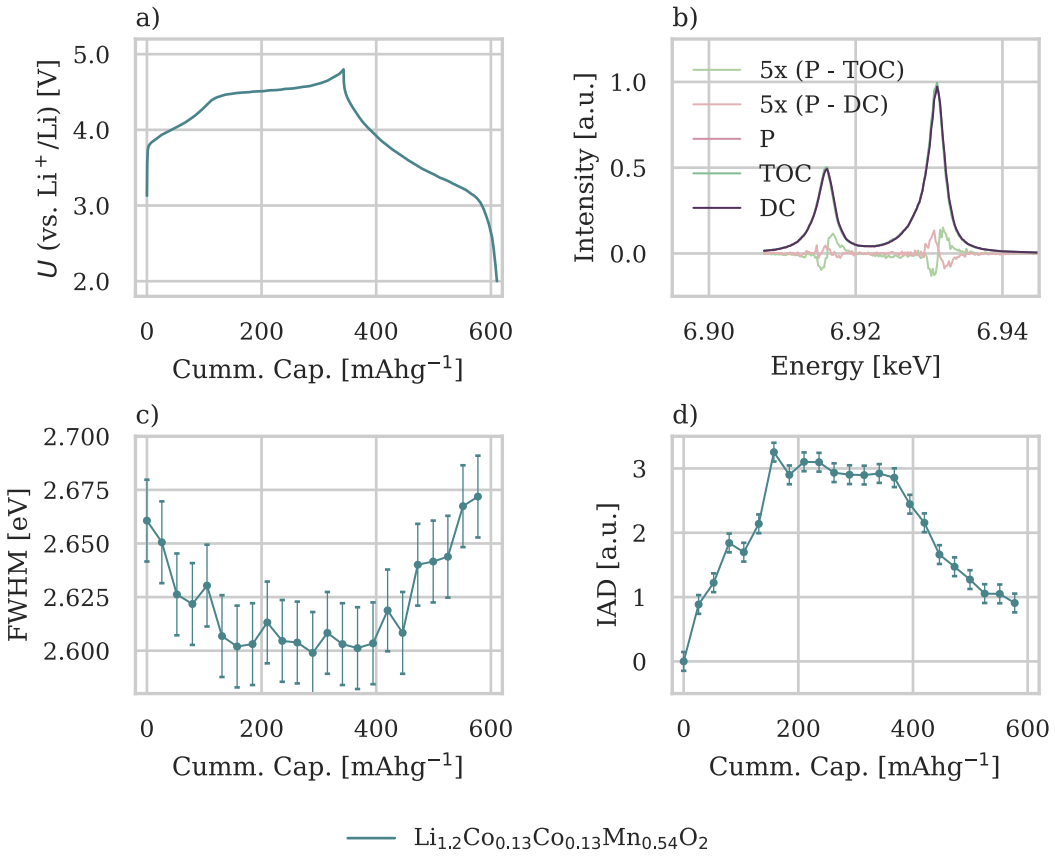


Figure 4.13: *Operando* Co K_α XES for Li-rich NMC. a) Voltage profile; b) Example spectra and differences, scaled by 5.0 for visibility. The letters indicate the state of charge: P: Pristine; TOC: Top-of-charge; DC: Discharged. c) FWHMs of the $K_{\alpha 1}$ emission lines; d) IADs of the K_α spectra.

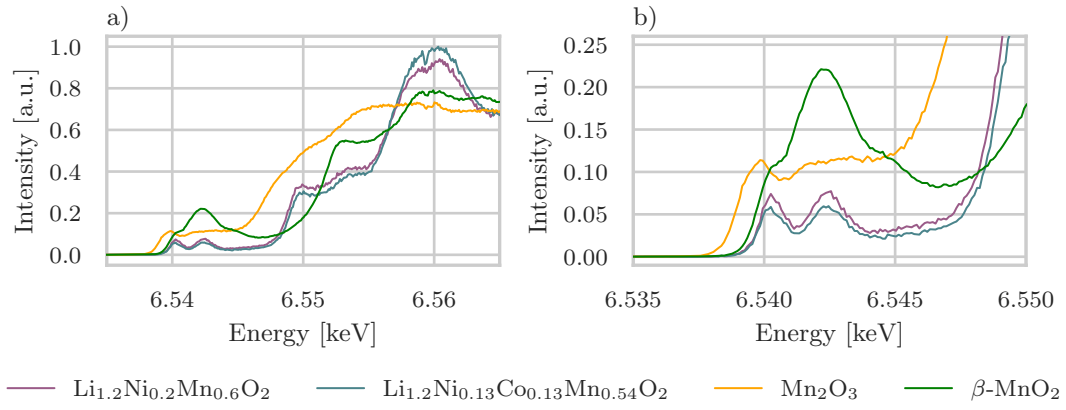


Figure 4.14: Mn K edge HERFD XANES spectra for $Li_{1.2}Ni_{0.2}Mn_{0.6}O_2$, $Li_{1.2}Ni_{0.13}Co_{0.13}Mn_{0.54}O_2$, and reference compounds. a) K edges; b) Pre-edge regions.

XRD, potentially indicating that orbital overlap or a similar factor play a role.

Lastly, the differences between the observations made with XANES and XES could be based on the interaction between the 3d states and the core hole for the latter technique, where the 3d electronic configuration of the excited state does not correspond to the ground state. The different spin would then change the observations. To assess this, in-depth modelling of the system would be required. The strong interaction between Co and its neighbours poses an additional constraint that prevents a conclusive result with regards to the highest oxidation state of Co in the charged compound.

4.4.3 Manganese Oxidation States

Manganese is expected to be redox-inactive in Li-rich NM and Li-rich NMC, as it is in a Mn^{4+} ($3d^3$) oxidation state, based on the compositions of the compounds.[21,22] In fig. 4.14 the Mn K edge HERFD-XANES spectra for the two materials and reference compounds are presented. There are broad similarities between the K edge of β-MnO_2 and the ones of the pristine compounds. In the pre-edge region, two peaks are expected for TMs with a d^3 valence, arising from excitations into the t_{2g} and e_g states. These are observed experimentally for both Li-rich NM and Li-rich NMC, located at 6,540.3 eV and 6,542.5 eV, respectively, as well as for β-MnO_2. The observed intensities differ between the layered compounds and

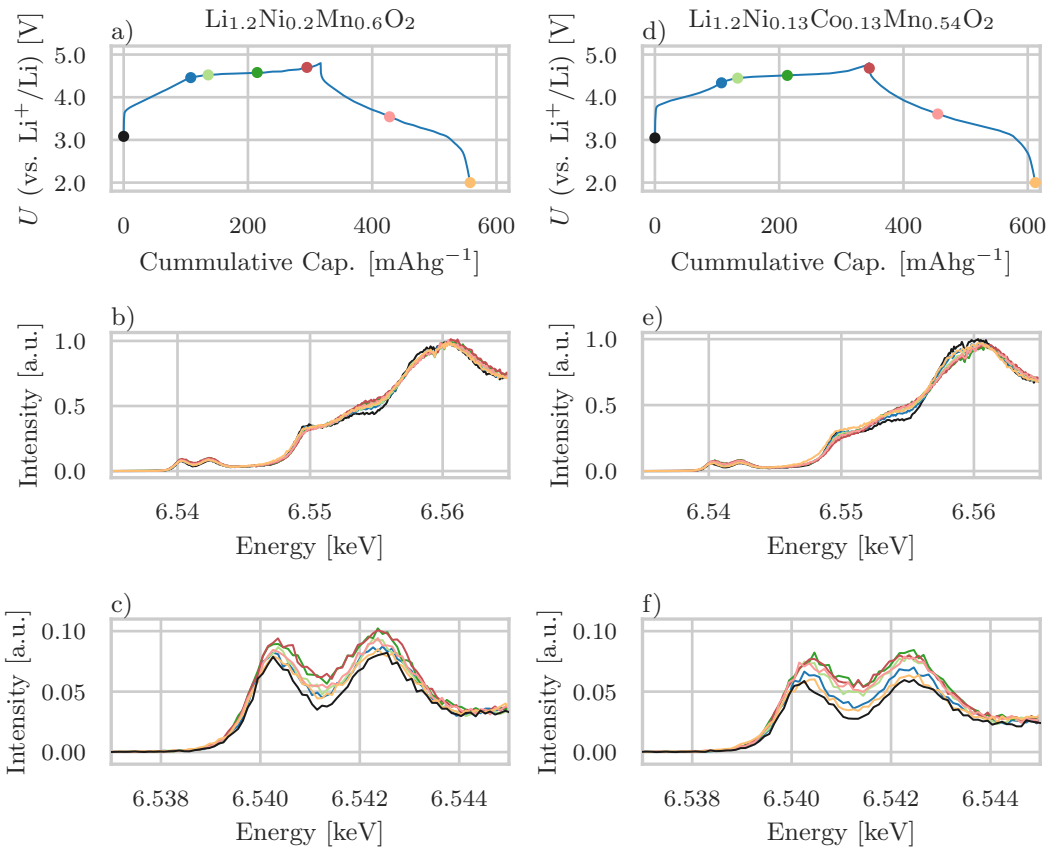


Figure 4.15: *Operando* Mn K edge HERFD-XANES for Li-rich NM and Li-rich NMC. a, d) Voltage profiles, with colour-coded dots indicating the capacities corresponding to the selected spectra. b, e) Mn K edge; c, f) Pre-edge region.

rutile β-MnO_2, likely due to the different crystal structures. The energy position of the peak for Mn_2O_3 (Mn^{3+}) is shifted to lower energies. It can therefore be assumed that Mn^{4+} is present in Li-rich NM and Li-rich NMC. Unlike for Ni and Co, no non-local excitations into hybridised states of adjacent TMs are evident in the two compounds.

Operando K edge HERFD-XANES spectra are depicted in fig. 4.15. Over the first cycle, neither the main edge nor the pre-edge positions change significantly and only slight changes of the peak intensities are observed. The pre-edge spectral area increases slightly with state of charge, and in the fully discharged compound the pristine spectrum is recovered. This is not observed for the K edge itself, where the spectrum is altered permanently, suggesting that Mn^{4+} is retained while structural changes occur.

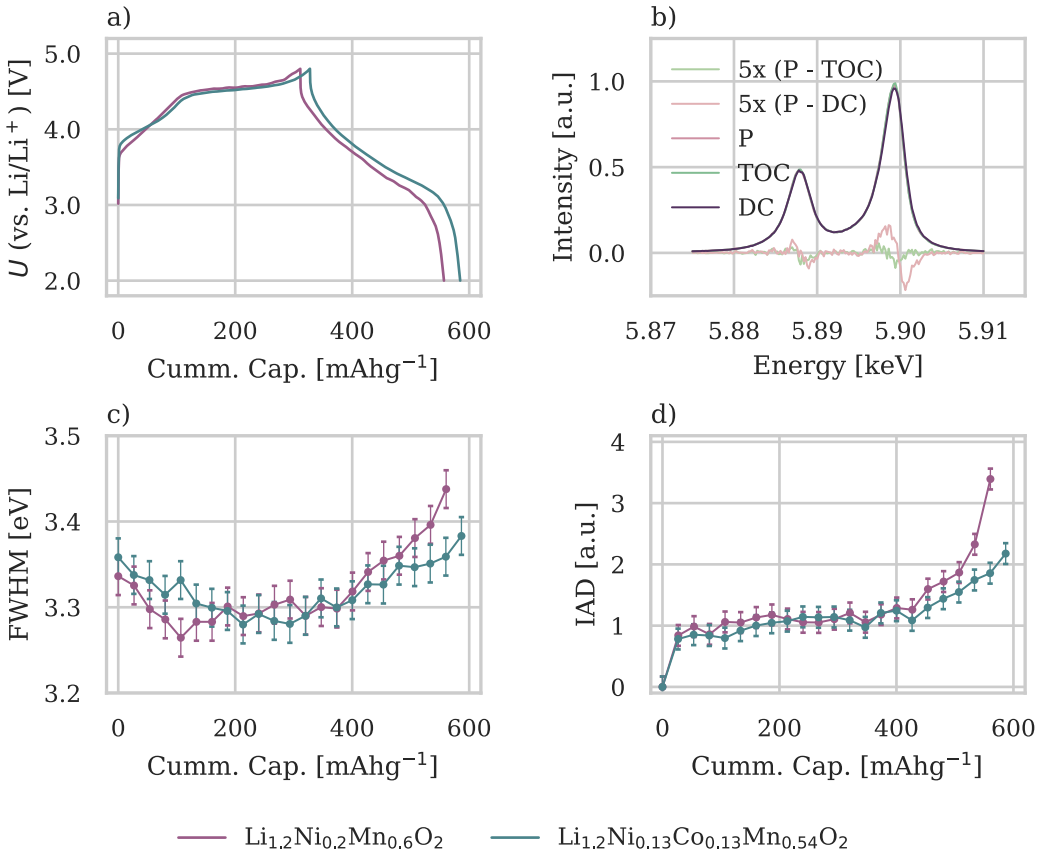


Figure 4.16: Mn K_α XES for $Li_{1.2}Ni_{0.2}Mn_{0.6}O_2$ and $Li_{1.2}Ni_{0.13}Co_{0.13}Mn_{0.54}O_2$.

To investigate this further, *operando* $K_{\alpha 1}$ XES data was obtained (fig. 4.16), which shows significant changes of the FWHM over the entire cycle. This is significant, as Mn is expected to be redox-inactive, and the spin state should not change from the initial d^3 hs (S = 3/2). During charging, the FWHM of Li-rich NM decreases until the end of region 1, where it stays approximately constant, before increasing again on discharge. For Li-rich NMC, the decrease occurs constantly until the end of region 2, followed by a monotonous decrease on discharge. As observed for Co, these changes are well correlated with the unit cell volume changes, suggesting that the difference might occur due changes of the orbital overlap.

The IADs show a sudden jump immediately on charging and then remain constant until the middle of the discharge, where they increase until the end of discharge, and are only weakly correlated with the FWHM changes. This again, suggests that the changes of the

XES spectra are not due to a change in Mn 3d spin but due to other effects. The XES data does not present a coherent picture and is too complex to be analysed qualitatively, and modelling is required.

The lack of an energy shift of the pre-edges, however, as well as the small changes of the intensies, suggest that Mn is not redox-active in either Li-rich NM or Li-rich NMC. The small changes of the XANES main edges likely arise from structural changes, as the EXAFS data show considerable activity surrounding the TMs, while the Mn-O distances remain constant.[25,148,201] These local structural changes are expected, as most O redox activity is expected surrounding Mn in these compounds.[21,22,25,44]

4.5 Summary and Discussion

There is considerable interest in the oxidation states of TMs and O in Li-rich materials.[21,22,37,44,57,202] While it is usually assumed that full TM oxidation occurs across the sloping "TM redox" region (region 1), it was shown here that this is true for $Li_{1.2}Ni_{0.13}Co_{0.13}Mn_{0.54}O_2$, but not for $Li_{1.2}Ni_{0.2}Mn_{0.6}O_2$. The latter never reaches Ni^{4+}, suggesting that more capacity is charge compensated for via O redox than previously assumed.

TM K edge HERFD-XANES and K_α XES are hard X-ray techniques that allow for truly bulk sensitive probing of the valence state population in TM oxide compounds.
For Li-rich NM and Li-rich NMC, the analysis of the pristine HERFD-XANES spectra, including the pre-edge region, could be performed qualitatively and the observed phenomena were explained through a combination of octahedral 3d crystal field theory and non-local transitions into the 3d states of adjacent TMs (indirect $1s_{TM} \rightarrow 3d_{TM'}$ transitions).[129,190–193] For *operando* spectra obtained during the first cycle, this approach was still successful for Ni and Mn, whereas for Co an analysis without modelling was not

possible. The observed oxidation states agree with the structural information, with bond lengths decreasing as the TM oxidation states increase in the spectroscopic data, and vice versa.

The XES proved harder to interpret, and seems to be more strongly affected by even small changes of the surrounding structure. This was e.g. observed for Mn, where significantly changing FWHMs and IADs of the K_α emission spectra were observed, while the XANES K pre-edge showed almost no change.

The complexities of the Li-rich systems, containing multiple, interacting TMs with changing spin states, varying lattice parameters, and changes of the ligands due to O redox and O loss, make a qualitative or semi-quantitative interpretation difficult and modelling of the electronic transitions, based on accurate structural models, is required to fully interpret this data.

Still, several conclusions about the TM oxidation state changes in the two materials can be drawn from the data, particularly based on the HERFD-XANES pre-edge regions, in conjunction with EXAFS.

It is evident that TM oxidation continues into region 2 in both compounds, mainly through Ni in Li-rich NM, and Co in Li-rich NMC, suggesting that the bands formed by hybridised TM 3d / O 2p states overlap with the one formed by the unhybridised O 2p states responsible for reversible O redox.[44,141,173] There is strong evidence that Ni^{4+} is present at the end of region 1 in Li-rich NMC, while the data for Li-rich NM suggests that the element is never fully oxidised to its tetravalent state, and only reaches its maximum oxidation state of approximately $Ni^{3.5+}$ towards the middle of the charge plateau in region 2.

A potential explanation for the different behaviour observed for the two materials, could be the tendency of Li-rich NM to form a Ni-rich surface, which is observed to a much lower extent in Li-rich NMC.[41,202–204] O loss is associated with the surface of the active material, potentially resulting in a higher fraction of O loss in the areas with high amounts of Ni,

preventing the full oxidation in Li-rich NM.[21,22,41,42] In Li-rich NMC, a larger fraction of the Ni is in the bulk, allowing it to be fully oxidised. This outlines a way forward, and the amount of surface Ni should be quantified, e.g. using secondary ion mass spectrometry (SIMS) or atom probe tomography.

The rapid oxidation of Ni in Li-rich NMC appears to correlate with a reduction in Co during the second half of region 1, as suggested by the EXAFS bond lengths, as well as the XANES and XES. The changes to the Co data, however, are small, with noise preventing a definite conclusion, but correlate well with the inflection point seen in the voltage profile, which suggests two different single-phase reactions.
The results are of particular interest, as they inform the debate about the influence of Co on layered cathode materials. It is known that Co suppresses O loss and has a beneficial influence on general cathode homogeneity.[202] The results here suggest that it also has significant influence on the redox behaviour of Ni, enabling full oxidation to Ni^{4+}, potentially due to a more homogeneous structure.

Mn appears to be redox inactive during the entire first cycle, in accordance with previous reports.[21,22] Still, significant changes of the XES spectra are observed, which warrant a closer investigation, particularly with regards to the effects of O redox, whose influence should be most prominent around Mn.

To understand all of these phenomena, an in-depth analysis of the electronic structure would be of great interest. This could be achieved through *operando* TM K edge RIXS. By fully characterising the TM spin states at certain points along the voltage profile, the exact electronic configuration could be obtained. In conjunction with calculations of the observed electronic transitions, this would greatly advance the understanding of the complex interplay between TM and O redox.

Chapter 5

The Structure of Pristine Disordered Rocksalt Li_2MnO_2F

5.1 Introduction

Disordered rocksalt compounds, such as Li_2MnO_2F, are promising materials for Li ion cathode materials, owing to their large capacities, the flexibility to accommodate different species, as well as the multitude of O redox environments not found in layered compounds.[75–84] A detailed introduction is given in sec. 1.4. The pristine structures of these compounds are still subject to discussion, as the high-energy mechanochemical ball mill synthesis creates small domains, rendering traditional long-range structure analysis techniques, such as XRD, unsuitable to investigate their details. Solving the local structures of these materials is vital to understanding the redox processes, particularly O redox.

The structure-electrochemistry relationship of O redox was introduced in sec. 1.3 and is of particular interest here. In layered structures, the symmetry of the atomic arrangement limits the amount of collinear Li-O-Li configurations per O to a number between 0 (no Li excess in TM layer) and 1 (full honeycomb with Li), controlling the amount of O redox (fig. 5.1). In disordered rocksalts, however, the disorder between the cation sites results in

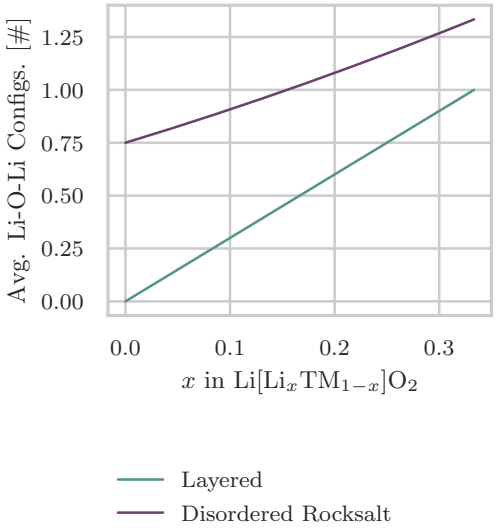


Figure 5.1: Statistically expected values for the number of collinear Li-O-Li configurations in layered and fully disordered rocksalt materials.

Li-O-Li arrangements even in stoichiometric compounds, and one configuration per O ion can be exceeded in Li-rich materials. This could have a significant impact on O redox, not only by increasing the number of redox-active Os, but by lowering the average voltage at which O redox is observed, when multiple collinear Li-O-Li configurations are present around a single O center.

Understanding the local arrangements has further implications, as the disordered structure requires a 0-TM percolation network for efficient Li diffusion, contrary to layered materials, where 1-TM networks between the sheets enable quick Li hopping. Depending on the amount of ordering on a local scale, the amount of accessible Li can vary significantly.[75]

Li_2MnO_2F exhibits capacities of up to 300 $mAhg^{-1}$ on first charge, approximately 30 % more than what is expected from TM redox alone, with a majority of it reversible.[88] The material shows broad XRD reflections that correspond to a $Fm\bar{3}m$ structure, and ^{19}F and ^{7}Li NMR data suggest that the chemical environments around the ions change after ball milling, demonstrating that it has a disordered rocksalt structure and is not a nanoscale mixture of the reactants.[88] Details of the local structure, however, are not well understood.

Pair distribution function (PDF) is a powerful tool for investigating the structure of matter and is described in detail in sec. 2.4.2. The technique treats the Bragg reflections and diffuse scattering equally, ultimately generating the PDF, a scattering power-weighted histogram of the interatomic distances. It therefore contains information on the immediate coordination environments, as well as the crystal structure, making it particularly useful for investigating disordered structures.[113–115,205–212] In conjunction with Reverse Monte Carlo (RMC), an approach for fitting complex, low-symmetry structures to experimental data, it can be used to analyse local environments with high precision.[117–119,209,210,213–215] The following chapter provides an in-depth analysis of the long-range and local structure of Li_2MnO_2F and investigates Li accessibility and O redox.

5.2 Experimental

Material Synthesis Li_2MnO_2F cathode material was prepared by Robert House via a mechanochemical ball-milling route. LiF (Sigma Aldrich, 99.995 %), Li_2O (Alfa Aesar, 99.5 %), and Mn_2O_3 (Sigma Aldrich, 99.9 %) were mixed in a 2:1:1 ratio in a mortar and pestle for 5 min in a glovebox (O_2 & H_2O < 0.1 ppm). The mixture was then transferred into a ZrO_2 ball-mill jar filled with 5 mm ZrO_2 balls, and hermetically sealed. The mixture was reacted in a planetary ball mill (Fritsch Pulverisette 7) at 750 rpm for 18 h total milling time, split into cycles consisting of 5 min milling, and 10 min pauses in between. Every six hours the powder was removed from the ball mill jar in a glovebox and mixed using mortar and pestle, to ensure homogeneity, as the reactants tended to stick to the walls of the jar.

Transmission Electron Microscopy Transmission electron microscope (TEM) images were collected by Shengda Pu on a JEOL JEM-300F instrument at 300 kV. Samples were prepared by the author by dispersing cathode powder in dimethyl carbonate (dried over a molecular sieve) in a glovebox (O_2 & H_2O < 0.1 ppm), and drop-casting the suspension onto a holey carbon TEM grid (Agar Scientific Ltd.). The samples were loaded onto a

special TEM sample holder for air sensitive samples in a glovebox, that prevented exposure to air during transfer into the TEM. The TEM was calibrated using a Pt standard sample. Electron PDF was extracted from electron scattering patterns by Konstantin Borisenko. The resulting PDFs were normalised to both the M-M/Anion-Anion and M-Anion peaks, as the attenuation due to varying thicknesses prevents other forms of normalisation.

Mn K Edge XANES Mn K edge XANES spectra were obtained for the as prepared material on beamline B-18 at Diamond Light Source, Didcot, UK. The XANES energy was controlled using a Si(111) double-bounce monochromator, and the energy was calibrated using a Mn foil. Data processing, including pre-edge subtraction and normalisation was performed as described in sec. 2.6 using the Athena package.[185] Mn HERFD-XANES spectra for the references were collected on beamline ID26 at the European Synchrotron Radiation Facility (ESRF), Grenoble, France. The incident beam was monochromatised using a cryogenically-cooled Si(311) crystal double bounce set-up, and tuned through the edge. The beam energy was calibrated using an Fe foil. Data was collected using four spherically bent Ge(333) crystals, arranged with the sample and an avalanche photodiode detector in a vertical Rowland geometry with a radius of 1 m. HERFD-XANES measurements were collected using the maximum of the Mn $K_{\alpha 1}$ emission line and data processing was performed using custom code written in Python3. The collected spectra were normalised using the spectral area between 6.530 - 6.630 keV.

Powder X-ray Diffraction Powder X-ray diffraction (XRD) patterns were collected on beamline I11, Diamond Light Source, Didcot, UK. The samples were loaded into borosilicate glass capillaries inside an Argon filled glovebox (O_2 & H_2O < 0.1 ppm), and sealed with epoxy. After removal from the glovebox the capillaries were flame sealed. XRD patterns were collected using a position-sensitive detector and radiation set to a wavelength of 0.82496 Å using a double-bounce Si(111) monochromator.

Data was analysed using the Rietveld method as implemented in the GSAS package, using the EXPGUI interface.[216,217] Instrument parameters were obtained by fitting a Silicon

standard. To analyse the Li_2MnO_2F structures, a statistically populated disordered rocksalt unit cell ($Fm\bar{3}m$) was fitted against the experimental data. A background function, lattice parameter a, as well as the peak shape and isotropic displacement factors U_{iso} were refined, while the fractional coordinates and occupancies were not changed.

Neutron Diffraction Neutron diffraction patterns were collected by James Somerville on the Spallation Neutron Source's NOMAD instrument at the Oak Ridge National Laboratory, Oak Ridge, TN, USA, using ~2 g of powder in vanadium cans.[218] The data was normalised against a Vanadium rod and background subtracted.

Neutron diffraction patterns of three detector banks were used to refine the structure via the Rietveld method as implemented in the GSAS package, using the EXPGUI interface.[216,217] Instrument parameters were provided by NOMAD, and remained fixed during the fitting. A statistically populated disordered rocksalt unit cell ($Fm\bar{3}m$) was used. A background function, lattice parameter a, as well as the peak shape and isotropic displacement factors U_{iso} were refined, while the fractional coordinates and occupancies were not changed.

Neutron Pair Distribution Function Neutron total scattering data was collected by James Somerville on the Spallation Neutron Source's NOMAD instrument at the Oak Ridge National Laboratory, Oak Ridge, TN, USA, using ~2 g of powder in vanadium cans.[218] The data was normalised against a Vanadium rod and background subtracted.

The total scattering function $S(q)$ was Fourier transformed up to q_{max} = 20 Å, using software developed for the NOMAD instrument, to generate $G(r)$.[218] 'Rietveld'-like fitting of $G(r)$ was performed using the PDFfit2 program as implemented in the PDFGUI frontend.[212,219] Instrument parameters were provided by NOMAD and remained fixed. The data was fit between 0.5 - 15 Å using a statistically populated disordered rocksalt unit cell ($Fm\bar{3}m$) with the crystallite size fixed to 5 nm, as suggested by TEM and $G(r)$ attenuation. A scale factor, the lattice parameter a, and isotropic displacement factors U_{iso} were refined,

while the fractional coordinates and occupancies were not changed.

Reverse Monte Carlo Fitting Reverse Monte Carlo (RMC) fitting was performed using the RMCProfile program package (Version 6.7.0).[118,119] Supercells were created from the unit cell obtained via the previously described refinement against neutron diffraction data, with randomly occupied cation and anion sites, according to the Li_2MnO_2F stoichiometry. The neutron $G(r)$, $S(q)$, and diffraction patterns obtained on NOMAD were simultaneously fit.

Distance window constraints of 1 Å between cations and anions and 2 Å for ions of the same polarity were used, to prevent the algorithm from fitting low amounts of short-distance artefacts of similar ions. To eliminate any influence of the starting configuration on the fit, the atoms were swapped randomly on the cation and anion sites, respectively, for ten minutes. This resulted in about 600,000 moves being performed, and ensured a random starting configuration for each run. For each fit the algorithm was first run for 180 mins with a maximum allowed movement window of 4.5 Å for all ions, forcing the atoms to predominantly stay on their sites but cause peak broadening in the calculated spectra. This ensured a good fit of the average structure, before the calculation was subsequently run for 1260 mins with a distance window of 10 Å, allowing the structure to disorder fully. Cation-cation and anion-anion swaps, where the ions switch their crystallographic sites, were allowed throughout, and were performed for 20 % of all moves. This provides the possibility of forming clusters of similar atoms, should they be suggested by the data. The total runtime was 24 h, resulting in about $16{\cdot}10^6$ generated moves. Convergence was monitored via χ^2 criteria, and visual inspection of the respective fits. Several trials with different weightings for the individual datasets were performed, to find values that enabled an adequate fit quality of $G(r)$, without compromising the long-range order.

Analysis of the RMC-Fit Structures Bond length and nearest neighbour analysis was performed using custom scripts implemented in the Python3 programming language and using the Python Materials Genomics library (pymatgen), which accounts for the

translational symmetry of the supercell.[220] Due to the strongly disordered rocksalt structure (and no evidence of tetrahedral sites in the fit structure), the first-shell coordinating ions of a given centre were determined by finding the six closest neighbours of opposite polarity to the centre. Similarly, the second shell species were obtained by identifying the twelve closest ions of the same polarity. The resulting dataset contained, for each ion, an entry with an individual identifier, its species, Cartesian coordinates, along with lists of the identifiers of the first two coordination shells.

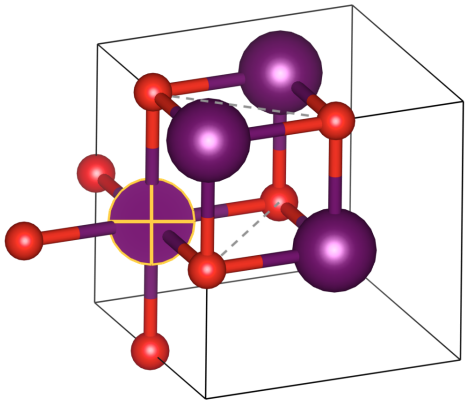


Figure 5.2: Section of a rocksalt unit cell. Red: Anions; Purple: Cations. The central site is highlighted.
The tetrahedral site formed by four of the anions is indicated via the grey dotted lines. The first- and second-shell neighbour relationships for the outlined in the text can be observed.

This data allowed for analysis of the percolation network, by identifying the 14 anions A forming the tetrahedral sites surrounding each Li centre. Using the nearest-neighbour data, the four anions per tetrahedral site have to fulfil the following two criteria (fig. 5.2):

1. Three anions are first-shell neighbours of the Li centre, and are therefore found in its first-shell neighbour list. One is not.

2. All four anions have to be one-another's second-shell neighbours, and are therefore contained within the others second-shell neighbour lists.

This was implemented by iterating through each of the six first-shell anions A for a given Li. For each A, the four closest ligands A', that are contained within the Li's first-shell neighbours, were found. Together, these five ligands span half of the coordinating octahedron surrounding the Li, and are part of four of the eight tetrahedral sites. For each

tetrahedral site, three of its four *A* are contained within these five ligands. By repeatedly fixing one *A*, and iterating through the other four, the three approximately orthogonal ligands were found by evaluating if they conform to criterion 2. The fourth ligand was then found by iterating through each *A*'s second-neighbour lists and evaluating the contained species with regards to the criteria outlined above. During this process, it was not discriminated between O^{2-} and F^{-}.

For each tetrahedral site, the adjacent cation species were found via a similar approach, based on the following criteria:

1. All cations surrounding a tetrahedral site are contained within the first-shell neighbour lists of (only) three of the anions.
2. All cations surrounding a tetrahedral site have to be contained within the second-shell neighbour lists of one another.

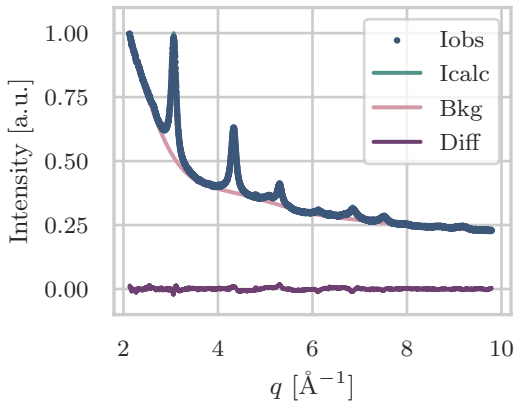
This logic-based approach was found to be very robust at identifying the nearest neighbours, and performed significantly better than bond angle or symmetry approaches. This is mainly based on the fact that no quantitative cutoffs (e.g. a bond length maximum, or angle range) need to be used. The approach hence adapts easily to the strong disorder.

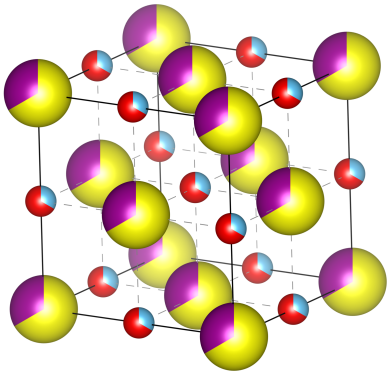
5.3 Long-Range Order

The long-range order of as-prepared Li_2MnO_2F was investigated via synchrotron XRD (fig. 5.3). The pattern shows significantly broadened peaks that can be fit satisfactorily with a statistically populated rocksalt structure (space group $Fm\bar{3}m$), in close agreement with literature.[88]

Owing to the weak X-ray scattering power of Li, neutron diffraction was additionally performed. The technique can distinguish between Li and Mn, due to the different coherent scattering lengths.† This is not the case for the anions, which scatter neutrons very similarly.

†The neutron scattering lengths are: b_{Li}: -1.90; b_{Mn}: -3.72; b_O: 5.803; b_F: 5.654.[221]

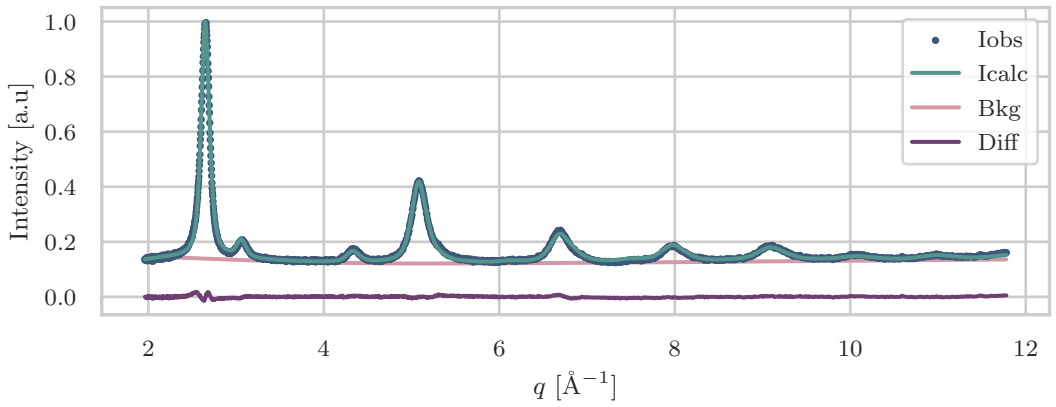




Wyckoff Pos.	Atom	x	y	z	Occ.	U_{iso}
4a	Li	0.0	0.0	0.0	0.667	0.0071
4a	Mn	0.0	0.0	0.0	0.333	0.0071
4b	O	0.5	0.5	0.5	0.667	0.0071
4b	F	0.5	0.5	0.5	0.333	0.0071

Composition: Li_2MnO_2F; Space group: $Fm\bar{3}m$; Lattice constant: a = 4.1021(5); Fit quality: χ^2 = 3.268.

Figure 5.3: XRD pattern and Rietveld fit of Li_2MnO_2F (top left), with corresponding unit cell (top right: Li: Yellow, Mn: Purple, O: Red, F: Blue.) and fit parameters (bottom).



,

Wyckoff Pos.	Atom	x	y	z	Occ.	U_{iso}
4a	Li	0.0	0.0	0.0	0.667	0.0146
4a	Mn	0.0	0.0	0.0	0.333	0.0146
4b	O	0.5	0.5	0.5	0.667	0.0146
4b	F	0.5	0.5	0.5	0.333	0.0146

Composition: Li_2MnO_2F; Space group: $Fm\bar{3}m$; Lattice constant: a = 4.1031(1); Fit quality: χ^2 = 5.075.

Figure 5.4: *Ex-situ* neutron diffraction pattern and Rietveld fit of pristine Li_2MnO_2F.

The diffraction pattern and Rietveld fit are presented in fig. 5.4. The refined unit cell is in close agreement to the XRD results and has a similar fit quality. This suggests that the average structure of the material is well described by a rocksalt structure with randomly populated anion and cation sites.

5.4 Morphology, Short-Range Order, and Local Structure

To investigate the morphology and crystallinity of the pristine compound, transmission electron microscopy (TEM) images were collected at several magnifications (fig. 5.5). It can be seen that the material consists of larger particles with sizes in the range of 50-300 nm, and clear lattice fringes are visible throughout the structure, arising from crystallites with sizes of ~5 nm. The crystallinity appears to be maintained up to the edge of the grains.

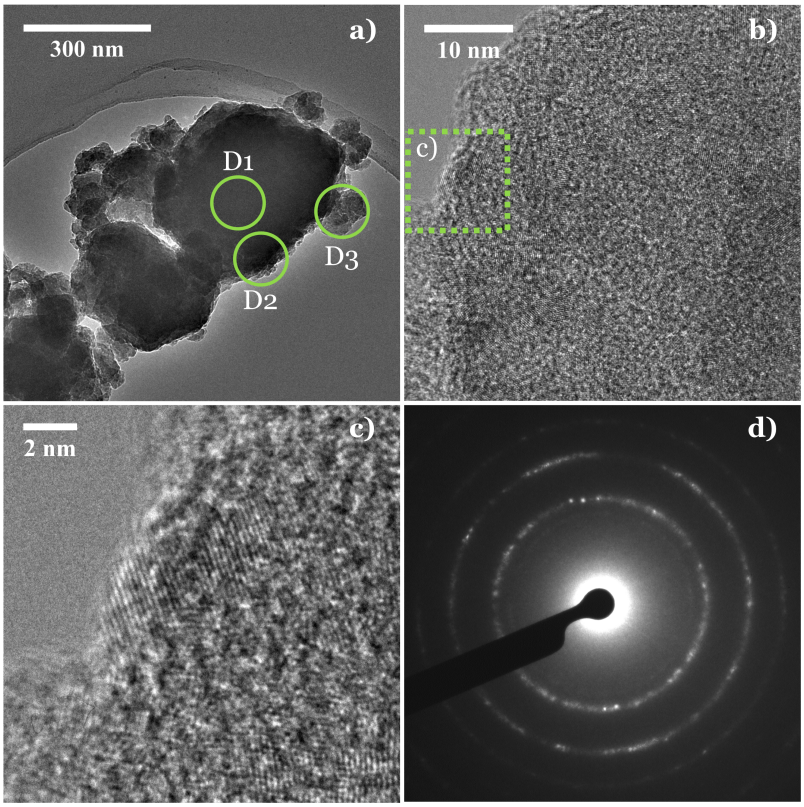


Figure 5.5: TEM images obtained for pristine Li_2MnO_2F.
a) Picture of typical grains, with SAED locations indicated by green rings. Obtained lattice constants: D1: 4.293 Å, D2: 4.287 Å, D3: 4.252 Å.
b) Selection of a particle with lattice fringes visible throughout.
c) Detail of b) with lattice fringes visible up to the edge of the particle.
d) Example SAED pattern.

To determine the lattice constants at different points of the grains, selected area electron diffraction (SAED) patterns were collected at various locations (D1-D3 in fig. 5.5). The patterns show that the material is polycrystalline, exhibiting rings with bright spots, which correspond to a rocksalt structures, that show a spread of lattice parameters around a = 4.275 Å. This is slightly larger than observed via XRD, but observed consistently in all SAED samples, and is attributed to an offset in the calibration of the TEM. The variations between individual TEM patterns however, are consistent and suggest inhomogeneity of the structure at the local scale.

To further analyse this inhomogeneity, electron pair distribution function was obtained from the SAED patterns, and the PDFs derived for locations D1-D3 are displayed in fig. 5.6. As electron PDF is difficult to normalise, due to the lack of information on the local composition, the data was normalised once to the metal-anion peak (M-A peak; ~2.1 Å), as well as the M-M / A-A peak at ~3.0 Å, respectively. The PDFs show clear differences in peak intensities and positions, supporting the hypothesis that disorder exists on a local scale. In all PDFs, the M-M / A-A peaks are very similar, suggesting that the distances are in close agreement throughout, while the M-A bond distances vary, indicating that there is a spread of local M-A coordination environments within the material.

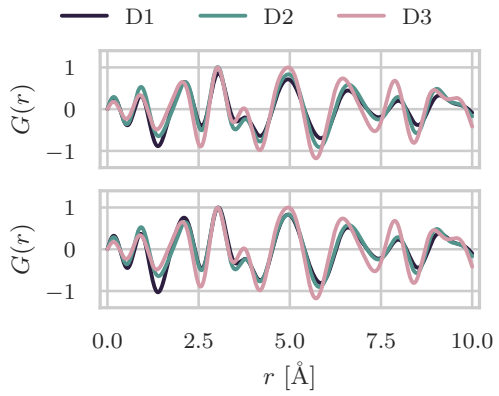
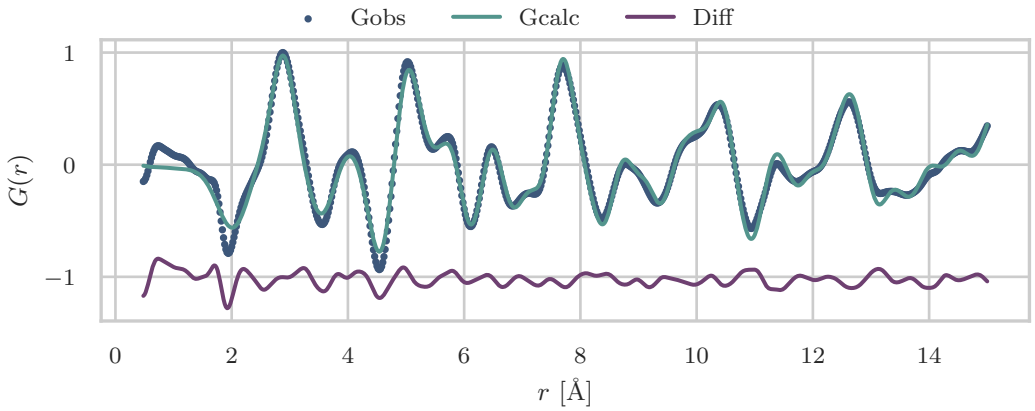


Figure 5.6: Electron PDF obtained for SAED collected at the areas depicted in fig. 5.5 a). Top: Normalised to first M-O/F-peak. Bottom: Normalised to first M-M-peak.

Neutron-based PDF is sensitive to Li and can be used to identify the Li sites, due to the



Wyckoff Pos.	Atom	x	y	z	Occ.	U_{iso}
4a	Li	0.0	0.0	0.0	0.667	0.0258
4a	Mn	0.0	0.0	0.0	0.333	0.0258
4b	O	0.5	0.5	0.5	0.667	0.0258
4b	F	0.5	0.5	0.5	0.333	0.0258

Composition: Li_2MnO_2F; Space group: $Fm\bar{3}m$; Lattice constant: a = 4.1025(8); Fit quality: R_{wp} = 0.178824.

,

Figure 5.7: *Ex-situ* neutron PDF and 'Rietveld - like' fit of pristine Li_2MnO_2F.

significantly different scattering lengths for the involved cations.[†] In fig. 5.7 the neutron $G(r)$ for Li_2MnO_2F is presented. A statistically populated rocksalt structure provides a good fit to the data (R_w values ≤0.3 are considered adequate for PDF), and is in close agreement with the values obtained for XRD and neutron diffraction. The M-A peak (~2 Å), however, is poorly fit, demonstrating that this average structure does not capture the local environments well.

Tetrahedral Manganese None of the results indicate the presence of occupied tetrahedral sites, which could be present due to the high-energy synthesis. X-ray and electron techniques, however, are not suitable for detecting low amounts of Li, and PDF suffers from increased Fourier noise in the low-r regions, potentially masking a small peak around ~1.5 Å. The pre-edge region of the TM K edge XANES spectra is highly sensitive to the presence of tetrahedral species, as the broken inversion symmetry greatly increases the probability for excitations to hybridised 3d/4s states. In fig. 5.8 the Mn K edge spectra for pristine Li_2MnO_2F are depicted, together with HERFD-XANES spectra for Mn_2O_3 (Mn^{3+}) and MnO_2 (Mn^{4+}) in octahedral environments. The low intensity of the pre-edge in Li_2MnO_2F, as well as the peak positions which fit well with those of Mn_2O_3, suggest that Mn is octahedrally coordinated and in a trivalent oxidation state, as expected from the stoichiometry and average structure.

[†]The coherent scattering lengths are: b_{Li} : −1.90; b_{Mn} : −3.72; b_O : 5.803; b_F : 5.654.[221]

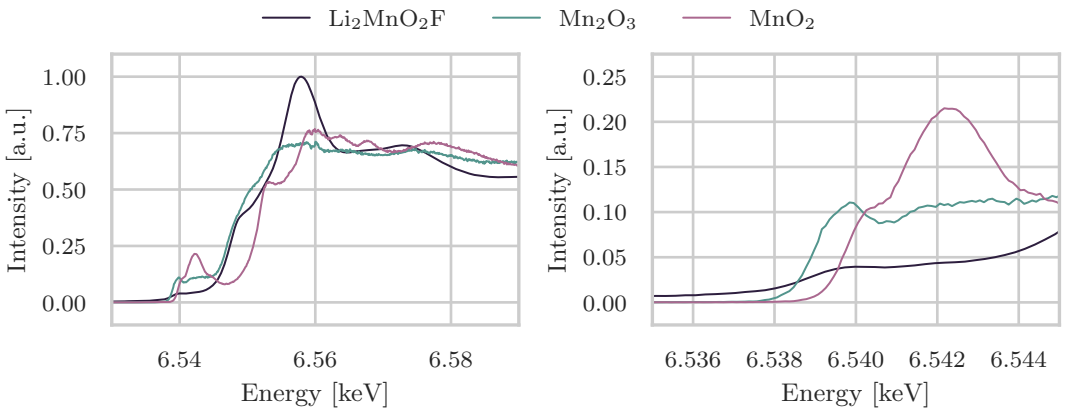


Figure 5.8: Mn K edge XANES Spectra for Li_2MnO_2F (transmission XANES) and reference compounds (HERFD-XANES): Left: K edge; Right: Pre edge region.
The peak positions of the Li_2MnO_2F pre edge correspond well with those of Mn_2O_3, and the low intensity suggests that all Mn is octahedrally coordinated.

5.5 Combined Reverse Monte-Carlo Refinement of Neutron PDF and Diffraction Patterns

To combine the information of the previous paragraphs and understand the local coordination environments and distortions, a combined RMC fit of the neutron PDF and diffraction data was performed. The RMC method is capable of introducing large degrees of disorder, provided this is supported by the data, making it a suitable tool for the analysis of the local structure.

5.5.1 Fit Parameters and Constraints

A 10 x 10 x 10 supercell with 8000 atoms and randomly populated anion and cation sites, according to the stoichiometry of Li_2MnO_2F, was created. The dimensions of the cell were based on the neutron diffraction refinement and the supercell lattice parameter a = 41.031 Å is close to the domain size in the material (~50 Å), to enable a representative fit of the disorder.

The neutron $G(r)$, the reduced scattering function $S(q)$, and the neutron diffraction data were fit simultaneously, with the latter used to prevent the RMC algorithm from

overfitting the PDF data. The explicit introduction of long-range order ensures that the sum of the local environments correspond to the average structure of the material, and leads the algorithm to converge on a physically meaningful result.[118,119] Fits without the explicit inclusion of the Bragg pattern lead to non-physical results.

A total of eight fits was performed, each capturing a 'snapshot' of the structure, and the results averaged.

5.5.2 Fit Results

The RMC calculations converged to fit strongly disordered rocksalt structures (fig. 5.10) An example fit is depicted in fig. 5.9. The fit quality of the $G(r)$ is improved significantly, compared to the 'Rietveld-like' refinement, particularly in the region around the M-A- (~2 Å) and M-M/A-A peaks (~3 Å), indicating that the fitted structure captures the local coordination environments significantly better. The fit qualities of $S(q)$, as well as the diffraction pattern are acceptable. The slightly worse diffraction pattern fit is due to the weighting of the datasets in the fit, where $G(r)$ was weighted more highly, to ensure a good fit of the local structure, whilst the diffraction data was weighted less heavily, to act only as a constraint. $S(q)$ was weighted very low, as it contains large amounts of high-noise data in the high q regions. The Bragg reflection positions observed in the calculated $S(q)$, however, fit well with the experimental data.

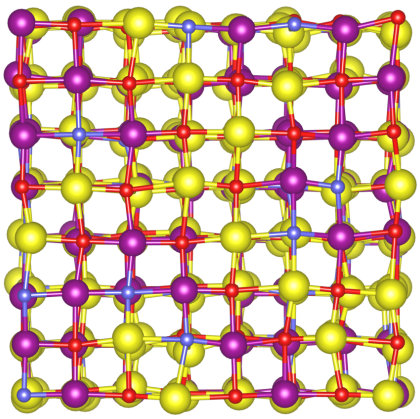


Figure 5.10: View along [100] of a section of a RMC-fit structure of pristine Li_2MnO_2F, showing the disordered rocksalt structure of the material.
Li: Yellow; Mn: Purple; O: Red; F: Blue.

A bond length distribution is depicted in fig. 5.11. Shorter M-A distances than obtained

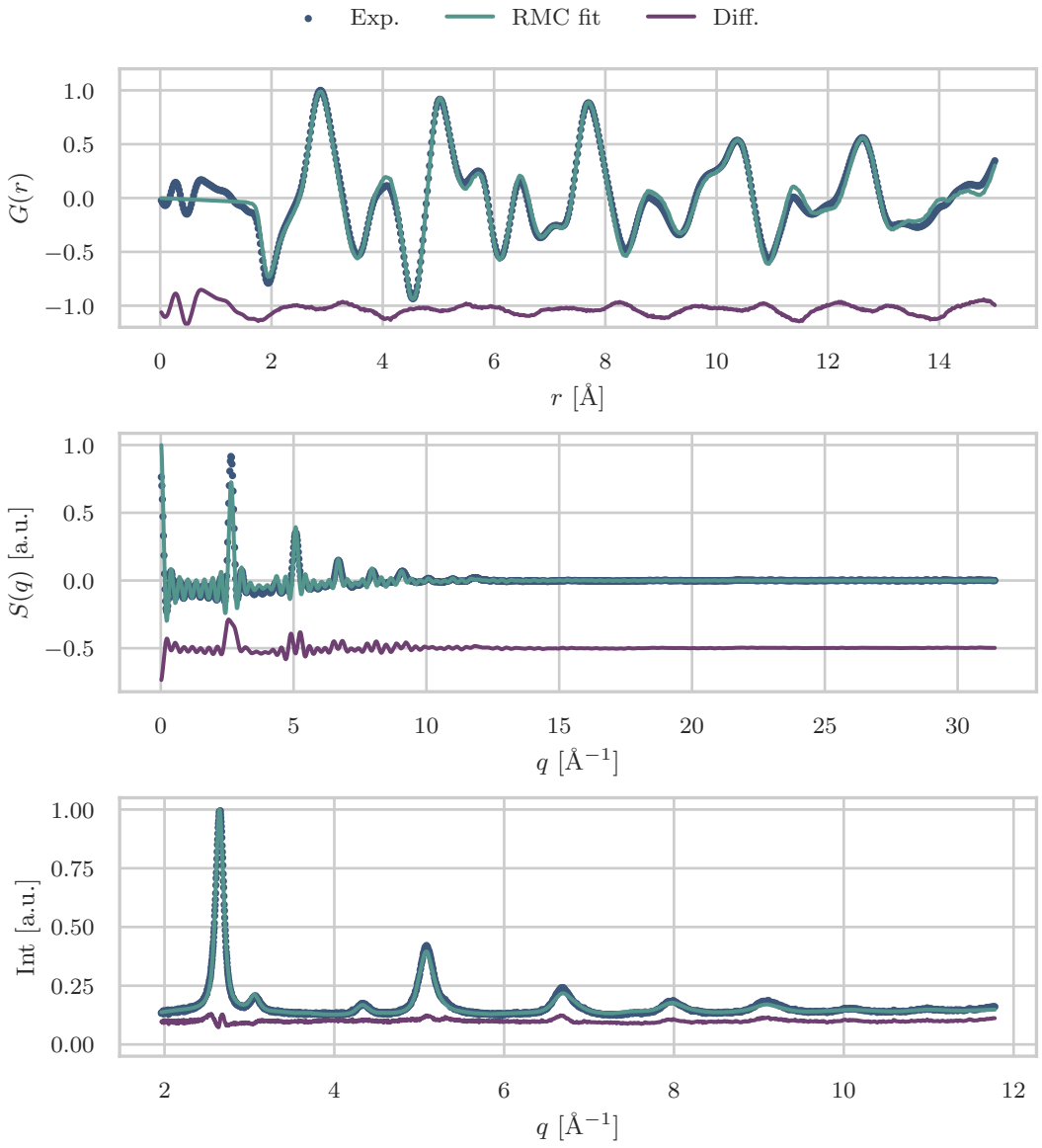
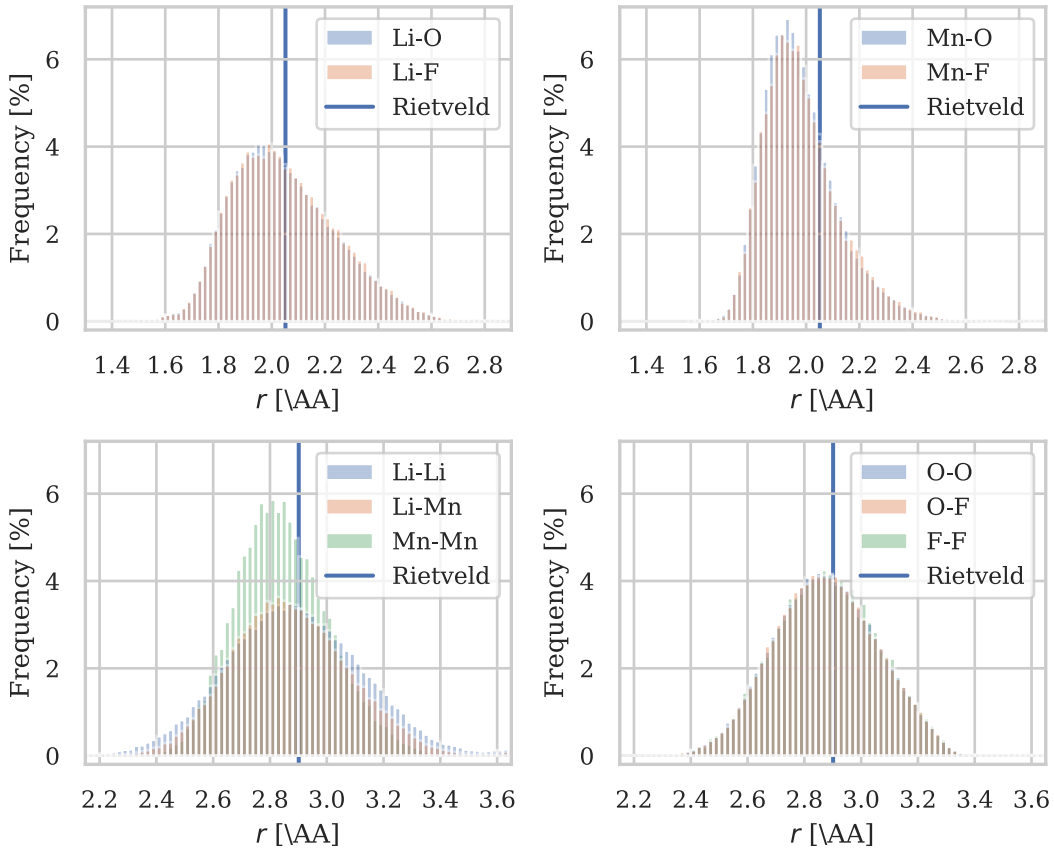


Figure 5.9: RMC Fit for neutron $G(r)$ (top), $S(q)$ (middle), and diffraction (bottom) of pristine Li_2MnO_2F.



Bond	RMC Bond Length [Å]	Std. Deviation [Å]	Rietveld* - RMC [%]
Li-O	2.046	0.197	-0.56
Li-F	2.049	0.198	-0.22
Mn-O	1.980	0.142	-7.15
Mn-F	1.984	0.144	-6.71
Li-Li	2.881	0.229	-2.05
Li-Mn	2.871	0.202	-2.98
Mn-Mn	2.844	0.164	-5.76
O-O	2.876	0.182	-2.54
O-F	2.876	0.181	-2.52
F-F	2.879	0.182	-2.23

* For reference: Rietveld fit: M-A: 2.0515 Å; M-M / A-A: 2.9013 Å.

,

Figure 5.11: Bond length distributions in pristine Li_2MnO_2F, obtained via RMC, compared to values obtained via Rietveld fitting against neutron diffraction data.

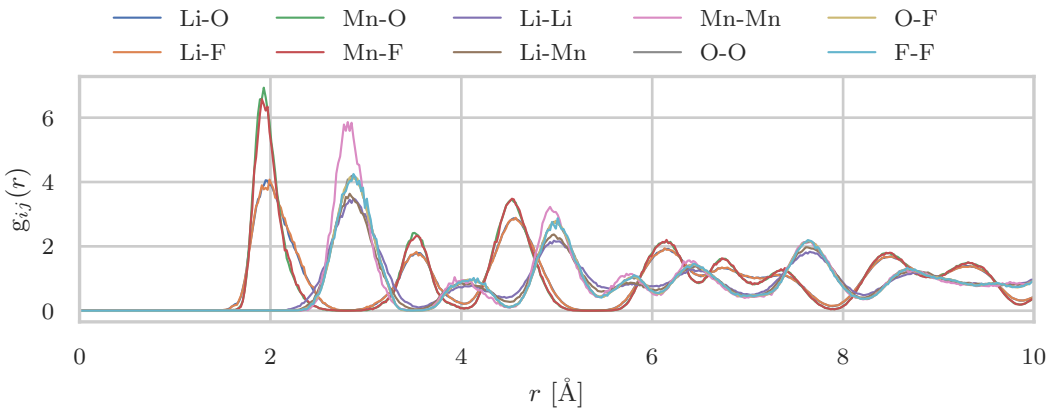


Figure 5.12: Partial pair correlation functions $g_{ij}(r)$ in pristine Li_2MnO_2F

via Rietveld fits are observed, with strongly skewed bond distance distributions, explaining the significantly improved fit of the PDF around ~2 Å. The distribution of the Mn-A bonds is much more narrow, compared to Li-A, suggesting that the Mn ions occupy more well-defined environments.

A narrow distribution and shorter distances are also observed for the Mn-Mn distances, whereas the Mn-Li and Li-Li distances show broad distributions and larger mean values. The A-A distances are distributed in an approximately Gaussian shape around a value close to the average value obtained from Rietveld fitting, and have almost identical distributions. The partial pair distribution functions $g_{ij}(r)$ (fig. 5.12), show that the small differences subside after ~8 Å for all sublattices, and the A-A and M-M, and A-M peaks merge, respectively.

Even though the difference in coherent scattering lengths for O and F is small, some differences should be observable, on average. Outside of a small preference for four F to coordinate Li, there seems to be little preference for either anion to coordinate a certain metal (fig. 5.13), and the distribution closely follows what is expected from a binomial distribution with $p_{Li} = 2/3$, and $p_{Mn} = 1/3$.

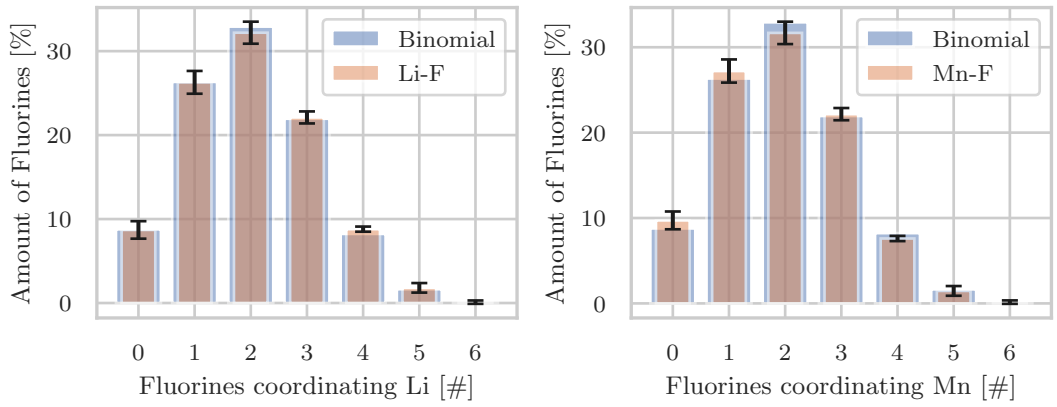


Figure 5.13: Histograms of the cation coordination with fluorine in Li_2MnO_2F, compared to the estimate for a binomial distribution (p_{Li} = 2/3, and p_{Mn} = 1/3). Error bars indicate 95 % confidence intervals for the observed values.

To quantify the short-range order in a system with two species, the Warren-Cowley parameter α^{kl} can be used.[215,222,223] It is defined as:

$$\alpha^{kl} = 1 - \frac{p^{kl}}{c_k} = 1 - \frac{p^{lk}}{c_l} \qquad (5.1)$$

Table 5.1: Average Warren-Cowley parameters and 2·standard deviations σ (95 % confidence interval) obtained for RMC-fit Li_2MnO_2F.

A-B	α^{kl}	2·σ
Li-Mn	0.07	0.012
O-F	0.004	0.022

where k and l are the two species, α^{kl} is the Warren-Cowley parameter for species centred at k, and l is located in the shell that will be analysed. p is the fraction of actually present l in the shell, and c is the theoretical concentration, equal to the statistical probability of finding the respective species in the next shell assuming random occupation (e.g. c_{Li} = 2/3, and c_{Mn} = 1/3 for Li_2MnO_2F). α^{kl} = 0 for a solid solution, where the species are randomly distributed, $1 \geq \alpha^{kl} > 0$ if there is a clustering of similar species, and $\alpha^{kl} < 0$ if there is a preference for dissimilar species.

Although Li_2MnO_2F has a total of four elements, the approach can be used to assess the disorder in the cation and anion lattices, respectively. Warren-Cowley parameters were calculated for all fit structures, and the average values and standard deviations are presented in tab. 5.1. The averaged values are close to zero, demonstrating the statistical occupation of

the cation and anion sublattices, respectively.

5.5.3 Percolation Network Analysis

As discussed in sec. 1.4.2, percolation theory predicts that a network of octahedral Li sites, connected by tetrahedral sites with no coordinating TMs (0-TM sites), is formed in Li-rich disordered rocksalt compounds, enabling facile Li movement.[75]

To assess the amount of Li connected via a 0-TM percolation network in Li_2MnO_2F, the degree of connectivity between all adjacent octahedral Li sites was analysed, as discussed in the experimental section. Sites were determined to be 'connected' with one another if they shared at least one 0-TM tetrahedral site and furthermore determined to be part of the percolation network, if a direct path through 'connected' sites could be established to one of the outermost Li sites of the supercell.

The average results for the RMC-fit supercell show that ~1.75 Li (87 %) are accessible in the pristine material (fig. 5.14), which is in good agreement with percolation theory, which predicts ~1.8 Li to be accessible.[75] Interestingly, almost all Li that is connected to a 0-TM site, is connected to the percolation network, and almost no isolated clusters of 0-TM-connected sites exist. The percolation network within Li_2MnO_2F explains the large amount of Li that can be extracted from the compound (~1.4 mols / 300 $mAhg^{-1}$ up to 4.8 V), but also suggests that additional Li could be extracted, up to a theoretical capacity of ~390 $mAhg^{-1}$, compared to 447 $mAhg^{-1}$ full Li extraction capacity.

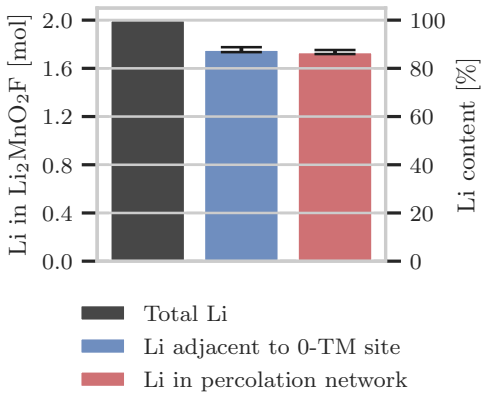


Figure 5.14: Percolation network and accessible Li in Li_2MnO_2F. Error bars indicate 95 % confidence intervals for the observed values.

5.5.4 Oxygen Redox Environments in Li_2MnO_2F

O redox depends on the presence of collinear Li-O-Li configurations, in which the poor overlap between Li and O states results in an electrochemically-accessible O 2p state (sec. 1.3).[21,22,44] Owing to the disorder of the RMC-fit structure, the criterion for collinear Li-O-Li configurations was expanded, to include Li that occupy the required sites but have Li-O-Li angles that deviate from 180°. A plot of these angles shows that the data fall into two groups, as expected (fig. 5.15). Interestingly, the high-angle group is not centered around 180°, and exactly collinear Li-O-Li configurations seem to be unfavourable. For the analysis of O redox, the group with angles exceeding 150° were assumed to be redox-active.

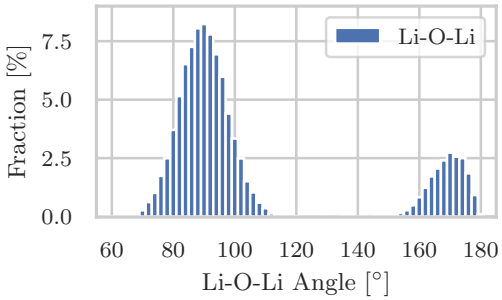


Figure 5.15: Li-O-Li bond angle distribution obtained for the RMC-fit structure of Li_2MnO_2F.

For each O in the structure, the total number of coordinating Li, as well as the number of them fulfilling the O redox criterion were obtained, and the values are depicted in fig. 5.16.

The distribution of Li around O closely follows a binomial distribution with $p_{Li} = 2/3$, and $p_{Mn} = 1/3$, which would be expected for a perfectly statistical population (or if the scattering difference between O and F were zero). Within the bins for 0 - 3 Li coordinating O, the number of Li-O-Li configurations is slightly higher than expected statistically.
For O, coordinated with four Li, it is expected that four times more sites with single Li-O-Li configurations, compared to two Li-O-Li, are observed. Experimentally, a ratio of 9:1 is observed, indicating that there is a penalty associated with locating four O in the same plane as the Li, likely due to the larger size of the O^{2-} ion.[224]

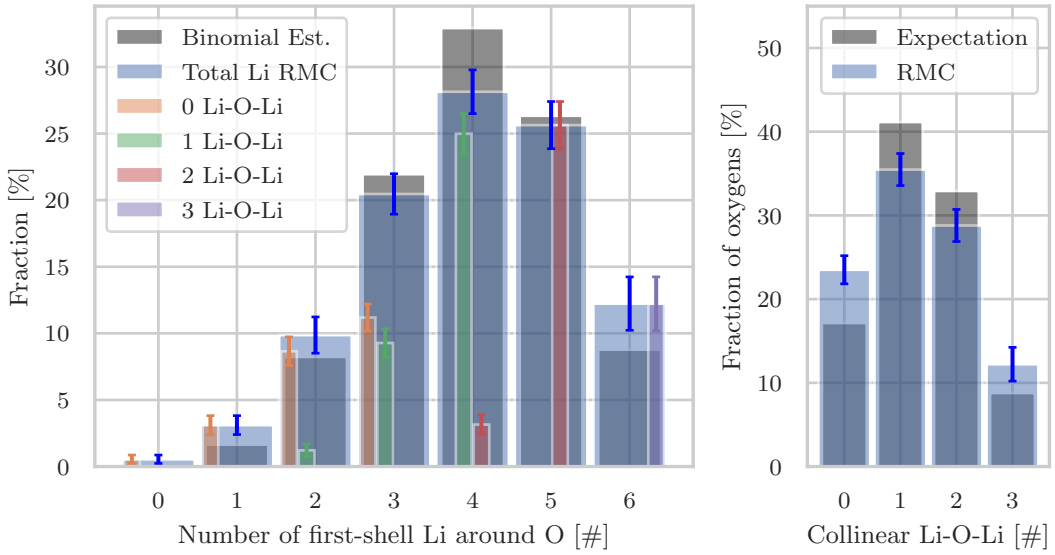


Figure 5.16: Oxygen coordination environments in pristine Li_2MnO_2F. Error bars indicate 95 % confidence intervals for the observed values.
Left: Distribution of Li around O in the Li_2MnO_2F structure (blue, grey), along with their fraction in collinear Li-O-Li configurations (other colours). The small colourbars indicate the kind and fraction of collinear Li-O-Li configurations for each case. Binomial distribution for $p_{Li} = 2/3$, and $p_{Mn} = 1/3$.
Right: Fraction of O vs. number of collinear Li-O-Li configurations, with calculated expected values for a random distribution.

The lower than expected total number of O coordinated with four Li, as well as the low number of Li-O-Li arrangements, results in a lower than expected total number of Os with one and two Li-O-Li configurations (fig. 5.16). There are, however, almost 1.5 times more O with a sixfold Li coordination than expected, which result in three Li-O-Li configurations on a single O. These O are likely redox-active at a low potential, and the ones at the surface should be liable to O loss due to underbonding, when all coordinating Li are extracted.[225] On average, 1.30 collinear Li-O-Li coordinations per O atom are found, close to the 4/3 expected from a perfectly disordered structure.[75]

5.6 Summary and Discussion

The previously unknown local structure of Li_2MnO_2F was solved using a combination of neutron PDF, neutron diffraction, and RMC fitting. The results highlight the importance of advanced structural characterisation techniques for battery research, particularly for complex structures like disordered rocksalts or conversion materials.

It was demonstrated that Li_2MnO_2F assumes a disordered rocksalt structure at a local level, with an almost perfectly statistical distribution of anions and cations. Interestingly, there is some ordering around oxygen, and Li_2MnO_2F was found to have an average of 1.3 collinear Li-O-Li configurations per O, close to the theoretically expected value for a perfectly disordered rocksalt (4/3). The configurations per O, however, do not follow the expected distribution, and a preference for zero- and sixfold Li-coordinated oxygen was found.

This emphasises the requirement to understand the local structure and coordination environments, in order not to assign wrong amounts of O redox and O loss. An O with six Li ligands will be oxidised at a lower potential than an O with a single Li-O-Li configuration and can be subject to O loss, if located at the surface of the particle.[51,225] This requires

detailed, quantitative understanding of the O coordination environments, in order to engineer materials that are suitable for practical applications.

As expected, a percolation network was observed, making ~1.75 Li (87 %) of the structure's Li accessible.[75] This is in close agreement with the expected value from percolation theory (~ 1.8), and resembles the maximum of the accessible Li in the compound.[75] The number of actually removable Li is an important limit for rocksalt LiB cathodes, in addition to the TM redox capacity, as it is the physical limit of the theoretical Li extraction capacity. An understanding of the cation disorder is therefore vital for all disordered compounds.

The simultaneous fitting of a combination of total scattering data and diffraction with RMC was found to be a powerful tool for understanding these important details, particularly with neutron-based data, due to the sensitivity for Li. Neutrons furthermore offer the potential for 'silencing' individual scatterers by mixing isotopes with scattering lengths of opposite signs at an appropriate ratio, and generating scattering patterns where one species does not contribute. E.g. Li could be silenced via a combination of ^{6}Li (b = 2.00) and ^{7}Li (b = -2.22), and the resulting PDF and diffraction data added to the refinement, which would allow for the precise separation of Mn and Li sites.[221]

This approach, however, cannot be used for F and O, whose isotopes scatter very similarly.[221] $K_{\beta''}$ XES, however, has previously been used to distinguish between different ligands, including F and O, around Mn, and its suitability should be investigated.[226]

Chapter 6

Voltage and Capacity Fade of Li_2MnO_2F

6.1 Introduction

Disordered rockstalts exhibit significant voltage and capacity fading over the cycle life, which needs to be controlled if the compounds are to be used in applications.[77–81] Li_2MnO_2F is one of the most promising candidates within this space, as it is based on non-toxic elements and exhibits combined TM and O redox, resulting a a first-charge capacity exceeding 300 $mAhg^{-1}$, 30 % more than expected from TM redox (214 $mAhg^{-1}$).[88]

The compound's capacity fade can be separated into two regions (fig. 6.1): First, a non-linear region, occuring over the first eight to ten cycles, in which the capacity drops down to ~215 $mAhg^{-1}$, 80 % of the initial capacity, and matching the TM redox capacity (fig. 6.1). Simultaneously, the average discharge voltage is decreased. Over the subsequent cycles the capacity fade is approximately linear and depends largely on cycle count.[88]

Previous reports showed via XRD that the long-range structure is retained over the first 100 cycles, and that the material also appears not to suffer from significant Mn dissolution.[88]

As discussed in the previous chapter, as well as sec. 2.4.2, PDF analysis is a powerful tool for investigating the local structure of matter. In this chapter it is used to analyse changes

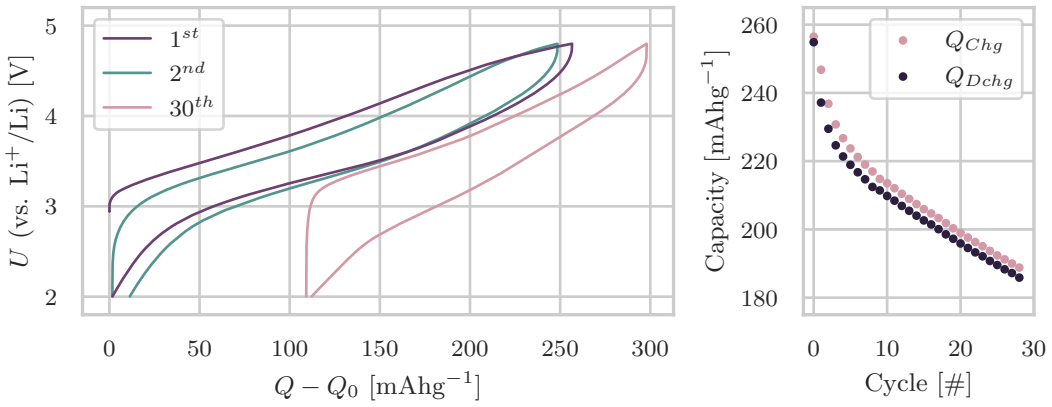


Figure 6.1: Electrochemical data for Li_2MnO_2F. Voltage profiles for selected cycles (left), and cyclic charge and discharge capacities (right).

of the local structure in cycled Li_2MnO_2F. Similarly, electrochemical techniques, including electrochemical impedance spectroscopy (EIS), are used to study the electrochemical behaviour.

6.2 Experimental

Material Synthesis Li_2MnO_2F cathode material was prepared as described in chapter 5.2.

Free-Standing Cathode Pellet Preparation Self-supporting cathode pellets with a ratio of 80 %m AM, 10 %m carbon black (acetylene; 99.9+ % Alfa Aesar), and 10 %m PTFE (Imperial Chemical Industries Ltd.) were prepared inside of a glovebox (O_2 & H_2O < 0.1 ppm) using vacuum-dried constituents, as described in sec. 2.3.1.

Coin Cell and *Ex-Situ* Sample Preparation Cathodes were assembled in 2332 coin cells (Hohsen Corp.) as described in sec. 2.3.2. Li metal anodes and dry LP30 electrolyte (Sigma Aldrich / Merck), soaked into glass fibre separators (Whatman GF-D), were used. A BioLogic MPG-2 battery tester was used to perform the required electrochemical profile. For *ex-situ* sample preparation, cycled coin cells were opened inside of a glovebox (O_2 & H_2O < 0.1 ppm) within 1 h after termination of the test profile, washed with dry DMC, and dried.

Three-Electrode Electrochemical Testing Three-electrode cells were assembled inside of a glovebox (O_2 & H_2O < 0.1 ppm) as described in sec. 2.3.3, using cathodes as described above, Li metal anodes and reference electrode. The glass fibre separators (Whatman GF-D) were saturated with dry LP30 electrolyte (Sigma Aldrich / Merck), and hermetically vacuum sealed in aluminised pouches. The cells were clamped between two pieces of acrylic plastic, using large binder clips. For charge and discharge profiles a BioLogic MPG-2 battery tester was used, and the cells cycled between 2.0 - 4.8 V at 50 mAg^{-1} and 30 °C.

Electrochemical Impedance Spectroscopy Electrochemical impedance spectroscopy (EIS) was collected in a three electrode set-up, using Li metal as a reference, which has been shown in the past to possess a high reversibility in different electrolytes, including LP 30.[227–230] Clamped pouch cell assemblies as described in the previous paragraph were used. EIS spectra were collected at 30 °C using a BioLogic VMP3 electrochemical workstation in a range of 200 kHz - 0.1 Hz. Potentiostatic experiments were performed with sinusoidal waves of 7 mV maximum amplitude. The obtained data was fitted using the ZView software (Scribner Associates Inc.).

Transmission Electron Microscopy Transmission electron microscope (TEM) images were collected by Shengda Pu on a JEOL JEM-300F instrument at 300 kV. Samples were prepared by the author by removing cycled cathodes from coin cells inside of an Ar-filled glovebox (O_2 & H_2O < 0.1 ppm). The cathodes were washed three times using dry dimethyl carbonate, and then sonicated for five minutes in the same solvent. Particles from the resulting suspension were drop-cast onto a holey carbon TEM grid (Agar Scientific Ltd.). The samples were loaded onto a special TEM sample holder for air sensitive samples in the glovebox, that prevented exposure to air during transfer into the TEM.

***Operando* and *Ex-situ* XANES and EXAFS** Mn K edge XAS spectra were collected on beamline B-18 at the Diamond Light Source, Didcot, UK. The energy was controlled using a Si(111) double-bounce monochromator, and calibrated using a Mn foil. *Ex-situ* samples

for the as prepared material, as well as cycled cathodes, were sealed in aluminised pouches, inside of an Ar-filled glovebox (O_2 & H_2O < 0.1 ppm), to prevent air exposure. The ten cycle *ex-situ* sample data was collected by Edouard Boivin and John-Joseph Marie.

Operando K edge EXAFS data was collected on the same beamline, using the previously described *operando* cell in transmission. Cells were assembled in an Ar filled glovebox (O_2 & H_2O < 0.1 ppm), as described in 3.3. Cathode pellets, as described above, with ∅ 6 mm, and Li metal anodes with a thickness of ~125 μm were used, and dry LP30 electrolyte (Sigma Aldrich / Merck), soaked into glass fibre separators (Whatman GF-D). Cells were galvanostatically cycled between 2.0 - 4.8 V using a BioLogic MPG-2 battery cycler at a temperature of ~30 °C. The temperature was controlled via two PID-controlled cartridge heaters connected to the bottom of an aluminium sample holder, in which the cells were mounted (pic. 3.13). Even though no beam damage was observed, the incident beam was rastered across the area of the cathode, and each location only visited once. At each point five spectra were collected for each edge, and averaged for the subsequent analysis.
For all samples, data processing was performed using the Athena package.[185] The pre-edge subtraction, data normalisation, and $\chi(E)$ extraction was performed as described in secs. 2.6 and 2.6.2. $\chi(k)$ was weighted by k^2 and Fourier transformed up to k = 12 Å^{-1} to obtain $|\chi(r)|$.

***Ex-situ* X-ray Pair Distribution Function** *Ex-situ* total scattering data was collected by Olaf Borkiewicz on beamline 11-ID-B at the Advanced Photon Source (APS), Argonne, IL, USA. Samples were packed in sealed polyimide capillaries in an Ar filled glovebox (O_2 & H_2O < 0.1 ppm) by the author. Data was collected using a Si(311)-monochromated beam with λ =0.21130 Å, a spot size of 0.5 x 0.5 mm, and an area detector. The distance to the detector was calibrated using a CeO_2 standard and the background contribution of an empty capillary and air was measured and subtracted. Sample 2D data was integrated and rebinned using the GSAS-II package, and the total scattering function $S(q)$ extracted.[184]

$S(q)$ was Fourier transformed up to q = 24 Å to obtain the PDF $G(r)$, using the PDFGetX3 program package.[211] 'Rietveld-like' fitting of the PDF was performed using the PDFfit2 program as implemented in the PDFGUI frontend.[212,219] The data were fit between 0.5 - 15 Å using a statistically populated disordered rocksalt unit cell ($Fm\bar{3}m$) with the crystallite size fixed to 5 nm, as suggested by TEM data and $G(r)$ attenuation. No influence of the Li fraction on the fit quality was determined, due to the weak scattering of the element, and the occupancies were set based on the first-charge capacity. Instrument broadening was set to zero, as the parameter did not improve the fit quality. A scale factor, a dampening factor, the lattice parameter a, and isotropic displacement factors U_{iso} were refined, while the fractional coordinates and occupancies were not changed.

Preparation of Multi-Cycled Samples for *Ex-situ* Neutron Pair Distribution Function To obtain neutron scattering data on multi-cycled cathode materials, large amounts (~2 g) of cycled active material are required. As all additives, such as carbon and binder, scatter strongly in Neutron experiments, the number of additives and their amounts should be reduced to an absolute minimum. Preliminary tests showed that Li_2MnO_2F cannot be cycled without a significant amount of carbon as a conductive additive, while the binder was found to be optional.

A custom cell, called BFC (after the neutron scattering length b and reduced total scattering function F), was designed and built, to ease handling of binder-free powder (fig. 6.2). The design features are large base (1), made of aluminium (7075 - T6), with an outside diameter of 140 mm, with a pocket into the which an insulating insert (2, PEEK) is fit, that electrically insulates the anode from the cathode. An AM/carbon mixture was dispersed on the bottom of the cell, within the confines of the insulating insert, using a sieve, and covered with a glass fibre separator (Whatman GF-D). A circular Li metal foil anode with 95 mm diameter was placed on top of the powder and the separator soaked with electrolyte. The stack was then

covered with a copper spacer (5), and a disc spring (6) was placed on top, where it rests in a groove to prevent slipping. An FKM O-ring (3) was placed inside of a dedicated groove in the base (1), and a PLA insulating ring (4) placed around it, to prevent electrical contact between the lid (7) and the base (1). The depth of the groove and thickness of the ring result in an O-ring compression of 30 % when the cell is fully assembled, creating a hermetic seal. A 3-D-printed PLA screw insulator ring (8) was inserted into the designated holes in the lid (7) and the assembly placed on top of the spring (6). M3 x 25 cap screws (9) were then inserted into the holes in the screw insulator (8) and the lid (7) assembly and screwed into the dedicated tapped holes in the base (1), connecting the two parts mechanically.

Multi-cycled samples were prepared by thoroughly mixing 80 % Li_2MnO_2F active material and 20 % carbon black (acetylene; 99.9+ %, Alfa Aesar) by grinding for 30 min using an agate mortar and pestle inside of an Ar-filled glovebox (O_2 & H_2O < 0.1 ppm). Two grams of the resulting powder were spread on the bottom of a BFC and the cell assembled as described above. Dry LP 30 electrolyte was used (Sigma Aldrich / Merck) and the cells cycled at a rate of 20 mAg^{-1} between 2.0 - 4.8 V. The cycled powder was extracted inside of an Ar-filled glovebox (O_2 & H_2O < 0.1 ppm) immediately after termination of the last cycle and washed five times using dry PC, with intermediate centrifugation (2.5 min, 1000 rpm, Thermo Fisher Heraeus

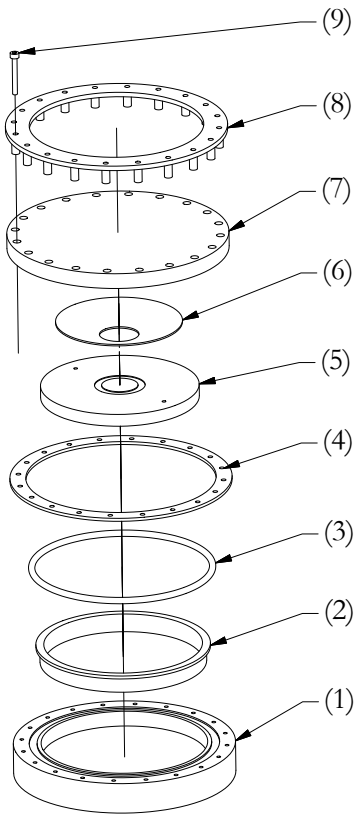


Figure 6.2: Exploded view of the BFC, designed to cycle cathode powder without binder. For scale: The outside diameter of the base (1) is 140 mm.

Multifuge X3) to separate out the liquid and solid phases. The washed powder was dried inside a heated glovebox antechamber for 12 h at 40 °C under vacuum.

Neutron Pair Distribution Function Neutron total scattering data was collected on the Polaris instrument at the ISIS Neutron and Muon Source, Didcot, UK with help from Helen Playford. For each sample 1.5 - 2.0 g of powder were loaded into vanadium cans and hermetically sealed, by the author and Robert House, and the total scattering data collected for six hours, respectively. In addition to the cycled powders, data was also collected on a carbon sample. For each dataset the scattering data from different detectors were combined using the Mantid software package and processed using the GudrunN software by Helen Playford. The carbon influence was subtracted, and the data up to 31 $Å^{-1}$ was Fourier transformed to obtain the PDF using the SToG program, as contained in the RMCProfile package, by Helen Playford.[118,119,231,232]

'Rietveld'-like fitting of $G(r)$ was performed using the PDFfit2 program as implemented in the PDFGUI frontend.[212,219] Instrument parameters were provided by Polaris and remained fixed. The data was fit between 0.5 - 15 Å using a statistically populated disordered rocksalt unit cell ($Fm\bar{3}m$) with Li content adjusted to the lost capacity and with crystallite size fixed to 5 nm. A scale factor, the lattice parameter a, and isotropic displacement factors U_{iso} were refined, while the fractional coordinates and occupancies were not changed.

6.3 Cycle-Dependent Morphology and Local Structure Changes

The morphology of Li_2MnO_2F was analysed for discharged cathodes after one and ten cycles via TEM (fig. 6.3). The particle sizes are very similar to those observed for the pristine compound discussed in chap. 5, and lattice fringes are visible throughout the

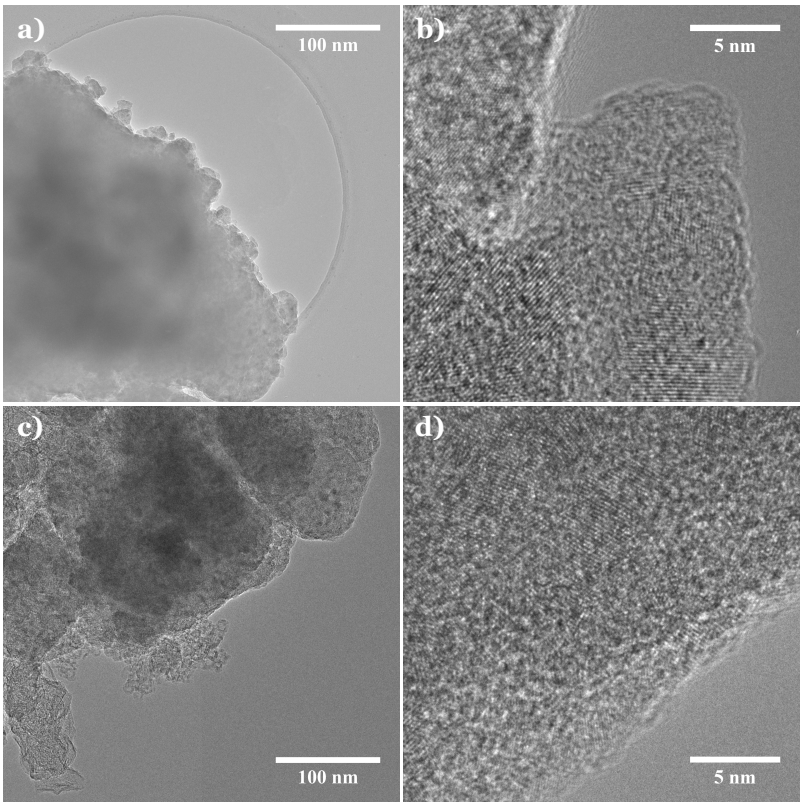


Figure 6.3: TEM images obtained for cycled Li_2MnO_2F, showing that the crystalline nature is maintained. a, b) 1 cycle, discharged. c, d) 10 cycles, discharged.

structure, arising of domains of ~50 Å size. This suggests that the material's morphology does not change significantly during cycling, and that a process such as pulverisation is not responsible for the decrease in performance.

Changes of the local structure were further analysed using X-ray PDF of multi-cycled samples. The influence of binder and carbon additives on the X-ray PDF was analysed and found to be small, and only occurs in the region < 4 Å (fig. A.3). As carbon and Li_2MnO_2F have no overlapping peaks, and the carbon influence dies down quickly due to the low structural coherence, the quality of structural fits is not affected significantly.

The X-ray PDF data, collected at intervals for the first 20 cycles (fig. 6.4), suggests a slight change in lattice parameters after the first cycle. On subsequent cycles, no significant structural changes are observed, even though the capacity has already decreased to ~75 % of its initial value. The peak positions and intensities of the metal-anion (M-A), as well as the M-M and A-A peaks remain constant in the charged and discharged state, respectively.

The data were fit with statistically populated Li_2MnO_2F disordered rocksalt unit cells (space group $Fm\bar{3}m$; fig. 6.4 e & f). Differences in the lattice parameters are observed between the charged and discharged samples, with the structure contracting by ~2 % on charge. Interestingly, the M-A peak shifts by only ~-0.04 Å at the same time. A slight increase in lattice parameter is also observed after discharging the material for the first time, and will be investigated later in this chapter. The quality of the fits is good in the region above ~5 Å, and poor below, suggesting that the average rocksalt structure is retained.

To investigate the Li environments, which are hard to observe in X-ray-based techniques, neutron PDF was obtained for samples collected after one, five, and 30 cycles (fig. 6.5). The attenuation of the $G(r)$ functions is similar to the one observed for the pristine sample, supporting the previous observation that the material is not pulverised. The data were fit

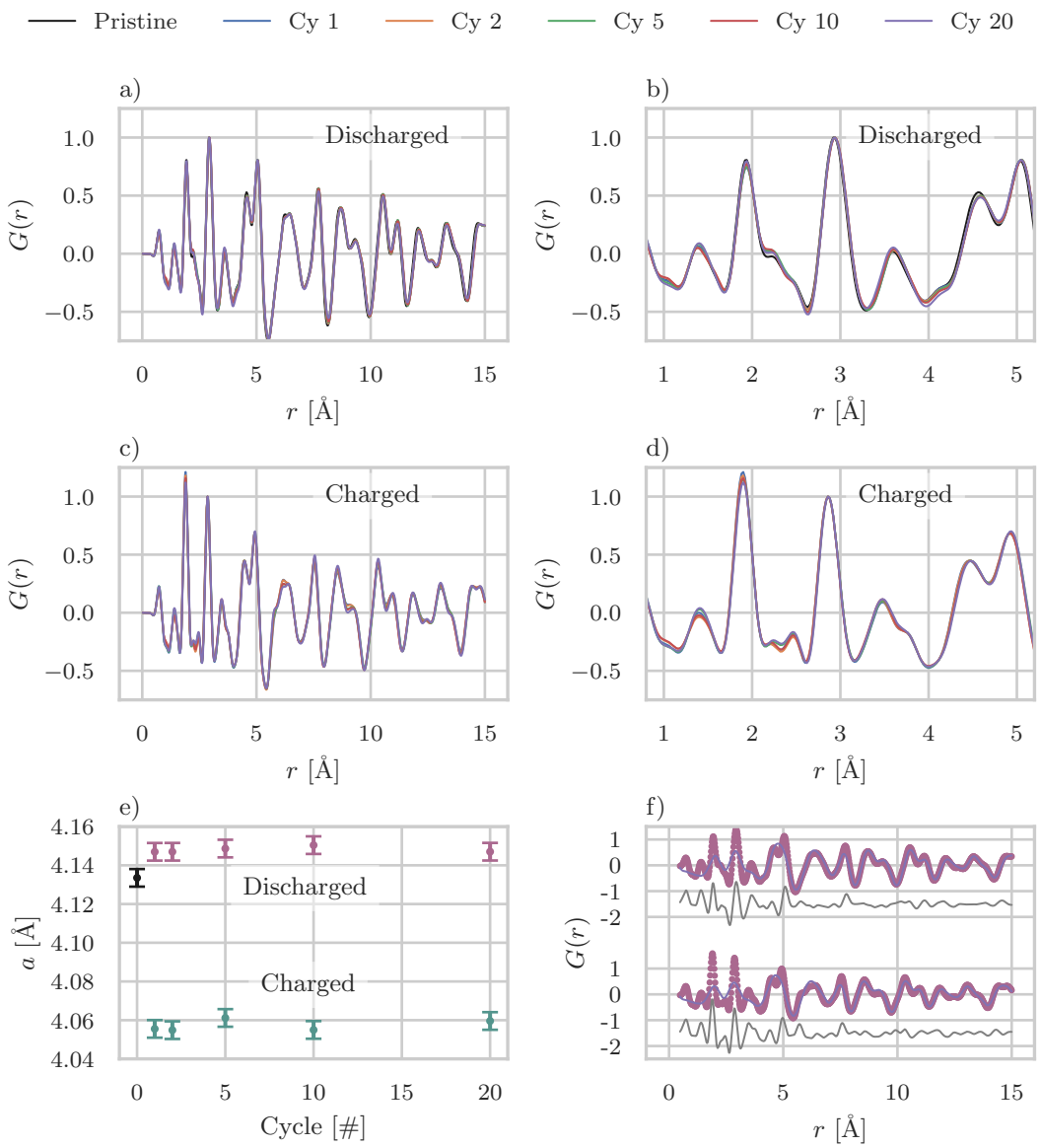


Figure 6.4: *Ex-situ* X-ray PDF of cycled Li_2MnO_2F. a, b) Discharged; c, d) Charged; e) Lattice parameters fit to the PDF: Black: Pristine; Purple: Discharged, Green: Charged. f) Sample fits as obtained for discharged (top) and charged (bottom) Li_2MnO_2F cathodes after 20 cycles, displacing large errors below 5 Å.

Table 6.1: Lattice parameter a for multi cycled, discharged Li_2MnO_2F as obtained from 'Rietveld-like' fitting of neutron PDF. Details in sec. 5.4 for the pristine material and sec. A.4 for the cycled compound.

	Pristine	1 Cy. Dchg.	5 Cy. Dchg.	30 Cy. Dchg.
a	4.1025(8)	4.1393(2)	4.1547(8)	4.1320(9)

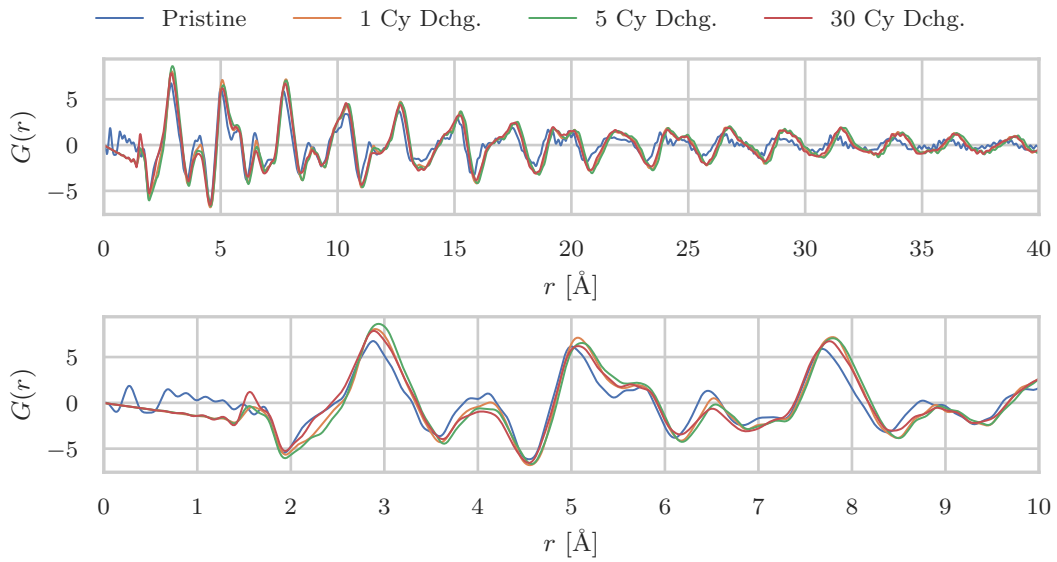


Figure 6.5: *Ex-situ* Neutron PDFs of Li_2MnO_2F. Top: Plotted up to 40 Å, showing that the structural coherence is retained on cycling. Bottom: Plotted up to 10 Å.

with statistically populated unit cells (space group $Fm\bar{3}m$), with the Li content adjusted according to the lost capacity, and good fit qualities around R_{wp} = 20 % were obtained (figs. A.4, A.5, A.6). Similar to the X-ray PDF, an increase in lattice parameters is observed after the first discharge, compared to the pristine material (tab. 6.1).

The cycled neutron PDF shows changes to the M-A peak bond lengths after the first and fifth discharge. The intensity of the peak decreases below 2 Å, while it increases in the region around 2.3 Å, forming a pronounced shoulder in the peak. This region mainly rises from Li-A bonds in the pristine compounds, as discussed in chapter 5, with Mn-A peaks forming a localised peak centred at ~2 Å. This suggests that at least part of the Li environments are changed over the first cycles. As F and O are hard to distinguish using both X-rays and

neutrons, no assumptions can be made regarding the changes of the Li neighbours. The shoulder at 2.3 Å is not observed after 30 cycles, likely due to the loss of Li from the lattice.

This is further supported by Mn K edge EXAFS, collected for samples of pristine and ten-cycle discharged Li_2MnO_2F (fig. 6.6). The observed Mn-A peaks are virtually identical, whereas the Mn-M peak intensity is decreased and shifted to a lower r. This indicates that Li is lost from the lattice, as the Mn-Mn distances in the pristine material were found to be shorter than those observed for Mn-Li.

The increase in lattice parameters during the first discharge was investigated using *operando* Mn K edge XANES (fig. 6.7). Over the first charge, the Mn-M peak maximum shifts continuously to lower r on charge, and the intensity decreases. On discharge the reverse occurs, and the peak is shifted to its original position after ~ 70 % of the discharge. The total intensity of the Mn-M peak is not recovered after full discharge. In conjunction with the observation in PDF, where no changes of the M-A peak intensity in the Mn region are observed, this suggests that the expanded lattice parameter arises due to Li extraction. Interestingly, the Mn-O distances are not changed during the entire cycle, in agreement with the previous observations.

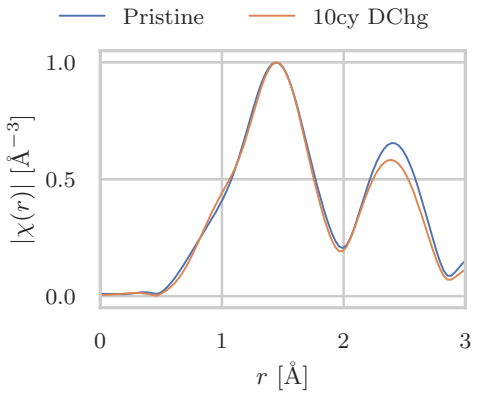


Figure 6.6: *Ex-situ* Mn K edge EXAFS of pristine and ten-cycle discharged Li_2MnO_2F.

The influence of the Mn oxidation state was further analysed via *operando* Mn K edge XANES (fig. 6.8). The data show that the K edge and pre-edge region predominantly change during the first 80 % of the charge cycle, suggesting that Mn is oxidised in this region. Similarly, it is almost fully reduced to its original value during the first 80 % of the discharge,

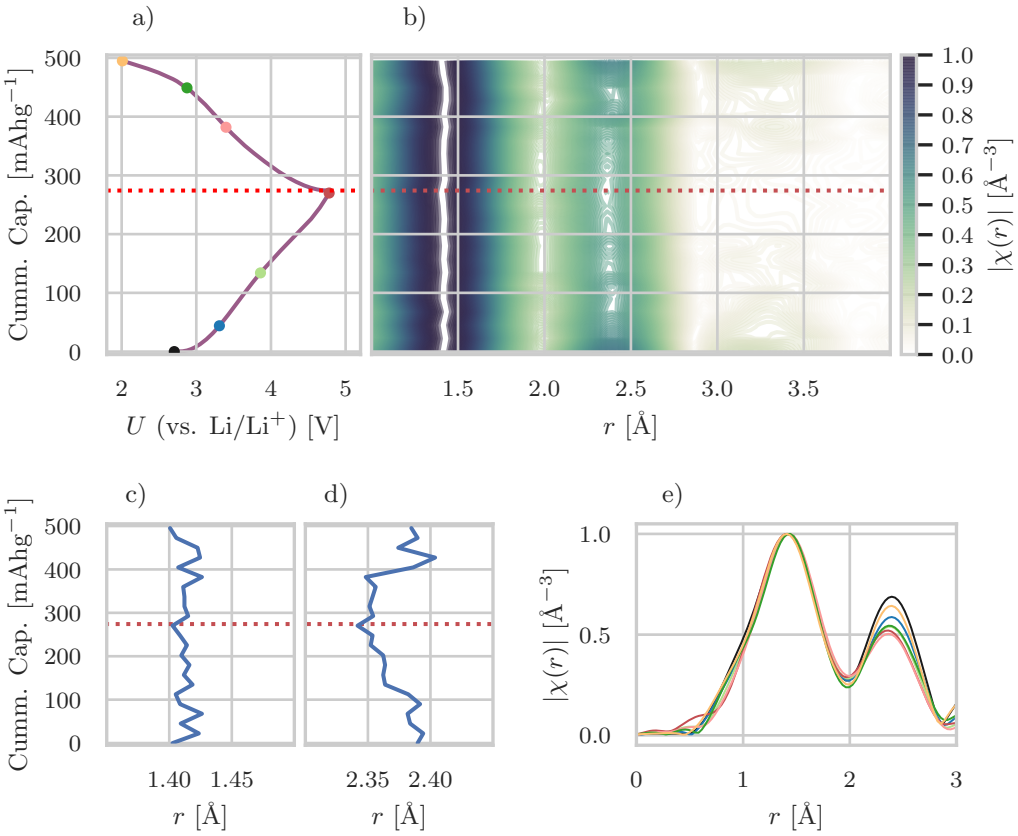


Figure 6.7: *Operando* Mn K edge EXAFS for the first cycle of Li_2MnO_2F. a) Voltage profile, with coloured markers corresponding to the spectra in e; b) Contour plot of the EXAFS region; c) M-A peak positions; d) Mn-M peak positions. e) Selected spectra, colour matched to the dots in a.

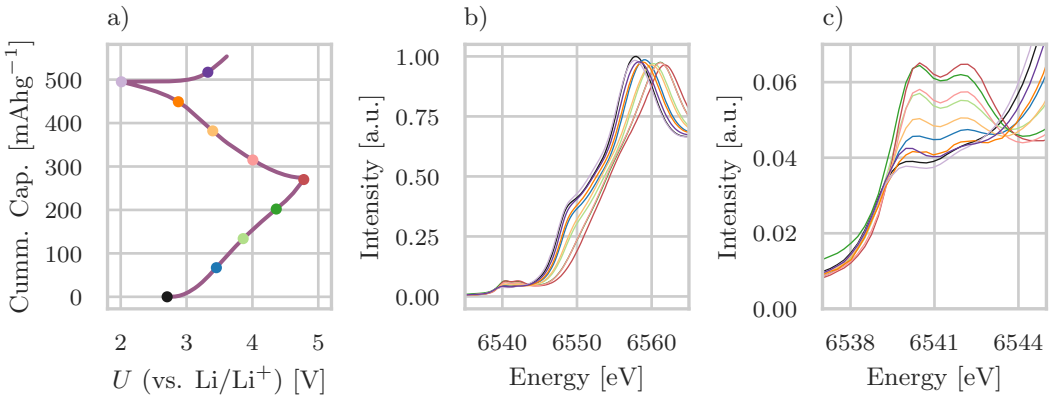


Figure 6.8: Operando Mn K edge XANES for the first cycle of Li_2MnO_2F. a) Voltage profile, with coloured markers corresponding to the spectra in b and c; b) Mn K edge; c) Pre-edge region.

suggesting O redox activity in the regions with reduced Mn oxidation state changes. The pristine spectra are almost recovered, suggesting that Mn is fully reduced to Mn^{3+} after the first cycle.

In summary, the structural changes of Li_2MnO_2F during the first 30 cycles appear to be based on the effects of Li extraction and reinsertion into the material, and no other significant structural transformations are observed. The capacity loss is therefore likely either linked to cathode dissolution or a surface phenomenon, and is investigated in the following.

6.4 Cycle-Dependent Electrochemical Characterisation

A potential reason for the fade could be the dissolution of Mn into the electrolyte, limiting the available redox capacity. Although reported not to occur in a significant manner for Li_2MnO_2F, Mn dissolution has previously been observed in some Li cathodes, through the formation of soluble Mn^{2+} species.[88,233–236] These can be expected to be deposited on the anode, where they can be detected through an increase in resistance. To investigate this phenomenon, cathodes were cycled in three-electrode cells against Li, using a Li metal reference (fig. 6.9). The data show that the anode overpotential is very low and, although

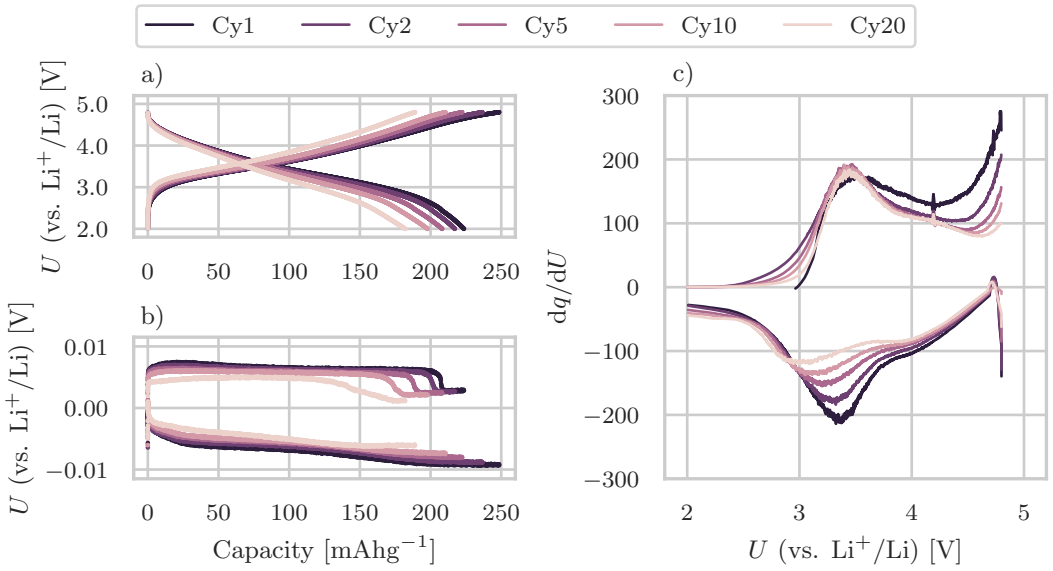


Figure 6.9: Three-electrode electrochemistry of Li_2MnO_2F, cycled at 50 mAg^{-1} vs. a Li metal counter electrode (U_c), using a Li metal reference (U_r).
a) $U - U_r$ (positive electrode); b) U_c - U_r (negative electrode); c): Differential capacity dQ/dU vs. U obtained for the positive electrode.

slightly inconsistent during discharge, it does not change significantly over the first 20 cycles and its overall magnitude is too small to explain the large capacity loss.

The origin of the loss is therefore likely based on a process occurring at the cathode, as supported by a differential capacity plot for the working electrode, obtained for the same data (fig. 6.9, c). On charge, a peak at ~3.5 V is observed, which can be assigned to Mn^{4+}/Mn^{3+} redox, as well a large redox-active region at higher voltages, whose magnitude decreases on subsequent cycles. This region is likely linked to O redox, as the behaviour is similar to the one observed for layered Li-rich materials, and decreases with increasing cycles, in a similar fashion as the capacity.[140] It should be mentioned that almost no O loss has been reported for Li_2MnO_2F.[88]

On the first discharge, a large peak at ~3.3 V is observed, which can be assigned to the reduction of Mn^{4+}. Just as for other Li-rich materials, the O redox peaks are not symmetrical. and a significant amount of the high-voltage charge capacity is not returned at

potentials >4.0 V.[21,22,25,140] A small shoulder, at ~4.0 V, could likely arise from O redox, as it does in some layered compounds.[140]

On subsequent cycles, the peak assigned to Mn oxidation remains very constant, and its position is not shifted, while the Mn reduction peak continuously shifts to lower energies. The shift is non-linear, with the majority occurring over the first few cycles, corresponding approximately to the rate of the initial capacity fade of the material. Interestingly, the shoulder at ~4.0 V is very symmetrical for both oxidation and reduction, suggesting a low overpotential, usually not observed for O redox.[140]

To further understand these differences between the oxidation and reduction processes, electrochemical impedance spectroscopy (EIS) was collected for cycled three-electrode cells with Li metal reference and counter electrodes. Spectra were recorded for cells relaxed to OCV after discharging to 2.0 V (fig. 6.10), cells held at 2.0 V (fig. A.7), and cells held at 4.8 V (fig. A.8).

Nyquist plots of the data consistently show significantly larger semicircles for the cathode, compared to the anode, indicating impedances approximately one to two orders of magnitude lower for the latter. No increase in anode impedance is observed with cycle count, in accordance with the previous observations, and the spectra are not discussed further.

The data observed for the cathode at OCV show two pronounced semicircles, and the cathode impedance grows significantly with increasing cycle life, a trend that is also observed in the data collected at 2.0 V and 4.8 V.

The spectra were fit using an equivalent circuit consisting of a series connection of a single resistor (R1), and three parallel resistor-constant phase element (CPE) parallel cells (R-CPE). Two R-CPE cells were required to satisfactorily fit the first semicircle, suggesting two overlapping processes.[237,238] Fits with equivalent circuits containing a total of two

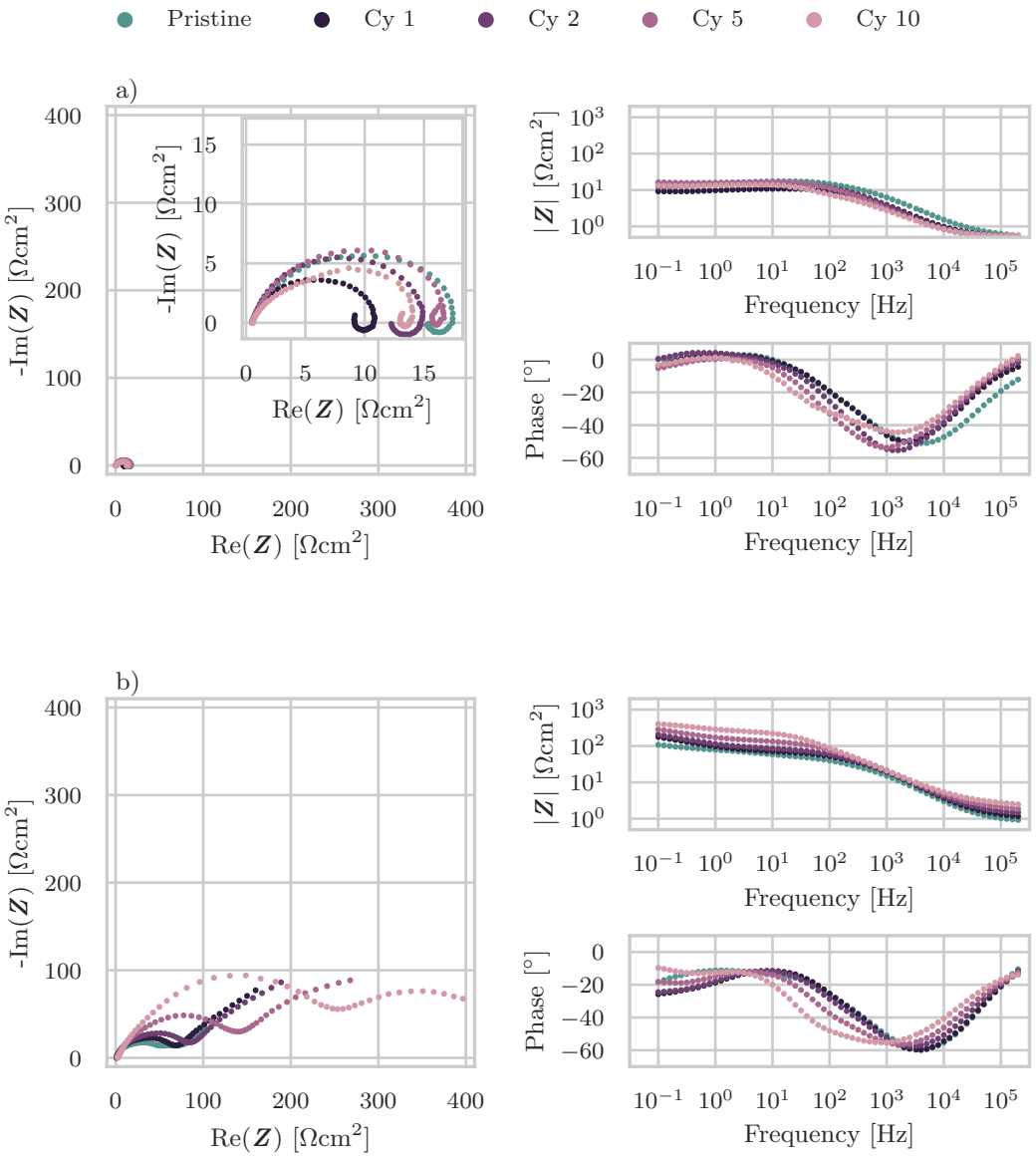


Figure 6.10: Three-electrode impedance spectra obtained for cycled, discharged Li_2MnO_2F at OCV .
a) Nyquist (left) and Bode plots (right) obtained for the anode.
b) Nyquist (left) and Bode plots (right) obtained for the cathode. Fit parameters are listed in tab. A.16.

R-CPE cells, as well as Warburg elements, converged to worse goodness of fits. Each R-CPE circuit accounts for a process on the cathode, signified by a semicircle in the Nyquist plots, whilst R1 accounts for the purely ohmic resistance contributions to the cell, mainly based on the electrolyte conductivity. The derived total direct current (DC) resistances, as well as an example fit, are depicted in fig. 6.11 a & b, and the fit parameters for all fits are listed in the appendix (tabs. A.16, A.17, A.18).
The total DC resistances for the discharged cells at OCV, as well as for the 2.0 V voltage hold, are consistently larger than those observed at 4.8 V. Interestingly, the discharge resistance grows over the first five cycles, before decreasing again, and the first-cycle resistance is recovered after ten cycles.

To study the evolution of the DC resistance for a full cycle, a cell was charged and discharged using constant magnitude DC pulses of 10 min duration, separated by 30 min rest intervals, and the resistances extracted using Ohm's law (fig. 6.11 c & d). During charging, small overpotentials are observed, and the resistance of the cathode is hence low. Only towards the end of charge a slightly increased resistance is evident. On discharge, however, the overpotential increases significantly with decreasing voltage, and grows very large during the later stages of the cycle. These observations match the behaviour observed in EIS, namely that the cathode resistance on discharge is significantly larger than on charge. The values obtained via DC pulses, however, are ~2x larger than those found via EIS, likely due to low-frequency contributions not captured by the frequency range of the EIS experiments.

To understand the origin of the large resistance, the effective capacitances of the CPEs for a given R-CPE cells were obtained from the EIS data via the following equation:[239,240]

$$C = Y^{\frac{1}{\alpha}} R^{\frac{1-\alpha}{\alpha}} \tag{6.1}$$

where C is the real capacitance, Y is the observed capacitance of the CPE (which does not have a physical meaning), R is the resistance of the corresponding resistor, and α is a

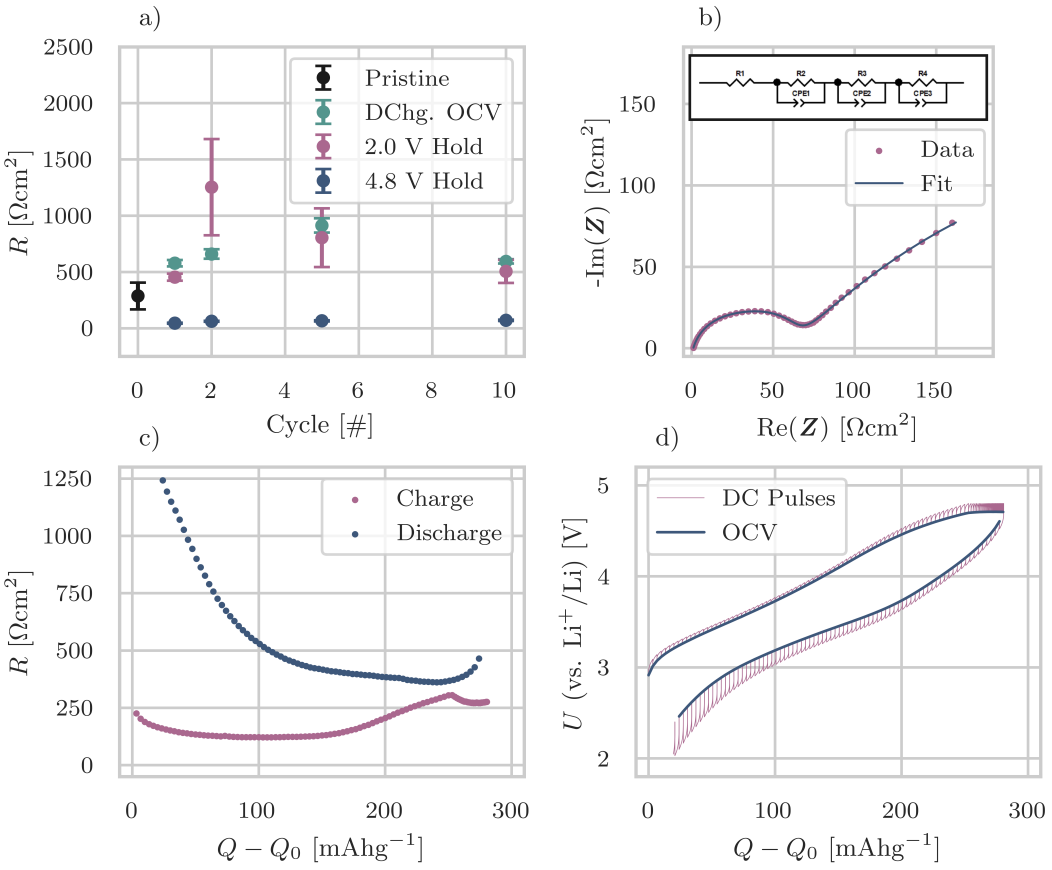


Figure 6.11: Total resistance for Li_2MnO_2F cathodes.
a) Total resistances obtained via fits of the EIS data, using the equivalent circuit depicted in the sample fit b); c) Resistances obtained via DC pulses for the first cycle; d) First cycle voltage profile obtained via DC pulses and corresponding OCV curve for interpolated resting voltages.

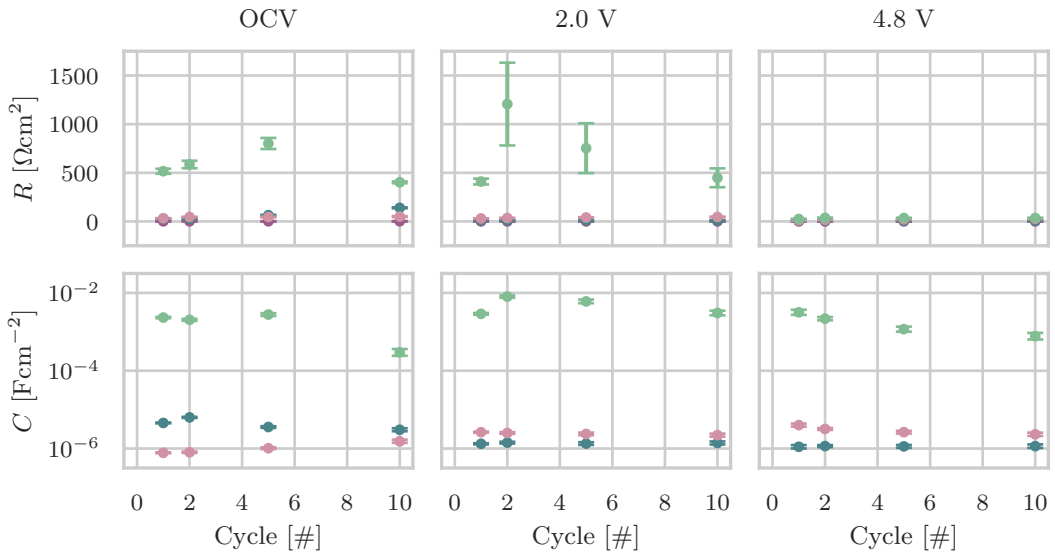


Figure 6.12: Cycle-dependent fitted resistances (top) and capacitances (bottom) obtained via EIS. The colours indicate the three R-CPE elements used during fitting.
Data for cells probed at OCV after discharging to 2.0 V ('OCV'), held at 2.0 V ('2.0 V'), and held at 4.8 V ('4.8 V').

parameter influencing the shape of the R-CPE semicircle (sec. 2.1.5). The values for C and the corresponding R are depicted in fig. 6.12.

It can be seen that the high total resistance, observed at OCV and 2.0 V, is dominated by an R-CPE circuit associated with a high-capacitance element, on the order of mFcm^{-2} to tens of mFcm^{-2}. The resistance can be assigned to a charge transfer process, whose R-C elements usually contribute in the medium-frequency region and have capacitances of a similar magnitude.[237,238]

The large charge transfer resistance R_{ct} causes a large overpotential, limiting the amount of charge that can be returned to the cell during galvanostatic experiments. The values seem to peak within the first five cycles, and then decrease. This behaviour is well correlated with the observed initial capacity fade, suggesting that it is the origin of the low coulombic efficiency. Similar behaviour, where high R_{ct} values were observed on discharge, has previously been reported for layered $Li_{1.2}Ni_{0.13}Co_{0.13}Mn_{0.54}O_2$, where it was linked to the sluggish kinetics of

O redox.[140] As 'excess' capacities, surpassing TM redox, are only observed over the first ten cycles, this suggests a potential explanation for the observed rapid change observed for the first few cycles.

6.5 Summary and Discussion

Disordered rocksalt compounds exhibit significant voltage and capacity fading over the first few to first tens of cycles.[77–80,84,88,92] Here it was shown that in Li_2MnO_2F part of this fade is based on an increased charge transfer resistance on discharge, which limits the ability to reinsert Li ions.

The voltage and capacity fade in Li_2MnO_2F can be split into two regions: A rapid initial decay over the first few cycles, and a gradual fade over the subsequent cycle life. No evidence was found that suggests a significant structural change with increasing cycle count, and all data suggests that the rocksalt $Fm\bar{3}m$ space group is maintained through a stable Mn-based lattice.

The charge transfer resistance R_{ct} was found to be significantly higher on discharge than on charge, and peaking over the first few discharge cycles.[21,22,140–142,241] This is likely linked to the slow kinetics of O redox, as has been observed for layered materials, and results in a reduced Coulombic efficiency over the first few cycles, which is the likely reason for the initial, fast capacity decay.[55,140–142]

The same effect, however, does not appear to be responsible for the continued, nearly linear capacity fade. This gradual capacity fade remains more elusive, as the high impedance of the first few cycles has reduced to similar magnitude as after the first cycle, yet the asymmetry between the charge and discharge peaks in the differential capacity continues to grow. This

suggests that another effect, in addition to R_{ct}, is present. The observed capacity is within the limits of the Mn^{4+}/ Mn^{3+} redox couple, which should be fully active within the large voltage window and exhibit quick kinetics, while the observed behaviour corresponds more to what has been reported for O redox.[25,140] The well-maintained oxidation peak also suggests that a significant loss of active material is not the underlying reason. This corroborates what has previously been reported, where the observed mass loss from the cathode was minute over the first 100 cycles.[88] At no point is the structure limited by charge carriers, and even after 30 cycles only 75 % of the accessible Li have been used.

The observed behaviour in the differential capacity, in conjunction with the EIS, points towards either a thermodynamic effect, influencing the extraction and insertion potentials, potentially linked to O redox, or a diffusion effect. Transport phenomena, such as solid-state diffusion, were not probed by the frequency range of the EIS and could be the underlying reason. This requires further study, to identify the exact mechanism.
Neutron PDF suggests a change in Li-A environments, which appears to be the most promising lead. O redox and TM migration have been shown to be highly correlated in 3d and 4d Li-rich materials, and it can be assumed that the redox-activity leads to some form of local structural reorganisation.[25,47,56,57,63,64,241] Owing to the randomly populated disordered rocksalt structure, the migration of low amounts of Mn into adjacent octahedral sites would be hard to detect, as the coordination environment might not change substantially. Some degree of migration can be expected to take place, given the amount of five- and six-fold Li-coordinated oxygen in the structure, as discussed in the previous chapter. Upon delithiation, these O are likely highly unstable, and might cause local changes, creating vacancies and leading to Mn migration.

It is possible that this effect was not registered here, due to the reduced quality of the neutron PDF obtained for electrochemically multicycled material, as several background contributions were subtracted. By chemically delithiating the material, e.g. via exposure to

NO_2, phase pure compounds could be synthesised and analysed via RMC, to accurately solve the 'charged' structure and determine where vacancies exist. In this context, 'silencing' of the Li via a combination of ^{6}Li (b = 2.00) and ^{7}Li (b = -2.22) would be very beneficial, as any changes to the Mn bonds would be directly visible.[221] Similarly, electrochemically multi-cycled, 'Li-silenced' material could be used with 'isotope-regular' Li metal and electrolyte, to investigate the locations of reinserted Li.

The structural transformations of Li-rich rocksalts remain elusive. Detailed understanding of the structure-electrochemistry relationship, however, is paramount for making practical use of this highly promising class of compounds.

Chapter 7

Summary and Outlook

Oxygen redox is one of the most promising approaches for increasing the specific energy of cathodes, however its complex structure-electrochemistry relationship, the resulting voltage hysteresis, as well as sluggish kinetics have prevented its commercial use, so far.[21,22,25,44,140]

The slow kinetics observed in the material require significant stack pressure to overcome the effects, while the complex electrochemistry exhibited by the materials benefits from the use of more *operando* techniques. In chapter 3, a design for a new *operando* cell, capable of reliably producing the required stack pressure was presented. It is transparent for hard X-rays, including the K absorption and emission edges of TMs commonly used in Li ion cathodes. By using rigid glassy carbon windows, as well as a long compression spring to apply the stack pressure, it can accommodate a variety of cell stack thicknesses, making it versatile and easy to use.

During use of the cell it was found that its high mass poses a problem, as some beamlines struggle to accommodate an array of several high-mass cells simultaneously. While the transparency of the cell is sufficiently low to enable fast collection times and allow several cells to be used in parallel, the mass has prevented this in some instances. A redesign should therefore entail the partial replacement of high-density metals with polymers, as well as a size reduction. Similarly, a change of the shape to a rectangular cross-section would be

beneficial, as it would increase the stacking density of cells used side-by-side.

In chapter 4, this *operando* cell was used to investigate the TM redox behaviour of $Li_{1.2}Ni_{0.2}Mn_{0.6}O_2$ and $Li_{1.2}Ni_{0.13}Co_{0.13}Mn_{0.54}O_2$ using K edge HERFD-XANES and XES. The former allows for the direct study of the TM 3d states using hard X-rays, and therefore enables the real-time collection of truly bulk sensitive data. K_α XES is a great complement, as it can be collected using the same experimental setup with only minor changes, and contains information on the TM spin state.
The obtained data show that, on first charge, TMs are active far into the regions usually associated with O redox, namely the plateau at ~4.6 V, demonstrating overlap of the TM and O bands. Similarly, it was found that Ni is fully oxidised to Ni^{4+} in $Li_{1.2}Ni_{0.13}Co_{0.13}Mn_{0.54}O_2$, whereas it is not in $Li_{1.2}Ni_{0.2}Mn_{0.6}O_2$. The observations are more ambiguous for Co and Mn, predominantly because a qualitative analysis of the XES data proved difficult. Further work is required to understand the exact spin states of these elements, which will require modelling of the compounds. This should be supported via *operando* TM K edge RIXS at selected points along the first cycle, to understand the oxidation states in much more detail. Lastly, the origin of the difference in Ni oxidation state needs to be understood. One hypothesis is that it is based on the tendency of $Li_{1.2}Ni_{0.2}Mn_{0.6}O_2$ to form Ni-rich surfaces, which are in close contact with the electrolyte.[41,202–204] This requires validation through surface analysis, e.g. via SIMS.

Although O redox was initially identified in layered TM oxides, it has also been observed in disordered rocksalt compounds, including Li_2MnO_2F.[88] In these materials the structure-electrochemistry relationship is even more complex, as the highly disordered structure enables many different O environments.
In chapter 5, the structure of Li_2MnO_2F was solved using a combined fit of neutron PDF and diffraction patterns via RMC. The obtained structure demonstrates that the cations and anions are almost perfectly statistically distributed in the compound, and reproduced

the results expected from percolation theory, as well as the expected average number of O redox arrangements. Interestingly, however, the distribution of collinear Li-O-Li configurations differs from the expected one, demonstrating the importance of solving the local structures of this class of compounds.

The used methodology was found to be a powerful tool for the simultaneous analysis of the long- and short-range order, which is, however, limited to pristine compounds, owing to the sensitivity of neutron techniques to additives such as carbon. Future work should focus on identifying a method for cycling large amounts of cathode powder, without the need for conductive additives, as no carbon isotope with a negative scattering length exists, and the element cannot be 'neutron silenced'.

A promising additional technique is $K_{\beta''}$ XES, which has previously been used to distinguish different ligands surrounding Mn, and it should be investigated if it can be used to accurately distinguish between F and O around Mn.[130,226]

In chapter 6, the capacity fade of Li_2MnO_2F was explored in detail, to understand why rocksalt cathodes suffer from a reduced capacity with increasing cycle count. This fade was split into two regions, a first, rapid one, occurring over the first ~10 cycles, and a more gradual one, observed subsequently. No significant structural reorganisation was observed with several bulk-sensitive local probes, outside of a change in Li-anion bond distances after reinsertion. Simultaneously, a large discrepancy between the internal resistance of the cathode on charge and discharge was found, that was traced to a large charge-transfer resistance in the regions associated with O redox. This is likely based on the sluggish kinetics associated with the phenomenon, and was identified as the reason for the initial voltage fade over the first few cycles, as the low Coulombic efficiency on discharge prevents full Li reinsertion. A second mechanism was found to be responsible for the continued fade, but was not traced to a surface phenomenon, and is likely related to mass transport in the cathode. A closer investigation is required, including EIS up to very low frequencies, to study the diffusion behaviour of the electrodes. Similarly, as explained in the previous

section, neutron PDF of additive-free, multi cycled material would be invaluable, and would allow for RMC fitting of the cycled structure. Similarly, 'silencing' Li in multi-cylced material would be very valuable. This way, many details, including vacancies, potential ion clustering, as well as diffusion paths and O environments, could be assessed directly.

The cathode research space continues to be exciting, and it is evident that advanced experimental techniques are required to understand the minute details that ultimately dominate macroscopic cathode behaviour. While much research effort is put into solid-state electrolytes, safe, high-energy cathode materials are crucial for increasing the energy density of all possible cells, and should remain a focus of the field.

Appendix A

Appendix

A.1 *Operando* Cell X-ray Transmission for the 3d TM K Edges.

In chapter 3 the X-ray transmission of the *operando* cell in certain conditions is presented. For reference, tab. A.1 lists the direct transmission through the cells at the 3d TM K edge energies, excluding contributions from the cell stack.

Table A.1: X-ray transmission through the *operando* cell at 0° scattering angle and the energies of the 3d absorption K edges.

Element	Sc	Ti	V	Cr	Mn	Fe	Co	Ni	Cu	Zn
Transmission [%]	1.6	4.7	10.3	17.9	26.7	35.9	44.9	53.1	60.2	66.6

A.2 First-Cycle *Operando* X-ray Diffraction Patterns And Fit Details for $Li_{1.2}Ni_{0.2}Mn_{0.6}O_2$ and $Li_{1.2}Ni_{0.13}Co_{0.13}Mn_{0.54}O_2$

To understand the evolution of the long-range structure in chapter 4, *operando* XRD was obtained for $Li_{1.2}Ni_{0.2}Mn_{0.6}O_2$ and $Li_{1.2}Ni_{0.13}Co_{0.13}Mn_{0.54}O_2$ (figs. A.2, A.1). In Li-rich

NMC, over the TM redox section of the voltage profile (< 125 $mAhg^{-1}$), the (003) reflection shifts to lower scattering angles, indicating an expansion of the c-axis. Simultaneously the (110) reflection shifts to higher q, indicating a contraction of the a-axis. The superstructure reflections (SS), arising from in-ab-plane ordering of the TM ions and Li, shift to higher q, as well. Across the voltage plateau, and for ~ 100 $mAhg^{-1}$ on discharge, the peak positions remain almost constant, with a slight shift towards higher q for the (003) reflection, and a minute shift to lower q for (110). Afterwards, the revert to approximately the positions of the pristine material. Similar observations are made for Li-rich NM (fig. A.1).

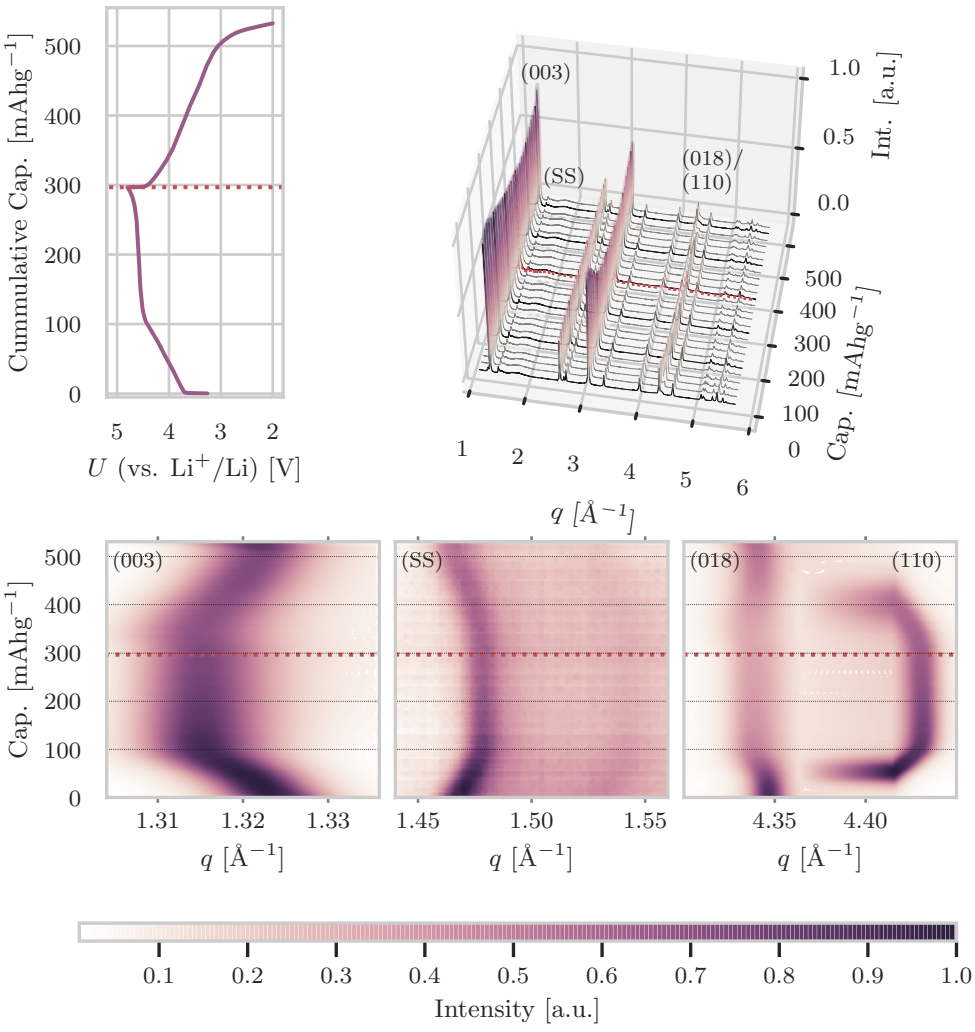


Figure A.1: *Operando* XRD of $Li_{1.2}Ni_{0.2}Mn_{0.6}O_2$.

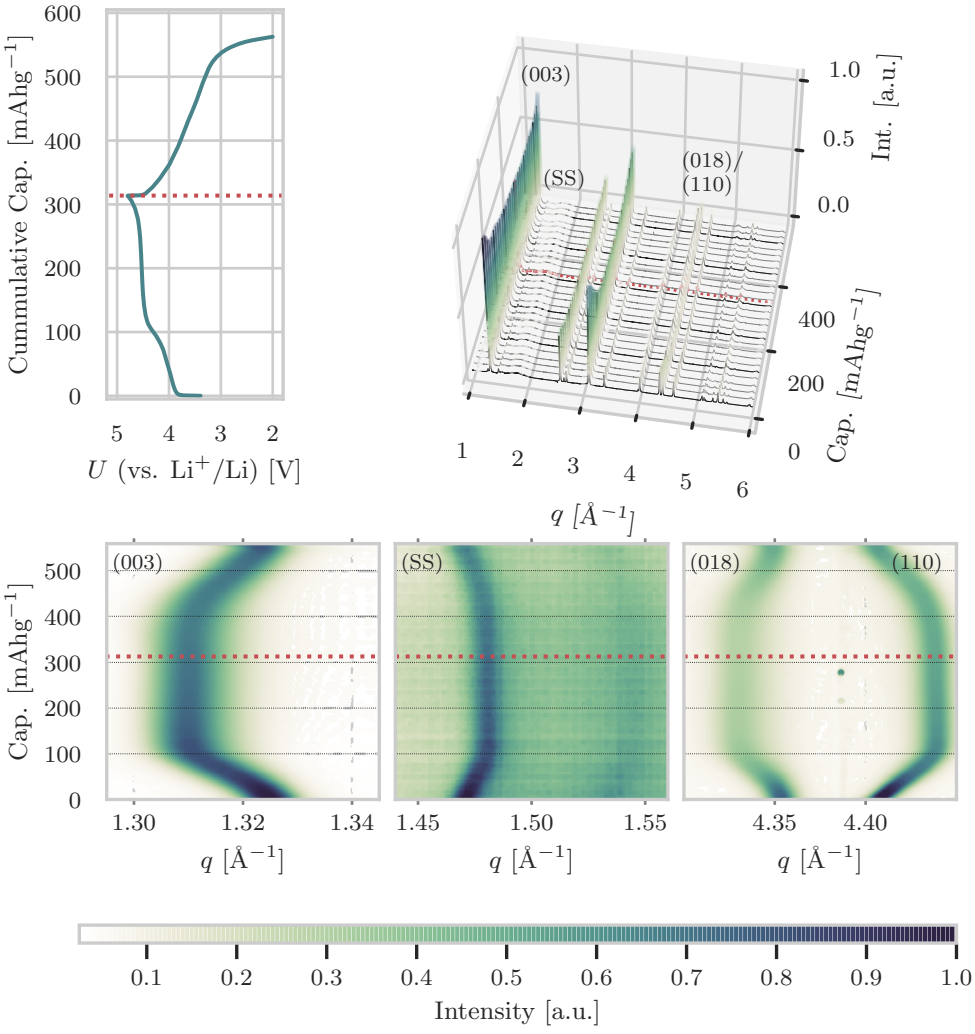


Figure A.2: *Operando* XRD of $Li_{1.2}Ni_{0.13}Co_{0.13}Mn_{0.54}O_2$.

Fitted Parameters Structures were refined against the XRD patterns, which were defined by R$\bar{3}$m space groups. An overview of the common fit parameters is given in tab. A.2. The used Li fraction depended on the respective capacity. Li was removed from Wyckoff Pos. 3a. Fit quality varied between patterns. All variables are listed in tab. A.3 for Li-rich NM and tab. A.4 for Li-rich NMC.

Table A.2: Common XRD refinement parameters for Li-rich layered materials.

Wyckoff Pos.	Atom	x	y	z	Occ.
3a	Li	0.0	0.0	0.0	Various
3b	Li	0.0	0.0	0.5	0.2
3b	Ni	0.0	0.0	0.5	0.2
3b	Mn	0.0	0.0	0.5	0.6
6c	O	0.0	0.0	0.24080	1.0

Space group: R$\bar{3}$m.

Table A.3: XRD: Refined parameters for $Li_{1.2}Ni_{0.2}Mn_{0.6}O_2$

Cumm. Cap. [mAhg^{-1}]	a [Å]	c [Å]	Volume [Å^3]	Li fraction [mol]	R_{wp} [%]
0	2.85827	14.24109	100.75835	1.2	20.9
9	2.85534	14.24332	100.56758	1.171	22.6
18	2.85254	14.24946	100.4139	1.143	20.6
28	2.84982	14.25406	100.25471	1.111	20.0
37	2.84716	14.25926	100.10406	1.083	19.7
47	2.84462	14.26568	99.9708	1.051	18.7
56	2.84216	14.27319	99.84992	1.022	18.7
65	2.83989	14.28203	99.7524	0.994	18.3
75	2.83742	14.28929	99.6298	0.962	18.0
84	2.8347	14.29385	99.47024	0.934	20.1
93	2.83249	14.2976	99.34163	0.905	19.9
103	2.83092	14.29924	99.2431	0.873	20.2
112	2.83011	14.29913	99.1854	0.845	19.3
122	2.82995	14.30022	99.18187	0.813	19.0
131	2.83034	14.30324	99.2301	0.784	19.0
140	2.83025	14.30303	99.22188	0.756	18.9
150	2.83023	14.3027	99.21839	0.724	18.3
159	2.83072	14.30622	99.27689	0.696	21.6
169	2.83113	14.30723	99.31322	0.664	19.6
178	2.83146	14.30809	99.34189	0.635	19.3
187	2.83158	14.30794	99.34939	0.607	18.9
197	2.83192	14.30893	99.38009	0.575	18.6
206	2.8323	14.31004	99.41439	0.546	18.5
216	2.83237	14.30968	99.41687	0.515	18.3
225	2.83245	14.30924	99.41986	0.486	18.4
234	2.83336	14.31547	99.52643	0.458	22.4
244	2.83343	14.3136	99.51876	0.426	19.7
253	2.83394	14.31541	99.56712	0.397	19.5
263	2.83392	14.31456	99.55972	0.366	19.3
272	2.83407	14.31445	99.56953	0.337	19.3
281	2.8341	14.31388	99.5675	0.309	19.1
291	2.83433	14.31436	99.58681	0.277	19.2
300	2.83462	14.31512	99.61276	0.248	19.0
310	2.83488	14.31586	99.63636	0.28	18.6
319	2.83533	14.31847	99.68629	0.309	20.1
328	2.83556	14.31794	99.6988	0.337	19.6
338	2.83604	14.31735	99.72841	0.369	19.3
347	2.83725	14.31807	99.81825	0.397	18.8
357	2.83842	14.31722	99.89513	0.429	18.5
366	2.83983	14.31578	99.98399	0.458	18.5
376	2.84153	14.31531	100.1008	0.489	18.2
385	2.84262	14.31011	100.14075	0.518	18.4
394	2.84313	14.30403	100.13412	0.546	21.9
404	2.84537	14.3025	100.28152	0.578	19.4
413	2.84718	14.29997	100.39091	0.607	19.7
423	2.8486	14.29533	100.45871	0.638	19.8
432	2.8507	14.29341	100.59352	0.667	19.4
441	2.85266	14.29053	100.71177	0.696	19.5
451	2.85467	14.28829	100.83773	0.727	19.6
460	2.85725	14.2888	101.02336	0.756	18.8
470	2.85902	14.28666	101.13351	0.788	18.8
479	2.85943	14.27899	101.1086	0.816	20.6
488	2.86117	14.27727	101.21901	0.845	20.9
498	2.86332	14.27762	101.37411	0.876	20.8
507	2.86466	14.27642	101.46055	0.905	21.6
517	2.86455	14.27232	101.42331	0.937	23.8
526	2.86695	14.2847	101.6817	0.965	18.5
532	2.8655	14.28275	101.56505	0.984	20.0

Table A.4: XRD: Refined parameters for $Li_{1.2}Ni_{0.13}Co_{0.13}Mn_{0.54}O_2$

Cumm. Cap. [mAhg^{-1}]	a [Å]	c [Å]	Volume [Å^3]	Li fraction [mol]	R_{wp} [%]
0	2.85076	14.22509	100.11648	1.2	9.6
9	2.84923	14.23014	100.04488	1.171	9.9
18	2.84731	14.24021	99.9804	1.143	9.7
28	2.8453	14.25254	99.92606	1.111	9.7
37	2.84329	14.26634	99.88146	1.082	9.8
47	2.84128	14.28166	99.84771	1.05	10.0
56	2.83927	14.2982	99.82196	1.022	10.1
65	2.83741	14.31508	99.80868	0.993	10.3
75	2.8357	14.33149	99.80253	0.961	10.5
84	2.83413	14.34741	99.80333	0.933	11.3
93	2.83286	14.36085	99.80729	0.904	10.6
103	2.83189	14.371	99.80942	0.872	10.7
112	2.83133	14.37671	99.8096	0.844	10.5
122	2.83114	14.37955	99.81595	0.812	10.4
131	2.83107	14.38142	99.82351	0.783	10.3
140	2.83104	14.38247	99.82919	0.755	10.2
150	2.83105	14.38303	99.83355	0.723	10.2
159	2.83107	14.38333	99.83678	0.694	10.0
169	2.83108	14.38353	99.8393	0.662	9.9
178	2.83111	14.38336	99.84036	0.634	9.8
187	2.83115	14.38326	99.84191	0.605	9.8
197	2.83119	14.38309	99.84348	0.573	9.9
206	2.83121	14.38276	99.84318	0.544	9.9
216	2.83127	14.38249	99.84497	0.513	10.1
225	2.8313	14.3823	99.84632	0.484	10.1
234	2.83135	14.3821	99.84846	0.455	10.4
244	2.83139	14.38182	99.84922	0.424	9.5
253	2.83142	14.38143	99.84873	0.395	9.6
263	2.83146	14.38121	99.84944	0.363	9.7
272	2.83149	14.38097	99.84988	0.334	9.9
281	2.83152	14.38069	99.85032	0.306	10.1
291	2.83155	14.38055	99.85137	0.274	10.1
300	2.83156	14.38024	99.84997	0.245	10.4
310	2.83155	14.38007	99.84785	0.277	10.8
319	2.83161	14.38	99.85156	0.306	10.8
328	2.8317	14.37996	99.8582	0.334	9.9
338	2.83182	14.3798	99.86563	0.366	9.9
347	2.83197	14.37969	99.8751	0.395	10.0
357	2.83215	14.3793	99.88522	0.427	10.2
366	2.83236	14.37823	99.89228	0.455	10.1
376	2.83262	14.37683	99.90139	0.487	10.2
385	2.83292	14.37473	99.90784	0.516	10.3
394	2.8333	14.37219	99.91703	0.544	10.3
404	2.8337	14.36888	99.92174	0.576	9.3
413	2.83416	14.36486	99.92653	0.605	9.2
423	2.83471	14.36023	99.93293	0.637	9.2
432	2.83536	14.35486	99.9414	0.665	9.1
441	2.83607	14.34811	99.94431	0.694	9.0
451	2.83694	14.34053	99.95332	0.726	9.2
460	2.83796	14.33172	99.96349	0.755	9.1
470	2.83912	14.32232	99.97948	0.786	9.3
479	2.84035	14.31254	99.99822	0.815	10.4
488	2.84174	14.30231	100.02399	0.844	8.7
498	2.84315	14.29211	100.05248	0.875	8.7
507	2.84461	14.28219	100.08526	0.904	8.7
517	2.84609	14.2729	100.12429	0.936	8.4
526	2.8476	14.26373	100.16649	0.965	8.4
535	2.84941	14.25403	100.22517	0.993	8.4
545	2.85132	14.24508	100.29706	1.025	8.1
554	2.85225	14.24476	100.35986	1.054	8.5
560	2.85275	14.24968	100.42994	1.073	8.1

A.3 Influence of Carbon and Binder on X-ray PDFs

In chapter 6 *ex-situ* X-ray PDF of cycled cathodes is used. To analyse the difference between the $G(r)$ obtained for pristine material, and the same material in a cathode, the functions for both are plotted in fig. A.3

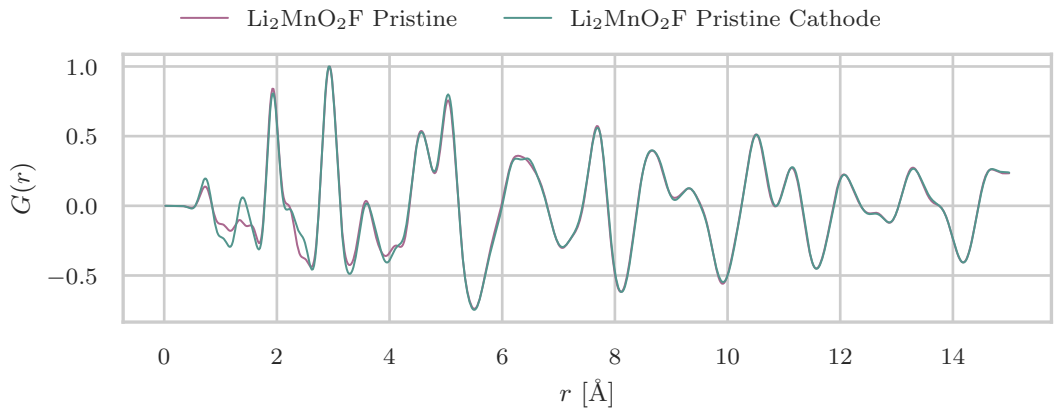


Figure A.3: Influence of binder and carbon on cathode X-ray PDF.

A.4 X-ray PDF Fit Details for Multi-Cycled Li_2MnO_2F Cathodes

In chapter 6 *ex-situ* X-ray PDF of cycled cathodes is presented. The following tables contain the 'Rietveld-like' fit parameters for each.

Table A.5: *Ex-situ* X-ray PDF and 'Rietveld - like' fit of a pristine Li_2MnO_2F cathode.

Wyckoff Pos.	Atom	x	y	z	Occ.	U_{iso}
4a	Li	0.0	0.0	0.0	0.667	0.0165567
4a	Mn	0.0	0.0	0.0	0.333	0.0165567
4b	O	0.5	0.5	0.5	0.667	0.0165567
4b	F	0.5	0.5	0.5	0.333	0.0165567

Space group: $Fm\bar{3}m$; Lattice constant: a = 4.13353; Fit quality: R_{wp} = 0.352028.

Table A.6: *Ex-situ* X-ray PDF and 'Rietveld - like' fit of a first-cycle discharged Li_2MnO_2F cathode.

Wyckoff Pos.	Atom	x	y	z	Occ.	U_{iso}
4a	Li	0.0	0.0	0.0	0.667	0.01652
4a	Mn	0.0	0.0	0.0	0.333	0.01652
4b	O	0.5	0.5	0.5	0.667	0.01652
4b	F	0.5	0.5	0.5	0.333	0.01652

Space group: $Fm\bar{3}m$; Lattice constant: a = 4.14697; Fit quality: R_{wp} = 0.347092.

Table A.7: *Ex-situ* X-ray PDF and 'Rietveld - like' fit of a second-cycle discharged Li_2MnO_2F cathode.

Wyckoff Pos.	Atom	x	y	z	Occ.	U_{iso}
4a	Li	0.0	0.0	0.0	0.667	0.0164753
4a	Mn	0.0	0.0	0.0	0.333	0.0164753
4b	O	0.5	0.5	0.5	0.667	0.0164753
4b	F	0.5	0.5	0.5	0.333	0.0164753

Space group: $Fm\bar{3}m$; Lattice constant: a = 4.147; Fit quality: R_{wp} = 0.346222.

Table A.8: *Ex-situ* X-ray PDF and 'Rietveld - like' fit of a fifth-cycle discharged Li_2MnO_2F cathode.

Wyckoff Pos.	Atom	x	y	z	Occ.	U_{iso}
4a	Li	0.0	0.0	0.0	0.667	0.0165214
4a	Mn	0.0	0.0	0.0	0.333	0.0165214
4b	O	0.5	0.5	0.5	0.667	0.0165214
4b	F	0.5	0.5	0.5	0.333	0.0165214

Space group: $Fm\bar{3}m$; Lattice constant: a = 4.14865; Fit quality: R_{wp} = 0.350854.

Table A.9: *Ex-situ* X-ray PDF and 'Rietveld - like' fit of a tenth-cycle discharged Li_2MnO_2F cathode.

Wyckoff Pos.	Atom	x	y	z	Occ.	U_{iso}
4a	Li	0.0	0.0	0.0	0.667	0.0166705
4a	Mn	0.0	0.0	0.0	0.333	0.0166705
4b	O	0.5	0.5	0.5	0.667	0.0166705
4b	F	0.5	0.5	0.5	0.333	0.0166705

Space group: $Fm\bar{3}m$; Lattice constant: a = 4.15041; Fit quality: R_{wp} = 0.353614.

Table A.10: *Ex-situ* X-ray PDF and 'Rietveld - like' fit of a twentieth-cycle discharged Li_2MnO_2F cathode.

Wyckoff Pos.	Atom	x	y	z	Occ.	U_{iso}
4a	Li	0.0	0.0	0.0	0.667	0.0161504
4a	Mn	0.0	0.0	0.0	0.333	0.0161504
4b	O	0.5	0.5	0.5	0.667	0.0161504
4b	F	0.5	0.5	0.5	0.333	0.0161504

Space group: $Fm\bar{3}m$; Lattice constant: a = 4.14702; Fit quality: R_{wp} = 0.407362.

Table A.11: *Ex-situ* X-ray PDF and 'Rietveld - like' fit of a first-cycle charged Li_2MnO_2F cathode.

Wyckoff Pos.	Atom	x	y	z	Occ.	U_{iso}
4a	Li	0.0	0.0	0.0	0.46	0.0169305
4a	Mn	0.0	0.0	0.0	0.333	0.0169305
4b	O	0.5	0.5	0.5	0.667	0.0169305
4b	F	0.5	0.5	0.5	0.333	0.0169305

Space group: $Fm\bar{3}m$; Lattice constant: a = 4.05551; Fit quality: R_{wp} = 0.496171.

Table A.12: *Ex-situ* X-ray PDF and 'Rietveld - like' fit of a second-cycle charged Li_2MnO_2F cathode.

Wyckoff Pos.	Atom	x	y	z	Occ.	U_{iso}
4a	Li	0.0	0.0	0.0	0.46	0.0167382
4a	Mn	0.0	0.0	0.0	0.333	0.0167382
4b	O	0.5	0.5	0.5	0.667	0.0167382
4b	F	0.5	0.5	0.5	0.333	0.0167382

Space group: $Fm\bar{3}m$; Lattice constant: a = 4.05485; Fit quality: R_{wp} = 0.482335.

Table A.13: *Ex-situ* X-ray PDF and 'Rietveld - like' fit of a fifth-cycle charged Li_2MnO_2F cathode.

Wyckoff Pos.	Atom	x	y	z	Occ.	U_{iso}
4a	Li	0.0	0.0	0.0	0.46	0.0162591
4a	Mn	0.0	0.0	0.0	0.333	0.0162591
4b	O	0.5	0.5	0.5	0.667	0.0162591
4b	F	0.5	0.5	0.5	0.333	0.0162591

Space group: $Fm\bar{3}m$; Lattice constant: a = 4.06116; Fit quality: R_{wp} = 0.485304.

Table A.14: *Ex-situ* X-ray PDF and 'Rietveld - like' fit of a tenth-cycle charged Li_2MnO_2F cathode.

Wyckoff Pos.	Atom	x	y	z	Occ.	U_{iso}
4a	Li	0.0	0.0	0.0	0.46	0.0157986
4a	Mn	0.0	0.0	0.0	0.333	0.0157986
4b	O	0.5	0.5	0.5	0.667	0.0157986
4b	F	0.5	0.5	0.5	0.333	0.0157986

Space group: $Fm\bar{3}m$; Lattice constant: a = 4.05497; Fit quality: R_{wp} = 0.483935.

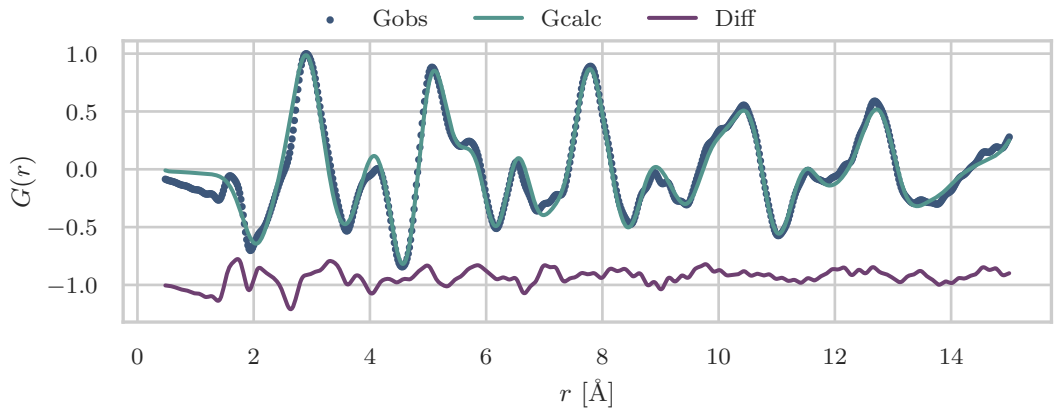
Table A.15: *Ex-situ* X-ray PDF and 'Rietveld - like' fit of a twentieth-cycle charged Li_2MnO_2F cathode.

Wyckoff Pos.	Atom	x	y	z	Occ.	U_{iso}
4a	Li	0.0	0.0	0.0	0.46	0.0152824
4a	Mn	0.0	0.0	0.0	0.333	0.0152824
4b	O	0.5	0.5	0.5	0.667	0.0152824
4b	F	0.5	0.5	0.5	0.333	0.0152824

Space group: $Fm\bar{3}m$; Lattice constant: a = 4.05959; Fit quality: R_{wp} = 0.485128.

A.5 Neutron PDF Fit Details for Multi-Cycled Li_2MnO_2F

In chapter 6 *ex-situ* neutron PDF of cycled cathodes is presented. The following tables contain the 'Rietveld-like' fit parameters for each.

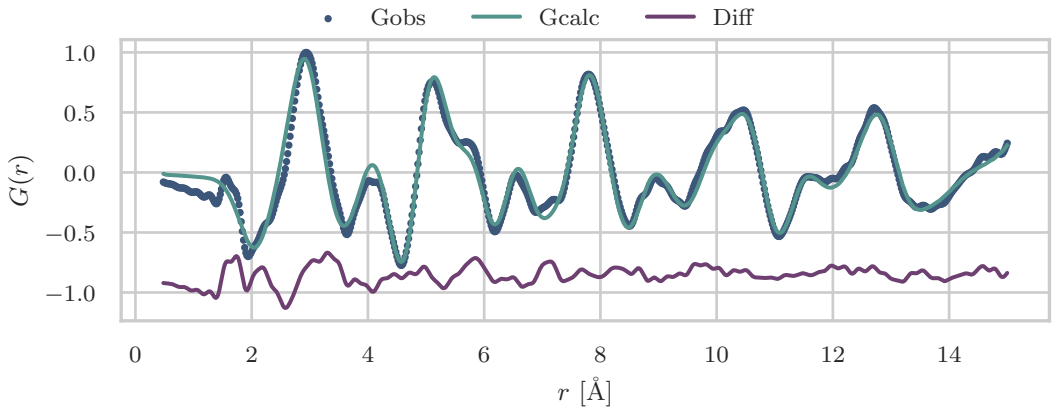


Wyckoff Pos.	Atom	x	y	z	Occ.	U_{iso}
4a	Li	0.0	0.0	0.0	0.517	0.0274
4a	Mn	0.0	0.0	0.0	0.333	0.0274
4b	O	0.5	0.5	0.5	0.667	0.0274
4b	F	0.5	0.5	0.5	0.333	0.0274

Space group: $Fm\bar{3}m$; Lattice constant: a = 4.1393(2); Fit Quality: R_{wp} = 0.193115.

,

Figure A.4: *Ex-situ* neutron PDF and 'Rietveld - like' fit of first cycle discharged Li_2MnO_2F.

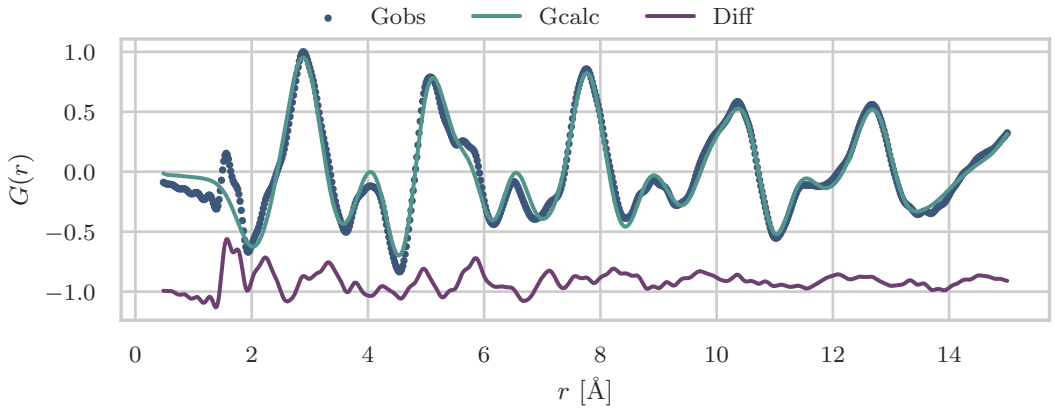


Wyckoff Pos.	Atom	x	y	z	Occ.	U_{iso}
4a	Li	0.0	0.0	0.0	0.641	0.0318
4a	Mn	0.0	0.0	0.0	0.333	0.0318
4b	O	0.5	0.5	0.5	0.667	0.0318
4b	F	0.5	0.5	0.5	0.333	0.0318

Space group: $Fm\bar{3}m$; Lattice constant: a = 4.1547(8); Fit Quality:R_{wp} = 0.205658.

,

Figure A.5: *Ex-situ* neutron PDF and 'Rietveld - like' fit of five cycle discharged Li_2MnO_2F.



Wyckoff Pos.	Atom	x	y	z	Occ.	U_{iso}
4a	Li	0.0	0.0	0.0	0.517	0.0368
4a	Mn	0.0	0.0	0.0	0.333	0.0368
4b	O	0.5	0.5	0.5	0.667	0.0368
4b	F	0.5	0.5	0.5	0.333	0.0368

Space group: $Fm\bar{3}m$; Lattice constant: a = 4.1320(9); Fit Quality: R_{wp} = 0.228836.

,

Figure A.6: *Ex-situ* neutron PDF and 'Rietveld - like' fit of 30 cycle discharged Li_2MnO_2F.

A.6 Impedance Spectra and Fit Parameters for Multi-Cycled Li_2MnO_2F

In chapter 6 three-electrode impedance data is discussed. The following section contains the collected spectra and fit parameters for all data not presented in the chapter itself.

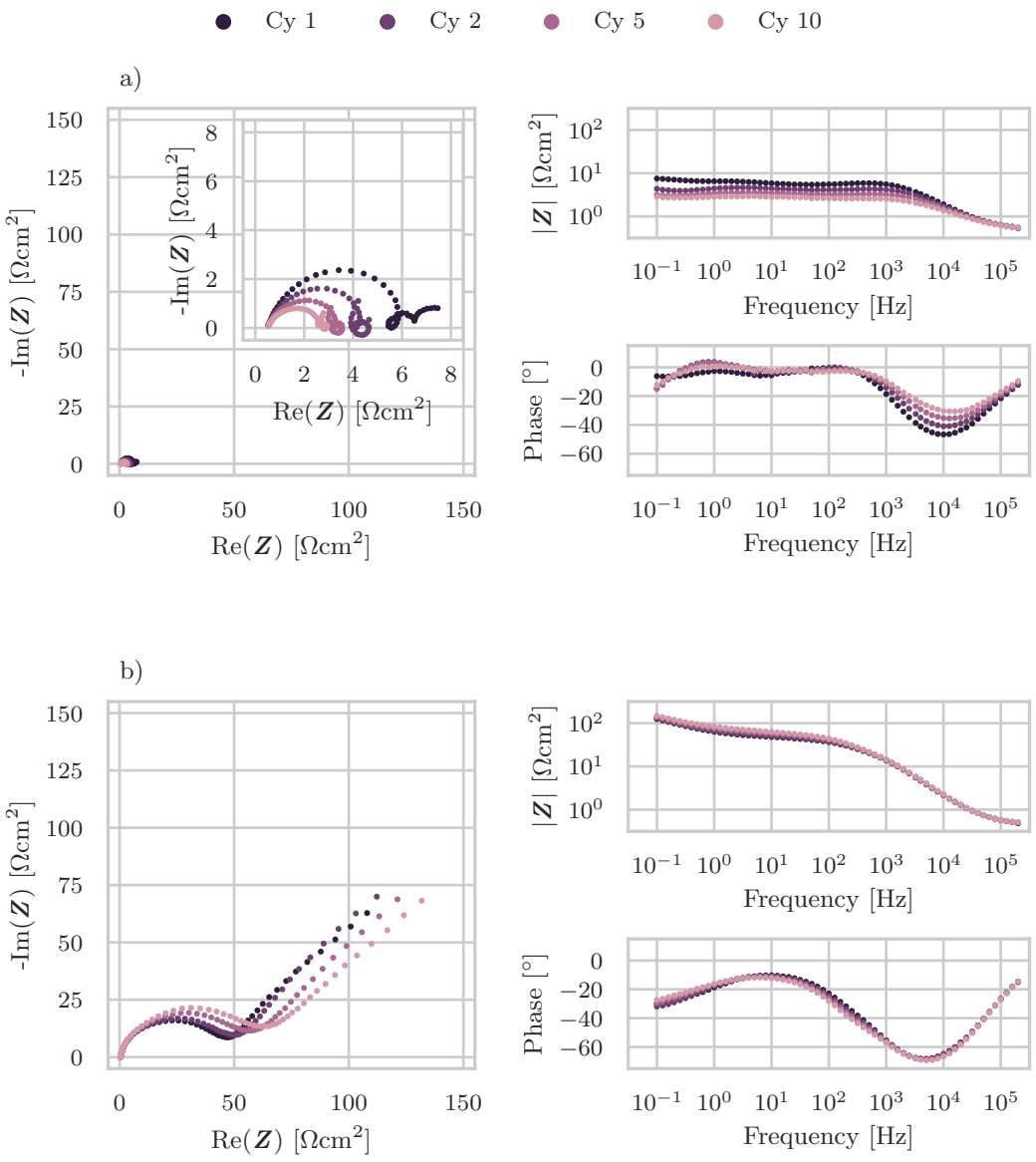


Figure A.7: Impedance of Li_2MnO_2F at 2.0 V voltage hold. Fitted parameters are listed in tab. A.17.

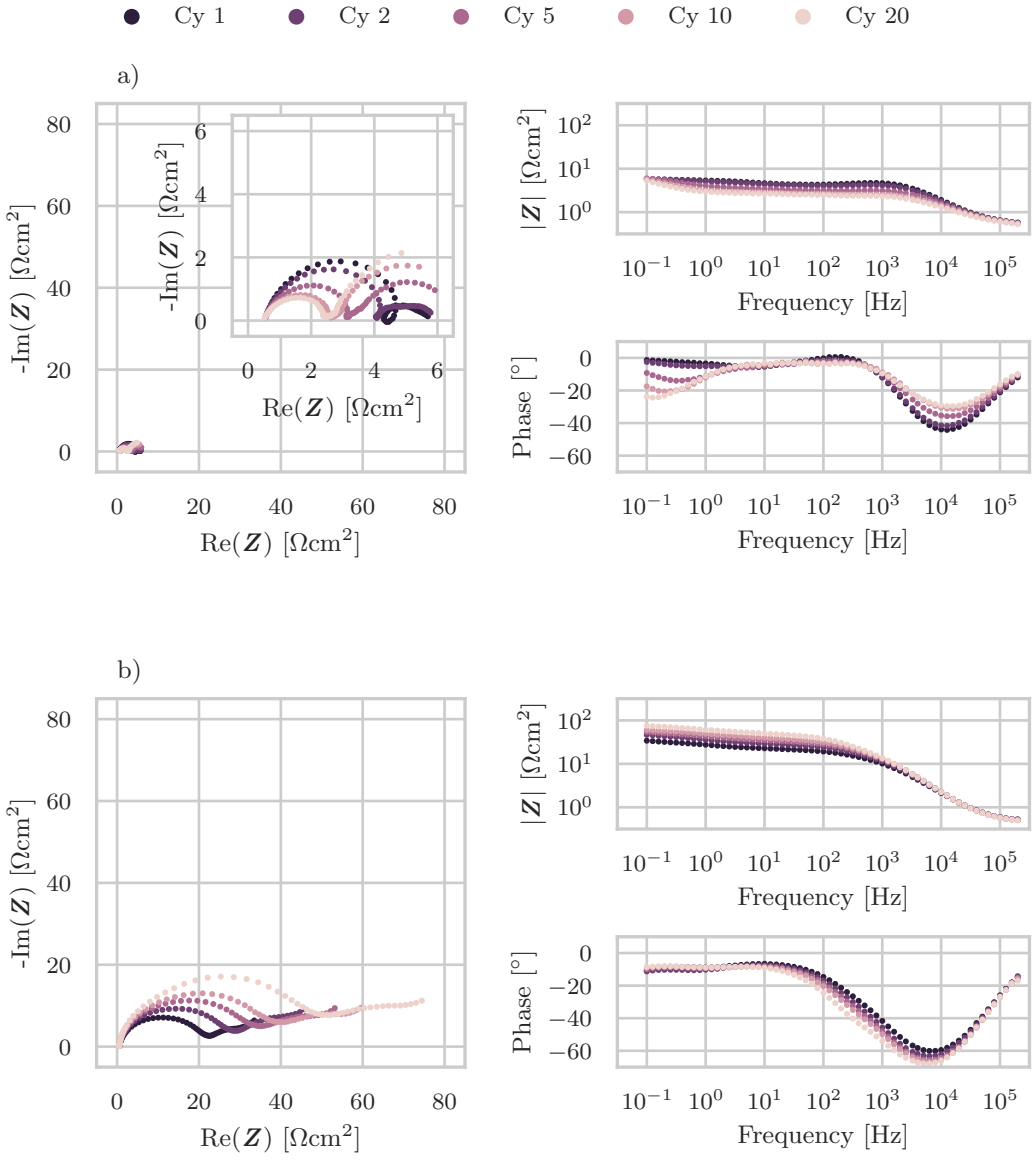


Figure A.8: Impedance of Li_2MnO_2F at 4.8 V voltage hold. Fitted parameters are listed in tab. A.18.

Table A.16: Fit Parameters for the cathode of cycled Li_2MnO_2F obtained at OCV after discharge in a three-electrode cell (fig. 6.10). Fit using the equivalent circuit depicted in fig. 6.11.

Cy	χ^2	R_1	Err R_1	R_2	Err R_2	Y_1	Err Y_1	α_1	Err α_1	R_3	Err R_3	Y_2	Err Y_2	α_2	Err α_2	R_4	Err R_4	Y_3	Err Y_3	α_3	Err α_3
1	4.2E-5	1.06	0.4	28.1	4.5	1.0E-4	4.4	0.91	1.4	32.5	3.6	3.4E-5	2.0	0.85	0.2	516	5.0	8.3E-3	0.7	0.53	1.0
2	6.6E-5	1.32	0.5	27.6	5.6	9.0E-5	5.8	0.98	1.7	45.6	3.3	4.4E-5	2.4	0.81	0.3	585	6.6	7.2E-3	0.9	0.53	1.4
5	1.0E-4	1.56	1.0	64.7	5.0	5.4E-5	4.1	0.97	1.4	45.7	7.2	5.2E-5	3.9	0.81	0.7	801	7.1	5.7E-3	1.3	0.45	1.1
10	1.0E-4	2.03	0.9	140	3.5	4.4E-5	2.8	0.98	1.2	49.7	9.2	8.5E-5	4.7	0.79	0.9	402	2.3	3.0E-3	2.5	0.47	0.9

Resistances (R_i) in Ωcm^2; Capacitances (Y_i) in Fcm^{-2}; Errors (Err) in %. The constant phase element exponents (α_i) are dimensionless.

Table A.17: Fit Parameters for the cathode of cycled Li_2MnO_2F obtained during a 2.0 V voltage hold in a three-electrode cell (fig. A.7).Fit using the equivalent circuit depicted in fig. 6.11.

Cy	χ^2	R_1	Err R_1	R_2	Err R_2	Y_1	Err Y_1	α_1	Err α_1	R_3	Err R_3	Y_2	Err Y_2	α_2	Err α_2	R_4	Err R_4	Y_3	Err Y_3	α_3	Err α_3
1	8.1E-5	0.46	0.4	12.8	7.7	2.2E-5	4.5	0.97	1.0	31.0	3.4	1.0E-4	4.5	0.84	0.6	410	7.3	1.2E-2	0.9	0.60	1.1
2	1.7E-4	0.45	0.7	11.1	10	2.1E-5	7.6	0.98	1.5	35.2	3.7	9.6E-5	4.4	0.84	0.9	1207	35	1.3E-2	1.4	0.57	1.9
5	3.3E-4	0.45	1.2	11.0	18	1.9E-5	11	0.99	2.5	40.4	6.5	7.6E-5	5.6	0.86	2.3	753	34	1.2E-2	2.1	0.55	3.5
10	4.8E-4	0.45	1.5	10.2	21	1.8E-5	15	1.00	3.0	46.3	6.8	6.8E-5	7.3	0.87	2.8	449	22	1.1E-2	2.4	0.55	4.2

Resistances (R_i) in Ωcm^2; Capacitances (Y_i) in Fcm^{-2}; Errors (Err) in %. The constant phase element exponents (α_i) are dimensionless.

Table A.18: Fit Parameters for the cathode of cycled Li_2MnO_2F obtained during a 4.8 V voltage hold in a three-electrode cell (fig. A.8).Fit using the equivalent circuit depicted in fig. 6.11.

Cy	χ^2	R_1	Err R_1	R_2	Err R_2	Y_1	Err Y_1	α_1	Err α_1	R_3	Err R_3	Y_2	Err Y_2	α_2	Err α_2	R_4	Err R_4	Y_3	Err Y_3	α_3	Err α_3
1	1.8E-4	0.46	1.1	8.48	17	3.3E-5	4.0	0.91	1.5	11.4	15	1.5E-4	8.1	0.85	3.8	25.1	5.8	4.0E-2	2.6	0.48	4.2
2	9.3E-5	0.46	0.7	9.23	15	2.7E-5	4.1	0.93	1.6	16.3	10	1.2E-4	5.0	0.85	2.6	36.5	4.3	2.8E-2	1.5	0.51	3.1
5	1.6E-4	0.46	1.1	9.05	16	2.0E-5	6.7	0.97	1.9	21.5	8.8	8.8E-5	5.7	0.87	2.8	35.3	4.5	2.0E-2	2.2	0.52	3.7
10	2.1E-4	0.46	1.2	8.70	17	1.8E-5	8.1	0.98	2.0	26.0	7.8	7.3E-5	6.7	0.87	2.8	35.7	4.5	1.6E-2	2.7	0.53	3.8

Resistances (R_i) in Ωcm^2; Capacitances (Y_i) in Fcm^{-2}; Errors (Err) in %. The constant phase element exponents (α_i) are dimensionless.

References

[1] J. L. Heilbron in *The American Historical Review*, University of California Press, **1979**, p. 309.

[2] A. Volta, *Philosophical Transactions of the Royal Society of London* **1800**, *90*, 403.

[3] H. Toftlund, *Ionics* **2001**, *7*, 161.

[4] J. W. Ritter, *Magazin für den Neußten Zustand der Naturkunde* **1803**, *6*, 97.

[5] W. J. Sinsteden, *Annalen der Physik* **1854**, *168*, 220.

[6] G. Planté, *Recherches Sur l'Électricité*, Gauthier-Villars, Imprimeur-Libraire, Paris, **1883**.

[7] B. Scrosati, *Journal of Solid State Electrochemistry* **2011**, *15*, 1623.

[8] M. S. Whittingham, *Journal of The Electrochemical Society* **1976**, *123*, 315.

[9] K Mizushima, P. C. Jones, P. J. Wiseman, J. B. Goodenough, *Materials Research Bulletin* **1980**, *15*, 783.

[10] M. M. Thackeray, W. I. David, P. G. Bruce, J. B. Goodenough, *Materials Research Bulletin* **1983**, *18*, 461.

[11] R. Yazami, P. Touzain, *Journal of Power Sources* **1983**, *9*, 365.

[12] M. B. Armand in *NATO Conference Series 6: Materials Science*, *Vol. 2*, Plenum Press, **1980**, p. 145.

[13] A. Yoshino, K. Sanechika, T. Nakajima, US patent 4668595A, **1986**.

[14] T. Nagaura, K. Tozawa, *Progress in Batteries & Solar Cells* **1990**, *9*, 209.

[15] T. Ohzuku, R. J. Brodd, *Journal of Power Sources* **2007**, *174*, 449.

[16] Nobel Foundation, Nobel Media AB 2020, Press release: The Nobel Prize in Chemistry 2019, https://www.nobelprize.org/prizes/chemistry/2019/press-release/ (accessed: 2020-03-04), **2019**.

[17] G. E. Blomgren, *Journal of The Electrochemical Society* **2017**, *164*, A5019.

[18] N. Nitta, F. Wu, J. T. Lee, G. Yushin, *Materials Today* **2015**, *18*, 252.

[19] T. V. Satyavani, A. Srinivas Kumar, P. S. Subba Rao, *Engineering Science and Technology an International Journal* **2016**, *19*, 178.

[20] A. Mauger, C. M. Julien, *Batteries* **2018**, *4*, 39.

[21] K. Luo, M. R. Roberts, N. Guerrini, N. Tapia-Ruiz, R. Hao, F. Massel, D. M. Pickup, S. Ramos, Y. S. Liu, J. Guo, A. V. Chadwick, L. C. Duda, P. G. Bruce, *Journal of the American Chemical Society* **2016**, *138*, 11211.

[22] K. Luo, M. R. Roberts, R. Hao, N. Guerrini, D. M. Pickup, Y.-S. Liu, K. Edström, J. Guo, A. V. Chadwick, L. C. Duda, P. G. Bruce, *Nature Chemistry* **2016**, *8*, 684.

[23] Z. Lu, D. D. MacNeil, J. R. Dahn, *Electrochemical and Solid-State Letters* **2001**, *4*, A191.

[24] Z. Lu, L. Y. Beaulieu, R. A. Donaberger, C. L. Thomas, J. R. Dahn, *Journal of The Electrochemical Society* **2002**, *149*, A778.

[25] R. A. House, U. Maitra, M. A. Pérez-Osorio, J. G. Lozano, L. Jin, J. W. Somerville, L. C. Duda, A. Nag, A. Walters, K.-J. Zhou, M. R. Roberts, P. G. Bruce, *Nature* **2020**, *577*, 502.

[26] N. Yabuuchi, H. Yoshida, S. Komaba, *Electrochemistry* **2012**, *80*, 716.

[27] C. Delmas, C. Fouassier, P. Hagenmuller, *Physica B+C* **1980**, *99*, 81.

[28] H. Koga, L. Croguennec, P. Mannessiez, M. Ménétrier, F. Weill, L. Bourgeois, M. Duttine, E. Suard, C. Delmas, *The Journal of Physical Chemistry C* **2012**, *116*, 13497.

[29] P. Yan, A. Nie, J. Zheng, Y. Zhou, D. Lu, X. Zhang, R. Xu, I. Belharouak, X. Zu, J. Xiao, K. Amine, J. Liu, F. Gao, R. Shahbazian-Yassar, J. G. Zhang, C. M. Wang, *Nano Letters* **2015**, *15*, 514.

[30] C. Storey, I. Kargina, Y. Grincourt, I. J. Davidson, Y. C. Yoo, D. Y. Seung, *Journal of Power Sources* **2001**, *97-98*, 541.

[31] B. Ammundsen, J. Paulsen, I. Davidson, R.-S. Liu, C.-H. Shen, J.-M. Chen, L.-Y. Jang, J.-F. Lee, *Journal of The Electrochemical Society* **2002**, *149*, A431.

[32] K. Numata, C. Sakaki, S. Yamanaka, *Chemistry Letters* **1997**, *26*, 725.

[33] Z. Lu, J. R. Dahn, *Journal of The Electrochemical Society* **2002**, *149*, A815.

[34] M. Jiang, B. Key, Y. S. Meng, C. P. Grey, *Chemistry of Materials* **2009**, *21*, 2733.

[35] N. Tran, L. Croguennec, M. Ménétrier, F. Weill, P. Biensan, C. Jordy, C. Delmas, *Chemistry of Materials* **2008**, *20*, 4815.

[36] A. R. Armstrong, M. Holzapfel, P. Novk, S Christopher, S.-h. Kang, M. M. Thackeray, P. G. Bruce, L. Ni, L. Mn, P. Nova, C. S. Johnson, *Journal of the American Chemical Society* **2006**, *128*, 8694.

[37] C. P. Grey, W. S. Yoon, J. Reed, G. Ceder, *Electrochemical and Solid-State Letters* **2004**, *7*, 290.

[38] Y. S. Hong, Y. J. Park, X. Wu, K. S. Ryu, S. H. Chang, *Electrochemical and Solid-State Letters* **2003**, *6*, A166.

[39] A. Ito, Y. Sato, T. Sanada, M. Hatano, H. Horie, Y. Ohsawa, *Journal of Power Sources* **2011**, *196*, 6828.

[40] N. Yabuuchi, K. Yoshii, S. T. Myung, I. Nakai, S. Komaba, *Journal of the American Chemical Society* **2011**, *133*, 4404.

[41] H. Koga, L. Croguennec, M. Ménétrier, P. Mannessiez, F. Weill, C. Delmas, *Journal of Power Sources* **2013**, *236*, 250.

[42] H. Koga, L. Croguennec, M. Ménétrier, K. Douhil, S. Belin, L. Bourgeois, E. Suard, F. Weill, C. Delmas, *Journal of The Electrochemical Society* **2013**, *160*, A786.

[43] M. Oishi, T. Fujimoto, Y. Takanashi, Y. Orikasa, A. Kawamura, T. Ina, H. Yamashige, D. Takamatsu, K. Sato, H. Murayama, H. Tanida, H. Arai, H. Ishii, C. Yogi, I. Watanabe, T. Ohta, A. Mineshige, Y. Uchimoto, Z. Ogumi, *Journal of Power Sources* **2013**, *222*, 45.

[44] D.-H. Seo, J. Lee, A. Urban, R. Malik, S. Kang, G. Ceder, *Nature Chemistry* **2016**, *8*, 692.

[45] N. Yabuuchi, R. Hara, M. Kajiyama, K. Kubota, T. Ishigaki, A. Hoshikawa, S. Komaba, *Advanced Energy Materials* **2014**, *4*, 1301453.

[46] N. Yabuuchi, R. Hara, K. Kubota, J. Paulsen, S. Kumakura, S. Komaba, *Journal of Materials Chemistry A* **2014**, *2*, 16851.

[47] K. Du, J. Zhu, G. Hu, H. Gao, Y. Li, J. B. Goodenough, *Energy and Environmental Science* **2016**, *9*, 2575.

[48] P. Rozier, M. Sathiya, A.-R. Paulraj, D. Foix, T. Desaunay, P.-L. Taberna, P. Simon, J.-M. Tarascon, *Electrochemistry Communications* **2015**, *53*, 29.

[49] U. Maitra, R. A. House, J. W. Somerville, N. Tapia-Ruiz, J. G. Lozano, N. Guerrini, R. Hao, K. Luo, L. Jin, M. A. Pérez-Osorio, F. Massel, D. M. Pickup, S. Ramos, X. Lu, D. E. McNally, A. V. Chadwick, F. Giustino, T. Schmitt, L. C. Duda, M. R. Roberts, P. G. Bruce, *Nature Chemistry* **2018**, *10*, 288.

[50] A. J. Perez, D. Batuk, M. Saubanère, G. Rousse, D. Foix, E. McCalla, E. J. Berg, R. Dugas, K. H. Van Den Bos, M. L. Doublet, D. Gonbeau, A. M. Abakumov, G. Van Tendeloo, J. M. Tarascon, *Chemistry of Materials* **2016**, *28*, 8278.

[51] R. A. House, U. Maitra, L. Jin, J. G. Lozano, J. W. Somerville, N. H. Rees, A. J. Naylor, L. C. Duda, F. Massel, A. V. Chadwick, S. Ramos, D. M. Pickup, D. E. McNally, X. Lu, T. Schmitt, M. R. Roberts, P. G. Bruce, *Chemistry of Materials* **2019**, *31*, 3293.

[52] M. Sathiya, G. Rousse, K. Ramesha, C. P. Laisa, H. Vezin, M. T. Sougrati, M.-L. Doublet, D. Foix, D. Gonbeau, W. Walker, A. S. Prakash, M. Ben Hassine, L. Dupont, J.-M. Tarascon, *Nature Materials* **2013**, *12*, 827.

[53] M. Sathiya, A. M. Abakumov, D. Foix, G. Rousse, K. Ramesha, M. Saubanère, M. L. Doublet, H. Vezin, C. P. Laisa, A. S. Prakash, D. Gonbeau, G. Vantendeloo, J. M. Tarascon, *Nature Materials* **2015**, *14*, 230.

[54] B. Mortemard de Boisse, G. Liu, J. Ma, S.-i. Nishimura, S.-C. Chung, H. Kiuchi, Y. Harada, J. Kikkawa, Y. Kobayashi, M. Okubo, A. Yamada, *Nature Communications* **2016**, *7*, 11397.

[55] G. Assat, A. Iadecola, C. Delacourt, R. Dedryvère, J. M. Tarascon, *Chemistry of Materials* **2017**, *29*, 9714.

[56] P. E. Pearce, A. J. Perez, G. Rousse, M. Saubanère, D. Batuk, D. Foix, E. McCalla, A. M. Abakumov, G. Van Tendeloo, M. L. Doublet, J. M. Tarascon, *Nature Materials* **2017**, *16*, 580.

[57] W. E. Gent, K. Lim, Y. Liang, Q. Li, T. Barnes, S. J. Ahn, K. H. Stone, M. McIntire, J. Hong, J. H. Song, Y. Li, A. Mehta, S. Ermon, T. Tyliszczak, D. Kilcoyne, D. Vine, J. H. Park, S. K. Doo, M. F. Toney, W. Yang, D. Prendergast, W. C. Chueh, *Nature Communications* **2017**, *8*, 2091.

[58] E. McCalla, A. M. Abakumov, M. Saubanere, D. Foix, E. J. Berg, G. Rousse, M.-L. Doublet, D. Gonbeau, P. Novak, G. Van Tendeloo, R. Dominko, J.-M. Tarascon, *Science* **2015**, *350*, 1516.

[59] Y. Xie, M. Saubanère, M. L. Doublet, *Energy and Environmental Science* **2017**, *10*, 266.

[60] M Saubanere, E McCalla, J.-M. Tarascon, M.-L. Doublet, *Energy and Environmental Science* **2016**, 984.

[61] M. Sathiya, J. B. Leriche, E. Salager, D. Gourier, J. M. Tarascon, H. Vezin, *Nature Communications* **2015**, *6*, 1.

[62] J. R. Croy, K. G. Gallagher, M. Balasubramanian, Z. Chen, Y. Ren, D. Kim, S. H. Kang, D. W. Dees, M. M. Thackeray, *Journal of Physical Chemistry C* **2013**, *117*, 6525.

[63] J. R. Croy, H. Iddir, K. Gallagher, C. S. Johnson, R. Benedek, M. Balasubramanian, *Physical Chemistry Chemical Physics* **2015**, *17*, 24382.

[64] X. Rong, J. Liu, E. Hu, Y. Liu, Y. Wang, J. Wu, X. Yu, K. Page, Y. S. Hu, W. Yang, H. Li, X. Q. Yang, L. Chen, X. Huang, *Joule* **2018**, *2*, 125.

[65] J. Reed, G. Ceder, *Chemical Reviews* **2004**, *104*, 4513.

[66] K. G. Gallagher, J. R. Croy, M. Balasubramanian, M. Bettge, D. P. Abraham, A. K. Burrell, M. M. Thackeray, *Electrochemistry Communications* **2013**, *33*, 96.

[67] K. Kleiner, B. Strehle, A. R. Baker, S. J. Day, C. C. Tang, I. Buchberger, F. F. Chesneau, H. A. Gasteiger, M. Piana, *Chemistry of Materials* **2018**, *30*, 3656.

[68] A. Boulineau, L. Simonin, J. F. Colin, C. Bourbon, S. Patoux, *Nano Letters* **2013**, *13*, 3857.

[69] D. Qian, B. Xu, M. Chi, Y. S. Meng, *Physical Chemistry Chemical Physics* **2014**, *16*, 14665.

[70] M. N. Obrovac, O. Mao, J. R. Dahn, *Solid State Ionics* **1998**, *112*, 9.

[71] Y. Sakurai, H. Arai, J. I. Yamaki, *Solid State Ionics* **1998**, *113-115*, 29.

[72] K. Kang, D. Carlier, J. Reed, E. M. Arroyo, G. Ceder, L. Croguennec, C. Delmas, *Chemistry of Materials* **2003**, *15*, 4503.

[73] S. H. Chang, S. G. Kang, S. W. Song, J. B. Yoon, J. H. Choy, *Solid State Ionics* **1996**, *86-88*, 171.

[74] K. Ozawa, Y. Nakao, L. Wang, Z. Cheng, H. Fujii, M. Hase, M. Eguchi, *Journal of Power Sources* **2007**, *174*, 469.

[75] J. Lee, A. Urban, X. Li, D. Su, G. Hautier, G. Ceder, *Science* **2014**, *343*, 519.

[76] C. Delmas, S. Brèthes, M. Ménétrier, *Journal of Power Sources* **1991**, *34*, 113.

[77] M. Freire, N. V. Kosova, C. Jordy, D. Chateigner, O. I. Lebedev, A. Maignan, V. Pralong, *Nature Materials* **2015**, *15*, 1.

[78] R. Chen, S. Ren, M. Knapp, D. Wang, R. Witter, M. Fichtner, H. Hahn, *Advanced Energy Materials* **2015**, *5*, 1401814.

[79] T. Sato, K. Sato, W. Zhao, Y. Kajiya, N. Yabuuchi, *Journal of Materials Chemistry A* **2018**, *6*, 13943.

[80] K. Sato, M. Nakayama, A. M. Glushenkov, T. Mukai, Y. Hashimoto, K. Yamanaka, M. Yoshimura, T. Ohta, N. Yabuuchi, *Chemistry of Materials* **2017**, *29*, 5043.

[81] N. Yabuuchi, M. Takeuchi, M. Nakayama, H. Shiiba, M. Ogawa, K. Nakayama, T. Ohta, D. Endo, T. Ozaki, T. Inamasu, K. Sato, S. Komaba, *Proceedings of the National Academy of Sciences of the United States of America* **2015**, *112*, 7650.

[82] N. Yabuuchi, M. Nakayama, M. Takeuchi, S. Komaba, Y. Hashimoto, T. Mukai, H. Shiiba, K. Sato, Y. Kobayashi, A. Nakao, M. Yonemura, K. Yamanaka, K. Mitsuhara, T. Ohta, *Nature Communications* **2016**, *7*, 13814.

[83] M. Nakajima, N. Yabuuchi, *Chemistry of Materials* **2017**, *29*, 6927.

[84] J. Lee, D. A. Kitchaev, D.-H. Kwon, C.-W. Lee, J. K. Papp, Y.-S. Liu, Z. Lun, R. J. Clément, T. Shi, B. D. McCloskey, J. Guo, M. Balasubramanian, G. Ceder, *Nature* **2018**, *556*, 185.

[85] R. J. Clement, Z. Lun, G. Ceder, *Energy and Environmental Science* **2020**, *13*, 345.

[86] J. C. Fisher, *Journal of Applied Physics* **1951**, *22*, 74.

[87] A. Urban, A. Abdellahi, S. Dacek, N. Artrith, G. Ceder, *Physical Review Letters* **2017**, *119*, 176402.

[88] R. A. House, L. Jin, U. Maitra, K. Tsuruta, J. W. Somerville, D. P. Förstermann, F. Massel, L. Duda, M. R. Roberts, P. G. Bruce, *Energy and Environmental Science* **2018**, *11*, 926–932.

[89] N. Recham, J. N. Chotard, L. Dupont, C. Delacourt, W. Walker, M. Armand, J. M. Tarascon, *Nature Materials* **2010**, *9*, 68.

[90] N. Pereira, F. Badway, M. Wartelsky, S. Gunn, G. G. Amatucci, *Journal of The Electrochemical Society* **2009**, *156*, A407.

[91] A. R. Naghash, J. Y. Lee, *Electrochimica Acta* **2001**, *46*, 2293.

[92] R. Chen, S. Ren, M. Yavuz, A. a. Guda, V. Shapovalov, R. Witter, M. Fichtner, H. Hahn, *Physical Chemistry Chemical Physics* **2015**, *17*, 17288.

[93] S. Ren, R. Chen, E. Maawad, O. Dolotko, A. A. Guda, V. Shapovalov, D. Wang, H. Hahn, M. S. Fichtner Ren, R Chen, D Wang, H Hahn, M Fichtner, E Maawad, O Dolotko, A. A. Guda, V Shapovalov, *Advanced Science* **2015**, *2*, 1500128.

[94] Y. Tomita, H. Nasu, Y. Izumi, J. Arai, S. Otsuka, Y. Yamane, K. Yamada, Y. Kohno, K. Kobayashi, *Journal of Power Sources* **2016**, *329*, 406.

[95] N. Takeda, S. Hoshino, L. Xie, S. Chen, I. Ikeuchi, R. Natsui, K. Nakura, N. Yabuuchi, *Journal of Power Sources* **2017**, *367*, 122.

[96] D. A. Kitchaev, Z. Lun, W. D. Richards, H. Ji, R. J. Clément, M. Balasubramanian, D. H. Kwon, K. Dai, J. K. Papp, T. Lei, B. D. McCloskey, W. Yang, J. Lee, G. Ceder, *Energy and Environmental Science* **2018**, *11*, 2159.

[97] M. E. Orazem, B. Tribollet, *Electrochemical Impedance Spectroscopy*, 2nd ed., Wiley, Hoboken, NJ, **2017**.

[98] C. Julien, A. Mauger, K. Zaghib, H. Groult, *Materials* **2016**, *9*, 595.

[99] C. N. Rao, *Materials Science and Engineering B* **1993**, *18*, 1.

[100] N. Yabuuchi, Y.-C. Lu, A. N. Mansour, T. Kawaguchi, Y. Shao-Horn, *Electrochemical and Solid-State Letters* **2010**, *13*, A158.

[101] K. M. Shaju, P. G. Bruce, *Advanced Materials* **2006**, *18*, 2330.

[102] M. Leonardi, M. Villacampa, J. C. Menendez, *Chemical Science* **2018**, *9*, 2042.

[103] P. C. Tsai, B. Wen, M. Wolfman, M. J. Choe, M. S. Pan, L. Su, K. Thornton, J. Cabana, Y. M. Chiang, *Energy and Environmental Science* **2018**, *11*, 860.

[104] H. Kondo, H. Sawada, C. Okuda, T. Sasaki, *Journal of the Electrochemical Society* **2019**, *166*, A1285.

[105] R. Amin, D. B. Ravnsbæk, Y. M. Chiang, *Journal of the Electrochemical Society* **2015**, *162*, A1163.

[106] H. Tukamoto, A. R. West, *Journal of the Electrochemical Society* **1997**, *144*, 3164.

[107] W. L. Bragg, *Nature* **1912**, *90*, 410.

[108] W. H. Bragg, *Nature* **1912**, *90*, 360.

[109] P. J. Brown, A. G. Fox, E. N. Maslen, M. A. O'Keefe, B. T. M. Willis in *International Tables for Crystallography*, (Ed.: E. Prince), International Union of Crystallography, Wiley, **2006**, p. 554.

[110] P. Scherrer in *Kolloidchemie Ein Lehrbuch*, Springer, Berlin, Heidelberg, **1912**, p. 387.

[111] *The Rietveld Method*, (Ed.: R. A. Young), International Union of Crystallography, Oxford University Press, New York, **1995**.

[112] B. H. Toby, *Powder Diffraction* **2006**, *21*, 67.

[113] T. Egami in *Local Structure from Diffraction*, (Eds.: S. Billinge, M Thorpe), Springer, Boston, MA, **1998**, p. 1.

[114] E. Takeshi, S. J. Billinge, *Underneath the Bragg Peaks: Structural Analysis of Complex Materials*, *Vol. 16*, (Eds.: E. Takeshi, S. J. Billinge), Elsevier, **2012**.

[115] S. J. L. Billinge in *Uniting Electron Crystallography and Powder Diffraction. NATO Science for Peace and Security Series B: Physics and Biophysics*, (Eds.: U. Kolb, K. Shankland, L. Meshi, A. Avilov, W. David), Springer, Dordrecht, **2012**, p. 183.

[116] N. Metropolis, S. Ulam, *Journal of the American Statistical Association* **1949**, *44*, 335.

[117] R. L. McGreevy, L. Pusztai, *Molecular Simulation* **1988**, *1*, 359.

[118] M. G. Tucker, D. A. Keen, M. T. Dove, A. L. Goodwin, Q. Hui, *Journal of Physics Condensed Matter* **2007**, *19*, 335218.

[119] M. Tucker, M. Dove, A. Goodwin, D. Keen, H. Playford, W. A. Slawinski, RMCProfile User Manual (Code Verison 6.7.0), http://www.rmcprofile.org/imagesFhj/d/d5/Rmcprofile_v6.7_manual.pdf (accessed: 2020-02-06), **2017**.

[120] D. B. Williams, C. B. Carter, *Transmission Electron Microscopy - A Textbook for Materials Science*, Springer, **2009**.

[121] J. E. Penner-Hahn in *Comprehensive Coordination Chemistry II*, *Vol. 2*, Elsevier Ltd, **2003**, p. 160.

[122] P. Glatzel, U. Bergmann, *Coordination Chemistry Reviews* **2005**, *249*, 65.

[123] B. H. Bransden, C. J. Joachain, *Physics of Atoms and Molecules*, Longman Scientific & Technical, Harlow, **1983**.

[124] J. A. Bearden, A. F. Burr, *Reviews of Modern Physics* **1967**, *39*, 125.

[125] A. J. Achkar, T. Z. Regier, E. J. Monkman, K. M. Shen, D. G. Hawthorn, *Scientific Reports* **2011**, *1*, 1.

[126] T. C. Weng, G. S. Waldo, J. E. Penner-Hahn, *Journal of Synchrotron Radiation* **2005**, *12*, 506.

[127] P. Glatzel, U. Bergmann, J. Yano, H. Visser, J. Robblee, W. Gu, F. De Groot, G. Christou, V. Pecoraro, S. Cramer, V. Yachandra, *Journal of the American Chemical Society* **2004**, *126*, 9946.

[128] P. Glatzel, G. Smolentsev, G. Bunker, *Journal of Physics: Conference Series* **2009**, *190*, 012046.

[129] F. De Groot, G. Vanko, P. Glatzel, *Journal of Physics Condensed Matter* **2009**, *21*, 104207.

[130] M. Bauer, *Physical Chemistry Chemical Physics* **2014**, *16*, 13827.

[131] P. Eisenberger, P. M. Platzman, H. Winick, *Physical Review Letters* **1976**, *36*, 623.

[132] H. H. Johann, *Zeitschrift für Physik* **1931**, *69*, 185.

[133] A. C. Thompson, D. T. Attwood, E. M. Gullikson, M. R. Howells, J. B. Kortright, A. L. Robinson, J. H. Underwood, K.-J. Kim, J. Kirz, I. Lindau, P. Pianetta, H. Winick, G. P. Williams, J. H. Scofield, *X-Ray Data Booklet*, 2nd ed., (Eds.: A. C. Thompson, D. Vaughan), Lawrence Berkeley National Laboratory, Berkeley, CA, **2001**.

[134] R. D. Cowan, *The Theory of Atomic Structure and Spectra*, University of California Press, **1981**.

[135] P. Glatzel, *X-Ray Fluorescence Emission Following K Capture and 1s Photoionization of Mn and Fe in Various Chemical Environments*, PhD Thesis, University of Hamburg, **2001**.

[136] G. Vanko, T. Neisius, G. Molnar, F. Renz, S. Karpati, A. Shukla, F. De Groot, *Journal of Physical Chemistry B* **2006**, *110*, 11647.

[137] S. Lafuerza, H. Gretarsson, F. Hardy, T. Wolf, C. Meingast, G. Giovannetti, M. Capone, A. S. Sefat, Y.-J. Kim, P. Glatzel, L. de Medici, *Physical Review B* **2017**, *96*, 045133.

[138] P. Glatzel, M Sikora, M Fernandez-Garcia, *European Physical Journal: Special Topics* **2009**, *169*, 207.

[139] O. J. Borkiewicz, K. M. Wiaderek, P. J. Chupas, K. W. Chapman, *The Journal of Physical Chemistry Letters* **2015**, *6*, 2081.

[140] G. Assat, D. Foix, C. Delacourt, A. Iadecola, R. Dedryvère, J.-M. Tarascon, *Nature Communications* **2017**, *8*, 2219.

[141] G. Assat, J.-M. Tarascon, *Nature Energy* **2018**, *3*, 373.

[142] H. Konishi, T. Hirano, D. Takamatsu, A. Gunji, X. Feng, S. Furutsuki, *Journal of Power Sources* **2015**, *298*, 144.

[143] S. M. Bak, Z. Shadike, R. Lin, X. Yu, X. Q. Yang, *NPG Asia Materials* **2018**, *10*, 563.

[144] B. Song, S. J. Day, T. Sui, L. Lu, C. C. Tang, A. M. Korsunsky, *Physical Chemistry Chemical Physics* **2016**, *18*, 4745.

[145] T. Kim, B. Song, A. J. Lunt, G. Cibin, A. J. Dent, L. Lu, A. M. Korsunsky, *Materials & Design* **2016**, *98*, 231.

[146] T. Kim, B. Song, A. J. Lunt, G. Cibin, A. J. Dent, L. Lu, A. M. Korsunsky, *Chemistry of Materials* **2016**, *28*, 4191.

[147] S. Pongha, B. Seekoaon, W. Limphirat, P. Kidkhunthod, S. Srilomsak, Y. M. Chiang, N. Meethong, *Advanced Energy Materials* **2015**, *5*, 1500663.

[148] H. Koga, L. Croguennec, M. Ménétrier, P. Mannessiez, F. Weill, C. Delmas, S. Belin, *The Journal of Physical Chemistry C* **2014**, *118*, 5700.

[149] O. J. Borkiewicz, B. Shyam, K. M. Wiaderek, C. Kurtz, P. J. Chupas, K. W. Chapman, *Journal of Applied Crystallography* **2012**, *45*, 1261.

[150] N. Takeda, I. Ikeuchi, R. Natsui, K. Nakura, N. Yabuuchi, *ACS Applied Energy Materials* **2019**, *2*, 1629.

[151] Z. Q. Deng, A. Manthiram, *Journal of Physical Chemistry C* **2011**, *115*, 7097.

[152] V. Pralong, V. Gopal, V. Caignaert, V. Duffort, B. Raveau, *Chemistry of Materials* **2012**, *24*, 12.

[153] J. S. Kim, C. S. Johnson, J. T. Vaughey, M. M. Thackeray, S. A. Hackney, W. Yoon, C. P. Grey, *Chemistry of Materials* **2004**, *16*, 1996.

[154] A. H. Whitehead, M. Schreiber, *Journal of the Electrochemical Society* **2005**, *152*, A2105.

[155] Element Six Technologies Limited, EP Poly 10.0x10.0mm, 0.60mm thick, NP, tech. data, https://e6cvd.com/uk/application/electrochemistry/pe-10x10-mm-0-6-mm-thick.html (accessed: 2019-08-18).

[156] HTW Hochtemperatur-Werkstoffe GmbH, Sigradur G, tech. data, http://www.htw-germany.com/technology.php5?lang=en&navo=2&navi=16 (accessed: 2020-01-09), **2006**.

[157] DuPont de Nemours Inc., DUPONT KAPTON® Summary of Properties, tech. datasheet., https://www.dupont.com/content/dam/dupont/products-and-services/membranes-and-films/polyimde-films/documents/DEC-Kapton-summary-of-properties.pdf (accessed: 2020-01-09), **2017**.

[158] J. V. Macpherson, *Physical Chemistry Chemical Physics* **2015**, *17*, 2935.

[159] Element Six Technologies Limited, The Element Six CVD Diamond Handbook, tech. rep., https://e6cvd.com/media/wysiwyg/pdf/E6_CVD_Diamond_Handbook.pdf (accessed: 2020-01-09), **2015**.

[160] E. B. Saloman, J. H. Hubbell, X-ray Attenuation Coefficients (Total Cross Sections): Comparison of the Experimental Data Base With the Recommended Values of Henke and the Theoretical Values of Scofield for Energies Between 0.1-100 keV, tech. rep., NBSIR 86-3431, **1986**.

[161] E. B. Saloman, J. H. Hubbell, J. H. Scofield, *Atomic Data and Nuclear Data Tables* **1988**, *38*, 1.

[162] M. D. Stoller, S. A. Stoller, N. Quarles, J. W. Suk, S. Murali, Y. Zhu, X. Zhu, R. S. Ruoff, *Journal of Applied Electrochemistry* **2011**, *41*, 681.

[163] Lee Spring Limited, Compression Spring Specifications LWM16 090 2344S, tech. data, https://www.leespring.co.uk/uk_product_spec.asp?partnum=LWM160902344S&springType=C&subType= (accessed: 2020-01-08).

[164] J. R. A. Davis, *Properties and Selection: Nonferrous Alloys and Special-Purpose Materials, Vol. 2*, 10th ed, ASM International, Materials Park, Ohio, **1990**, p. 1117.

[165] Alcoa Corporation, ALLOY 7075 - Understanding Cold Finished Aluminum Alloys, tech. datasheet., https://www.spacematdb.com/spacemat/manudatasheets/alcoa_alloy_7075.pdf (accessed: 2020-01-09), **2004**.

[166] Gleich GmbH Metallplatten Service, EN AW 7075 [AlZn5,5MgCu], tech. datasheet, https://gleich.de/files/en_aw_7075.en.pdf (accessed. 2020-01-09).

[167] Smiths Metal Centres Limited, 7075 Aluminium, tech. datasheet, https://www.smithmetal.com/pdf/aluminium/7xxx/7075.pdf (accessed: 2020-01-09), **2018**.

[168] Smiths Metal Centres Limited, PEEK (PolyEtherEtherKetone), tech. datasheet, https://www.smithmetal.com/pdf/plastics/peek.pdf (accessed: 2020-01-09), **2018**.

[169] Smiths Metal Centres Limited, 316 / 316L Stainless, tech. datasheet, https://www.smithmetal.com/pdf/stainless/316-316l-stainless.pdf (accessed:2020-01-09), **2018**.

[170] Aurubis Finland Oy, Cu-OF, tech. datasheet, https://finland.aurubis.com/fileadmin/media/pdf/EN/industiral-products-specifications-2013fall/CU_OF.pdf (accessed: 2020-01-10).

[171] Polymax Limited, FKM 75 ShA, tech. datasheet, https://www.polymax.co.uk/media/documents/Datasheet/fkm_viton_75sha_oring_polymax.pdf (accessed: 2020-01-08).

[172] G. Assat, C. Delacourt, D. A. D. Corte, J.-M. Tarascon, *Journal of The Electrochemical Society* **2016**, *163*, A2965.

[173] M. Okubo, A. Yamada, *ACS Applied Materials and Interfaces* **2017**, *9*, 36463.

[174] J. M. Tarascon, G. Vaughan, Y. Chabre, L. Seguin, M. Anne, P. Strobel, G. Amatucci, *Journal of Solid State Chemistry* **1999**, *147*, 410.

[175] N. Guerrini, L. Jin, J. G. Lozano, K. Luo, A. Sobkowiak, K. Tsuruta, F. Massel, L.-C. Duda, M. R. Roberts, P. G. Bruce, *Chemistry of Materials* **2020**, *32*, 3733.

[176] X. Liu, D. Wang, G. Liu, V. Srinivasan, Z. Liu, Z. Hussain, W. Yang, *Nature Communications* **2013**, *4*, 1.

[177] M. Blum, L. Weinhardt, O. Fuchs, M. Bar, Y. Zhang, M. Weigand, S. Krause, S. Pookpanratana, T. Hofmann, W. Yang, J. D. Denlinger, E. Umbach, C. Heske, *Review of Scientific Instruments* **2009**, *80*, 123102.

[178] P. Jiang, J. L. Chen, F. Borondics, P. A. Glans, M. W. West, C. L. Chang, M. Salmeron, J. Guo, *Electrochemistry Communications* **2010**, *12*, 820.

[179] D. Asakura, Y. Nanba, M. Okubo, H. Niwa, H. Kiuchi, J. Miyawaki, M. Oshima, E. Hosono, Y. Harada, *Physical Chemistry Chemical Physics* **2019**, *21*, 26351.

[180] Y. C. Lu, E. J. Crumlin, T. J. Carney, L. Baggetto, G. M. Veith, N. J. Dudney, Z. Liu, Y. Shao-Horn, *Journal of Physical Chemistry C* **2013**, *117*, 25948.

[181] Y. C. Lu, E. J. Crumlin, G. M. Veith, J. R. Harding, E. Mutoro, L. Baggetto, N. J. Dudney, Z. Liu, Y. Shao-Horn, *Scientific Reports* **2012**, *2*, 1.

[182] W. C. Chueh, F. El Gabaly, J. D. Sugar, N. C. Bartelt, A. H. McDaniel, K. R. Fenton, K. R. Zavadil, T. Tyliszczak, W. Lai, K. F. McCarty, *Nano Letters* **2013**, *13*, 866.

[183] E. Hu, X. Yu, R. Lin, X. Bi, J. Lu, S. Bak, K. W. Nam, H. L. Xin, C. Jaye, D. A. Fischer, K. Amine, X. Q. Yang, *Nature Energy* **2018**, *3*, 690.

[184] B. H. Toby, R. B. Von Dreele, *Journal of Applied Crystallography* **2013**, *46*, 544.

[185] B. Ravel, M. Newville in Journal of Synchrotron Radiation, *Vol. 12*, **2005**, p. 537.

[186] M. Diaz-Lopez, Y. Joly, M. Freire, C. Colin, O. Proux, V. Pralong, P. Bordet, *Journal of Physical Chemistry C* **2018**, *122*, 29586.

[187] C. F. Petersburg, Z. Li, N. A. Chernova, M. S. Whittingham, F. M. Alamgir, *Journal of Materials Chemistry* **2012**, *22*, 19993.

[188] N. A. Chernova, M. Ma, J. Xiao, M. S. Whittingham, J. Breger, C. P. Grey, *Chemistry of Materials* **2007**, *19*, 4682.

[189] P. Glatzel, U. Bergmann, W. Gu, H. Wang, S. Stepanov, B. S. Mandimutsira, C. G. Riordan, C. P. Horwitz, T. Collins, S. P. Cramer, *Journal of the American Chemical Society* **2002**, *124*, 9668.

[190] G. Vankó, F. M. F. de Groot, S. Huotari, R. J. Cava, T. Lorenz, M. Reuther, *http://arxiv.org/abs/0802.2744* **2008**.

[191] F. Farges, *Physical Review B* **2005**, *71*, 155109.

[192] T. Uozumi, K. Okada, A. Kotani, O. Durmeyer, J. P. Kappler, E. Beaurepaire, J. C. Parlebas, *Europhysics Letters (EPL)* **1992**, *18*, 85.

[193] E. L. Shirley, *Journal of Electron Spectroscopy and Related Phenomena* **2004**, *136*, 77.

[194] A. Juhin, F. De Groot, G. Vanko, M. Calandra, C. Brouder, *Physical Review B - Condensed Matter and Materials Physics* **2010**, *81*, 1.

[195] J. Kawai, C. Suzuki, H. Adachi, T. Konishi, Y. Gohshi, *Physical Review B* **1994**, *50*, 11347.

[196] J. C. Garcia, J. Bareño, J. Yan, G. Chen, A. Hauser, J. R. Croy, H. Iddir, *The Journal of Physical Chemistry C* **2017**, *121*, 8290.

[197] J. Van Elp, J. L. Wieland, H. Eskes, P. Kuiper, G. A. Sawatzky, F. M. De Groot, T. S. Turner, *Physical Review B* **1991**, *44*, 6090.

[198] M. T. Czyzyk, R. Potze, G. A. Sawatzky, *Physical Review B* **1992**, *46*, 3729.

[199] F. De Groot, *AIP Conference Proceedings* **2007**, *882*.

[200] H. Niwa, K. Higashiyama, K. Amaha, W. Kobayashi, K. Ishii, Y. Moritomo, *Applied Physics Express* **2019**, *12*, 052005.

[201] L. Simonin, J. F. Colin, V. Ranieri, E. Canevet, J. F. Martin, C. Bourbon, C. Baehtz, P. Strobel, L. Daniel, S. Patoux, *Journal of Materials Chemistry* **2012**, *22*, 11316.

[202] E. Boivin, N. Guerrini, R. A. House, J. G. Lozano, L. Jin, G. J. Rees, J. W. Somerville, C. Kuss, M. R. Roberts, P. G. Bruce, *Advanced Functional Materials* **2021**, *31*, 1.

[203] M. Gu, A. Genc, I. Belharouak, D. Wang, K. Amine, S. Thevuthasan, D. R. Baer, J. G. Zhang, N. D. Browning, J. Liu, C. Wang, *Chemistry of Materials* **2013**, *25*, 2319.

[204] A. Devaraj, R. Colby, M. Gu, C. Wang, T. Tyliszczak, J. Zhang, J. Xiao, J. Zheng, I. Belharouak, D. Wang, K. Amine, S. Thevuthasan, *Microscopy and Microanalysis* **2013**, *19*, 964.

[205] P. K. Allan, J. M. Griffin, A. Darwiche, O. J. Borkiewicz, K. M. Wiaderek, K. W. Chapman, A. J. Morris, P. J. Chupas, L. Monconduit, C. P. Grey, *Journal of the American Chemical Society* **2016**, *138*, 2352.

[206] J. M. Stratford, P. K. Allan, O. Pecher, P. A. Chater, C. P. Grey, *Chemical Communications* **2016**, *52*, 12430.

[207] J. M. Stratford, M. Mayo, P. K. Allan, O. Pecher, O. J. Borkiewicz, K. M. Wiaderek, K. W. Chapman, C. J. Pickard, A. J. Morris, C. P. Grey, *Journal of the American Chemical Society* **2017**, *139*, 7273.

[208] H. Jung, P. K. Allan, Y. Y. Hu, O. J. Borkiewicz, X. L. Wang, W. Q. Han, L. S. Du, C. J. Pickard, P. J. Chupas, K. W. Chapman, A. J. Morris, C. P. Grey, *Chemistry of Materials* **2015**, *27*, 1031.

[209] C. J. Kerr, *NMR and Neutron Total Scattering Studies of Silicon-Based Anode Materials for Lithium-Ion Batteries*, PhD Thesis, University of Cambridge, **2016**.

[210] M. Diaz-Lopez, M. Freire, Y. Joly, C. V. Colin, H. E. Fischer, N. Blanc, N. Boudet, V. Pralong, P. Bordet, *Chemistry of Materials* **2018**, *30*, 3060.

[211] P. Juhas, T. Davis, C. L. Farrow, S. J. Billinge, *Journal of Applied Crystallography* **2013**, *46*, 560.

[212] T. Proffen, S. J. Billinge, *Journal of Applied Crystallography* **1999**, *32*, 572.

[213] N. Kitamura, N. Ishida, Y. Idemoto, *Electrochemistry* **2016**, *84*, 789.

[214] H. Y. Playford, A. C. Hannon, M. G. Tucker, D. M. Dawson, S. E. Ashbrook, R. J. Kastiban, J. Sloan, R. I. Walton, *Journal of Physical Chemistry C* **2014**, *118*, 16188.

[215] L. R. Owen, H. Y. Playford, H. J. Stone, M. G. Tucker, *Acta Materialia* **2016**, *115*, 155.

[216] B. H. Toby, *Journal of Applied Crystallography* **2001**, *34*, 210.

[217] A. Larson, R. B. Von Dreele, General Structure Analysis System (GSAS), Los Alamos National Laboratory Report LAUR 86-748, tech. rep., Los Alamos National Laboratory, **2004**.

[218] J. Neuefeind, M. Feygenson, J. Carruth, R. Hoffmann, K. K. Chipley, *Nuclear Instruments and Methods in Physics Research Section B: Beam Interactions with Materials and Atoms* **2012**, *287*, 68.

[219] C. L. Farrow, P. Juhas, J. W. Liu, D. Bryndin, E. S. Boin, J. Bloch, T. Proffen, S. J. Billinge, *Journal of Physics Condensed Matter* **2007**, *19*, 335219.

[220] S. P. Ong, W. D. Richards, A. Jain, G. Hautier, M. Kocher, S. Cholia, D. Gunter, V. L. Chevrier, K. A. Persson, G. Ceder, *Computational Materials Science* **2013**, *68*, 314.

[221] V. F. Sears, *Neutron News* **1992**, *3*, 26.

[222] J. M. Cowley, *Physical Review* **1950**, *77*, 669.

[223] J. M. Cowley, *Physical Review* **1965**, *138*, A1384.

[224] R. D. Shannon, *Acta Crystallographica Section A* **1976**, *32*, 751.

[225] R. A. House, G. J. Rees, M. A. Pérez-Osorio, J. J. Marie, E. Boivin, A. W. Robertson, A. Nag, M. Garcia-Fernandez, K. J. Zhou, P. G. Bruce, *Nature Energy* **2020**, *5*, 777–785.

[226] U. Bergmann, C. R. Horne, T. J. Collins, J. M. Workman, S. P. Cramer, *Chemical Physics Letters* **1999**, *302*, 119.

[227] M. Dolle, F. Orsini, A. S. Gozdz, J.-M. Tarascon, *Journal of The Electrochemical Society* **2001**, *148*, A851.

[228] C. G. Thurston, J. R. Owen, N. J. Hargreaves, *Journal of Power Sources* **1992**, *39*, 215.

[229] Q. Wu, W. Lu, J. Prakash, *Journal of Power Sources* **2000**, *88*, 237.

[230] A. Blyr, C. Sigala, G. Amatucci, D. Guyomard, Y. Chabre, J.-M. Tarascon, *Journal of the Electrochemical Society* **1998**, *145*, 194.

[231] O. Arnold, J. C. Bilheux, J. M. Borreguero, A. Buts, S. I. Campbell, L. Chapon, M. Doucet, N. Draper, R. Ferraz Leal, M. A. Gigg, V. E. Lynch, A. Markvardsen, D. J. Mikkelson, R. L. Mikkelson, R. Miller, K. Palmen, P. Parker, G. Passos, T. G. Perring, P. F. Peterson, S. Ren, M. A. Reuter, A. T. Savici, J. W. Taylor, R. J. Taylor, R. Tolchenov, W. Zhou, J. Zikovsky, *Nuclear Instruments and Methods in Physics Research Section A: Accelerators Spectrometers Detectors and Associated Equipment* **2014**, *764*, 156.

[232] A. K. Soper, Science & Technology Facilities Council, Rutherford Appleton Laboratory Technical Report RAL-TR-2011-013: GudrunN and GudrunX: Programs for Correcting Raw Neutron and X-ray Diffraction Data to Differential Scattering Cross Section. Tech. rep., Didcot, UK, **2011**.

[233] C. Zhan, J. Lu, A. Jeremy Kropf, T. Wu, A. N. Jansen, Y. K. Sun, X. Qiu, K. Amine, *Nature Communications* **2013**, *4*, 2437.

[234] D. H. Jang, Y. J. Shin, S. M. Oh, *Journal of The Electrochemical Society* **1996**, *143*, 2204.

[235] R. J. Gummow, A. de Kock, M. M. Thackeray, *Solid State Ionics* **1994**, *69*, 59.

[236] G. G. Amatucci, C. N. Schmutz, A. Blyr, C. Sigala, A. S. Gozdz, D. Larcher, J. M. Tarascon, *Journal of Power Sources* **1997**, *69*, 11.

[237] M Levi, G. Salitra, B Markovsky, H Teller, D Aurbach, U Heider, L Heider, *Journal of The Electrochemical Society* **1999**, *146*, 1279.

[238] U. Westerhoff, K. Kurbach, F. Lienesch, M. Kurrat, *Energy Technology* **2016**, *4*, 1620.

[239] B. Hirschorn, M. E. Orazem, B. Tribollet, V. Vivier, I. Frateur, M. Musiani, *Electrochimica Acta* **2010**, *55*, 6218.

[240] G. J. Brug, A. L. van den Eeden, M. Sluyters-Rehbach, J. H. Sluyters, *Journal of Electroanalytical Chemistry* **1984**, *176*, 275.

[241] J. Hong, W. E. Gent, P. Xiao, K. Lim, D.-H. Seo, J. Wu, P. M. Csernica, C. J. Takacs, D. Nordlund, C.-J. Sun, K. H. Stone, D. Passarello, W. Yang, D. Prendergast, G. Ceder, M. F. Toney, W. C. Chueh, *Nature Materials* **2019**, *18*, 256.